

GPO PRICE \$ _____

CFSTI PRICE(S) \$ _____

NASA CR-66398

Hard copy (HC) 3.00

VOLUME II DESIGN FEASIBILITY

Microfiche (MF) 165

14 APRIL 1967

ff 653 July 65

**PRELIMINARY DESIGN STUDY
OF
SLAMAST
SCOUT-LAUNCHED ADVANCED MATERIALS
AND STRUCTURES TEST-BED**

**VOLUME II
DESIGN FEASIBILITY**

CONTRACT NO. NAS 1-7014

Distribution of this report is provided in the interest
of information exchange. Responsibility for the contents
resides in the author or organization that prepared it.

N67-31097

FACILITY FORM 602

(ACCESSION NUMBER)

243

(PAGES)

CR-66398

(NASA CR OR TMX OR AD NUMBER)

(THRU)

(CODE)

(CATEGORY)

GENERAL  ELECTRIC
RE-ENTRY SYSTEMS DEPARTMENT

NASA CR-66398

VOLUME II DESIGN FEASIBILITY

14 APRIL 1967

**PRELIMINARY DESIGN STUDY
OF
SLAMAST
SCOUT-LAUNCHED ADVANCED MATERIALS
AND STRUCTURES TEST-BED**

**VOLUME II
DESIGN FEASIBILITY**

CONTRACT NO. NAS 1-7014

Prepared for

National Aeronautics and Space Administration
Langley Research Center
Langley Station
Hampton, Virginia

GENERAL  ELECTRIC

RE-ENTRY SYSTEMS DEPARTMENT

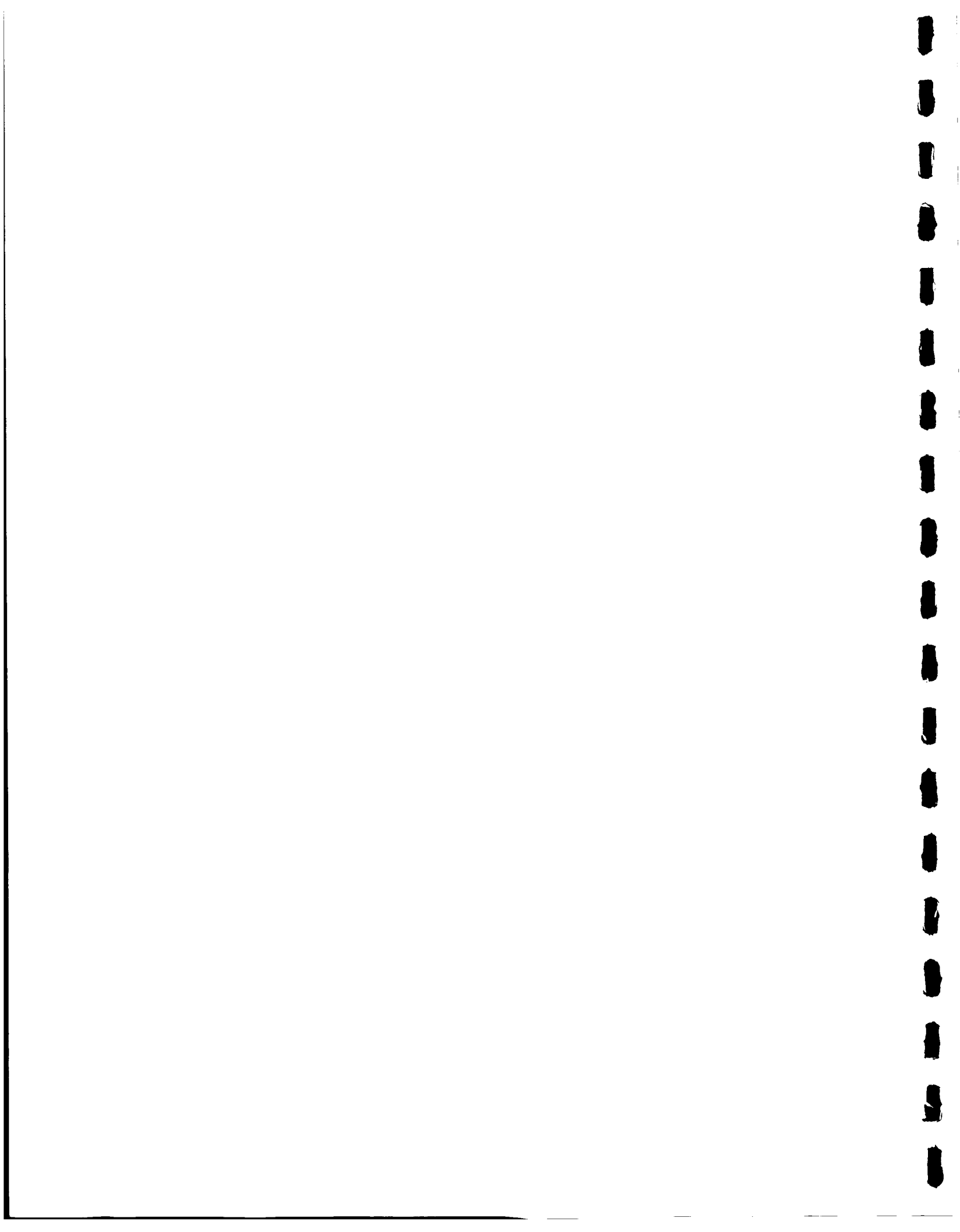
A Department Of The Missile and Space Division

3198 Chestnut Street, Philadelphia 4, Penna.

PRECEDING PAGE BLANK NOT FILMED.

ABSTRACT

This report presents the results of a feasibility study of a small, lifting re-entry vehicle test-bed capable of being launched by a Scout launch vehicle and capable of being recovered. The purpose of the study was to determine if it was possible to conduct meaningful, sub-scale, thermostructural experiments involving panels of interest of representative full scale, manned, lifting re-entry vehicles. The study was based upon the HL-10 vehicle concept.



CONTENTS

<u>Section</u>	<u>Page</u>
1. INTRODUCTION	1
2. SUMMARY	11
2.1 General	11
2.2 Capability	12
2.3 Flexibility	13
2.3.1 Boost and Re-entry	13
2.3.2 Pull-out	13
2.3.3 Glide	13
2.3.4 Recovery	14
2.3.5 Control System	14
2.4 Redundancy	14
2.4.1 Data Transmittal	14
2.4.2 Mission Termination	14R
2.4.3 Structure	15
2.4.4 Destruct	15
2.4.5 Pyrotechnic Initiation Devices	15
3. SYSTEM REQUIREMENTS	19
3.1 Development of General Requirements	19
3.1.1 Launch Vehicle	19
3.1.2 Design Trajectories	21
3.1.3 Communication	25
3.1.4 Recovery	26
3.1.5 Range Safety	26
3.2 Aerodynamic Studies	28
3.2.1 Aerodynamic Definitions and Nomenclature	28
3.2.2 Configuration Aerodynamics	36
3.2.3 Aerodynamic Performance, Stability, and Control	54
3.2.4 Aerodynamic Pressure Distributions and Loads	82
3.3 Flight Dynamics Studies	99
3.3.1 Trajectory Studies	99

CONTENTS (Cont'd)

<u>Section</u>		<u>Page</u>
	3.3.2 Design Trajectories	101
	3.3.3 Footprint Studies	101
	3.3.4 Recovery Envelope	102
	3.3.5 Tip-off Rate Tolerances	102
	3.3.6 Vehicle Inertia Characteristic Tolerances	103
	3.3.7 Re-entry Dynamics	103
3.4	Thermodynamic Studies	119
	3.4.1 Aerodynamic Heating	119
	3.4.2 Nose Cap Heating	119
	3.4.3 Skirt Heating	121
	3.4.4 Pitch Flap and Drag Brake Heating	125
	3.4.5 Nose Cap, Skirt, Pitch Flap, and Drag Brake Shear Stress	126
	3.4.6 Thermal Design Results	126
	3.4.7 Internal Environmental Control	131
	3.4.8 Material Selection	133
	3.4.9 Symbols and Subscripts	140
3.5	Instrumentation and Communication Studies	185
	3.5.1 Plasma Attenuation	185
	3.5.2 T/M and Instrumentation System Selection	189
	3.5.3 Trade-offs	191
3.6	Recovery Force Studies	215
	3.6.1 Introduction	215
	3.6.2 Basic Flight Conditions	215
	3.6.3 Development of Nominal Recovery Box	215
	3.6.4 Capabilities of Recovery Force Components	216
	3.6.5 Recovery Force Composition	216
	3.6.6 Proposed Recovery Area	217
3.7	Range Safety Studies	219
	3.7.1 Introduction	219
	3.7.2 Discussion	220
	3.7.3 Flight Termination Considerations	221

ILLUSTRATIONS

<u>Figure</u>		<u>Page</u>
1-1	Overall Program Schedule	2
1-2	Analysis Schedule	3
1-3	Subsystem Development Schedule	7
1-4	Integrated Test Schedule	9
2-1	SLAMAST S/C	16
2-2	SLAMAST Structural Arrangement	17
3.1-1	Scout Re-entry Performance at Burnout	20
3.1-2	SLAMAST/Scout Vehicle Launch Configuration	22
3.1-3	SLAMAST Typical Flight Mission Profile	24
3.2-1	SLAMAST Body Axes Coordinate System Representation	28
3.2-2	Basic SLAMAST External Dimensioning System	37
3.2-3	Ellipticity Variation with Fractional Length	37
3.2-4	Peripheral Surface Slope versus Meridian Angle	38
3.2-5	SLAMAST Plus Drag Brake Normalized Dimensions	38
3.2-6	Drag versus Mach Number	41
3.2-7	Drag versus Flap Deflection	42
3.2-8	Representative Recovery Trajectory with Drag Brake Flap	43
3.2-9	Dynamic Pressure and Mach Number for SLAMAST Recovery	44
3.2-10	Maximum Dynamic Pressure and Simultaneous Mach Number for SLAMAST Recovery	45
3.2-11	Location of Flap Center-of-Pressure for Laminar Separated Flow for $\delta_F = -30^\circ$	47
3.2-12	Hinge Moment versus Time - 63" Vehicle (1.6 m)	47
3.2-13	Effect of Varying Flap Deflection on Hinge Moment During Recovery	48
3.2-14	Inboard Split Flaps: Lift Force Characteristics	51
3.2-15	Inboard Split Flaps: Pitch Stability Characteristics	51
3.2-16	Inboard Split Flaps: Yawing Moment Characteristics	52
3.2-17	Inboard Split Flaps: Rolling Moment Characteristics	52
3.2-18	Inboard Split Flaps: Side Force Characteristics	53
3.2-19	Inboard Split Flaps: Yaw/Roll Coupling	53
3.2-20	Pitch Force Characteristics	55
3.2-21	Lift Force Variation with Pitch Angle	55
3.2-22	Drag Force Variation with Pitch Angle	56
3.2-23	Pitching Moment Characteristics	56
3.2-24	Pitching Moment Variation with Sideslip Angle	57
3.2-25	Axial Force Variation with Pitch Angle	57
3.2-26	Estimated Maximum Trimmed Lift Coefficient versus Mach Number	58
3.2-27	Variation of Flap Deflection with Angle-of-Attack for Trimmed Flight, $10 \leq M \leq 20$, Estimated	58
3.2-28	Effect of Center-of-Gravity Location on Trimmed Lift and Angle-of- Attack, Inboard Flaps at $M = 3.95$	62
3.2-29	Effect of Center-of-Gravity Location on Trimmed Lift and Angle-of- Attack, Inboard Flaps at $M = 4.63$	63

ILLUSTRATIONS (Cont'd)

<u>Figure</u>		<u>Page</u>
3.2-30	Effect of Center-of-Gravity Location on Lift-curve, Inboard Flaps at $M = 3.95$	64
3.2-31	Effect of Center-of-Gravity Location on Lift-curve, Inboard Flaps at $M = 4.63$	64
3.2-32	Effect of Center-of-Gravity Location on Trim (L/D) Ratio, Inboard Flaps at $M = 3.95$	65
3.2-33	Effect of Center-of-Gravity Location on Trim (L/D) Ratio, Inboard Flaps at $M = 4.63$	66
3.2-34	Typical Flap Effectiveness at $M = 10$	67
3.2-35	Flap Effectiveness at $\alpha = 0$ versus Mach Number	67
3.2-36	Flap Effectiveness versus Deflection at $\alpha = 0$, Selected Mach Numbers	68
3.2-37	Incremental Moment Due to Flap for $10 \leq M \leq 20$	68
3.2-38	Flap Effectiveness for $10 \leq M \leq 20$ versus Flap Deflection	69
3.2-39	Flap Effectiveness at $M = 4.63$ versus Angle-of-Attack	69
3.2-40	Flap Effectiveness at $M = 4.63$ versus Flap Deflection	70
3.2-41	Side Force Variation with Sideslip Angle	70
3.2-42	Rolling and Yawing Moment Variations with Sideslip Angle	71
3.2-43	Relative Location of Yaw Center-of-Pressure at $M = 3.95$	71
3.2-44	Relative Location of Yaw Center-of-Pressure at $M = 4.63$	72
3.2-45	Location of Pitch and Yaw Centers-of-Pressure at $M = 3.95$	72
3.2-46	Location of Pitch and Yaw Centers-of-Pressure at $M = 4.63$	73
3.2-47	Pitch Stability for 25° Differential Flaps at $M = 3.95$	73
3.2-48	Pitch Stability for 25° Differential Flaps at $M = 4.63$	75
3.2-49	Damping In Pitch Derivatives	75
3.2-50	Effect of Center-of-Gravity Location on Pitch Damping Derivatives	76
3.2-51	Damping In Roll Derivatives	76
3.2-52	Damping In Yaw Derivatives	77
3.2-53	Comparison of Estimated SLAMAST Dynamic Stability with SORTIE 1-D Test Data at 10.18 Mach Number	77
3.2-54	Comparison of SLAMAST and SORTIE 1-D Geometric Shape	78
3.2-55	Nose Cap Transverse Pressure Distribution for $\alpha = 0$	84
3.2-56	Nose Cap Transverse Pressure Distribution for $\alpha = 15^\circ$	84
3.2-57	Nose Cap Radial Pressure Distribution for $\alpha = 0$	85
3.2-58	Nose Cap Radial Pressure Distribution for $\alpha = 15^\circ$	85
3.2-59	Nose Cap Longitudinal Pressure Distribution for $\alpha = 0$ and 15°	86
3.2-60	Variation of Windward Ray Pressures for Wrapped Surface Regions	86
3.2-61	Modified Newtonian Pressure Distributions for Wrapped Surface Regions	87
3.2-62	Correlation of Flap Centerline Pressure for Laminar Separated Flow	88

ILLUSTRATIONS (Cont'd)

<u>Figure</u>		<u>Page</u>
3.2-63	Flap Pressure Distribution for Laminar Separated Flow	89
3.2-64	Cumulative Normal Force Coefficient Distribution	92
3.2-65	Cumulative Axial Force Coefficient Distribution	92
3.2-66	Incremental Moment Coefficient Distribution	93
3.2-67	Cumulative Moment Coefficient Distribution	93
3.2-68	Flap Panel Load Coefficient versus Flap Deflection Angle	94
3.2-69	Flap Panel Load Coefficient versus Flap Deflection Angle, Negative Angles-of-Attack	94
3.2-70	Flap Panel Load Coefficient versus Angle-of-Attack	95
3.2-71	Flap Hinge Moment Coefficient versus Angle-of-Attack	95
3.2-72	Flap Hinge Moment Coefficient versus Flap Deflection Angle	96
3.2-73	Flap Hinge Moment Coefficient versus Flap Deflection Angle, Negative Angles-of-Attack	96
3.2-74	Flap Hinge Moment Coefficient Variation with Angle-of-Attack for Trimmed Flight	97
3.3-1	SLAMAST Stagnation Heating, $\alpha_o = 25.3^\circ$	105
3.3-2	SLAMAST Stagnation Heating, $\alpha_o = 17.9^\circ$	105
3.3-3	SLAMAST Stagnation Heating, $\alpha_o = 13.9^\circ$	106
3.3-4	SLAMAST Maximum Stagnation Heat Rate	106
3.3-5	SLAMAST Re-entry, $\gamma_o = -1^\circ$	107
3.3-6	SLAMAST Re-entry, $\gamma_o = -1^\circ$	107
3.3-7	SLAMAST Re-entry, $\gamma_o = -1^\circ$	108
3.3-8	SLAMAST Re-entry, $\gamma_o = -1^\circ$	108
3.3-9	SLAMAST Re-entry, $\gamma_o = -10^\circ$	109
3.3-10	SLAMAST Re-entry, $\gamma_o = -10^\circ$	109
3.3-11	SLAMAST Re-entry, $\gamma_o = -10^\circ$	110
3.3-12	SLAMAST Re-entry, $\gamma_o = -10^\circ$	110
3.3-13	SLAMAST Range Safety Footprint, $\gamma_o = -1^\circ$, Failure at Re-entry . . .	111
3.3-14	SLAMAST Range Safety Footprint, $\gamma_o = -10^\circ$, Failure at Re-entry . . .	111
3.3-15	SLAMAST Range Safety Footprint, $\gamma_o = -1^\circ$, Failure at 350 Sec. from Re-entry	112
3.3-16	SLAMAST Range Safety Footprint, $\gamma_o = -10^\circ$, Failure at 350 Sec. from Re-entry	112
3.3-17	SLAMAST Range Safety Footprint, $\gamma_o = -10^\circ$, Failure at Re-entry . . .	113
3.3-18	SLAMAST Exospheric Motion, Longitudinal Axis Motion in Inertial Space	113
3.3-19	SLAMAST Exospheric Motion, Roll Phase Plane	114
3.3-20	SLAMAST Exospheric Motion, Pitch Phase Plane	114
3.3-21	SLAMAST Exospheric Motion, Yaw Phase Plane	115
3.3-22	Altitude versus Velocity	116
3.3-23	Angle of Attack History	117
3.3-24	Bank Angle History	118

ILLUSTRATIONS (Cont'd)

<u>Figure</u>		<u>Page</u>
3.4-1	Basic Dimensional Configuration	145
3.4-2	One-Degree Entry Trajectory and Angle of Attack History	146
3.4-3	Ten-Degree Entry Trajectory and Angle of Attack History	147
3.4-4	Pressure-Ratio Distribution for Zero Angle of Attack	147
3.4-5	Pressure-Ratio Distribution for Angle of Attack Not Equal to Zero at Mach 20	148
3.4-6	Pitch-Flap and Drag-Brake Pressure-Ratio Distribution at Mach 20	148
3.4-7	Stagnation Point Convective Heating Histories	149
3.4-8	Stagnation Point Pressure and Enthalpy Histories	149
3.4-9	Laminar and Turbulent Convective Heat Flux Distribution at Time of Maximum Heating	150
3.4-10	Boundary Layer Transition Criteria	150
3.4-11	Heating Correlations to the Windward Meridian, 1° Entry	151
3.4-12	Heating Correlations to the Leeward Meridian, 1° Entry	152
3.4-13	Heating Correlations to the Sideward Meridian, 1° Entry	153
3.4-14	Convective Heat Transfer Rates, 1° Entry, Windward Ray	154
3.4-15	Convective Heat Transfer Rates, 1° Entry Leeward Ray	154
3.4-16	Convective Heat Transfer Rates, 1° Entry, Sideward Ray	155
3.4-17	Convective Heat Transfer Rates, 1° Entry, Drag Brake and Pitch Flap	155
3.4-18	Windward Ray Shear-Stress Histories, 1° Entry	156
3.4-19	Leeward Ray Shear-Stress Histories, 1° Entry	156
3.4-20	Sideward Ray Shear-Stress Histories, 1° Entry	157
3.4-21	Drag Brake and Pitch Flap Shear-Stress Histories, 1° Entry	157
3.4-22	Nose Cap Stagnation Point ATJ Graphite Temperature and Ablation Histories, 1° Entry	158
3.4-23	Nose Cap Stagnation Point ATJ Graphite Temperature Profiles, 1° Entry	158
3.4-24	Nose Cap ATJ Graphite Temperature and Ablation Histories, $x/L = 0.0208$, Windward, 1° Entry	159
3.4-25	Nose Cap ATJ Graphite Temperature Profiles, $x/L = 0.0208$, Windward, 1° Entry	159
3.4-26	Nose Cap Phenolic Refrasil Temperature and Degradation Histories, $x/L = 0.0208$, Windward, 1° Entry	160
3.4-27	Nose Cap Phenolic Refrasil Temperature Profiles, $x/L = 0.0208$, Windward, 1° Entry	160
3.4-28	Nose Cap ATJ Graphite and Phenolic Refrasil Total Mass Addition Histories, 1° Entry	161
3.4-29	Skirt-Nominal Shield Requirements for ESM and Purple Blend as a Function of x/L , 1° Entry	161
3.4-30	Skirt-Nominal Shield Requirements for ESM and Purple Blend as a Function of Total Integrated Convective Heating, 1° Entry - Windward, Leeward, and Side	162

ILLUSTRATIONS (Cont'd)

<u>Figure</u>		<u>Page</u>
3.4-31	Skirt-ESM Temperature and Degradation Histories, $x/L = 0.0208$, Windward, 1° Entry	162
3.4-32	Skirt-ESM Temperature Profiles, $x/L = 0.0208$, Windward, 1° Entry	163
3.4-33	Skirt-ESM Temperature and Degradation Histories, $x/L = 1.0$, Windward, 1° Entry	163
3.4-34	Skirt-ESM Temperature Profiles, $x/L = 1.0$, Leeward, 1° Entry	164
3.4-35	Skirt-ESM Temperature and Degradation Histories, $x/L = 1.0$, Windward, 1° Entry	164
3.4-36	Skirt-ESM Temperature Profiles, $x/L = 1.0$, Leeward, 1° Entry	165
3.4-37	Skirt-ESM Temperature and Degradation Histories, $x/L = 0.15$, Side, 1° Entry	165
3.4-38	Skirt-ESM Temperature Profiles, $x/L = 0.15$, Side, 1° Entry	166
3.4-39	Skirt-ESM Temperature and Degradation Histories, $x/L = 0.364$, Windward, 10° Entry	166
3.4-40	Skirt-ESM Temperature Profiles, $x/L = 0.365$, Windward, 10° Entry	167
3.4-41	Skirt-ESM Total Mass Addition Histories, Windward, Leeward, and Side, 1° Entry	167
3.4-42	Skirt-Purple Blend Temperature and Degradation Histories, $x/L = 1.0$, Windward, 1° Entry	168
3.4-43	Skirt-Purple Blend Temperature Profiles, $x/L = 1.0$, Leeward, 1° Entry	168
3.4-44	Skirt-Purple Blend Temperature Degradation Histories, $x/L = 1.0$, Leeward, 1° Entry	169
3.4-45	Skirt-Purple Blend Temperature Profiles, $x/L = 1.0$, Leeward, 1° Entry	169
3.4-46	Skirt-Purple Blend Temperature and Degradation Histories, $x/L = 0.364$, Windward, 10° Entry	170
3.4-47	Skirt-Purple Blend Temperature Profiles, $x/L = 0.364$, Windward, 10° Entry	170
3.4-48	Skirt-Purple Blend Total Mass Addition Histories, Windward and Leeward, 1° Entry	171
3.4-49	Pitch-Flap and Drag Brake Phenolic Nylon Nominal Heat Shield Requirements, 1° Entry	171
3.4-50	Pitch-Flap Phenolic Nylon Temperature and Degradation Histories, $x/L = 1.0$, Leeward, 1° Entry	172
3.4-51	Pitch-Flap Phenolic Nylon Temperature Profiles, $x/L = 1.0$, Leeward, 1° Entry	172
3.4-52	Drag Brake Phenolic Nylon Temperature and Degradation Histories, $x/L = 1.0$, Windward, 1° Entry	173

ILLUSTRATIONS (Cont'd)

<u>Figure</u>		<u>Page</u>
3.4-53	Drag Brake Phenolic Nylon Temperature Profiles, $x/L = 1.0$, Windward, 1° Entry	173
3.4-54	Drag Brake and Pitch Flap Phenolic Nylon Total Mass Addition Histories	174
3.4-55	Backface Temperature and Heat Dissipation Profiles	175
3.4-56	Component Temperature Histories for Hot Structure, Air Conditioned, Textolite Structure	176
3.4-57	Component Temperature Histories for Hot Structure, Not Air Conditioned, Textolite Structure	177
3.4-58	Component Temperature Histories for Cold Structure, Air Conditioned, Textolite Structure	178
3.4-59	Component Temperature Histories for Cold Structure, Not Air Conditioned, Textolite Structure	179
3.4-60	Component Temperature Histories for Hot Structure, Air Conditioned with Insulating Washers	180
3.4-61	Component Temperature Histories for Cold Structure, Air Conditioned with Insulating Washers	181
3.5-1	Plasma Attenuation, S-band	186
3.5-2	Plasma Attenuation, C-band	186
3.5-3	2-D Inviscid Electron Density Profile Comparison	188
3.5-4	FM/FM Telemetry System Error versus Signal to Noise Ratio at I. F.	188
3.5-5	Slant Range and Flight Range Histories for Ship Location at 1700 Nautical Miles Down Range, -1° Re-entry Angle Trajectory	204
3.5-6	Down Range Ship Reception, Window Based on 5° Minimum Elevation Angle, -1° Re-entry Angle	204
3.5-7	Slant Range and Flight Range at 2000 Nautical Miles Down Range, -1° Re-entry Angle	207
3.5-8	Elevation Angle at 1700 Nautical Miles Down Range Location, -1° Re-entry Angle	208
3.5-9	Elevation Rates at 1700 Nautical Miles Down Range Location, -1° Re-entry Angle	209
3.5-10	Azimuth Rates at 1700 Nautical Miles Down Range Location, -1° Re-entry Angle	209
3.5-11	Maximum Azimuth Rates at 1700 Nautical Miles Down Range, -1° Re-entry Angle	210
3.5-12	Maximum Azimuth Rates at 2000 Nautical Miles Down Range Location, -1° Re-entry Angle	210
3.5-13	Pitch and Yaw Components of Aspect Angle for 1700 Nautical Miles Down Range Location, -1° Re-entry Angle	211
3.5-14	Pitch and Yaw Components of Aspect Angle at 2000 Nautical Miles Down Range Location, -1° Re-entry Angle	212
3.5-15	Antenna Pattern	213

ILLUSTRATIONS (Cont'd)

<u>Figure</u>		<u>Page</u>
3.6-1	Proposed Recovery Area	218
3.7-1	Range Safety Definition	221
3.7-2	SLAMAST Range Safety Footprint, Failure at Re-entry at -1°	222
3.7-3	SLAMAST Range Safety Footprint, Failure at Re-entry at -10°	223
3.7-4	SLAMAST Range Safety Footprint, Failure at 350 Seconds from Re-entry at -10°	224
3.7-5	SLAMAST Range Safety Footprint, Failure at 350 Seconds from Re-entry at -10°	225
3.7-6	Down Range Dispersion Failure at Re-entry, $\gamma_E = -10^\circ$	226
3.7-7	Cross Range Dispersion Failure at Re-entry, $\gamma_E = -10^\circ$	227
3.7-8	Down Range Dispersion Failure at Re-entry, $\gamma_E = -1^\circ$	228
3.7-9	Cross Range Dispersion Failure at Re-entry, $\gamma_E = -1^\circ$	229

TABLES

<u>Table</u>		<u>Page</u>
3.2-1	SLAMAST Static Force and Moment Coefficients for Modified Newtonian Flow	59
3.2-2	SLAMAST Rotary Derivatives in Pitch for Modified Newtonian Flow, Varying C. G. Location, and $\beta = 0$	79
3.2-3	SLAMAST Rotary Derivatives in Roll for Newtonian Flow and $\beta = 0$	80
3.2-4	SLAMAST Rotary Derivatives in Yaw for Modified Newtonian Flow and Varying Sideslip Angle	80
3.2-5	Secondary SLAMAST Rotary Damping Derivatives	81
3.3-1	Pertinent Trajectory Tabulations	100
3.3-2	Re-entry Condition Tolerances	103
3.4-1	Shield Structure Composites Analyzed	128
3.4-2	Thermophysical Properties and Reaction Kinetics Constants of Outer Shield Materials Employed in REKAP	142
3.4-3	Thermophysical Properties of Structural Materials Employed in REKAP	144
3.5-1	SLAMAST Measurements	192

1. INTRODUCTION

1. INTRODUCTION

This section of the report summarizes the system design effort performed during the SLAMAST study.

It includes a general description, aerodynamic, flight dynamics, thermodynamic, instrumentation, communication and recovery studies as well as subsystem specifications and preliminary hardware definition of the following subsystems:

- (1) Attitude Measurement and Control
- (2) Instrumentation and Communication
- (3) Recovery
- (4) Electrical Power and Distribution
- (5) Separation
- (6) Structural Design and Packaging

In addition, an Integrated Ground Test Plan and general descriptions of the mechanical and electrical Aerospace Ground Equipment (AGE) are presented along with a program description and detailed schedules (Figures 1-1 through 1-4).

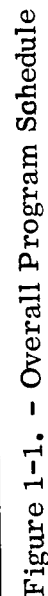
The proposed system is the result of several iterations. As originally conceived, it was thought the re-entry velocities of 25K fps (8.22K mps) or greater would be required to obtain environmental similitude with HL-10. This belief necessitated the use of a 4 stage Scout system and required a spacecraft length of approximately 48 inches (1.46 meters), the maximum which could be accommodated within the Scout shroud.

Subsequent progress in the trajectory analysis resulted in an established requirement for re-entry velocities of 20K fps (6.58K mps) or less. This allowed the use of a 3 stage Scout booster and relaxed the geometric constraints so that it was not necessary to use a 48-inch (1.46-meter) spacecraft. This, in turn, permitted a design consideration of spacecraft length as a function of approximate historical packaging efficiency using non "tailor-made" components.

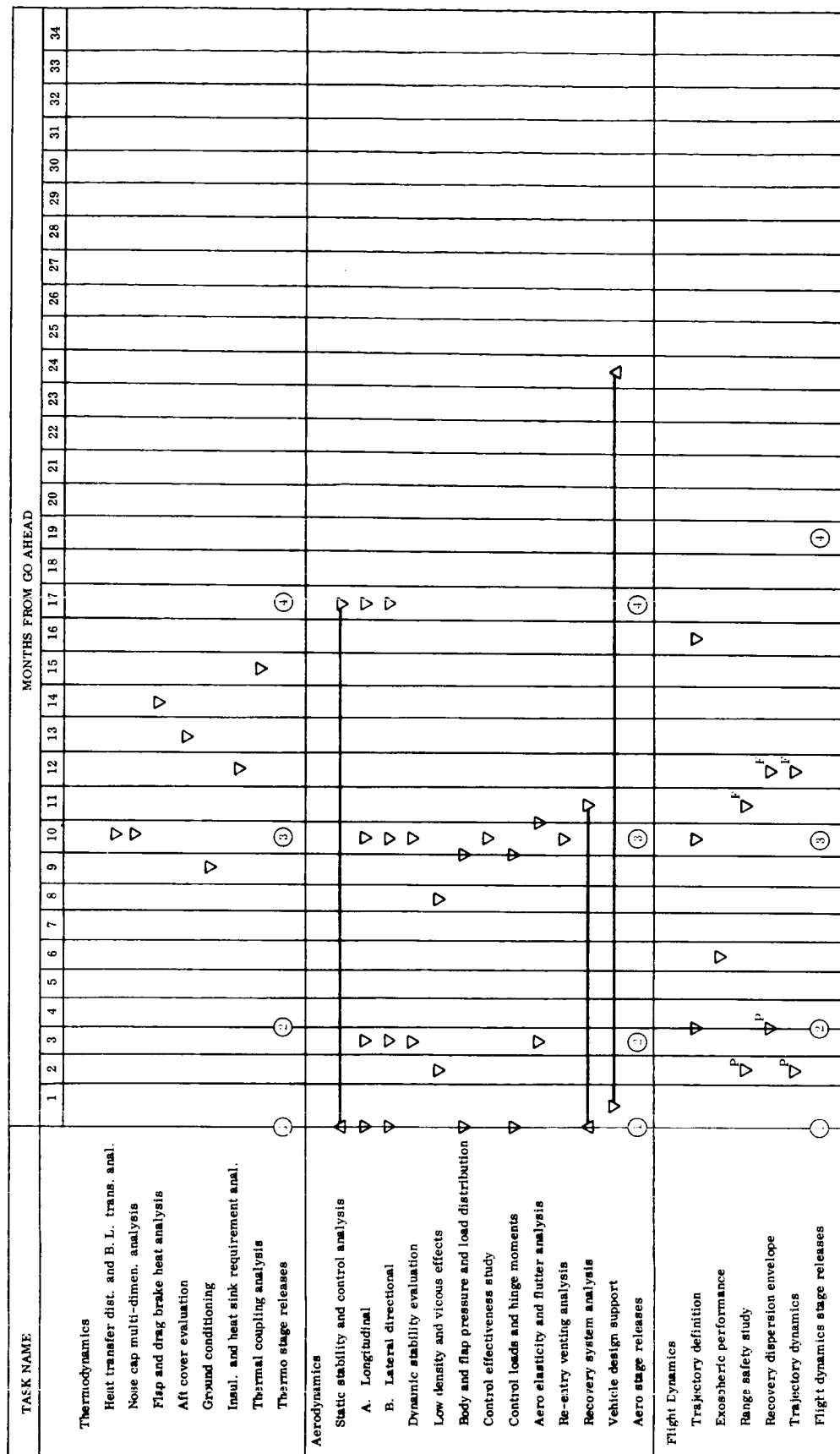
Although this was not a design optimization effort, the "test-bed" philosophy dictated a preliminary consideration of the costs involved and a reasonable effort to keep these costs compatible with the technical program objectives. Final selection of the "feasible" subsystems for design purposes was, therefore, predicated upon economic viability as well as technical feasibility.

The "test-bed" philosophy also resulted in consideration of the inherent versatility of the as-designed configuration and of alternate component or subsystem selections which could increase specific spacecraft capabilities.

Fundamentally, the selected design presented in this portion of the report represents a feasible hardware implementation of the requirements developed in the Systems Specification (ERS 0010-02-0027-1), dated 27 March 1967. It is a design solution.

 \wedge START

∇ COMPLETE



▽^P Preliminary Document

▽^F Final Document

▽ Document Release (General)

Figure 1-2. - Analysis Schedule

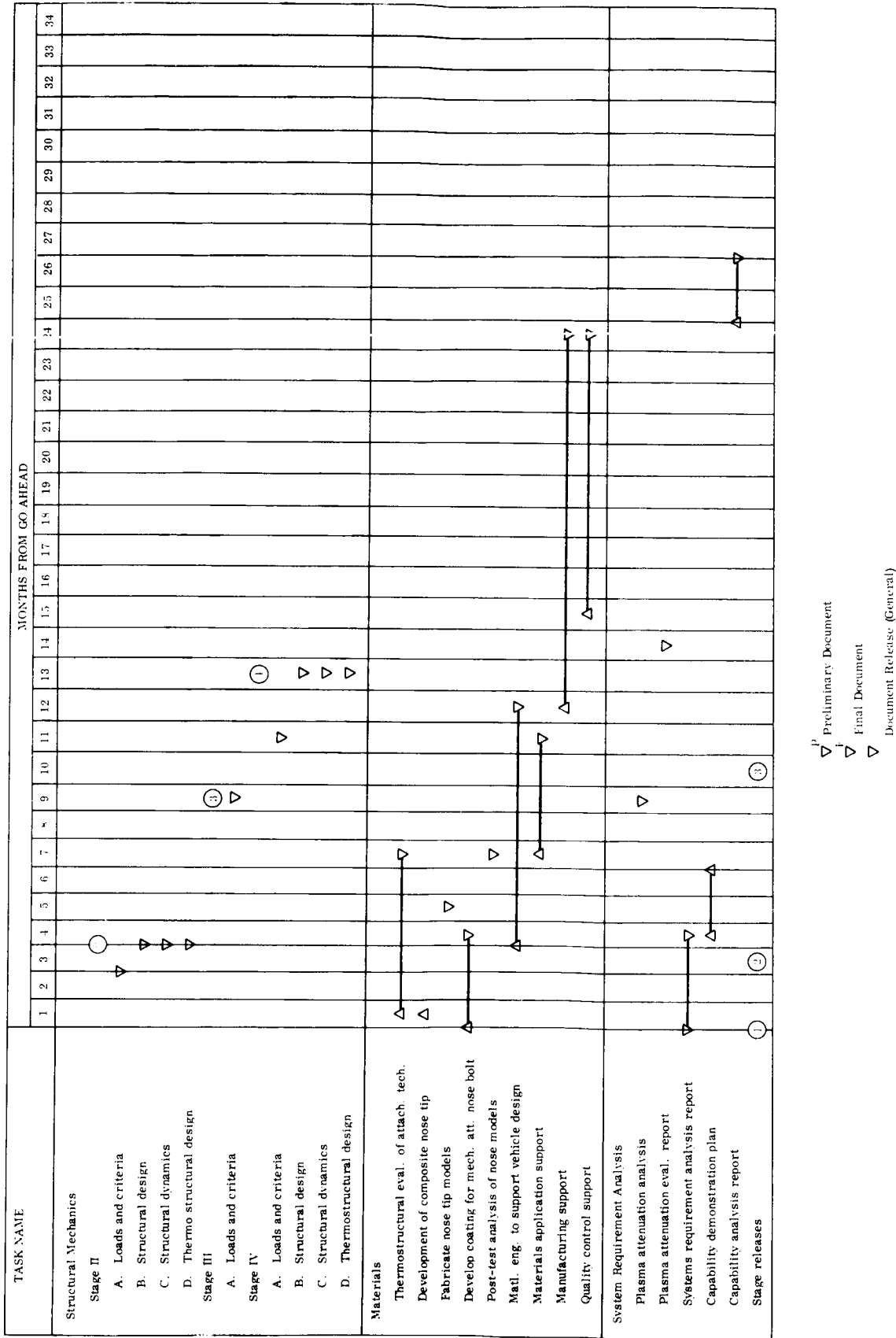


Figure 1-2. - Analysis Schedule (Continued)

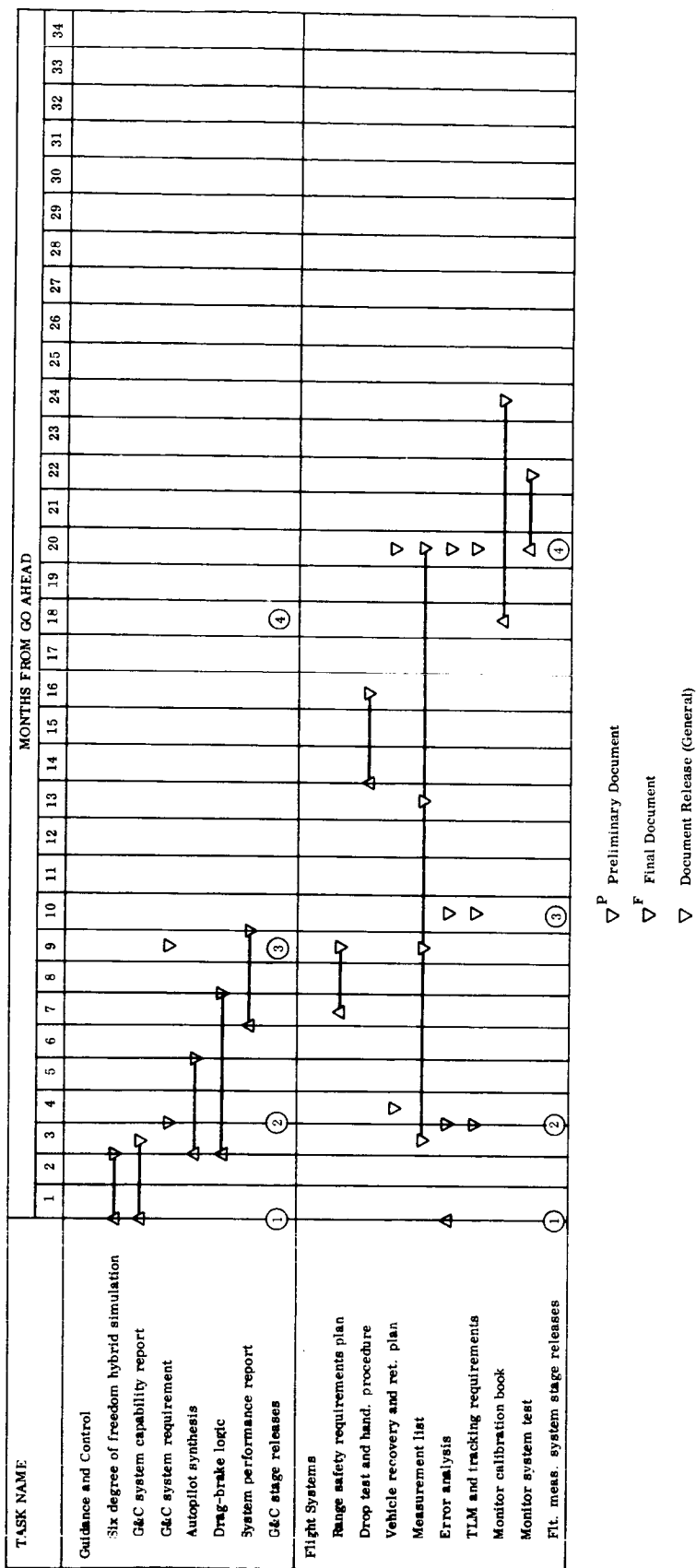
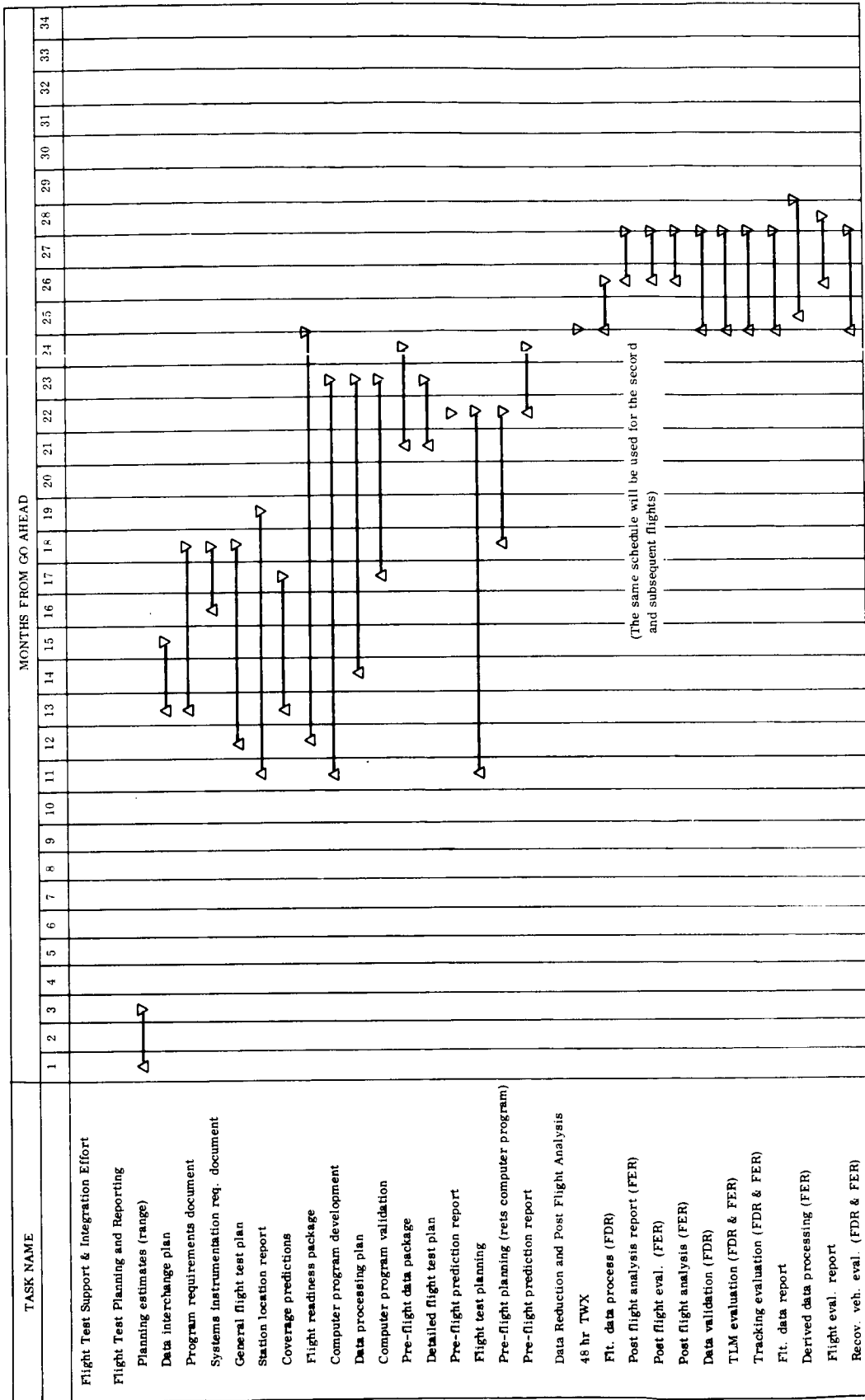


Figure 1-2. - Analysis Schedule (Continued)



▽^P Preliminary Document

▽^F Final Document

▽ Document Release (General)

Figure 1-2. - Analysis Schedule (Concluded)

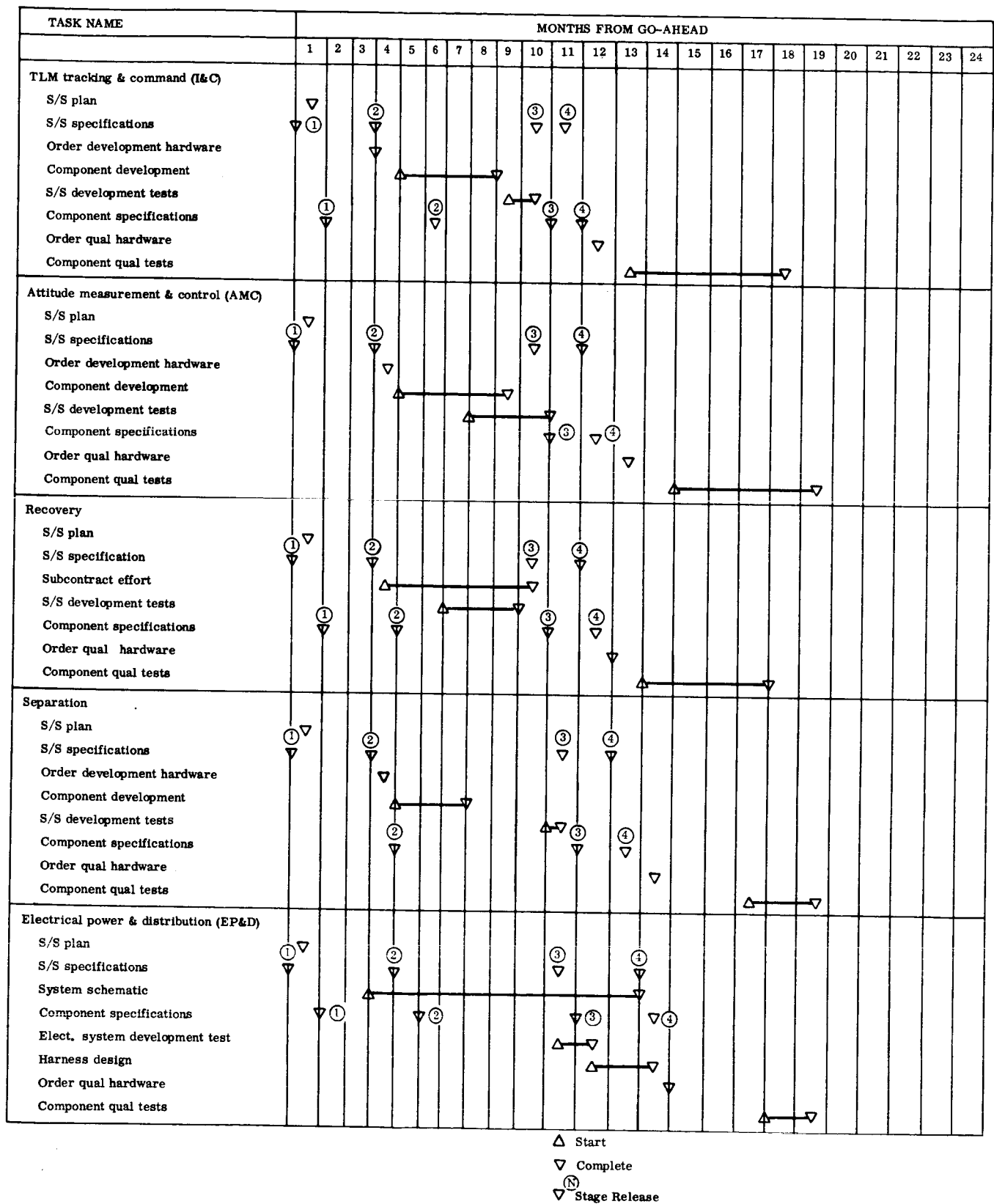


Figure 1-3. - Subsystem Development Schedule

[illegible]

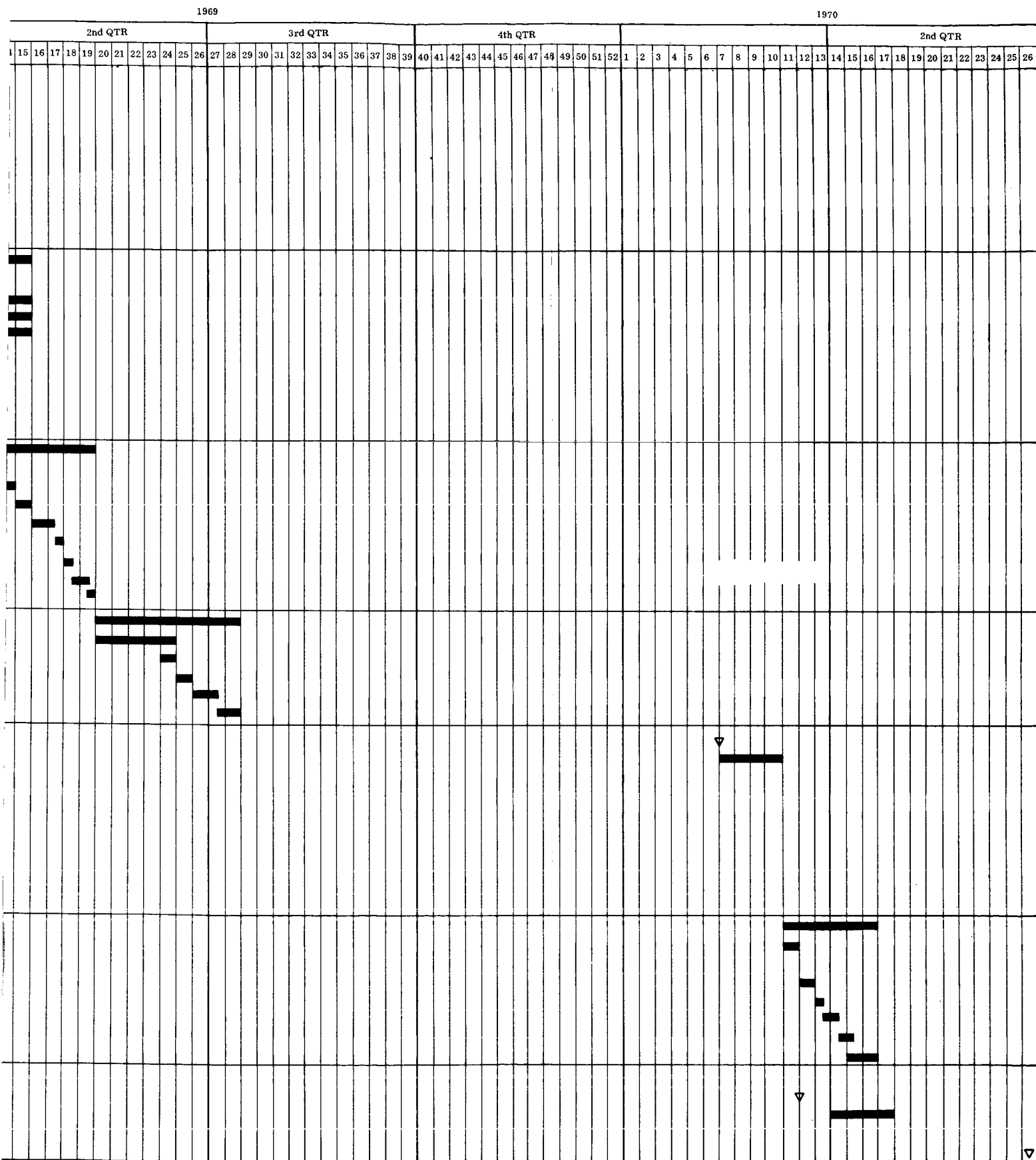


Figure 1-4. - Integrated Test Schedule

2. SUMMARY

2. SUMMARY

2.1 GENERAL

The requirements to which the SLAMAST spacecraft has been designed are given in the SLAMAST System Specification ERS 0010-02-0027,-1, dated 27 March 1967.

The SLAMAST spacecraft design chosen for feasibility demonstration is a modified elliptic-cone vehicle with a length of 63 inches (2.07 meters) and a weight of 305 pounds (138.2 kilograms). The ellipse major axis is 28.04 inches (0.805 meter) and the minor axis is 16.04 inches (0.788 meter).

It incorporates two flaps; the top (or pitch) flap is servomotor powered for variable angle control, whereas the bottom (or drag) flap is driven by a pneumatic one-shot device to a constant angle. These flaps are faired into flat areas on the spacecraft. This reduces the flap pivotal point design and thermal insulation problems without significantly affecting the aerodynamic performance of the craft. The vehicle has a nominal $W/C_L S$ of 250 lbs/ft² (1232.5 Kg/m²) with a maximum lift-to-drag ratio of 2.4 at 8 degrees angle-of-attack.

The selected structure is aluminum and is comprised of two integrally machined keel members which are stiffened by a series of webs and formers. This configuration provides integral hard points for separation and recovery subsystem attachments and is compatible with a removable access and test panel concept.

A mechanically attached graphitic nose tip and an ESM (GE-Silicone) heat shield are provided for thermal protection.

Figures 2-1 and 2-2 show the general configuration discussed above.

The instrumentation and communication subsystem consists of a C-band tracking and ground command link, an S-band PCM continuous data transmittal link (utilizing a "micro-miniaturized" multocoder) and record and playback capability. It includes those diagnostic and performance sensors necessary to gather the data defined in the measurements list.

The recovery subsystem is a subsonic subsystem and consists of a FIST ribbon decel parachute, a ballute, and an rf beacon location aid. The ballute is ram-air inflated and provides inherent spacecraft flotation capability. (The drag flap mentioned above may be considered a part of the retardation sequence prior to parachute deployment.) This system has been sized to provide a spacecraft water impact velocity of 100 fps (32.9 mps).

The separation subsystem consists of four collet assemblies, an in-flight disconnect (IFD), and auxiliary hardware. The collets are "finger and piston" devices which mechanically attach the spacecraft to the spacer. They are pneumatically operated and, upon command, gas pressure pushes the pistons forward. This releases the mechanical attachment and, by continued piston travel, imparts a separation velocity to the spacecraft.

The electrical power and distribution subsystem consists primarily of harnesses, a power switching module, a battery, an in-flight disconnect (SC to spacer) and a spacer-to-shroud-access-door umbilical for ground power accommodation.

The selected attitude measurement and control subsystem derives its reference orientation from a Whittaker PRYS platform. It utilizes a programmed sequence for mission accomplishment. Exospheric, 3-axis reaction control and attitude orientation after separation is provided by a Freon-14 gas expulsion system. Upon re-entry, the pitch control (only) is relinquished to the top flap. Roll and yaw control are maintained through the Freon-14 system. The design trajectories were characterized by a constant altitude trajectory from pull-out to drag brake initiation and this is obtained by modulation of the pitch flap angle roll nulling and yaw rate limiting during flight in the atmosphere. At the end of the experiment, the drag and pitch flaps are used in conjunction with each other to begin the ballistic mission termination.

The experimental specimens consist of two panels; one on the top (leeward) surface and another larger one on the bottom (windward) surface. The reference design for these panels duplicates (so far as is possible) the typical HL-10 design.

A cylindrical spacer is proposed. This spacer provides the spacecraft to booster mating interface. It is designed so that the spacecraft to spacer mechanical attachment takes advantage of the inherent hard-points in the spacecraft. The spacer assembly also includes the mounting arm of the umbilical for ground power access and the separation subsystem hardware (previously described).

2.2 CAPABILITY

As shown, the SLAMAST spacecraft will endure boost loads and will separate from the third stage of Scout at a timed interval from booster engine cut-off. It will orient itself at a predetermined pitch angle-of-attack (up to a maximum of 16 degrees) and will stabilize itself in null roll and yaw within a ± 5 degree dead band.

It will re-enter and pull out of its initial ballistic path (by using aerodynamic force), and will establish the time reference for recovery flap deployment and tape recorder playback based on the pull-out maneuver. (This compensates for booster burn-out altitude variations with resulting effects on separation time and its consequent perturbation of range.)

The angle-of-attack is modulated through the programmed pitch flap control to fly the predetermined trajectory.

After the timed glide portion of flight, the spacecraft will begin its mission termination by deploying both flaps. After a set time from this event, the recovery sequence proper begins with the deployment of the FIST type ribbon parachute.

The spacecraft will survive water impact at 100 fps (32.9 mps) and will subsequently float for 72 hours minimum. The RF beacon location aid will operate for a minimum of 10 hours.

During boost, re-entry and glide, all information is gathered from the included sensors and transmitted continuously over an S-band PCM system. During re-entry and glide, this information is also recorded. During mission termination (both flaps deployed), the continuous data transmittal and recorded data playback occurs simultaneously. The Electrical and Mechanical AGE required to handle, test, ship and check-out the spacecraft has also been included.

2.3 FLEXIBILITY

2.3.1 BOOST AND RE-ENTRY

The boost phase design loads arose from the 3 stage Scout environments as reflected in the Systems Specification; and, the proposed design will meet these requirements. The design bounds on re-entry path angle were from $\gamma_E = -1$ degree to $\gamma_E = -10$ degrees. The craft is capable of re-entering with any γ_E between these bounds. It is also flexible enough to re-enter at either steeper or shallower path angles. The factors which would have to be assessed against a specific γ_E outside the -1 degree to -10 degree bounds are; heat shield and reaction control impulse requirements.

2.3.2 PULL-OUT

The pull-out altitudes specified from a feasibility demonstration point of view are predicated on a pitch flap initial deployment angle of 40 degrees and are dependent primarily upon γ_E (i.e. $\gamma_E = -1$ degree causes a pull-out at approximately 145K feet and $\gamma_E = -10$ degrees causes a pull-out at approximately 115K feet). This altitude could also be varied by changing the initial pitch flap deployment angle ($\delta_F = 40$ degrees for higher pull-out, $\delta_F = 40$ degrees for lower pull-out). The factors which would have to be assessed against specific δ_F not equal to 40 degrees are: heat shield, structural strength, and spacecraft stability.

2.3.3 GLIDE

The pitch flap program chosen for feasibility demonstration provides for constant altitude flight through modulation of the angle-of-attack. This program could be modified to provide for angle-of-attack/altitude composite variations, etc. The factors which would need to be assessed against a specific glide path control scheme are: pitch flap actuator capability, available electrical power, programmer modifications, heat shield requirements, and spacecraft stability.

The roll control implementation scheme chosen for feasibility demonstration provides for roll nulling within a deadband of ± 5 degrees (from separation through to parachute deployment). This could be varied by establishing a desired roll history program. For example the craft could be banked approximately 90 degrees, kept in that attitude for a specific time, then reverse-banked through 180 degrees and finally returned to null for recovery initiation. The primary factors influenced by implementing something other than roll nulling are programmer changes, and total impulse and thrust level changes. (A significant increase in available impulse and thrust level could be provided by using a hot-gas system. This system also requires significantly less volume for a given impulse than the Freon-14 system.)

The level flight duration chosen for design feasibility is approximately 500 seconds. This can be varied by a simple timing change. The factors which would need to be assessed against a specific glide duration are heat shield (thermal insulation) requirements, retardation effectiveness for recovery, and reaction control impulse requirements.

2.3.4 RECOVERY

All design trajectories employed the drag flap as a retardation device and showed subsonic, low dynamic pressure conditions at parachute deployment. If less, high-altitude retardation was desired for higher ballistic termination velocities, the subsonic recovery system could be elevated to a Mach 1.5 capability by changing to a hemisflo parachute with small weight and volume penalties.

2.3.5 CONTROL SYSTEM

The attitude reference system chosen for design feasibility is a modified MARS platform (termed PRYS by Whittaker Corp.). The mission accuracy predicated on the errors derived from this platform (and ancillary hardware) is presented in (Section 4.1) of this volume. Other reference systems are available which could, at some increase in expense, increase the total mission accuracy.

2.4 REDUNDANCY

2.4.1 DATA TRANSMITTAL

The design provides for both continuous real time S-band data transmittal and data recording and playback without interruption of the real time capability. This assures data gathering even if factors such as plasma attenuation or ground receiver availability prevents continuous reception of telemetered data.

The playback mode will be initiated by either of two events:

- (1) Primary, the passage of a specified time from pull-out.
- (2) Back-up, the receipt of a ground command through on-board C-band via the FPS-16 radar.

2.4.2 MISSION TERMINATION

The deployment of the drag/pitch flaps for mission termination initiation will be effected through either of two events:

- (1) Primary, the passage of a specified time from pull-out.
- (2) Back-up, the receipt of a ground command through the on-board C-band command receiver/transponder via the FPS-16 radar.

2.4.3 STRUCTURE

The experiment panels are mounted so that they form the "lid" of a structural pan. The pan itself is an integral part of the spacecraft structure and has its own heat shield and structural integrity. A failure of the panel should not result in spacecraft failure.

2.4.4 DESTRUCT

Although no design implementation of a destruct system was pursued, the wealth of reference sensors and performance data measurements assure the availability of existing on-board equipment which can be used to signal the need for destruction and to provide initiating action to the chosen devices. The sensing of this need would be derived from totally redundant parameters.

2.4.5 PYROTECHNIC INITIATION DEVICES

All pyrotechnic devices will be provided with redundant and isolated circuits.

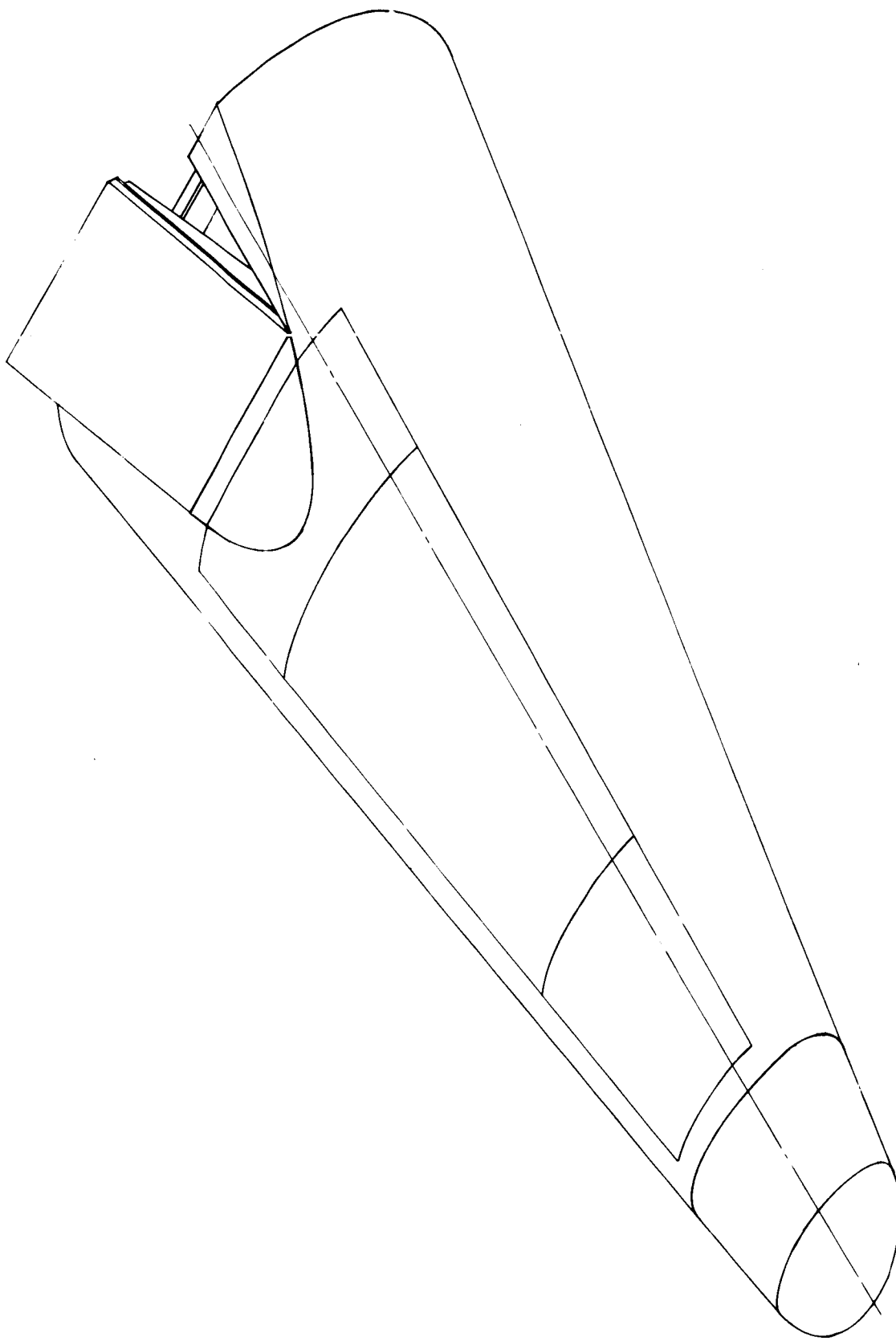
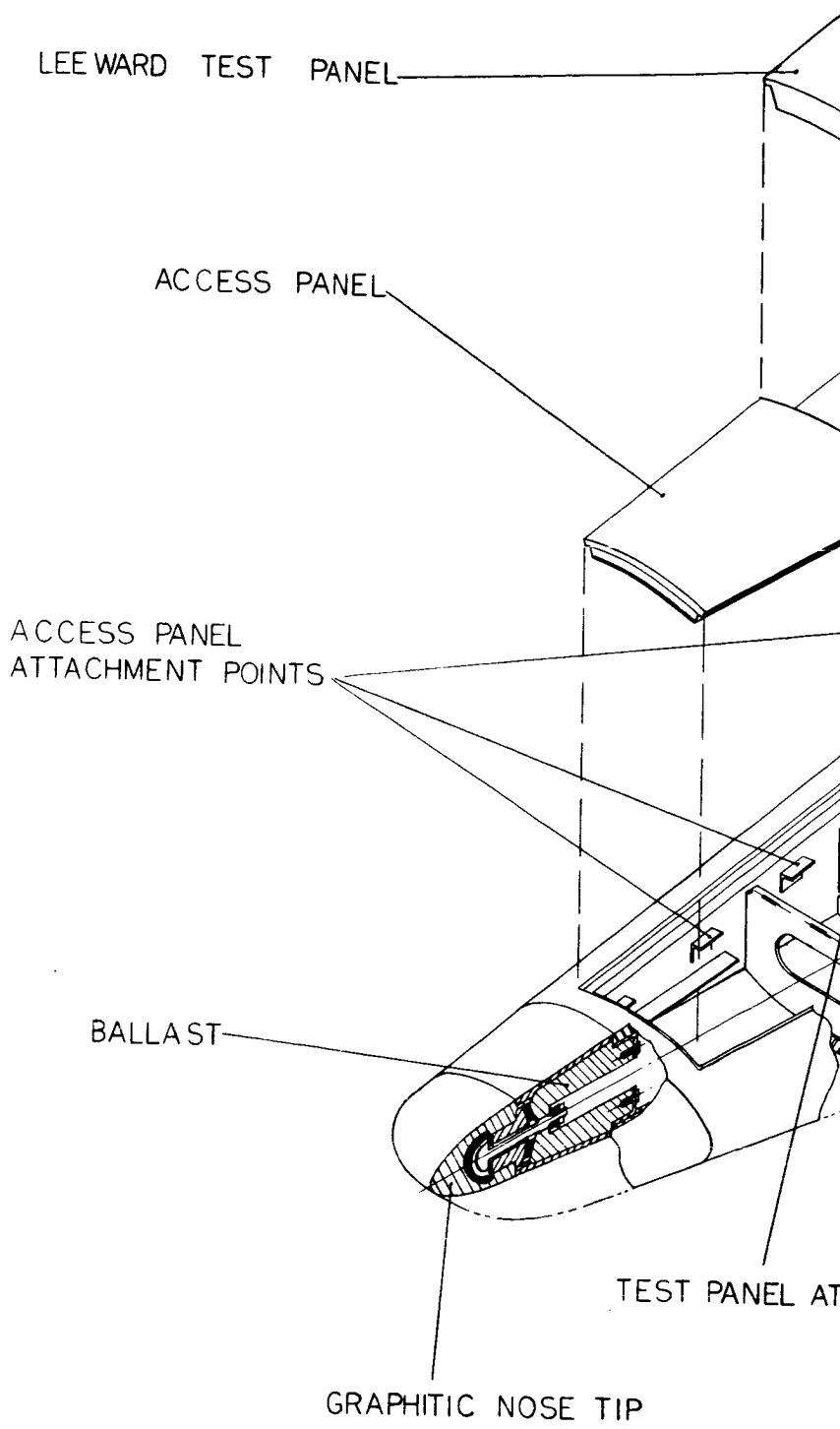
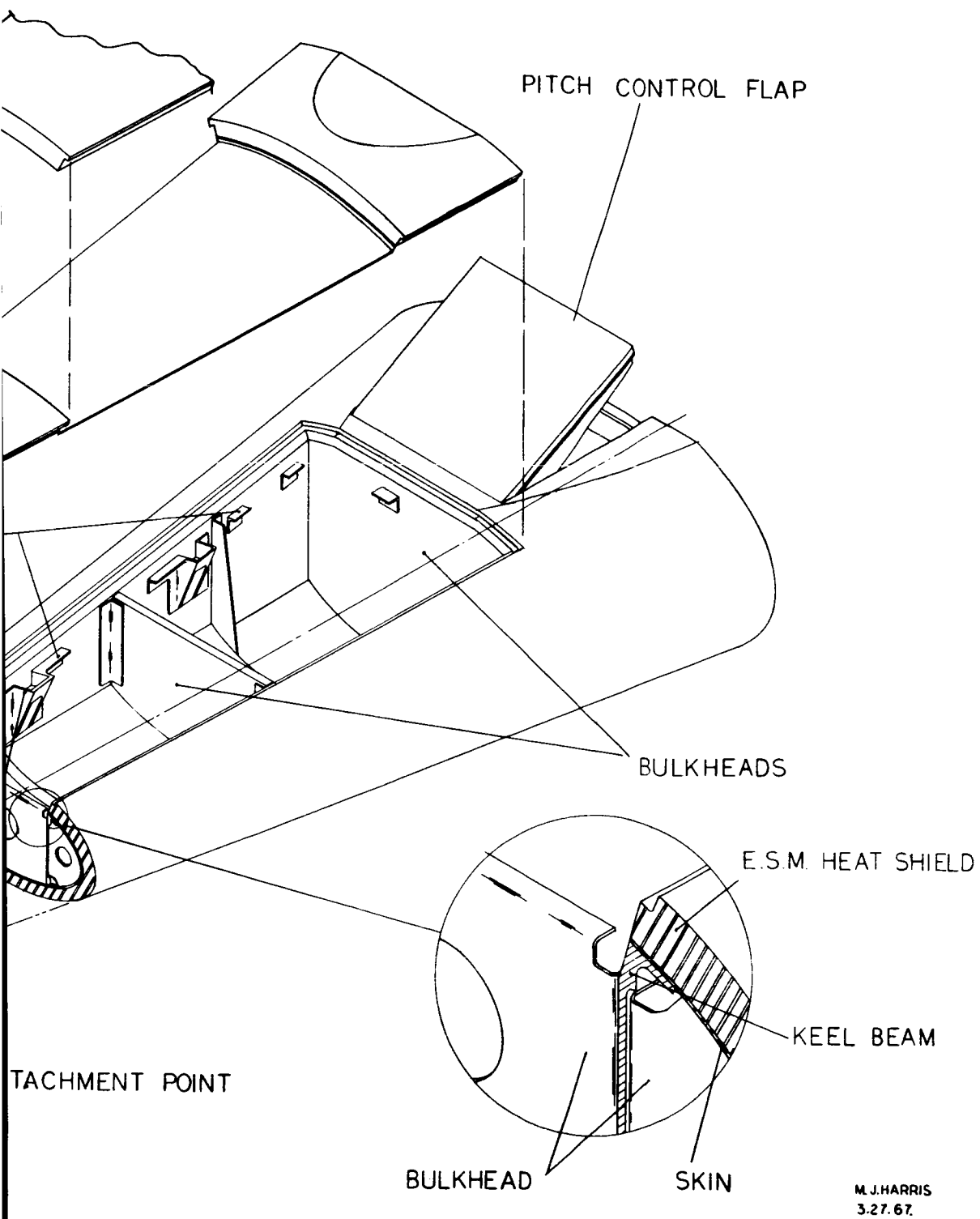


Figure 2-1. - SLAMAST S/C





M. J. HARRIS
3.27.67.

Figure 2-2. - SLAMAST Structural Arrangement

3. SYSTEM REQUIREMENTS

3. SYSTEM REQUIREMENTS

3.1 DEVELOPMENT OF GENERAL REQUIREMENTS

3.1.1 LAUNCH VEHICLE

The primary considerations in the choice of a launch vehicle or booster for a re-entry mission, such as the SLAMAST Program entails are:

(1) Re-entry vehicle velocity, flight path angle, and altitude of separation meet the criteria of re-entry vehicle experiment input conditions.

(2) The booster vehicle employed should provide an inexpensive method of duplicating the re-entry dynamics of full scale vehicle flights.

(3) Maximum use should be made of proven hardware and techniques while maintaining flexibility for providing a broad spectrum of performance capability.

The design feasibility study was undertaken on the basis of using the Scout booster, with the environmental simulation requirements determining the use of a three-or four-stage configuration. The choice of the Scout booster essentially fulfills the last two of three considerations listed above. The first and foremost experiment item will be enumerated in more detail in the following paragraphs.

The S/C design was initiated using a 48 inch length, 170 pound vehicle on a four-stage Scout. Re-entry design conditions were defined as follows:

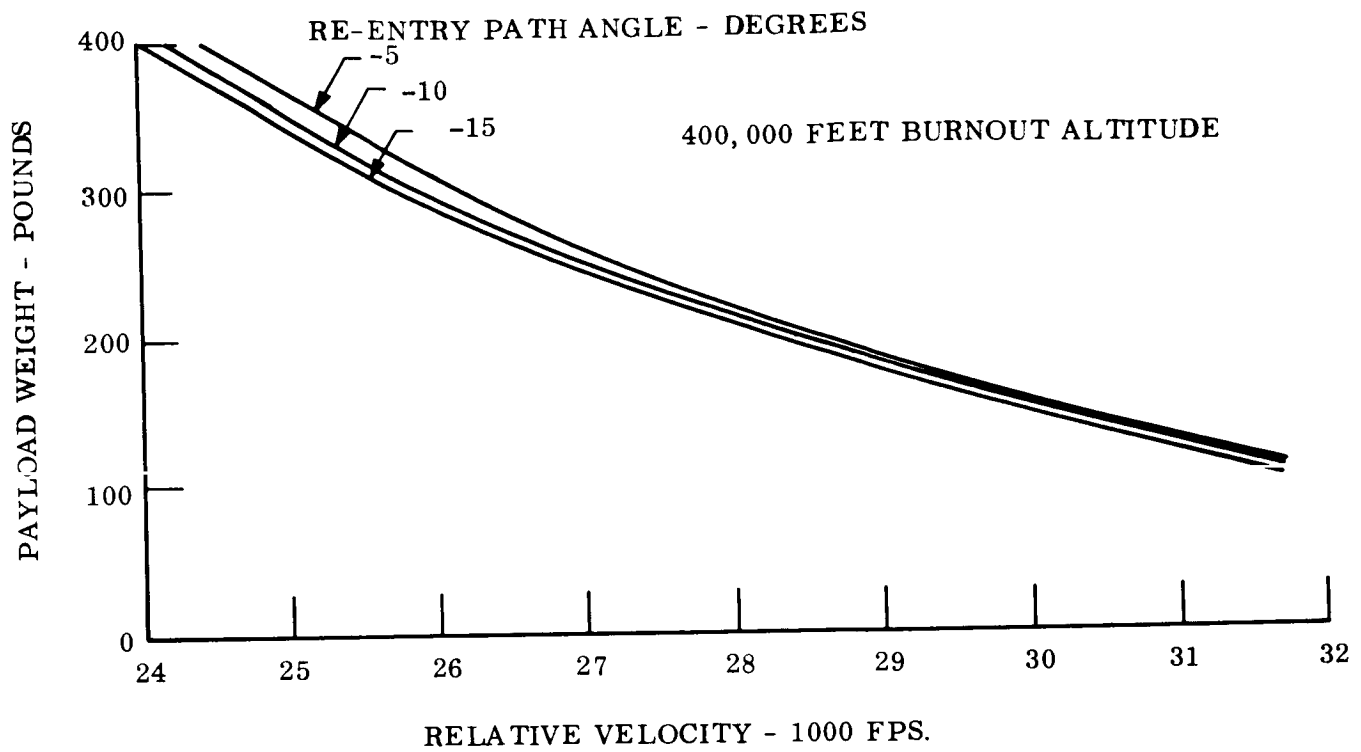
(1) Path angles, (γ_e) varying from 1 to 15 degrees down from the local horizontal.

(2) Velocity (V_e) of 25,000 feet per second.

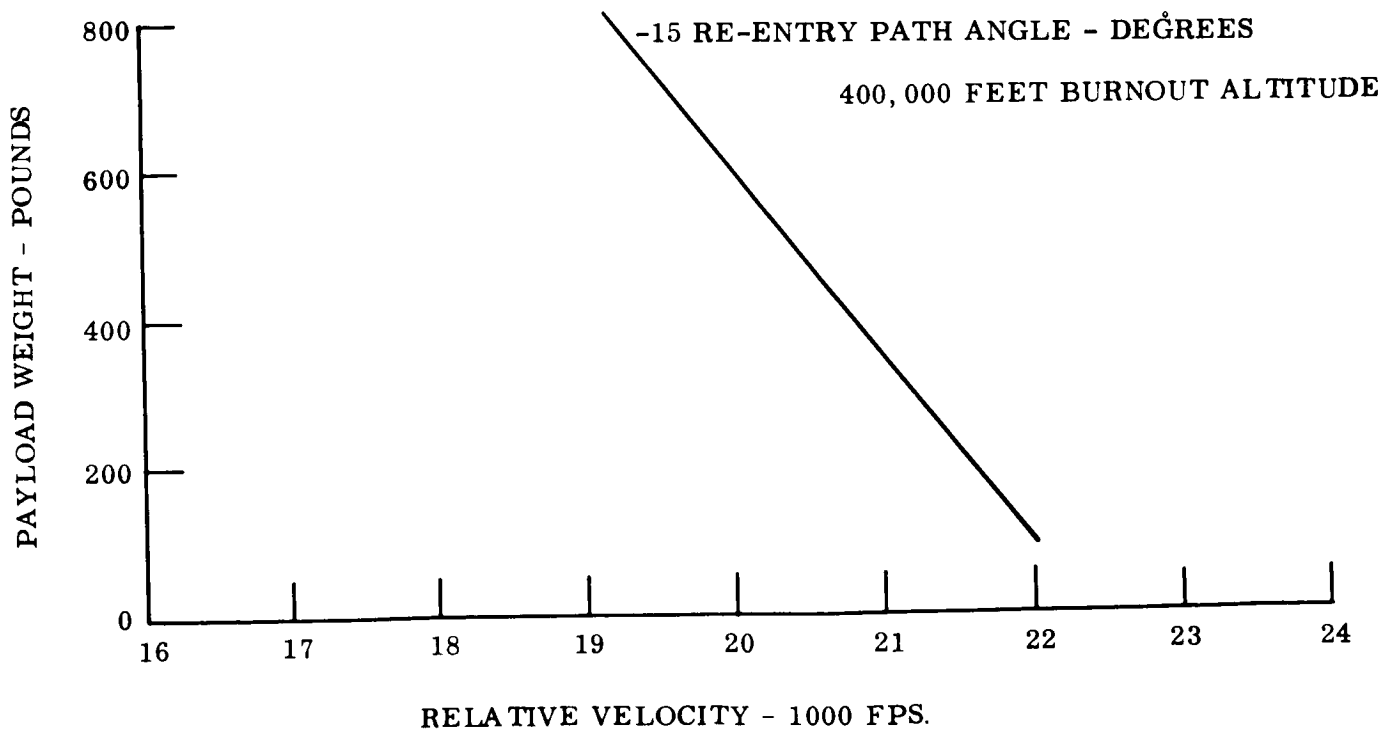
(3) Altitude (h_e) of 400,000 feet.

The Scout four-stage payload versus velocity performance curves shown in Figure 3.1-1 indicate a payload weight capability of 350 pounds or greater at a re-entry velocity of 25,000 feet per second at fourth stage burnout altitude of 400,000 feet for the flight path angle range under consideration (ref. 3.1-1). As the feasibility study progressed, it was established from a flight test environment and test panel configuration standpoint by the Thermodynamics and Structures groups that a re-entry velocity of 25,000 feet per second (ref. 3.1-2) is not required. Consequently the design re-entry conditions were changed to the following:

(1) Path angles (γ_e) varying from 1 to 10 degrees down from the local horizontal.



A. FOUR-STAGE PAYLOAD VS. VELOCITY



B. THREE-STAGE PAYLOAD VS. VELOCITY

Figure 3.1-1. - Scout Re-entry Performance at Burnout

(2) Velocity (V_e) of 20,000 feet per second.

(3) Altitude (h_e) of 400,000 feet.

The change in re-entry velocity permitted the use of a three-stage Scout booster configuration based on the payload versus velocity performance curves shown in Figure 3.1-1b, resulting from data obtained from the re-entry F Program. These indicate a payload weight capability of 600 pounds at a re-entry velocity of 20,000 feet per second for a -15 degree flight path angle at a third stage burnout altitude of 400,000 feet. Extrapolating the flight path angle to the SLAMAST range of -1 to -10 degree path angles provides sufficient weight margin to account for unknown boost trajectory parameters and variables.

The use of the three-stage Scout launch vehicle immediately provides two benefits to the SLAMAST vehicle; one, it permits the vehicle length to increase to 63 inches; and two, it removes the requirement for the despin of the S/C after separation. Item one provides more test panel flexibility and subsystem growth capability in addition to eliminating packaging problems encountered in the 48 inch vehicle, while item two reduces the impulse requirements of the altitude control gas system. Conversely, the use of a three-stage Scout requires the design of an interface adapter - separation system.

The expected SLAMAST Scout launch configuration is shown in Figure 3.1-2. A spacer separation unit is utilized as an interface adapter to attach the S/C to the third or upper stage of the Scout booster. A flight shroud is used during ascent. The S/C will be released after completion of the launch phase upon signal from the Scout third stage.

The SLAMAST S/C will be compatible with the payload launch design parameters and environment factors specified in the Scout Users Manual, including items such as payload separation, dynamic stabilization, payload thermal environment, and mechanical environments of acceleration and vibration. The preliminary S/C design and flight requirements are presently covered by two GE documents, the SLAMAST System Specification (Stage 1) identified as Specification ERS0010-02-0027-1 and the SLAMAST Systems Requirements Analysis identified as document 67SD613. Both are included as part of the SLAMAST Final Report data package and should be referred to for preliminary detailed information. The Systems Requirement Analysis contains the flight sequence of events.

3.1.2 DESIGN TRAJECTORIES

The total flight trajectory for a re-entry mission flight consists of the boost trajectory segment from lift-off until separation and a re-entry trajectory segment from separation until termination of the flight. Primary emphasis during the feasibility study has been on the re-entry trajectories since the level-of-effort available did not permit boost trajectory simulation. "Best available information" estimates were made for the boost trajectories, sufficient for the definitive purposes of this study. Detailed analysis in later phases of the SLAMAST Program would result in modifications that would incorporate delta changes to the assumed boost trajectory parameters.

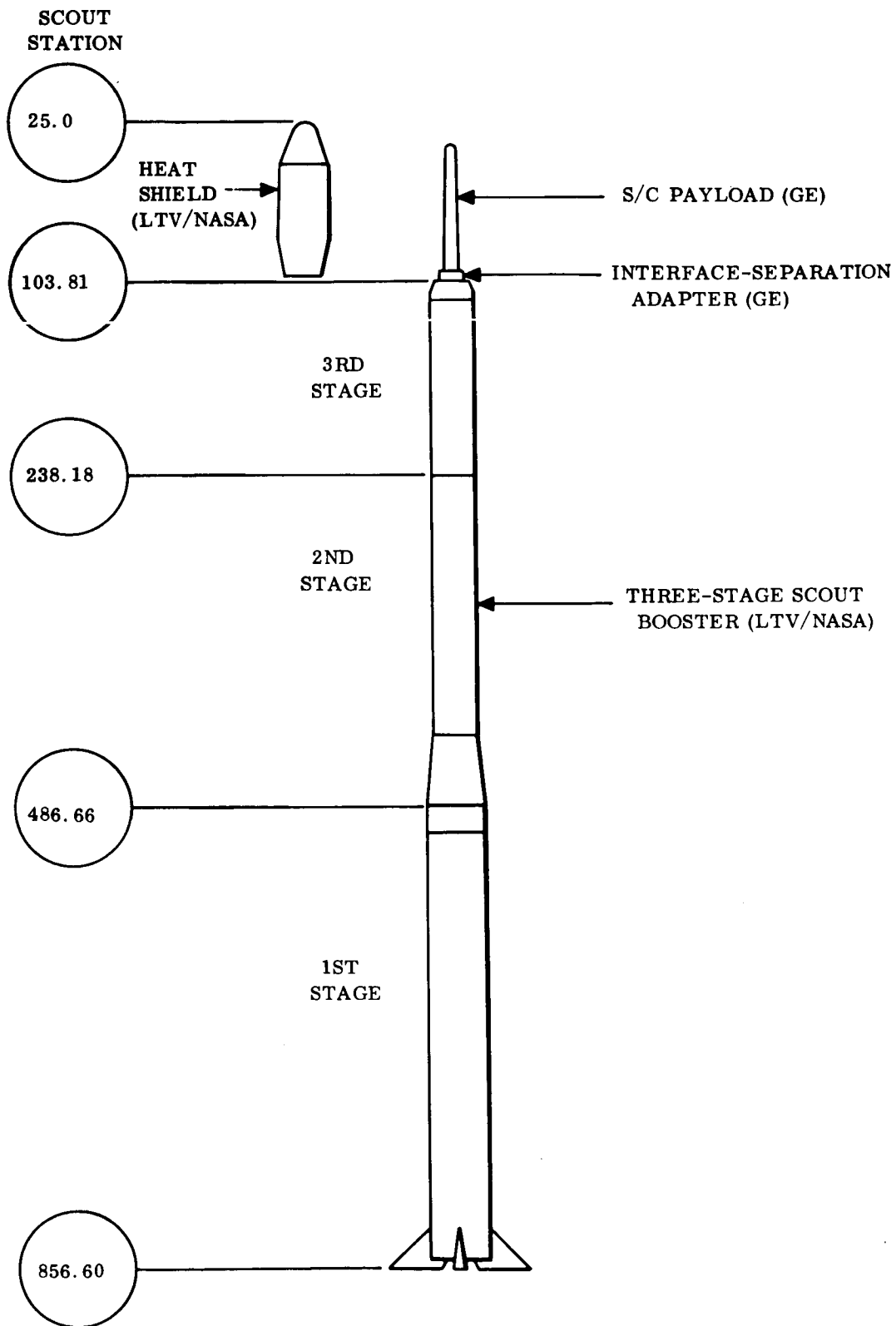


Figure 3.1-2. - SLAMAST/Scout Vehicle Launch Configuration

A pictorial representation of the SLAMAST flight mission profile is shown in Figure 3.1-3 for a -1 degree re-entry path angle. The pictorial representation subdivides the re-entry trajectory into three phases. Re-entry design trajectories have been generated for the bounding re-entry path angles (-1 and -10 degrees) and vehicle $W/C_L S$ covering the presently defined 63 inch S/C.

The powered flight phase for the three-stage Scout consists of the booster firing the first two stages sequentially, coasting beyond peak altitude and then firing the third stage to drive the payload back into the atmosphere. Re-entry capabilities can vary widely depending on the selection of pitch rates, staging times, and final stage attitude at ignition. Major considerations involving the launch phase include booster dispersions at time of separation (up- or down-range, cross-range, altitude), separation tip-off errors, and exact location of separation point. Nominal separation errors assuming ballistic re-entry parameters are magnified greatly in $L > D$ flights where flight times are of a much longer duration.

A revision of the reference time for the S/C deployment and recovery events has resulted from a ± 6 n. mi. tolerance in Scout burn-out (and separation) altitude input received from NASA. A second reference time (in addition to the one at separation) will be established during the pull-out maneuver based upon the change in sign of \dot{A}_x .

It would be desirable from a radar tracking and data monitoring standpoint for the S/C location at re-entry to be short, but within the look angle of the ground-based equipment at Bermuda for a Wallops Island launch. This would provide maximum time coverage of the separation re-entry pull-out sequence referenced to a precise location and maximum communications network coverage point. Every effort should be made to tailor the powered flight trajectory to fit this criteria, without overriding the experiment input re-entry conditions.

The re-entry design trajectories (from 400,000 feet) consist of exospheric flight, pull-out, constant altitude flight, deceleration, and terminal descent. Current experiment time is 700 seconds, defined as the time from re-entry at 400,000 feet until the deceleration phase is initiated. The resulting heat flux history appears to meet the criteria for a good experiment. The re-entry maneuvers are defined as follows:

(1) Pull-out. - A constant angle of attack providing the specified ballistic coefficient (approximately 250) is maintained from re-entry (400,000 feet) until a pull-out to horizontal flight is achieved.

(2) Horizontal Flight. - The angle of attack is modulated in the pitch plane to provide the lift necessary for horizontal flight. The angle of attack increases as the dynamic pressure decreases until the angle of attack for the specific $W/C_L S$ is attained.

(3) Recovery Terminal Glide. - With the dragbrake deployed, the angle of attack is reduced to zero (zero lift), and the vehicle glides to the subsonic velocity point where the ballute terminal recovery system is deployed.

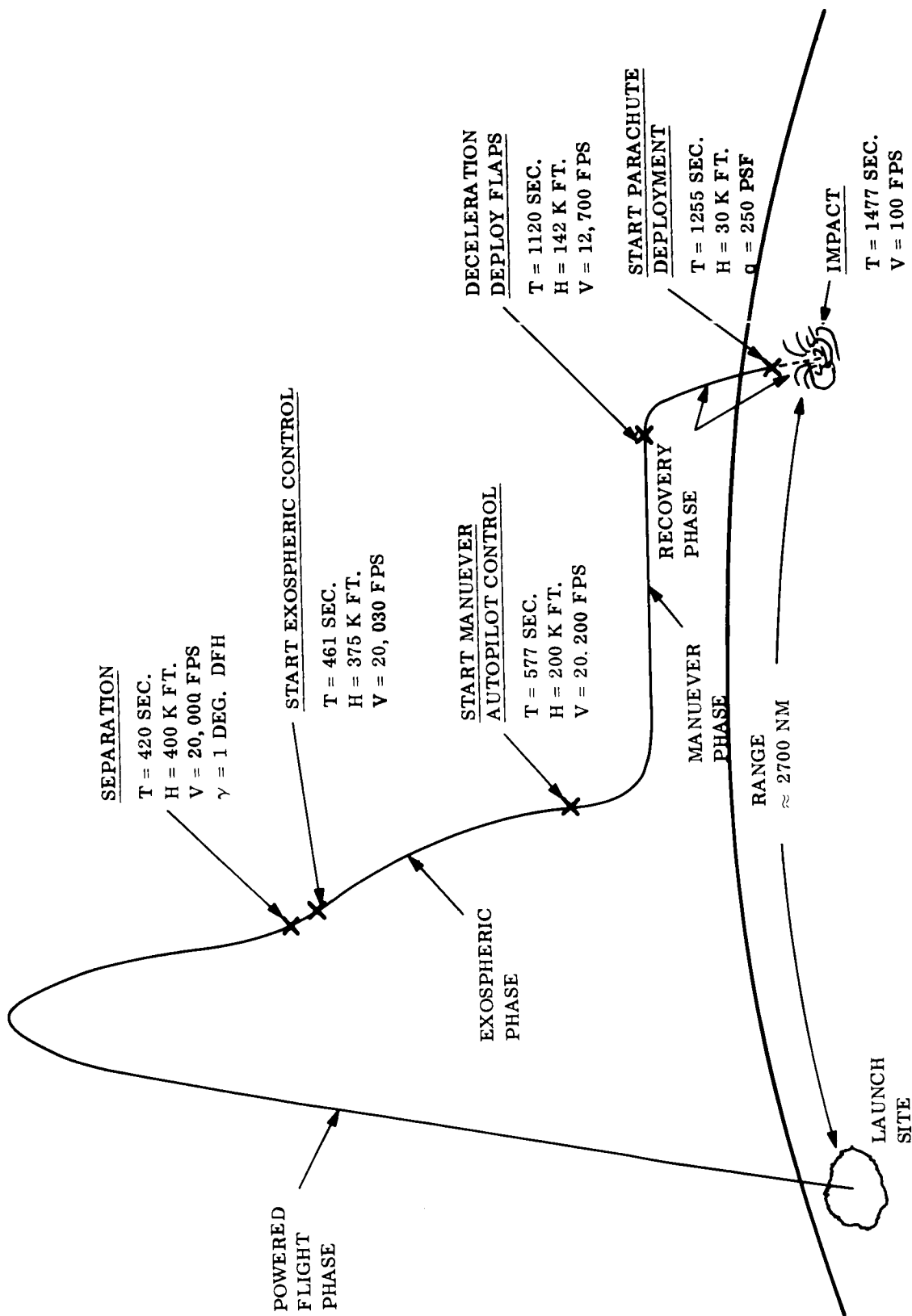


Figure 3.1-3. SLAMAST Typical Flight Mission Profiles

Time histories of velocity, altitude, stagnation, heat rate, dynamic pressure, angle of attack, axial and normal acceleration, and range, as well as altitude versus range have been generated for the two bounding design cases (re-entry at 20,000 feet per second with path angles of -1 and -10 degrees). These are discussed in more detail in Section 3.3. It is interesting to note that at the present lower design re-entry velocity the environment (heat flux) sensitivity to re-entry path angle variations is nearly eliminated.

On the basis of the latest design trajectories incorporating the drag brake deceleration system, it appears a single stage subsonic recovery subsystem will meet recovery requirements. This means the use of a single stage ballute is preferred rather than a two-stage deceleration chute and paraloon combination.

3.1.3 COMMUNICATION

The following criteria have been identified in the selection of an information retrieval system which will effectively fulfill the SLAMAST flight objectives:

- (1) The system shall provide adequate accuracy and time response resolution to permit reliable quantitative delineation of the thermostructural phenomena of interest.
- (2) The system shall provide sufficient diagnostic information to adequately interpret the control system functions during the vehicle development phase of operational testing.
- (3) The system shall require a minimum surface support force.
- (4) The system shall, if possible, be compatible with both the Eastern Test Range and the Apollo Ship data acquisition equipments.
- (5) The system shall be configured to provide in-flight data acquisition to minimize the probability of data loss.

The on-board communications subsystem resulting from the feasibility study will transmit in real time from separation until ballute deployment. Plasma attenuation investigations indicate blackout of real time data during pullout and a part of level flight during the 700 second experiment interval. A playback recorder will be utilized to record experiment interval data with two modes of playback initiation; through a ground command during the last 100 seconds of the experiment interval or automatically at the initiation of the deceleration phase. The communication subsystem configuration as a result of this study is as follows:

- (1) PCM/FM Telemetry with digital on-board data handling (eight bit sample encoding).
- (2) Nondestructive data playback (data remains on tape) from the on-board recorder with no provision for simultaneous record and playback.

(3) Capability for ground command initiated recorder (digital) playback.

(4) Programmed playback of the on-board recorder during the retardation sequence as backup.

(5) Continuous real-time telemetry at a power level of two watts except during recorder playback. During playback, the recorder and real-time information shall be mixed and transmitted at a two watt level.

(6) Incorporation of a C-band transponder and command receiver.

The communication subsystem is discussed thoroughly in Sections 3.5 and 4.2, including the results of studies and trade-offs in arriving at a recommended configuration and the multiplicity of ways S/C data can be retrieved.

3.1.4 RECOVERY

Requirements for the recovery of a vehicle with $L/D > 1$ are dependent upon the recovery zone footprint for the planned flight path and selected trajectory control scheme. Feasible recovery is based upon the recovery force providing adequate coverage of the recovery zone within allowable time constraints. For a limited-size recovery force the footprint size should be held to a minimum value. In an operational vehicle, maximum footprint size is desirable, while in a flying test-bed design such as SLAMAST the opposite holds true.

The SLAMAST range is controlled through the use of trajectory termination utilizing deceleration flaps. The sizing and location of the bounding trajectory recovery zones, recovery force configuration and deployment are discussed in more detail in Sections 3.3 and 3.6.

3.1.5 RANGE SAFETY

Range safety requirements are developed by determining criteria (generally through graphical means) denoting the extent of any range safety problem and comparing bounding trajectory worst-case malfunction footprints with the range safety limits. If the safety limits are exceeded in any case, a flight termination system must be employed by the S/C.

SLAMAST limits are established in Section 3.7 for vehicle malfunctions occurring at the time of S/C re-entry (400,000 feet) and at 350 seconds after re-entry. The conditions under which range safety constraints are exceeded are shown, and a brief discussion of a possible flight termination system is presented.

REFERENCES

- 3.1-1 LTV Corporation, "Scout User's Manual, "Vol. 1-5, August 1966.
- 3.1-2 Grasier, R., "SLAMAST Design Trajectories," PIR 8153-1830, January 1967.

3.2 AERODYNAMIC STUDIES

3.2.1 AERODYNAMIC DEFINITIONS AND NOMENCLATURE

The aerodynamic conventions, nomenclature, acronyms, symbols, and numerical values of representative constants are presented here to establish a clearer basis for understanding aerodynamic performance data and other material. By way of introduction to this material, lifting vehicular systems, represented by the SLAMAST geometry of Figure 3.2-1, employ NASA standard terminology and definitions; these generally differ from those used for axisymmetric ballistic vehicles. Consequently, a relatively comprehensive summary of terminology and definitions was prepared and is presented here both as an aid and as a consistent basis for understanding aerodynamic data presentations. The reader is referred to standard aerodynamic texts for more detailed definitions, explanations, and expositions than are presented here.

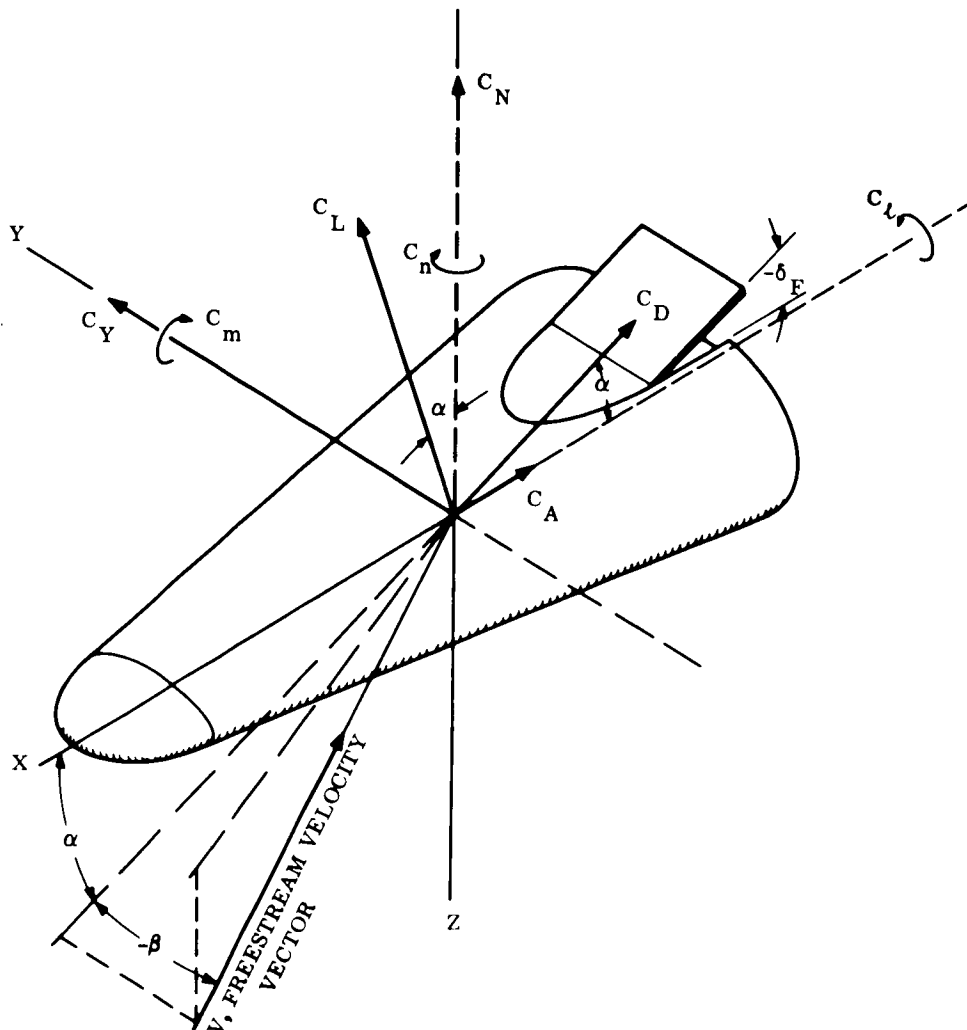


Figure 3.2-1. - SLAMAST Body Axes Coordinate System Representation

List of most common symbols

Axes system

The basic body axes are a set of orthogonal axes fixed with respect to the vehicle and to each other but at varying angles to the free-stream velocity vector. These axes are defined as follows and as shown in Figure 3.2-1:

- X Longitudinal axis of the vehicle, an arbitrary line in the vertical plane of symmetry, generally a center-line.
- Y Vehicle axis normal to the longitudinal axis and to the vertical plane of symmetry, originating at the moment reference center (or center-of-gravity).
- Z Body axis mutually perpendicular to both X and Y axes, originating at the moment reference center, lying in the vertical plane of symmetry.
- x, y, z Distances in percent l_{REF} , measured along the X-axis aft from the nose reference plane, and measured along the Y-axis right and Z-axis up from the common origin of the axes system, respectively.

Attitude angles

- α Pitch angle. - (the pitch component of angle-of-attack) - that angle between the vehicle's longitudinal axis and the component of the free-stream velocity vector lying in the X - Z plane, positive for rotation above the velocity vector, degrees.
- β Sideslip angle. - that angle between the free-stream velocity vector and its normal projection onto the body's X-Z plane degrees; negative as shown in Figure 3.2-1. (Yaw angle, ψ , is minus β , the side slip angle).
- ϕ Roll angle. - that angle of rotation of the X - Y plane from the local horizontal plane, measured in the Y - Z plane, positive for clockwise rotation as viewed from the rear, degrees.
- γ Flight path angle. - that angle between the free-stream velocity vector and its normal projection onto the local horizontal plane, positive when measured nose up, degrees. (The inertial flight path angle, γ_1 , is referenced to a space-fixed reference plane, such as a launch pad for an earth-oriented system. The symbol is also used for the ratio of specific heats, as defined later.)
- θ Pitch attitude angle. - that angle between the vehicle's longitudinal axis and its normal projection on the local horizontal plane, positive for nose above the local horizontal plane, degrees.

Forces

The positive direction of body-induced forces is away from the common origin of the axes and along the solid axes shown in Figure 3.2-1.

- N Normal force. - that force directed parallel to the Z axis, upward, and acting through the center-of-pressure, lbf. or kgf.

$$N = C_N qS. \quad C_N = C_L \cos \alpha + C_D \sin \alpha$$

- A Axial force. - that force directed parallel to the X axis, aft, and acting through the center-of-pressure, lbf. or kgf.

$$A = C_A qS. \quad C_A = C_D \cos \alpha - C_L \sin \alpha$$

- Y Side force. - that force directed parallel to the Y axis, right, and acting through the center-of-pressure, lbf. or kgf.

$$Y = C_Y qS.$$

- L Lift force. - that force normal to the component of the free-stream velocity vector, in the X-Z plane, upward, and acting at the vehicle's center-of-pressure, lbf. or kgf.

$$L = C_L qS.$$

$$C_L = C_N \cos \alpha - C_A \sin \alpha$$

- D Drag force. - that force parallel to the component of the free-stream velocity vector, in the X-Z plane, aft, and acting at the vehicle's center-of-pressure, lbf. or kgf.

$$D = C_D qS.$$

$$C_D = C_A \cos \alpha + C_N \sin \alpha$$

Moments and their reference locations

- m Pitching moment. - that moment about the Y axis, positive for clockwise rotation when viewed from the left vehicle side, ft. - lbf. or m - kgf.

$$m = C_m qSl_{REF}$$

- n Yawing moment. - that moment about the Z axis, positive for clockwise rotation when viewed from the vehicle top, ft. - lbf. or m - kgf.

$$n = C_n qSl_{REF}$$

- l Rolling moment. - that moment about the X axis, positive for clockwise rotation when viewed from the rear, ft. - lbf. or m - kgf.

$$l = C_l qSl_{REF}$$

x_{cp} Center of pressure location (at which resultant vehicle forces act) in body lengths from a reference plane, (see x_{cg} definition) perpendicular to the X-axis.

$$C.P._y = x_{cg} - \frac{\partial C_n}{\partial C_Y} ; \quad C.P._x = x_{cg} - \frac{\partial C_m}{\partial C_N}$$

x_{cg} Location of vehicle center of gravity in body lengths from a reference plane perpendicular to the X-axis. (The SLAMAST reference plane is located exactly at the nose origin; $x_{cg} = 0.569$.)

Other symbols (See references 3.2-1 through 3.2-3 for numerical values)

a Speed of acoustic pressure propagation, fps or mps. (Also local cross-section depth)

$$a = \sqrt{\gamma gRT}$$

C_p Pressure coefficient, dimensionless. $C_p = \frac{P_L - P_\infty}{q_\infty} = \frac{2}{\gamma M^2} \left(\frac{P_L}{P_\infty} - 1 \right)$

g Local value of the gravitational acceleration, ft/sec² or m/sec²

lbf Pounds force

lbm Pounds mass, or slugs (lbm = lbf/g)

M Mach number, dimensionless. $M = \frac{V}{a}$

p Static pressure, psf or kgsm

q Dynamic pressure, psf or kgsm. $q = \rho V^2/2 = \gamma PM^2/2$

R Reynolds' number, dimensionless, $R = \rho V l_{REF}/\mu$

V Velocity magnitude, fps or mps

η Missile body axis load factor; (positive in the negative direction of the respective body axis), in fractions of local gravitational acceleration.

ρ Mass density of air, lbm./ft³ or kgm/ft³

γ Ratio of specific heats (c_p/c_v); (about 1.401 for air); used also for flight path angle.

- μ Coefficient of kinematic viscosity, lbm/ft-sec
- T Temperature, degrees Fahrenheit ($^{\circ}\text{F}$), Celsius ($^{\circ}\text{C}$), Rankine ($^{\circ}\text{R}$), or Kelvin ($^{\circ}\text{K}$); $^{\circ}\text{K} = 273.16 + ^{\circ}\text{C}$; $^{\circ}\text{R} = 461.67 + ^{\circ}\text{F}$ (ref. 3, 2-3)
- R Gas constant (see Dimensions for values)

Subscripts

- ∞ Free-stream conditions
- a Sea level, standard day values
- F Flap (See Control Nomenclature for details)
- I Inboard, inviscid, inertial
- L Local, left
- O Outboard
- R Right
- o Condition of zero pitch angle, or before perturbation

p, q, and r Roll, Pitch and Yaw, respectively

Superscripts

- *
- At the condition for maximum lift-to-drag ratio
- 40 Forty degrees deflection (as in δ^{40}); similarly for other deflection angles.

Derivatives

- $C_{m_{\alpha}}$ The pitching moment derivative with respect to pitch angle; a plus value represents static pitch instability. $C_{m_{\alpha}}$ is usually taken as the slope of the C_m versus α curve at particular α 's, and is a direct measure (not a definition) of static longitudinal stability. (The static longitudinal stability is defined as $\partial C_m / \partial C_N$, and can usually be approximated by $\partial C_m / \partial C_N \approx \partial C_m / \partial C_L$ in the useful pitch angle range, per degree.)

$$C_{m_{\alpha}} = \frac{\partial C_m}{\partial \alpha}$$

- $C_{n_{\beta}}$ The yawing moment derivative with respect to side slip angle; a plus value represents static yaw stability, per degree.

$$C_{n_{\beta}} = \frac{\partial C_n}{\partial \beta}$$

$C_{l\beta}$ The rolling moment derivative with respect to side slip angle; a plus value represents static roll instability, per degree.

$$C_{l\beta} = \frac{\partial C_l}{\partial \beta}$$

$C_{N\alpha}$, $C_{L\alpha}$ Normal force-curve and lift-curve slope is typically measured at zero pitch angle (α_0) and at the pitch angle for maximum lift-drag ratio (α^*), per degree.

$$C_{N\alpha} = \frac{\partial C_N}{\partial \alpha}; \quad C_{L\alpha} = \frac{\partial C_L}{\partial \alpha}$$

K Induced drag factor - not strictly a derivative, but useful in pitch performance analysis. K is the averaged incremental drag increase divided by the square of the incremental lift increase, and is often presented in a somewhat modified form such as $K' = \Delta C_A / \alpha^2$

$$K = (C_D - C_{D_0}) / (C_L - C_{L_0})^2$$

Control Nomenclature

The flap axes system is a set of flap-fixed orthogonal axes free to rotate with flap deflection.

X_F Flap axis centered in the flap plane of symmetry and perpendicular to the hinge line at body-hinge line juncture.

Y_F Flap axis along the flap hinge line.

Z_F Flap axis mutually perpendicular to X_F and Y_F at their juncture.

δ_F Flap deflection angle; angle between the X - Y plane and the $X_F - Y_F$ plane in degrees. (Positive when in a direction to produce positive pitch force; hence, trailing edge upward deflection is negative deflection.)

F_{X_F} , F_{Y_F} , F_{Z_F} Flap force components in the X_F , Y_F , and Z_F directions, positive upward, right, and aft, respectively.

$$F_{X_F} = C_{X_F} q S; \quad F_{Y_F} = C_{Y_F} q S; \quad F_{Z_F} = C_{Z_F} q S$$

F_{N_F}, F_{A_F} Flap force components in the z and x directions of the Z and X - axes, positive up and aft, respectively.

$$F_{N_F} = C_{N_F} q S; F_{A_F} = C_{A_F} q S$$

Hm_F Flap hinge moment; moment about the Y_F axis (a positive hinge moment is clockwise when viewed from the left side, ft-lbf or m-kgf.
 C_h = Flap hinge moment coefficient, $hm = C_{hg} S_F l_F$

m_F, n_F, l_F Moment increments due to flaps, including flap interference contributions about the Y, Z, and X - axes, same positive sense as pitching, yawing, and rolling moments, respectively.

$$m_F = C_{m_F} q S l_{REF}; n_F = C_{n_F} q S l_{REF}; l_F = C_{l_F} q S l_{REF}$$

$l_{F_{REF}}$ Reference flap chord length, ft. or m.

l_{T_F} Reference flap moment arm, C. P. $_F$ to x_{cg} , in Body Lengths

S_F Reference flap area, sq ft or sq m

C. P. $_F$ Flap center of pressure location, usually in Body Lengths from the flap hinge line

\bar{V} Tail Volume, a measure of the relative control effectiveness;

$$\bar{V} = (l_{T_F} / l_{REF}) (S_F / S)$$

$C_{m_{\delta_F}}$ Flap moment derivative, $\partial C_{m_F} / \partial \delta_F$ (other flap derivatives for force and moment are similarly defined)

Dimensions

l_{REF} Vehicle reference length, ft or m (used along with S to reduce aerodynamic moments to non-dimensional form).

S Vehicle total projected planform area, sq ft or sq m (used to reduce aerodynamic forces and moments to non-dimensional form).

b Vehicle span, ft or m

w Vehicle local width, ft or m

SLAMAST Reference Lengths and Areas Currently in Study Use

Nomenclature	x _{cg}	Length			Area		
		inch	feet	meters	sq. in.	sq. ft.	sq. m.
Current 63"	0.569	63.00	5.25	1.6002	1132.816700	7.8667826	0.730848022
Basic	0.569	48.00	4.00	1.2192	657.598810	4.5666584	0.424256450
NASA Test ¹	0.540	17.98	1.4983333	0.456692	92.098	0.639569	0.59417950
Model ²	0.569	17.98	1.4983333	0.456692	92.269447	0.64076005	0.059528557
2/7 Scale ³	0.569	18.00	1.50	0.4572	92.474833	0.64218634	0.59661063

Notes:

- (1) References used to reduce 3.95 and 4.63 Mach number test data obtained in the NASA-LRC Unitary Plan Wind Tunnel;
- (2) Actual model references differ from NASA-data refs. to reflect careful area computations and design flight cg;
- (3) Actual 2/7 scale numerical values (the nominal 2/7 (0.2857143) scale model is 0.2853968 scale), presented here for comparison purposes only.

3.2.2 CONFIGURATION AERODYNAMICS

3.2.2.1 Baseline SLAMAST shape. - Presented here is the aerodynamically defined external geometry of the basic GE/RSD SLAMAST flying test-bed shape. This shape was employed in the current SLAMAST study effort, but has been somewhat modified by the addition of a dive brake as subsequently discussed. All dimensional data are normalized with respect to vehicle length.

Detailed information on the exact manner in which the elliptical cross-sections vary with length is presented along with the variation of peripheral surface slope and meridian angle, in a non-dimensional form valid for any vehicle length.

The aerodynamically-tailored shape shown in Figure 3.2-2 was originally defined by a careful balance of aerodynamic force, moment, stability, control effectiveness, and geometric factors. This same shape was used as the basis of model design and construction for the nominal 2/7 scale SLAMAST wind tunnel model.

Aerodynamic force and moment changes resulting from variation from the shape of Figure 3.2-2 require separate and detailed analysis. This is particularly true with respect to any and all variations in or near the upper-aft mounted control surface.

The dimensional data presented in Figure 3.2-2 is normalized with respect to length. Any dimension shown, when multiplied by vehicle length, will be correct for that vehicle. For example, dimensional data for a 50-in. version may be obtained by multiplying the presented values by 50, the angles and center-of-gravity position of Figure 3.2-2 remaining unchanged.

Figure 3.2-3 presents the variation of span (b), height (a), and ellipticity, (b/a), with fractional vehicle length. The analytical relationships that apply for the wrapped surface portion from the nose cap station to the vehicle base are also shown on the figure. Those relationships were simply derived from the 0.073958 and 0.222500 semi-span and 0.029271 and 0.127292 semi-height fractional length values for the nose cap ($X/L = 0.063125$) and base ($X/L = 1$) stations, respectively.

Figure 3.2-4 presents the variation of peripheral surface slope with meridian angle for cross-sections at the nose cap, and at 0.1, 0.2, 0.4, 0.6, 0.8, and 1.0 fractional length locations. The data of this figure is of particular value to design and to thermodynamic analysis. As examples, a constant peripheral slope could be a keel or longeron location along which attaching clips and brackets would not vary their angles with respect to a vertical or horizontal line. Consequently, one clip design could be used along such a constant slope line, rather than varying with longitudinal location. In the thermodynamic analysis of elliptic shapes, Lees has reported that the heating rates follow peripheral slope and not meridian angle, as reported in reference 3.2-4 and confirmed by the test information of reference 3.2-5. Thus, results for a constant slope trace on an elliptic conoid represent a comparable slope trace on a right circular cone and heating analyses may be simplified.

NOTES:

1. ALL CROSS SECTIONS ARE ELLIPTICAL.
2. THE CENTER-OF-GRAVITY IS LOCATED AT $.569 l_{REF}$.
3. VEHICLE REFERENCE AREA IS $.28541615 (l_{REF})^2$.

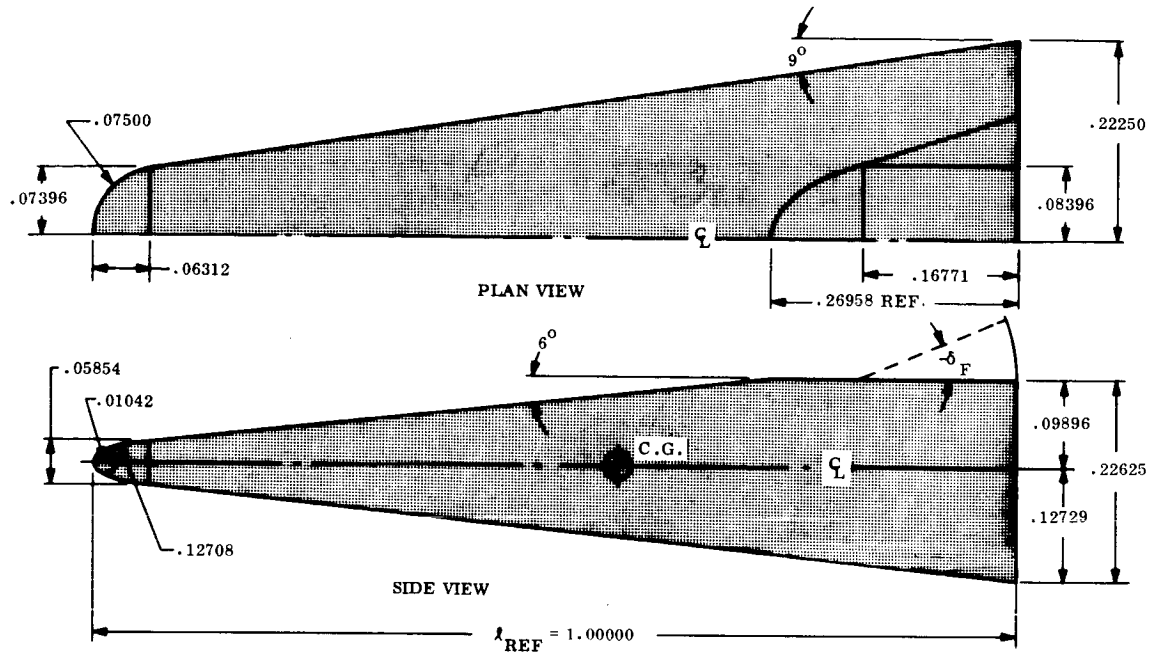


Figure 3.2-2. - Basic SLAMAST External Dimensioning System

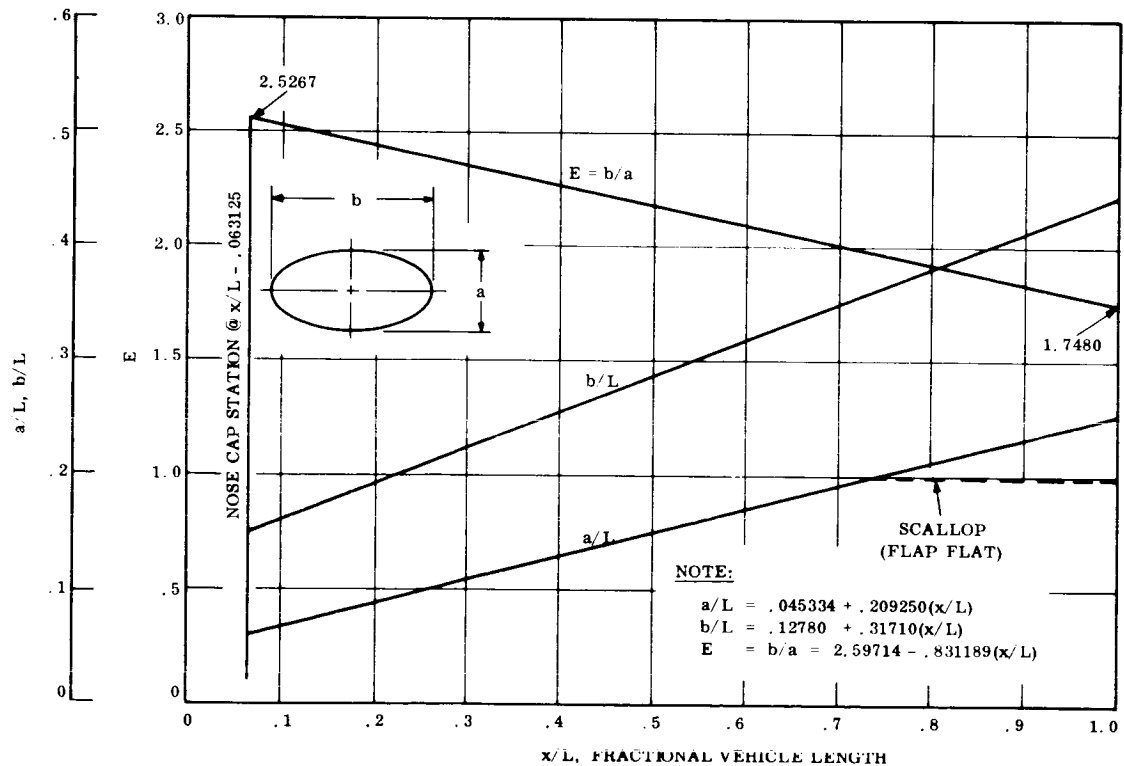


Figure 3.2-3. - Ellipticity Variation with Fractional Length

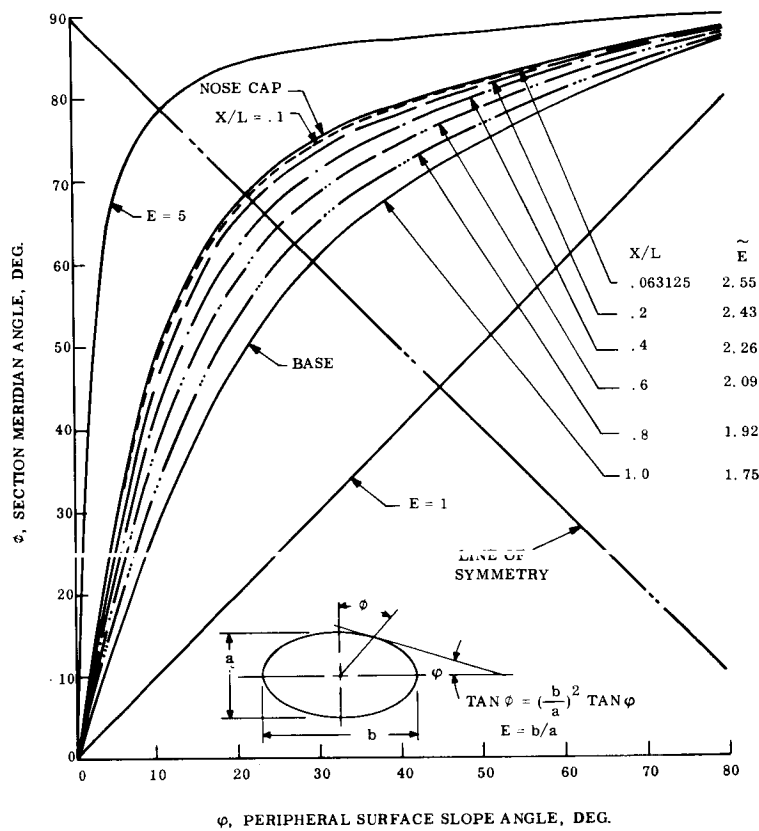


Figure 3.2-4. - Peripheral Surface Slope versus Meridian Angle

NOTES:

1. ALL CROSS SECTIONS ARE ELLIPTICAL.
2. THE CENTER-OF-GRAVITY IS LOCATED AT $.569 l_{REF}$.
3. VEHICLE REFERENCE AREA IS $.28541615 (l_{REF})^2$.

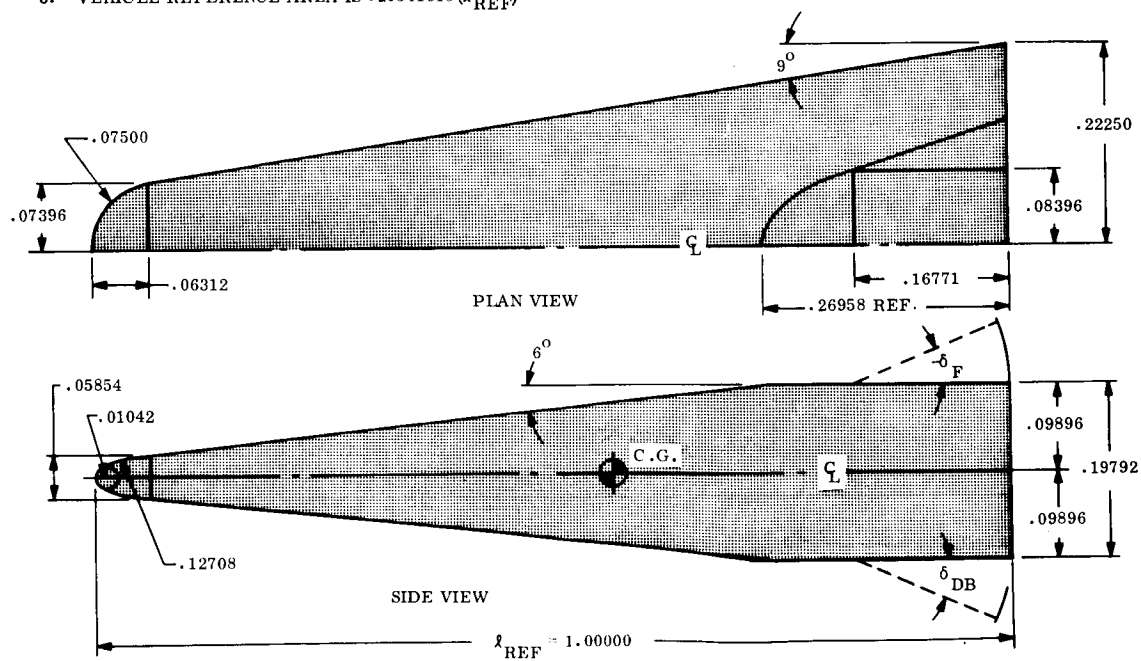


Figure 3.2-5. - SLAMAST plus Drag Brake Normalizes Dimensions

3. 2. 2. 2 SLAMAST plus drag brake. - The addition of a drag brake to the existing SLAMAST vehicle was incorporated as a means of increasing aerodynamic drag to permit ballistic flight following the environmental test period. The effects of such flight path management on the vehicle system include:

- (1) Lowered total flight time;
- (2) Reduced total integrated heat pulse and possibly reduced backface temperatures and heat shield weight;
- (3) Reduction in down-range excursion;
- (4) More precise control of recovery point;
- (5) Increased pitch stability (both drag brake and pitch flap rotated outward);
- (6) Reduction in transonic pitch and yaw angles-of-attack transients;
- (7) Use of a subsonic recovery system.

The drag brake geometry was assumed identical to the existing SLAMAST pitch flap and scallop. The "SLAMAST plus drag brake" aerodynamic configuration thus exhibits symmetry about both the HRP (Horizontal Reference Plane) and the VPS (Vertical Plane of Symmetry) compared to the baseline SLAMAST study shape which is symmetrical only about the VPS. Normalized non-dimensional data for the SLAMAST plus dive brake shape are presented in Figure 3. 2-5.

The side area change results in a lessened yaw stability, the amount of which requires separate analysis. However, on the basis of wind tunnel tests run with the scallop for the top flap the reduction in stability is not expected to be significant.

Aerodynamic drag, flap hinge moment, and flap effectiveness data are presented here for the current SLAMAST vehicle (with the drag brake). The estimates are for zero pitch angle-of-attack, at a reference center-of-gravity location of 56.9 percent vehicle length, and for Mach numbers to 20. The estimated error tolerances associated with the data vary with flap deflection, flight altitude, and Mach number and can be as high as 30 percent. Dimensional details are shown in Figure 3. 2-5.

The aerodynamic performance information required to assess the basic flight path characteristics is presented, along with results of an initial recovery time-history, and the consequent flap hinge moment (per flap) along that recovery flight path. The preliminary aerodynamic performance data consists of assessment of the changes in drag, in flap hinge moment, and in the change of vehicle pitching moment about a $0.569 l_{REF}$ center-of-gravity location with respect to flap deflections measured from the HRP. All the data are presented as functions of Mach number and flap deflection, based primarily on available test-derived flap incrementals for a shape somewhat similar to SLAMAST and for a five-degree cone plus flap configuration. More complete flap aerodynamic load and hinge moment information may be found in paragraph 3. 2. 4. 2.

3.2.2.2.1 Aerodynamic drag: - Drag coefficient estimations are presented in Figures 3.2-6 and 3.2-7 for the SLAMAST vehicle with a drag brake addition. The estimations are all at zero pitch angle-of-attack. The drag estimation errors of Figures 3.2-6 and 3.2-7 exist for the following reasons:

(1) Test data for the single-flap SLAMAST configuration exists only at 3.95 and 4.63 Mach number to a flap deflection of 46 degrees with respect to body centerline.

(2) Test data at zero pitch angle-of-attack is sensitive to body cross-sectional shape; an elliptical cross-section promoting more cross flow in the flap vicinity.

(3) The nearest related shape for which test data exists has a flap geometry which differs in

(a) trailing behind the body base,

(b) the presence of a stub delta wing blocking cross-flow, and,

(c) a forebody incorporating a canopy.

(4) The flap force sensitivity to local shock geometry, which geometry changes rapidly below a Mach number of about four.

The consequent ranges of possible error in the presented drag estimates are functions of Mach number, flap deflection, and flight altitude. For the purposes of the SLAMAST feasibility study, the drag error range is estimated for Mach numbers from one to five and flight altitudes to 175K feet as zero to plus 10 percent for zero flap deflection, minus 10 to plus 15 percent at 25° flap deflection, and plus to minus 20 percent at deflections higher than 40°. The same ranges apply for other Mach numbers if the flow is laminar.

The error ranges are necessarily approximate although a concerted effort was made to resolve the enumerated and other configurational differences in the available test data.

3.2.2.2.2 Initial recovery time histories: - Shown in Figure 3.2-7 are variations of drag with flap deflection. Initial trajectory runs employed approximate flap deflections of 15, 30, and 40 degrees. A limited amount of the resulting time histories are presented here as Figures 3.2-8, 3.2-9 and 3.2-10.

3.2.2.2.3 Flap effectiveness and hinge moment: - The variation of pitching moment due to the flap with flap deflection, $\Delta C_{m\delta_F}$, was determined for varying flap deflection at zero pitch angle and at Mach numbers of 3.95, 4.63, and 10 to 20. The obtained values were then faired by use of the drag progressions with Mach number to form the flap effectiveness versus Mach number information presented along with the other flap data of paragraph 3.2.3.2.

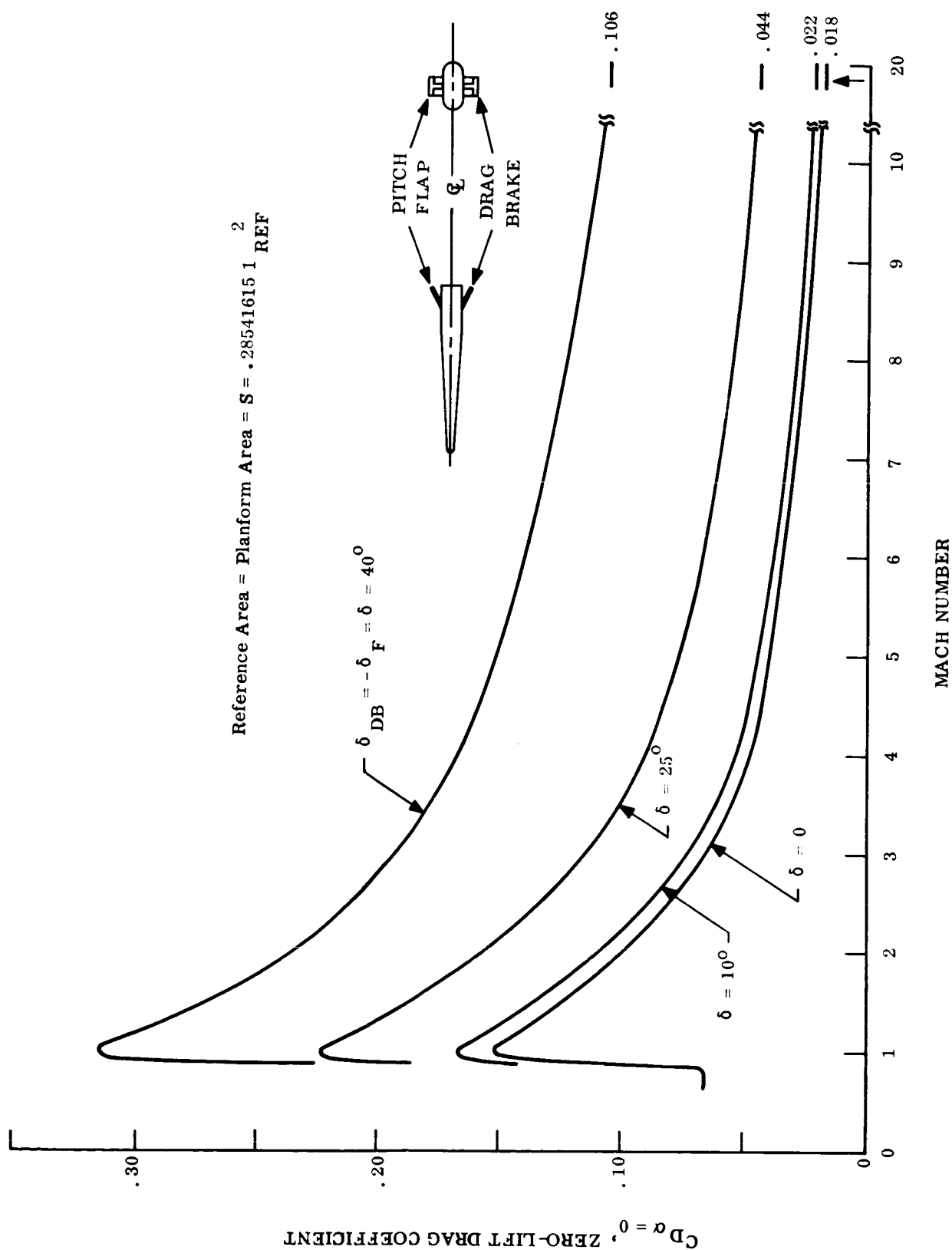


Figure 3.2-6. - Drag versus Mach Number

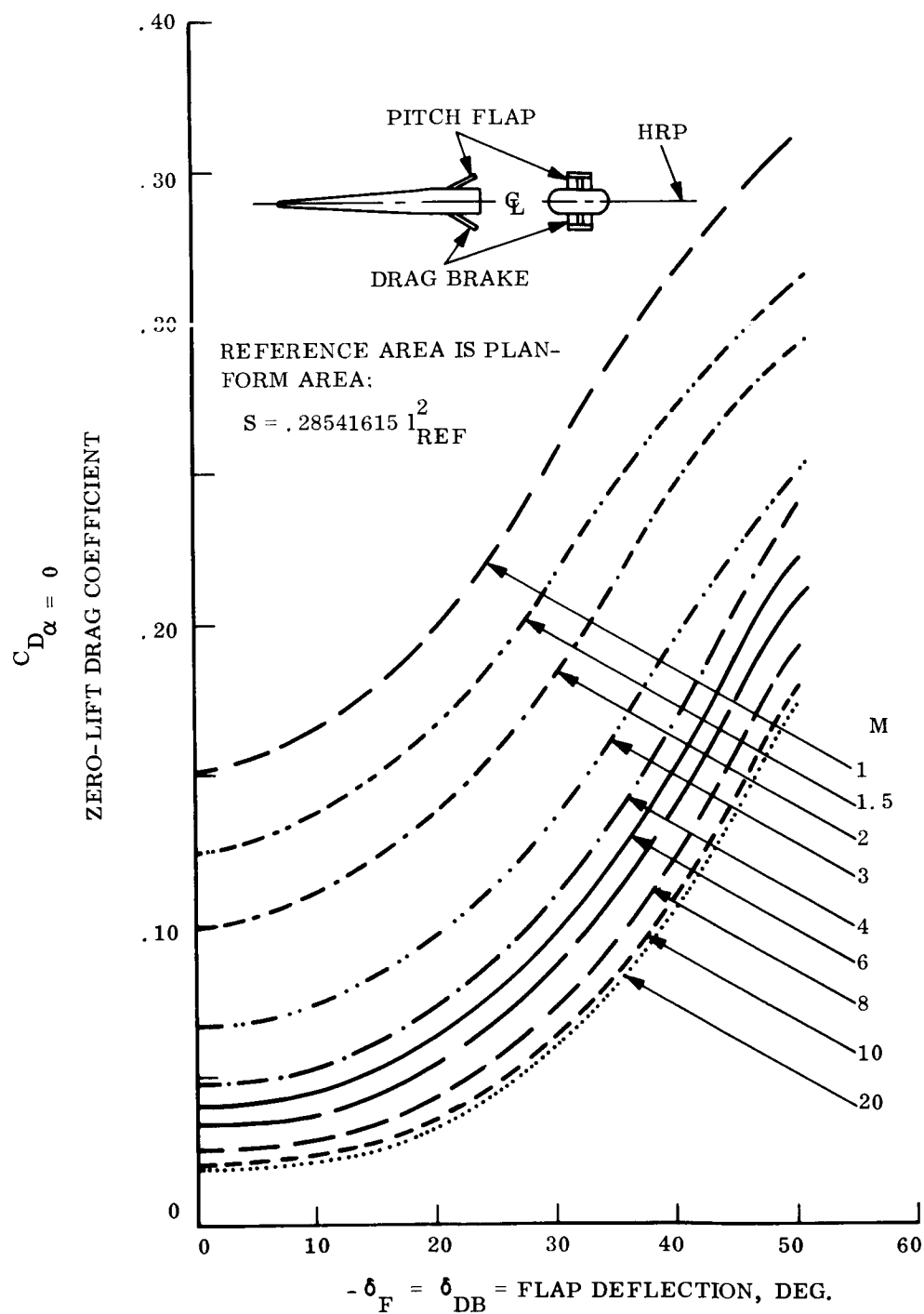


Figure 3.2-7. - Drag versus Flap Deflection

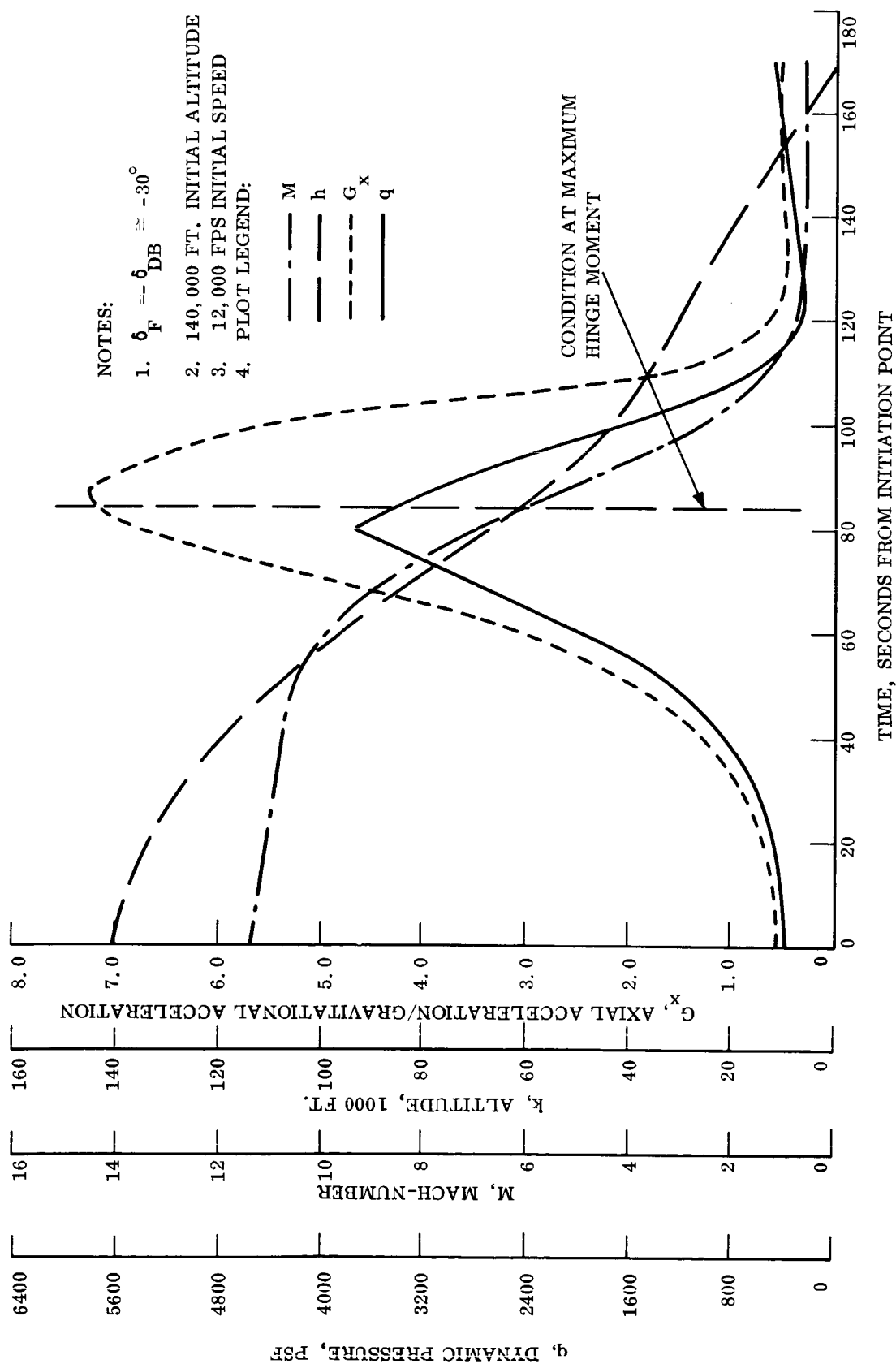


Figure 3.2-8. - Representative Recovery Trajectory with Drag Brake Flap

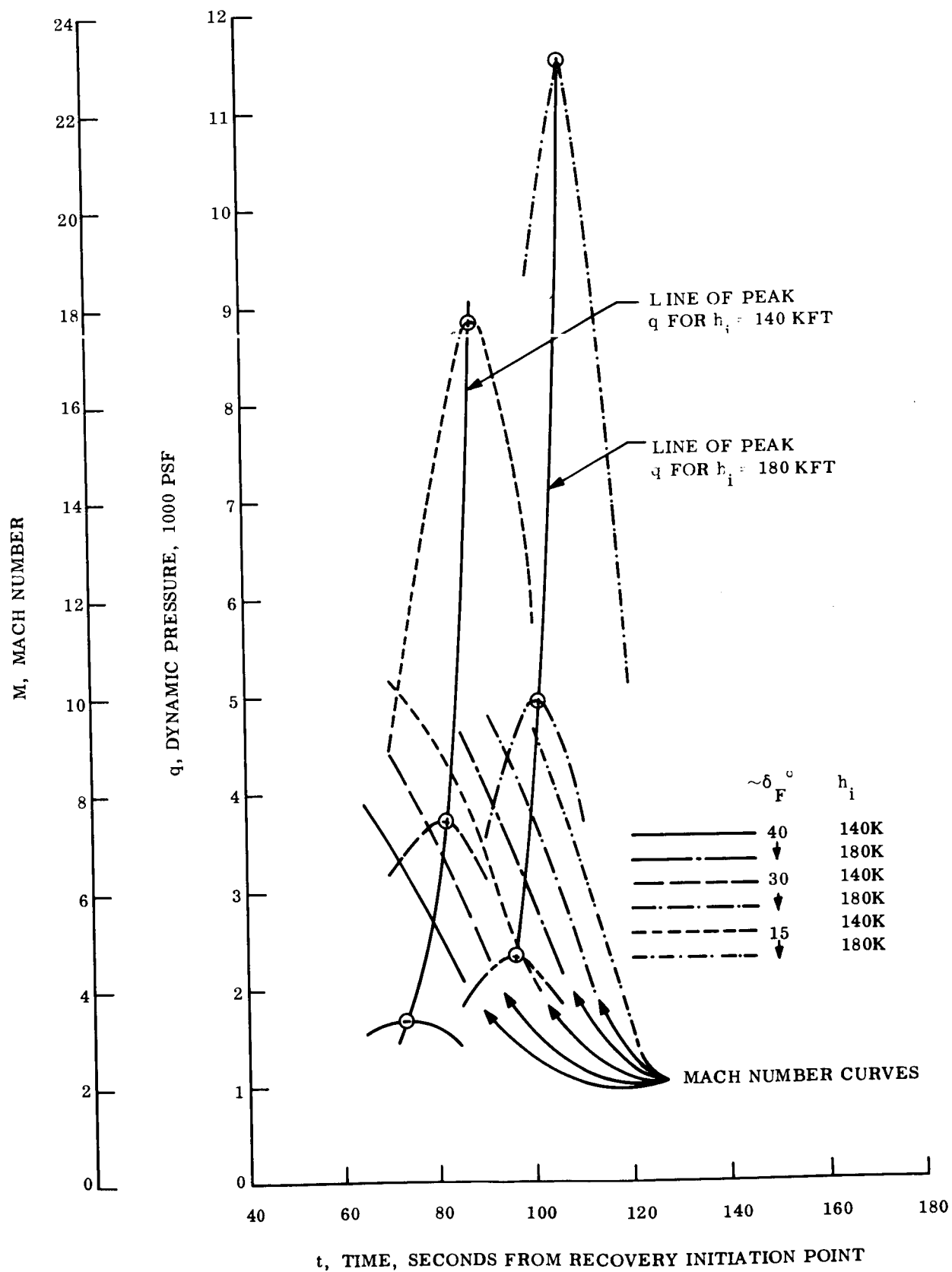


Figure 3.2-9. - Dynamic Pressure and Mach Number for SLAMAST Recovery

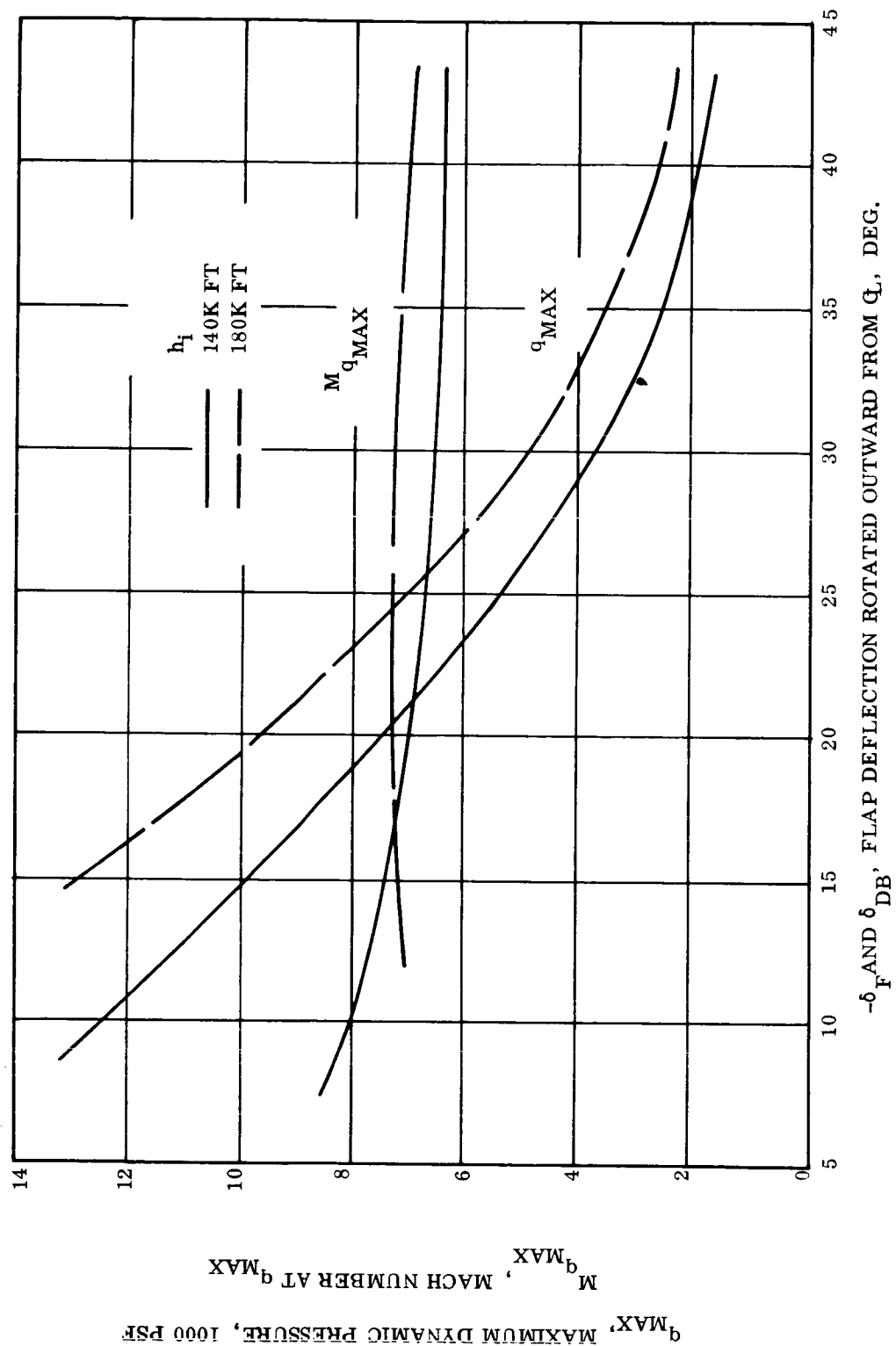


Figure 3.2-10. - Maximum Dynamic Pressure and Simultaneous Mach Number for SLAMAST Recovery

Figures 3.2-8, 3.2-9 and 3.2-10 show the flap effectiveness decreasing with increasing Mach number most markedly at the lowest deflections and very little at 40 degrees deflection. The rationale for the progression is related to the character of the flap pressure distribution: as the Mach number increases, and as laminar separation is assured, the pressure distribution changes such that the flap center-of-pressure moves aft. A higher pitching moment results from this center-of-pressure movement, created by a small increase in the flap force moment arm measured to the center-of-gravity (but also creating a much larger change in flap hinge moment).

The physical explanation is that the bow shock wave intercepts the flap surface at high flap deflections causing an abrupt pressure rise in the rearward flap region. The hinge moment information, in fact, is based on a flap center-of-pressure of 71.3 percent flap length as determined from an integration of the flap pressure distributions of Figure 3.2-63 plotted versus flap semi-span. That plot is shown here as Figure 3.2-11.

The hinge moments resulting from the trajectory and flap effectiveness data of the other figures of this section are presented in Figures 3.2-12 and 3.2-13 for the SLAMAST plus drag brake shape (63 inches [1.6 meter] length). For sizes other than the 1.6 meter version, hinge moments may be obtained by simply multiplying the hinge moment data by the scale ratio to the 63-inches length. Example: a 126-inches long vehicle would have a hinge multiplying factor of two cubed or eight; doubling length increases hinge moment eight times. This relationship arises from the nature of flap effectiveness and its frequent correlation by means of a control volume. If geometric similarity is maintained, moments vary as volume and thus as the cube of any reference length. In summary,

(1) Aerodynamic performance estimates are presented in this section for a SLAMAST shape variation embodying two flaps disposed so that the vehicle is symmetrical about the HRP.

(2) The estimates include an error tolerance of as much as plus to minus 30 percent.

(3) The advantages of the shape change include more precise range control, lessened thermodynamic severity, and better recovery system deployment.

(4) The disadvantages of the shape change include a reduction in allowable windward test panel length, added vehicle complexity, more difficulty in achieving a desirable c. g. location without increasing ballast, and a reduction in the yaw stability.

3.2.2.3 Split flaps. - The feasibility of splitting the pitch flap to provide roll control was experimentally investigated during the NASA/LRC Unitary Plan Wind Tunnel tests of the nominal 2/7 scale SLAMAST model. Outboard split flaps of the same area were also tested during this test period and will be reported on separately in the SLAMAST Wind Tunnel Data and Analysis Report (to be published).

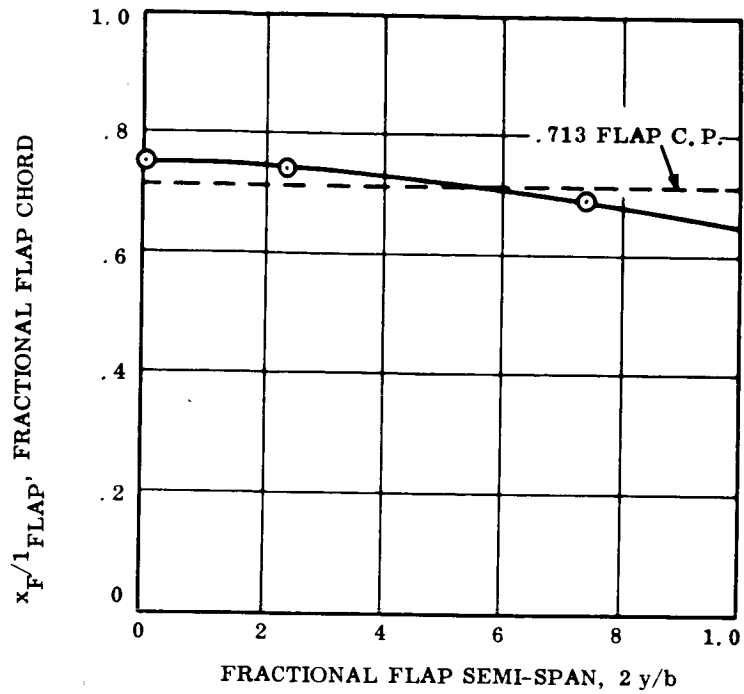
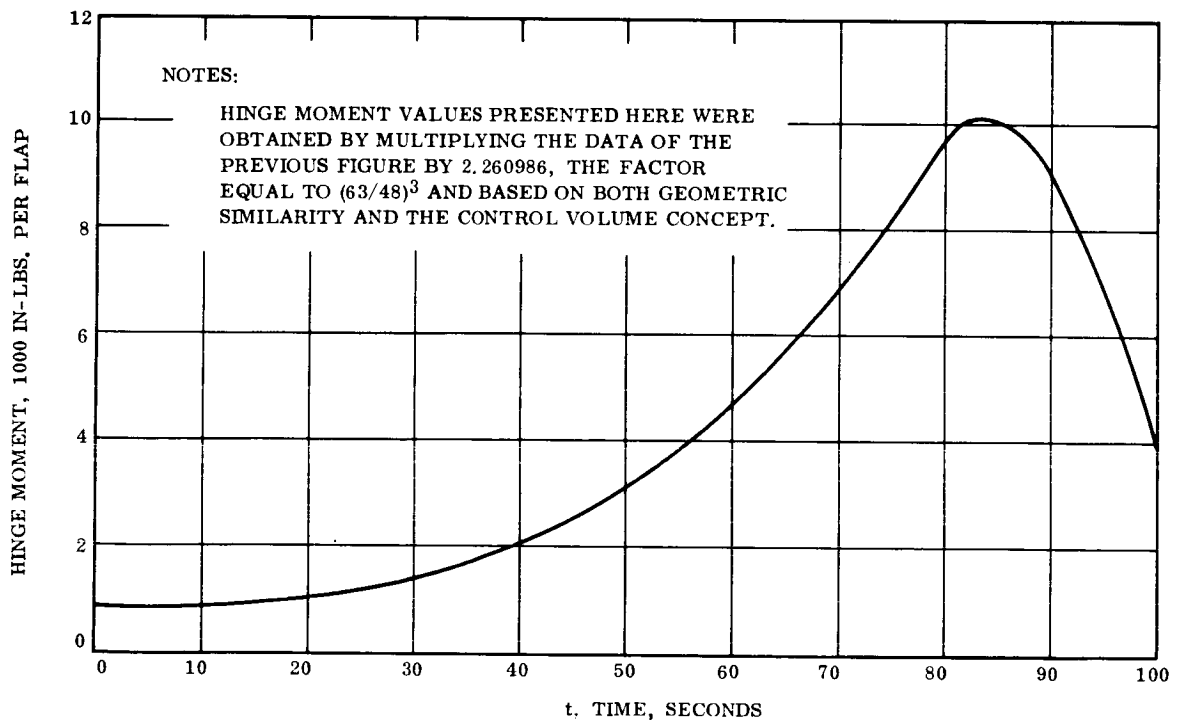


Figure 3.2-11. - Location of Flap Center-of-Pressure for Laminar Separated Flow for $\delta_F = -30^\circ$



Hinge Moment versus Time---63" Vehicle (1.6 m)

Figure 3.2-12. - Hinge Moment versus Time---63" Vehicle (1.6 m)

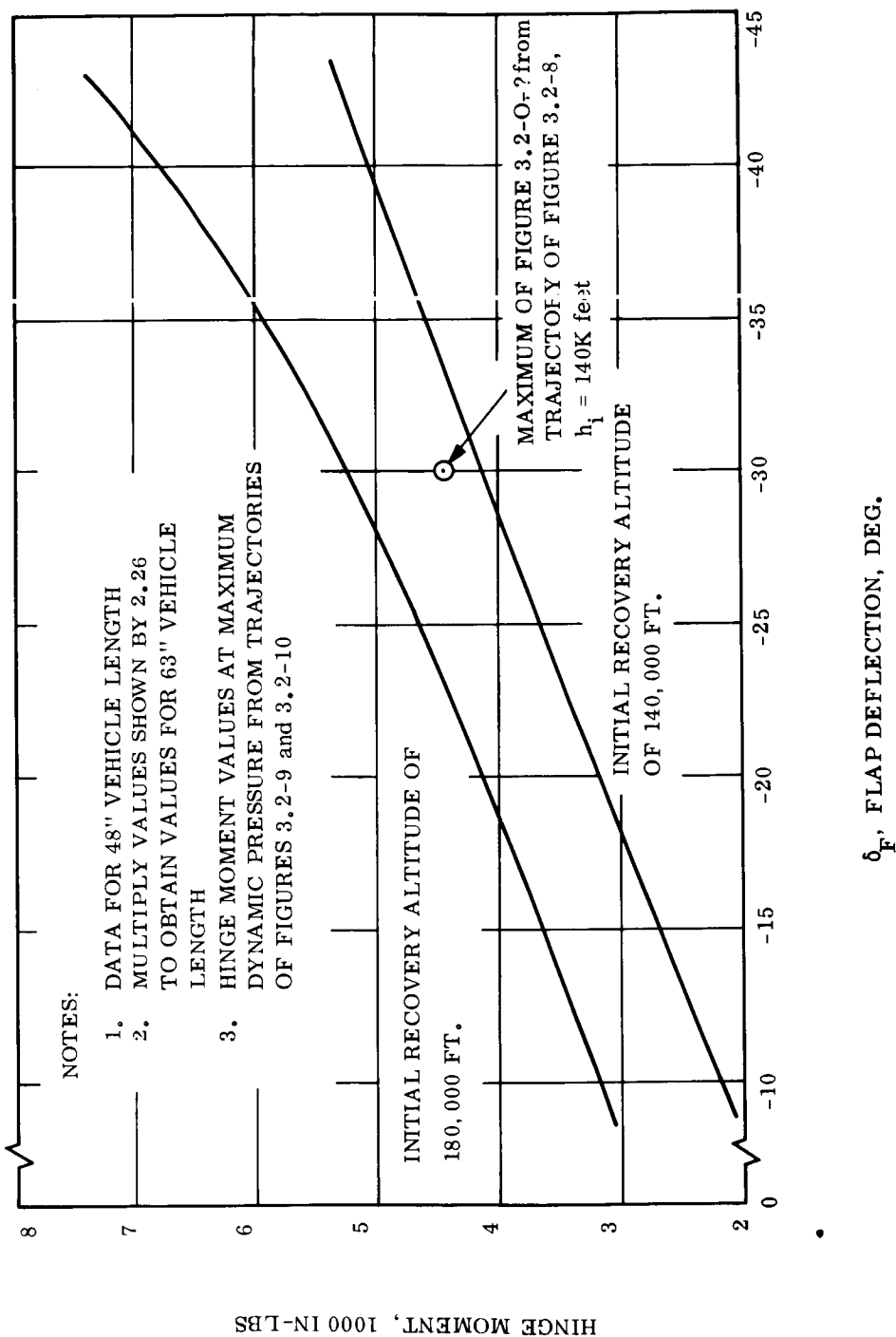


Figure 3.2-13. - Effect of Varying Flap Deflection on Hinge Moment During Recovery

The data of this section reveals the inboard split flap effects at 4.63 Mach number and zero yaw for differential deflections of 0, 15, and 25 degrees from a nominal minus six degrees pitch flap deflection. The effects on lift force, pitch stability, yawing moment, rolling moment, side force, and yaw/roll coupling are presented in Figures 3.2-14 through 3.2-19, respectively.

Examination of these figures reveals that the following characteristics are associated with split flap differential deflection:

- (1) Small lift decreases over the tested pitch angle-of-attack range (Figure 3.2-14).
- (2) Increased trimmed lift and pitch stability at trim (Figure 3.2-15) although these increases are typical of those obtained with both flaps deflected the same amount as the average of the differentially deflected flaps. (Figure 3.2-15).
- (3) Both yaw and roll moments are created that decrease slightly with positive pitch angle, and are approximately 16 ft-lbs nose left yaw and 8 ft-lbs left side down roll at a dynamic pressure of 200 psf (roughly equivalent to W/C_{LS} of 200 psf) for the 1.6 meters long vehicle with 25° differential flap; the yaw-roll combination is favorable towards a coordinated banked turn condition with enough roll power to trim out one-third inch lateral c. g. offset or comparable roll rate command. (Figures 3.2-16, 3.2-17 and 3.2-19).
- (4) The same 25° differential flap that produces 16 ft-lbs nose left yaw also produces a right-directed side force of some three lbs., the exact magnitude being somewhat indeterminate due to the data scatter and accuracy revealed in Figure 3.2-18.

Essentially the same trends were observed in the 3.95 Mach number data for these flaps as for the 4.63 data just commented on. In contrast, the outboard split flaps produced much greater yaw due to roll differential deflection arising from the outward cant of these split surfaces on deflection. However, the outboard flaps, deflected uniformly, did provide somewhat higher $(L/D)^*$'s and slightly less maximum trimmed lift coefficients.

Since both inboard and outboard split flaps exhibited yaw due to roll, the possibility of using skewed hinge lines for these surfaces to minimize yaw moments was briefly examined. Such skewed hinge line orientations that could produce pure flap-induced roll or pitch moments would do so only in a particular shock geometry at one flight condition. Further analysis may reveal, however, that acceptable across-the-Mach-number-range characteristics could be developed with particular hinge line orientation.

In any event, use of split flaps for vehicle roll control requires the use of another flap actuator and null-sensing mechanisms whose weight, space, and complexity become involved in trades with Reaction Control System added control gas weight, volume, and tankage. Another consideration is that for a given flap size the

trim angle of attack available is reduced when roll and pitch control are required simultaneously. This has a direct bearing on $W/C_L S$ and the range of pull-out altitudes available. Initial study trades favored the RCS system over aerodynamic split flap control. It is apparent that skewed hinge line arrangements and other aerodynamic changes could conceivably change the trade-off factors to favor split flaps. However, since this was a feasibility study rather than an optimization study the detail involved is not warranted at this time.

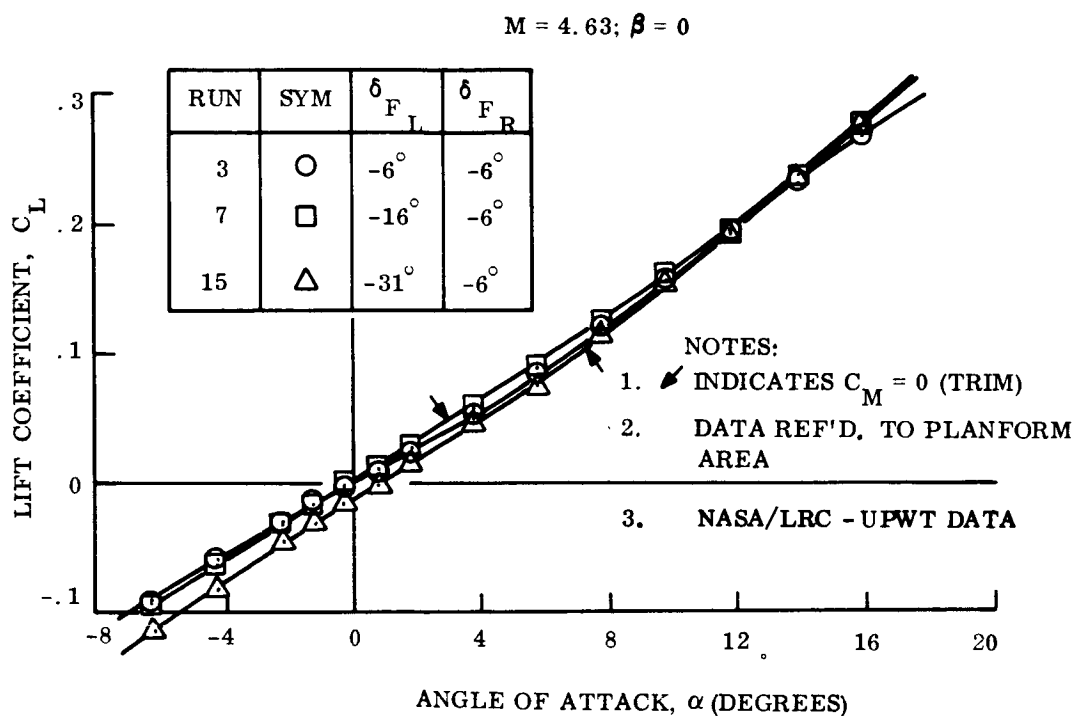


Figure 3.2-14. - Inboard Split Flaps: Lift Force Characteristics

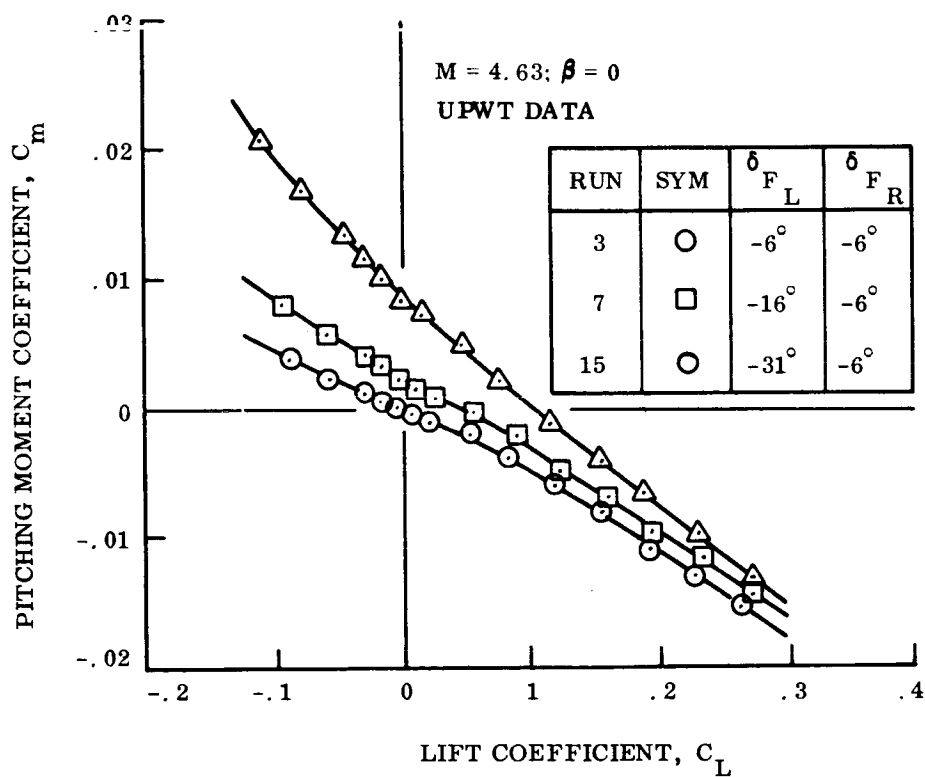


Figure 3.2-15. - Inboard Split Flaps: Pitch Stability Characteristics

YAWING MOMENT COEFFICIENT, C_n

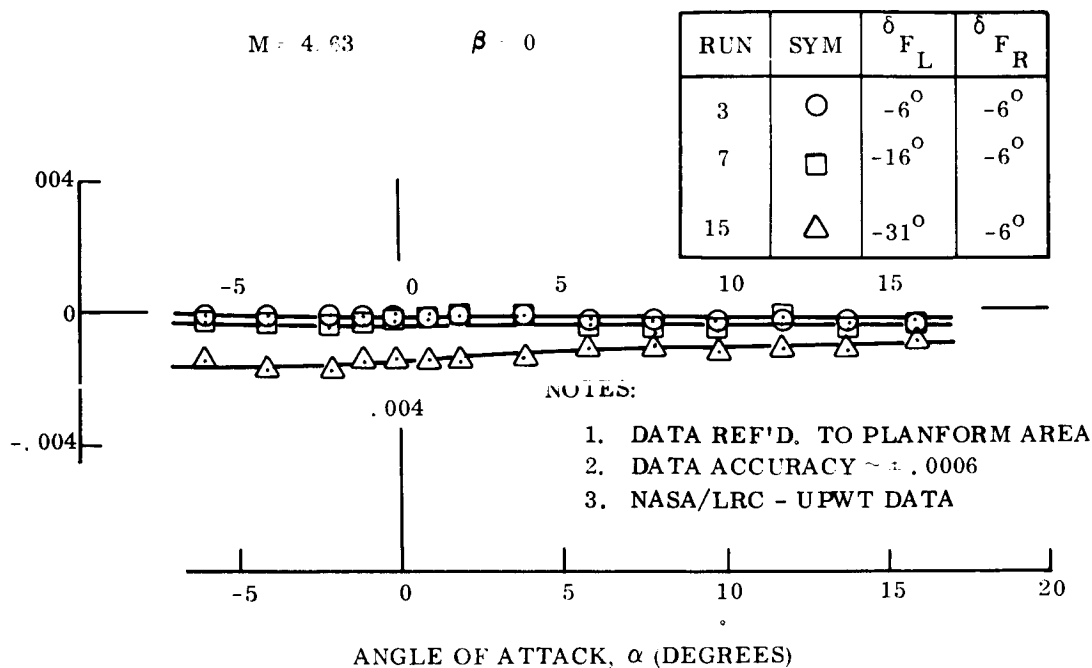


Figure 3.2-16. - Inboard Split Flaps: Yawing Moment Characteristics

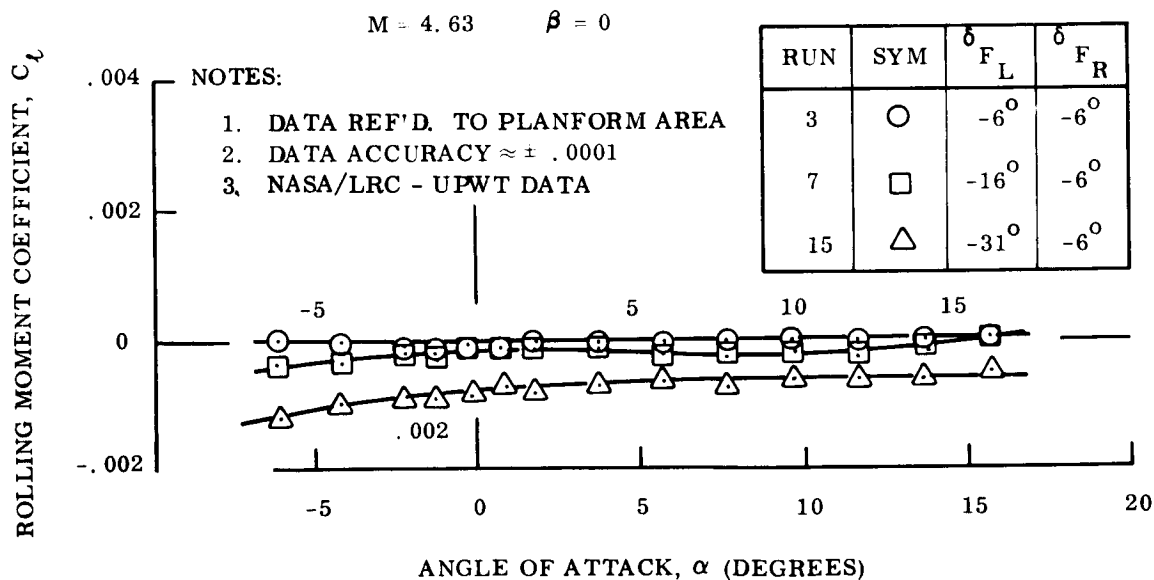


Figure 3.2-17. - Inboard Split Flaps: Rolling Moment Characteristics

NOTES:

1. FAIRINGS SHOWN ARE SPECULATIVE DUE TO DATA SCATTER & ACCURACY OF $\approx \pm .003$
2. DATA REF'D TO PLANFORM AREA
3. SYMBOL EXPLANATION: FOR TOP PLOT
4. NASA/LRC - UPWT DATA

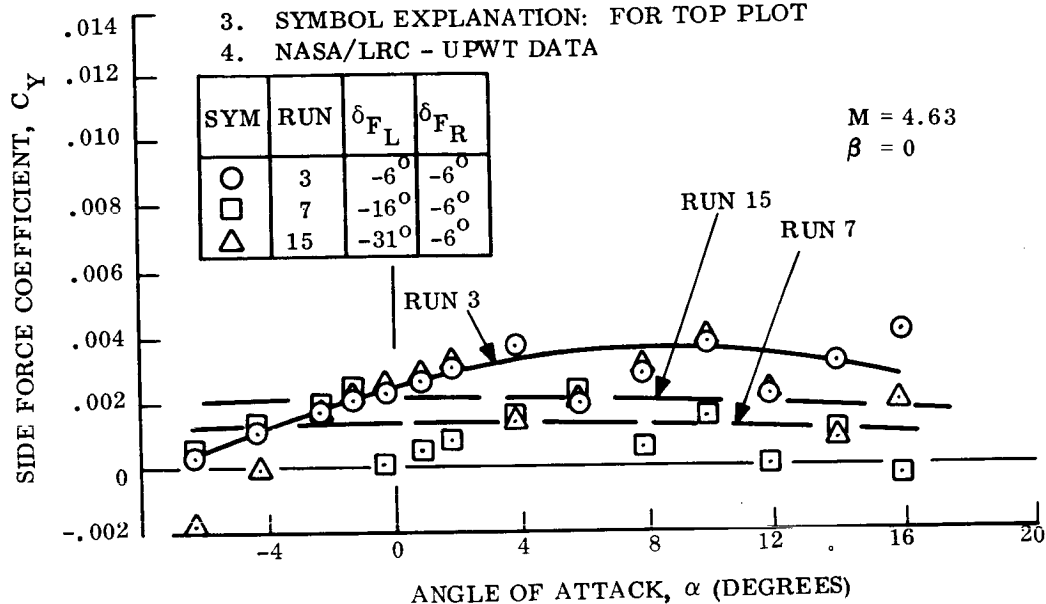


Figure 3.2-18. - Inboard Split Flaps: Side Force Characteristics

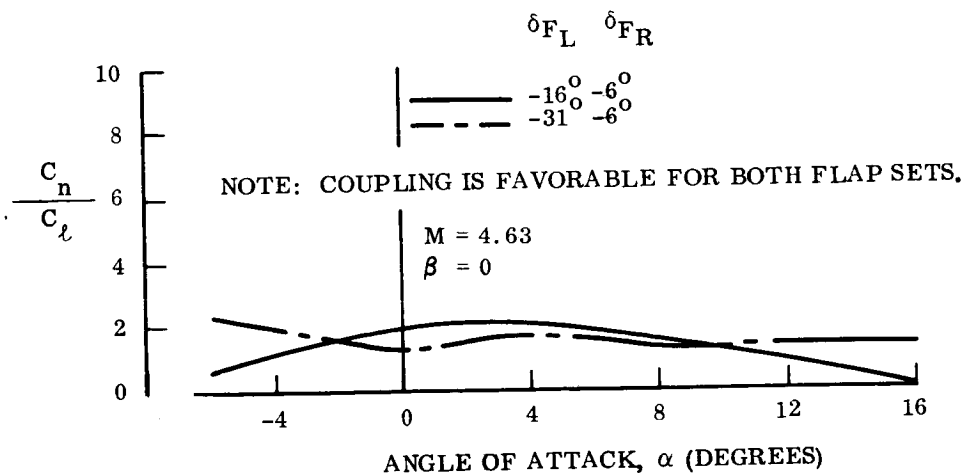


Figure 3.2-19. - Inboard Split Flaps: Yaw/Roll Coupling

3.2.3 AERODYNAMIC PERFORMANCE, STABILITY, AND CONTROL

3.2.3.1 Static force and moment. -

3.2.3.1.1 Hypersonic: - Aerodynamic force and moment data are presented here for the baseline SLAMAST shape of Figure 3.2-5. The information is intended for use only in regions where the assumptions of modified Newtonian flow apply, e.g., approximately $10 \leq M \leq 20$.

The static force and moment variations in pitch for the SLAMAST baseline vehicle are plotted as Figures 3.2-20 through 3.2-25 from the tabulated values of Table 3.2-1. The resulting load information is contained in paragraph 3.2.4.2.

All data are for body alone (flaps at zero deflection), for modified Newtonian flow, without viscous effects, and were obtained through use of the FAB (Force on Arbitrary Bodies) computer program. The single flap trim points incorporated in Figure 3.2-20 were obtained from the correlated flap effectiveness information of paragraph 3.2.3.2. Examination of the figures of this section reveals that:

(1) The maximum trim angle-of-attack is 16.0° with 40° of single flap deflection. The corresponding lift coefficient, drag coefficient, and L/D ratio are 0.215, 0.107, and 2.01, respectively.

(2) The vehicle may be trimmed throughout the angle-of-attack range from zero to 16.0° with flap settings less than 40° .

(3) Other control means, or enlarged flaps, are required for vehicle operation at angles above 16.0° .

(4) The present vehicle is statically stable throughout the trim angle-of-attack range.

3.2.3.1.2 Supersonic: - The estimated trimmed lift capability of SLAMAST versus Mach number is shown in Figure 3.2-26 for 0.569 length center-of-gravity position. Lift capabilities for three different flap arrangements are presented as derived from analysis of recent NASA-LRC wind tunnel tests of the nominal 2/7 scale SLAMAST model. Also shown in the figure are representative data regions for cones, elliptic cones, and elliptic conoids, derived from references 3.2-6 through 3.2-11 for an assumed trim pitch angle capability of 15° for Mach numbers less than 3.50. The solid line of Figure 3.2-26 is the resulting estimate of SLAMAST lift capability, based on the NASA results and the modified Newtonian estimates for $10 \leq M \leq 20$.

3.2.3.2 Static stability and control. - The variation of flap deflection angle with pitch angle-of-attack is presented in Figure 3.2-27 for $10 \leq M \leq 20$, and a 0.569 l_{REF} c.g. The variation was determined from a combination of forces and moments for the blunt-nosed SLAMAST shape and for a single flap. The body estimates were based on modified Newtonian Theory; the flap values were determined by subtracting flap deflected values from undeflected flap data on a right circular cone plus flap configuration. The incremental flap values were then verified by comparisons with other similarly derived data on a conoid and on a NASA model somewhat similar in shape to SLAMAST.

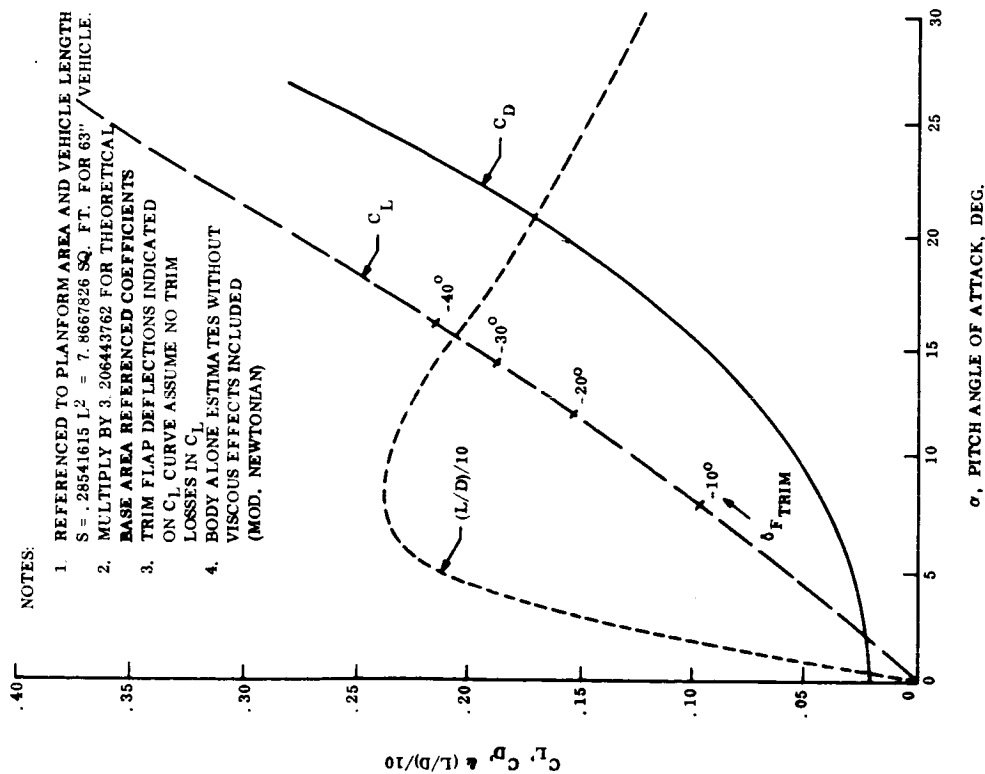


Figure 3.2-20. - Pitch Force Characteristics

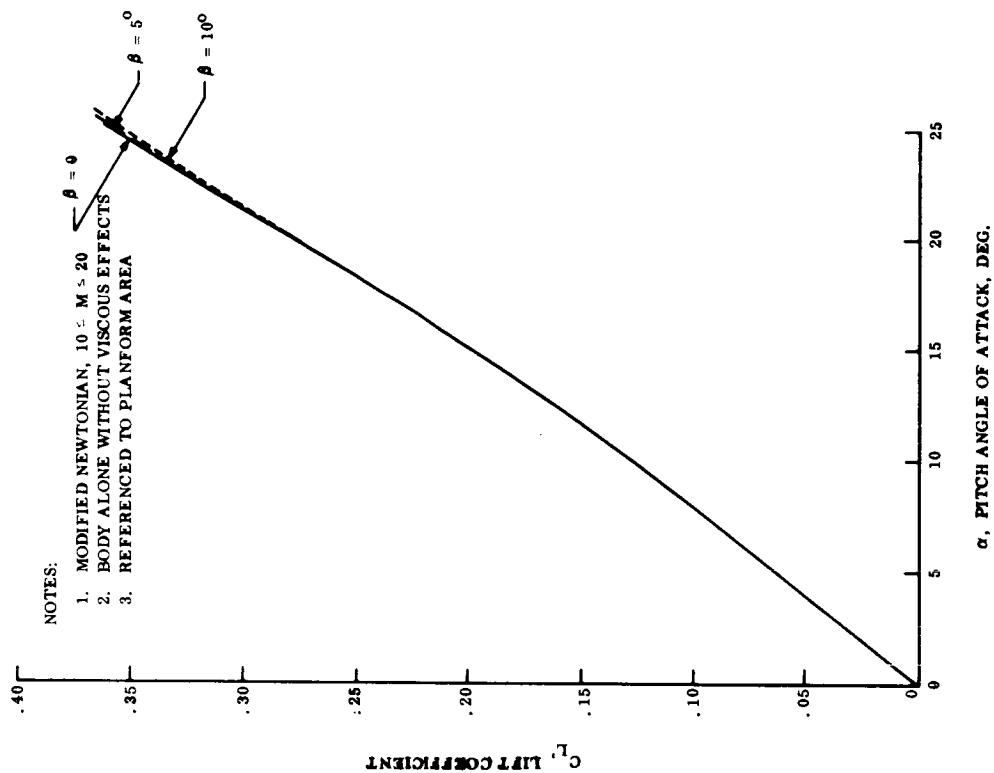


Figure 3.2-21. - Lift Force Variation with Pitch Angle

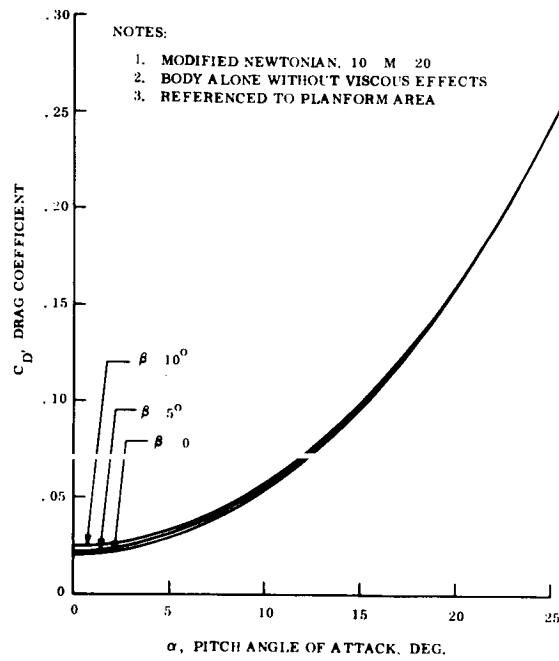


Figure 3.2-22. - Drag Force Variation with Pitch Angle

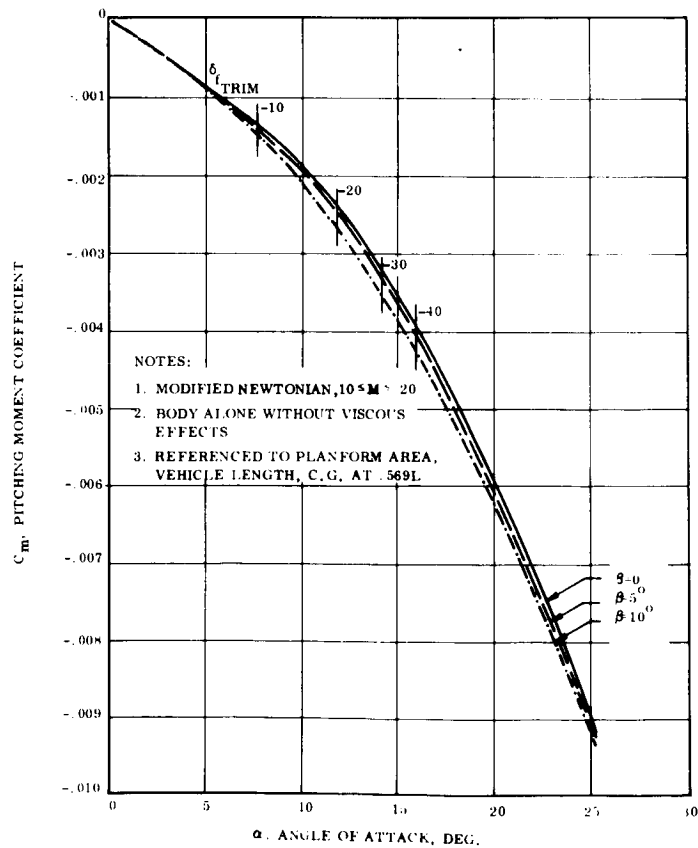


Figure 3.2-23. - Pitching Moment Characteristics

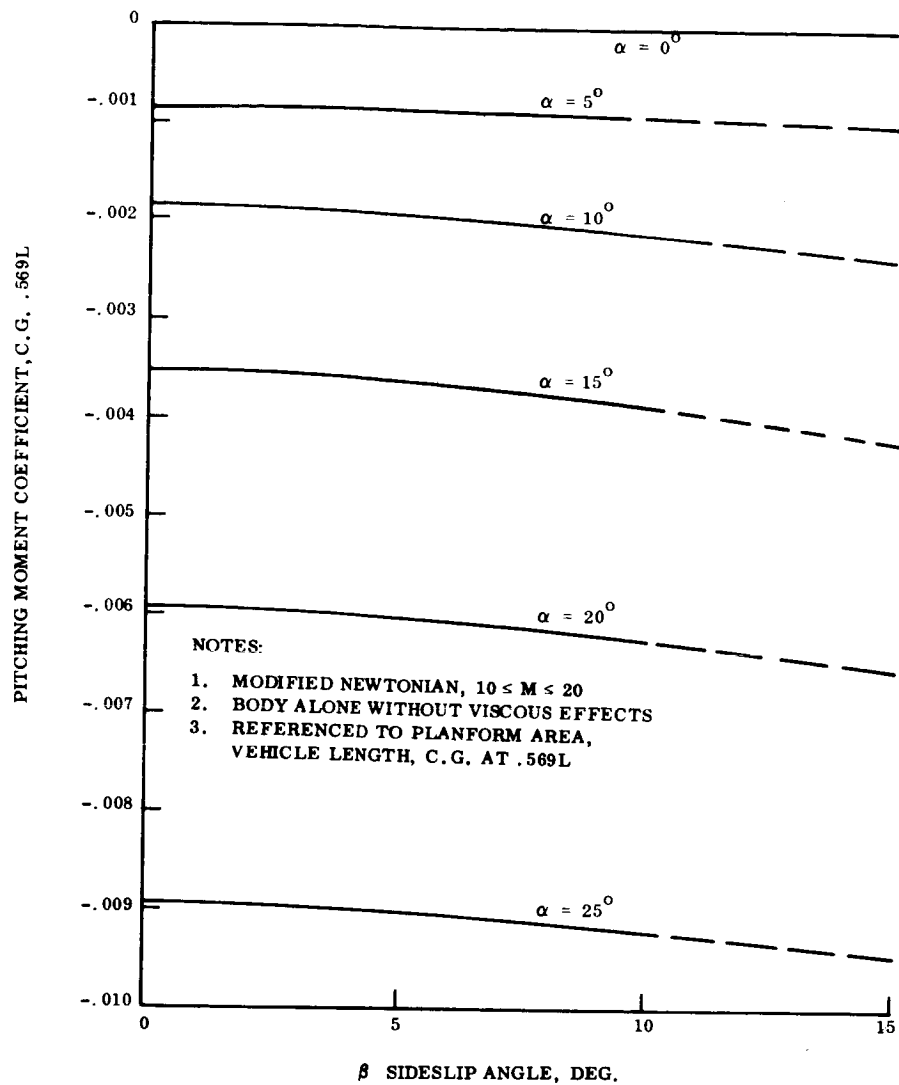


Figure 3.2-24. - Pitching Moment Variation with Sideslip Angle

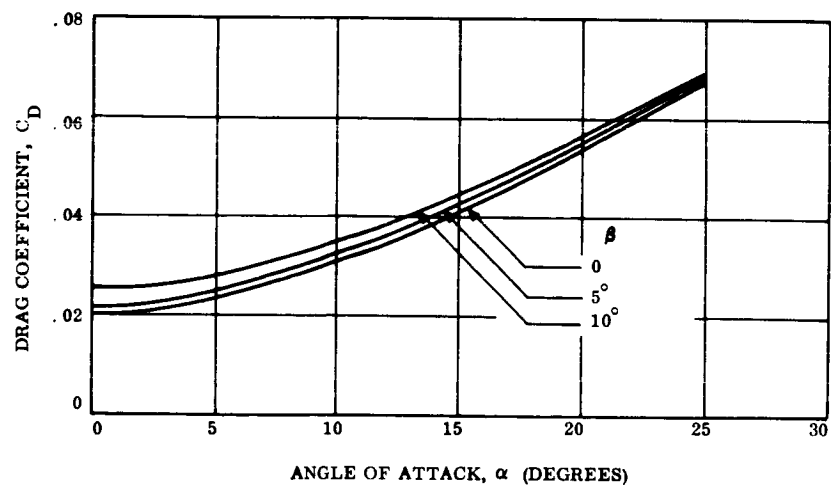


Figure 3.2-25. - Axial Force Variation with Pitch Angle

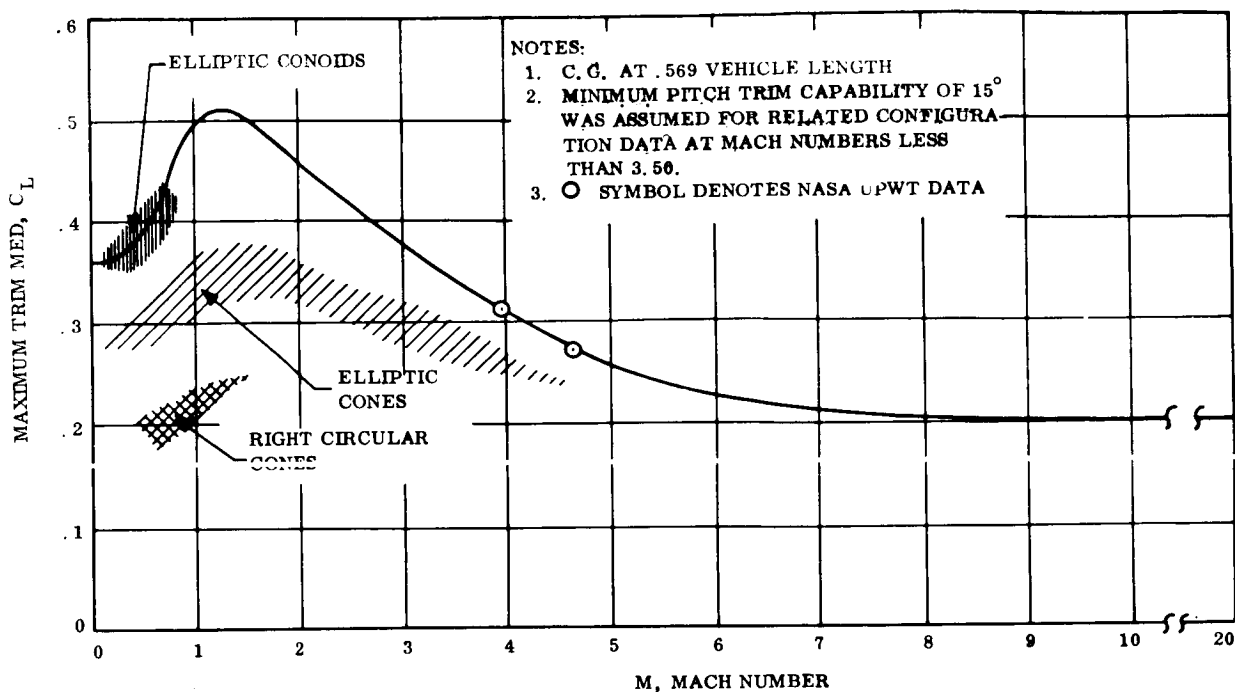


Figure 3.2-26. - Estimated Maximum Trimmed Lift Coefficient versus Mach Number

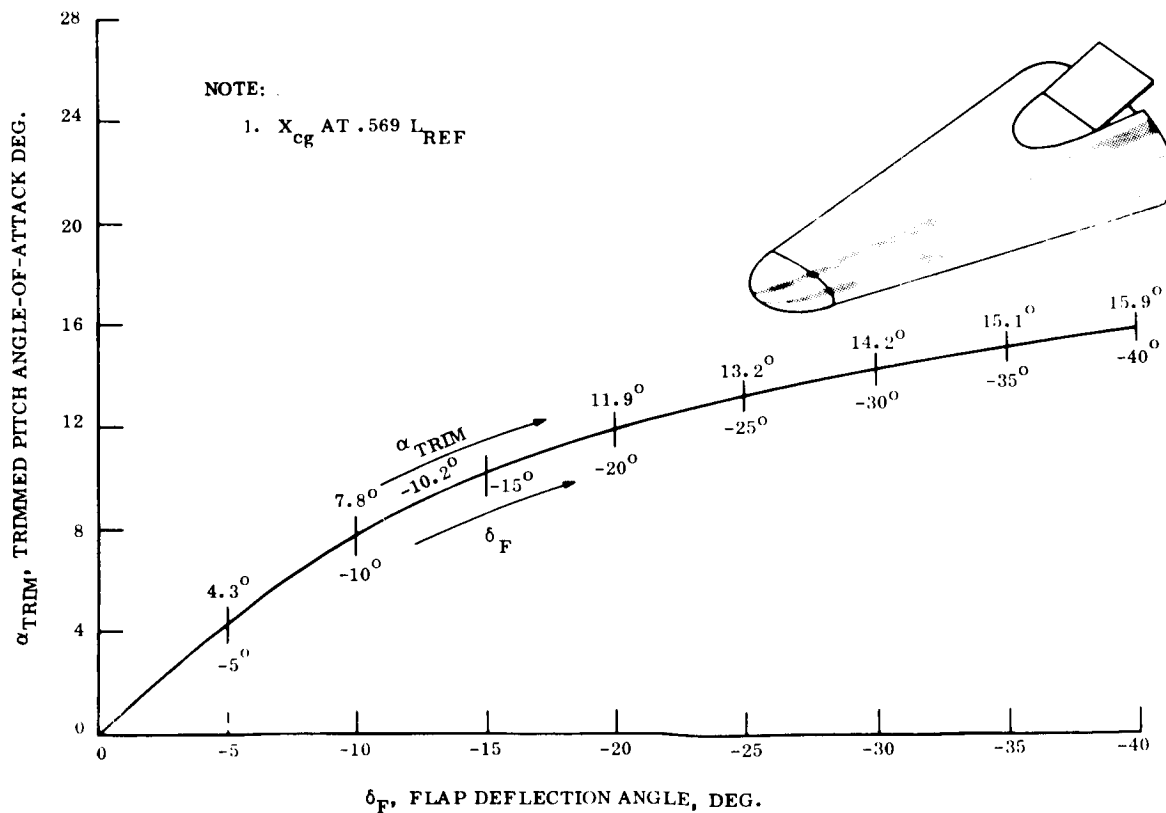


Figure 3.2-27. - Variation of Flap Deflection with Angle-of-Attack for Trimmed Flight, $10 \leq M \leq 20$, Estimated

TABLE 3.2-1. - SLAMAST STATIC FORCE AND MOMENT COEFFICIENTS FOR MODIFIED NEWTONIAN FLOW

α	β	C_A	C_N	C_Y	C_I	C_n	C_m	C_D	C_L	L/D
0	0	.020653	0	0	0	0	0	.020653	0	0
5		.023358	.065422				-.000857	.028970	.063137	2.1793
10		.030837	.133827				-.001854	.053607	.126439	2.3586
15		.041099	.218009				-.003540	.096124	.199944	2.0801
20		.053454	.317722				-.005936	.158898	.280279	1.7639
25		.067425	.430286				-.008933	.242954	.361477	1.4878
0	5	.021815	0	-.030153	0	.002259	0	.021815	0	0
5		.024491	.064929	-.029926	-.001078	.002242	-.000851	.030056	.062548	2.0809
10		.031716	.134050	-.030570	-.001923	.002289	-.001910	.054512	.126506	2.3207
15		.041749	.218196	-.032551	-.002486	.002459	-.003625	.096800	.199956	2.0657
20		.053921	.317458	-.034652	-.002921	.002654	-.006018	.159246	.279871	1.7575
25		.067748	.429408	-.036371	-.003260	.002818	-.009000	.242876	.360544	1.4845
0	10	.025257	0	-.059448	0	.004455	0	.025257	0	0
5		.027703	.064292	-.059701	-.002051	.004483	-.000882	.033201	.061632	1.8563
10		.034226	.134847	-.061959	-.003644	.004678	-.002095	.057121	.126854	2.2207
15		.043653	.218615	-.065738	-.004808	.005006	-.003868	.098747	.199868	2.0240
20		.055296	.316517	-.069677	-.005711	.005361	-.006247	.160216	.278515	1.7384
25		.068648	.426761	-.072973	-.006413	.005672	-.009178	.242573	.357764	1.4749

The remaining figures of this section Figures 3.2-28 through 3.2-40 present the effect of center-of-gravity location on the trim lift capability, pitch trim angle, and lift-to-drag ratio at 3.95 and 4.63 Mach numbers, as obtained from NASA Unitary Wind Tunnel results. A detailed discussion of the figures presenting these tunnel results, as well as of other wind tunnel test results, will be found in the "SLAMAST Wind Tunnel Data and Analysis Report" on the NASA tests. This report will be issued in the near future.

Some limited conclusions from inspection of these figures are, however, in order. The figures reveal that:

(1) The basic inboard flap geometry provides higher trim lift capability but lower $(L/D)^*$ than the outboard flap arrangement (data not shown here) at both test Mach numbers (3.95 and 4.63).

(2) The loss in trim effectiveness of the outboard flap arrangement is due to trimming moment losses attributable to a combination of flap resultant force vector canted outboard, away from the vertical plane of symmetry, and a counter-trim force induced by cross-flow acting on the flap outboard edges.

(3) The tunnel results for the basic configuration can be readily extrapolated to the earlier modified Newtonian estimates which, consequently, remain current for SLAMAST.

Additional information on differentially deflected split flaps is presented in paragraph 3.2.2.3 for the same inboard split flaps reflected in the data of this section. The plots of this section reveal that the pitch stability margin increases from minimum values of approximately one percent at both 3.95 and 4.63 Mach number for zero pitch angle, to values in excess of five percent at the maximum trim condition and at the design flight c.g. location of 56.9 percent vehicle length. These magnitudes are not expected to change appreciably at higher Mach numbers because the vehicle center-of-pressure location is relatively fixed at Mach numbers above five.

Since split-flap control combined with a reaction control system was thought to offer possibly better overall means of roll stabilization and control, split flaps were built into the test SLAMAST model. The basic flap arrangements were tested, as well as both inboard and outboard split flaps, at 3.95 and 4.63 Mach number in the NASA-LRC Unitary Plan Wind Tunnel to provide aerodynamic data for use in the SLAMAST contractual activity.

A combination of both inboard and outboard flaps that would increase control power, thus permitting the attainment of higher trimmed lift and a lower lift loading, $W/C_{L,S}$, was not tested nor were 25 percent oversize inboard flaps. Such increased control power could be required if weight increased, lift-curve were reduced, or predicted hypersonic control effectiveness could not be achieved in the vehicle design-to-flight evolution.

Although the stability margin could conceivably be reduced to provide higher trim angles of attack, the present stability margins at and near zero pitch angle of attack

are quite small. A better approach would be to increase control size. Outboard split flaps could be considered, with the flap hinge lines skewed to avoid the deleterious effects of outboard cant found with the outboard flap arrangement recently tested on the SLAMAST model in the NASA Unitary Plan Wind Tunnel.

3.2.3.3. Lateral-directional characteristics. -

3.2.3.3.1 Hypersonic: The lateral-directional characteristics are presented here for the baseline SLAMAST shape of Figure 3.2-2. The information is intended for use only in regions where the assumptions of modified Newtonian flow apply, e.g., approximately $10 \leq M \leq 20$.

The static variations of side force, yawing moment, and rolling moment coefficient with sideslip angle for the SLAMAST baseline vehicle are plotted in Figures 3.2-41 and 3.2-42 from the tabulated values of Table 3.2-1. All presented data are for body alone (flaps at zero deflection), for modified Newtonian flow, without viscous effects, and were obtained through use of the FAB (Force on Arbitrary Bodies) computer program. Examination of the figures of this section reveals that:

- (1) The present vehicle is statically stable throughout the trim pitch angle-of-attack range.
- (2) Control means are required to trim out either yawing or rolling moment.

3.2.3.3.2 Supersonic: Presented in Figures 3.2-43 through 3.2-48 are selected lateral-directional characteristics obtained from tests at 3.95 and 4.63 Mach number in the NASA-LRC Unitary Plan Wind Tunnel. No yaw runs were made during those tests and the lateral-directional information is limited to that obtained from five degree sideslip runs compared to the same model configuration at zero sideslip. However, one configuration was tested at both plus and minus sideslip angles and was consequently selected for this discussion of typical results. That model configuration employed outboard split flaps, differentially deflected 25° (right flap at -6° and left flap at -31°). The relative yaw center-of-pressure location aft of the pitch center is presented in Figures 3.2-43 and 3.2-44 in terms of fractional length, for 3.95 and 4.63 Mach number, respectively. The figures indicate that the vehicle's yaw center-of-pressure is approximately eight percent of vehicle length behind the pitch center near zero pitch angle, and above four percent at pitch angles above 12° , at both test Mach numbers, a slightly higher margin existing at the 4.63 Mach number test condition. This favorable difference in centers-of-pressures is due to the SLAMAST shape, tailored to be more stable in yaw and thus require little reaction control gas expenditure for vehicle yaw stabilization.

The relatively large excursions for the $\pm 5^\circ$ sideslip angle curves of Figures 3.2-43 and 3.2-44 are due to the difficulty of determining yaw derivatives from small yaw data. This is represented by the fractional length pitch and yaw center-of-pressure data of Figures 3.2-45 and 3.2-46 from which Figures 3.2-43 and 3.2-44 were prepared. A comparison of these four figures reveals that the zero sideslip curves of Figures 3.2-43 and 3.2-44 are the more meaningful, but also reveals that wind tunnel yaw runs are required for more adequate definition of the yawed vehicular characteristics.

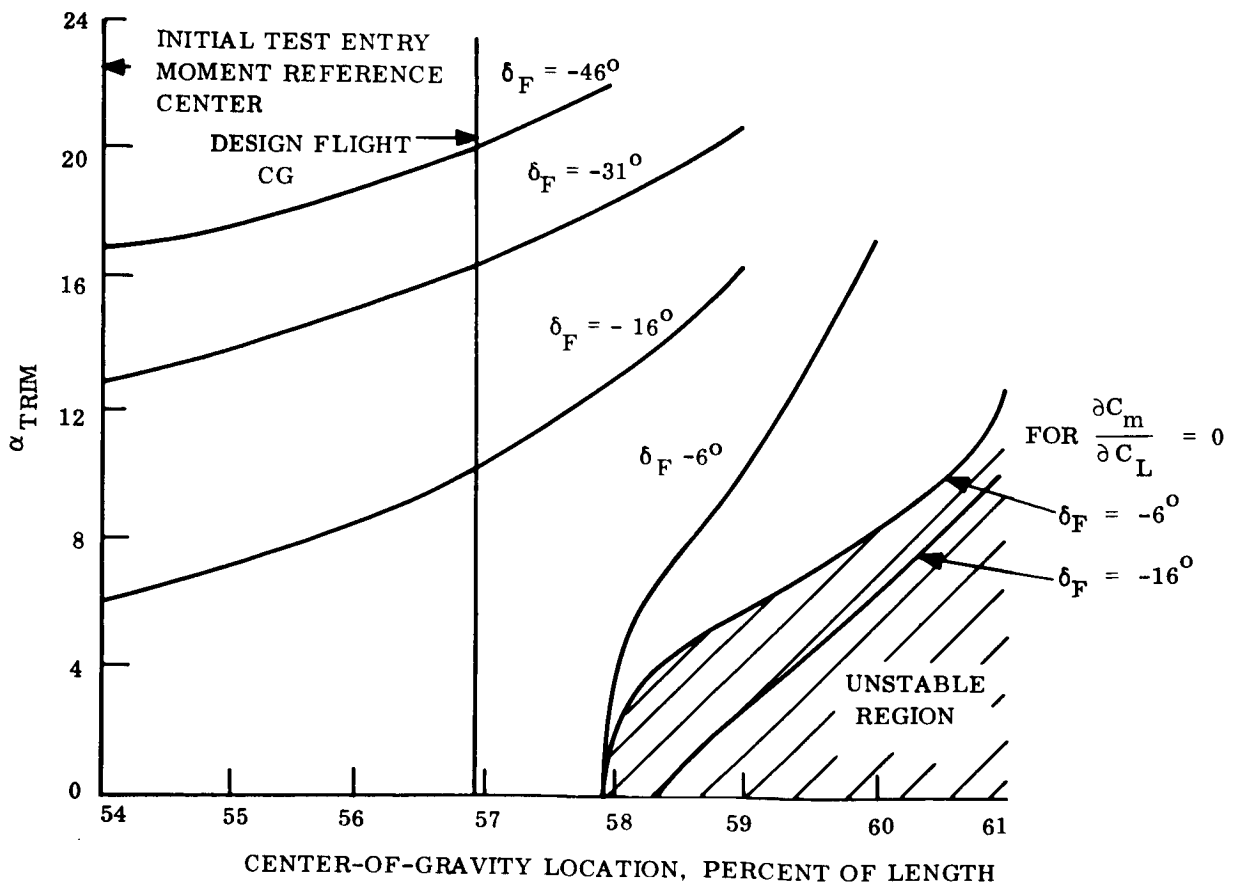
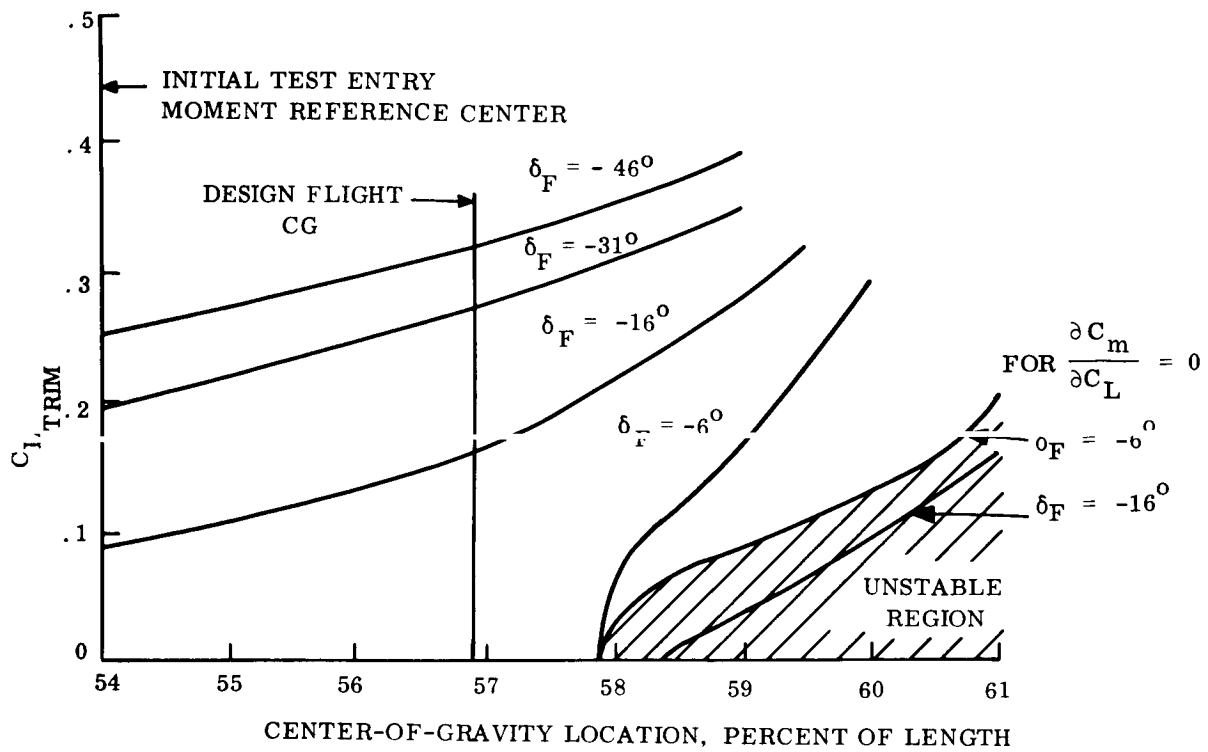


Figure 3.2-28. - Effect of Center-of-Gravity Location on Trimmed Lift and Angle-of-Attack, Inboard Flaps at $M = 3.95$ (as derived from NASA/LRC - UPWT data)

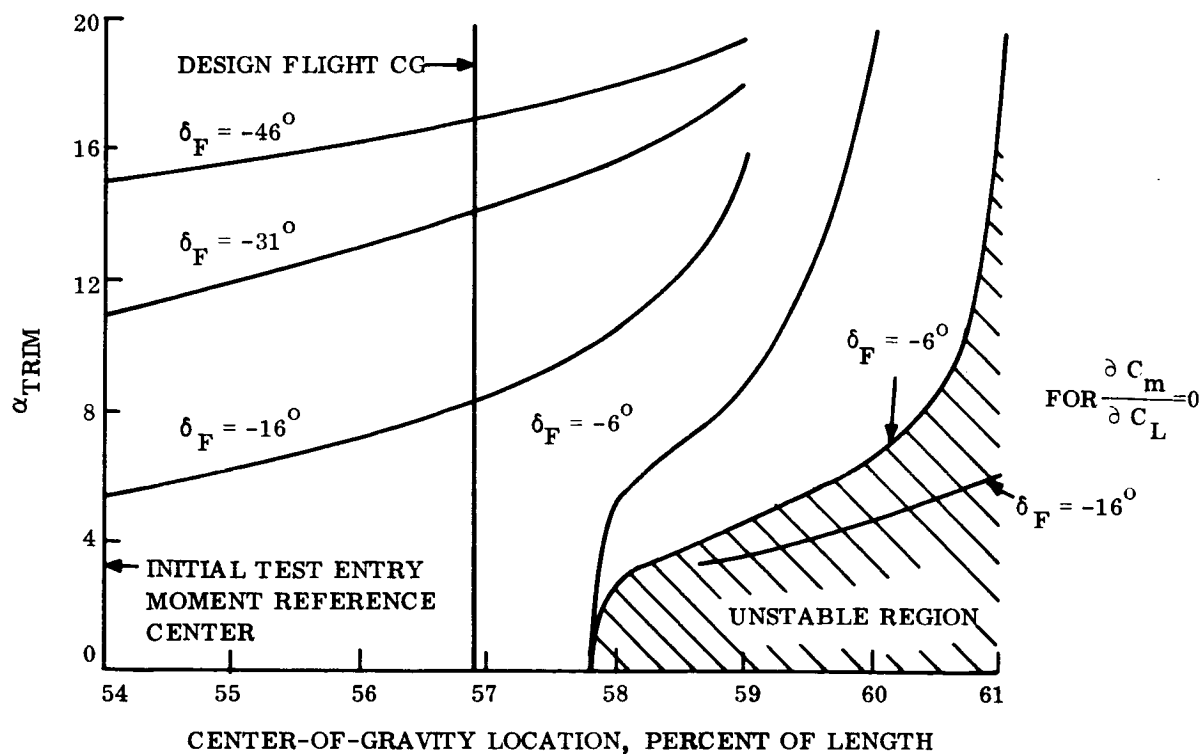
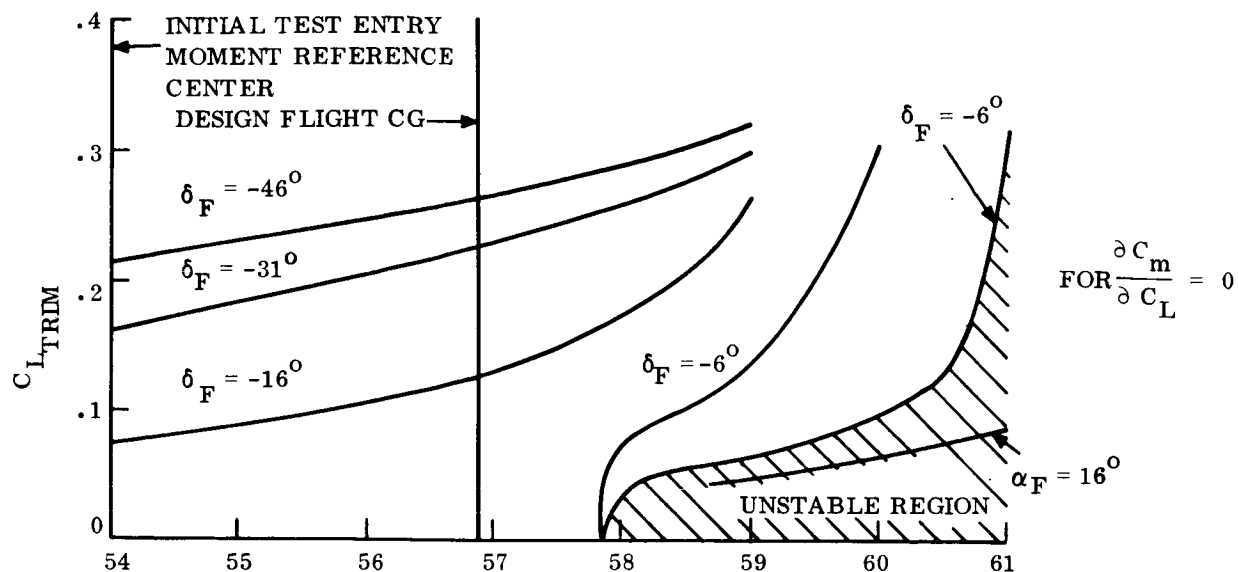


Figure 3.2-29. - Effect of Center-of-Gravity Location on Trimmed Lift and Angle-of-Attack, Inboard Flaps at $M = 4.63$

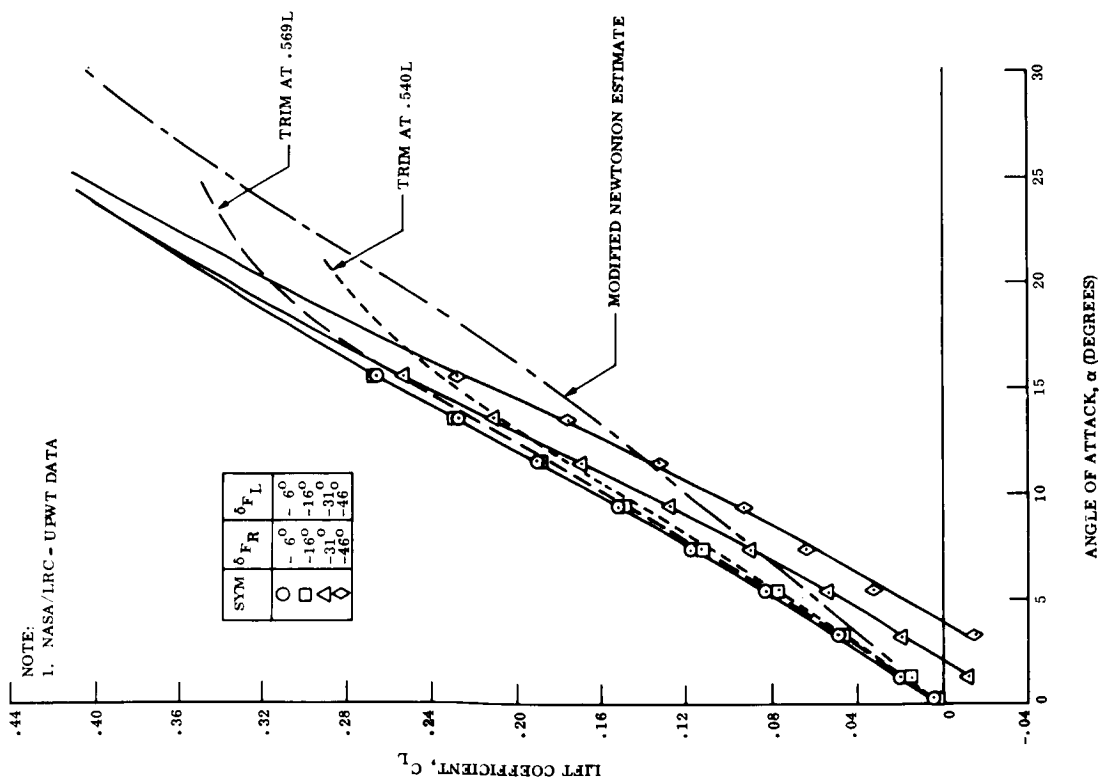


Figure 3. 2-30. - Effect of Center-of-Gravity
Location on Lift-curve, Inboard Flaps
at $M = 3.95$

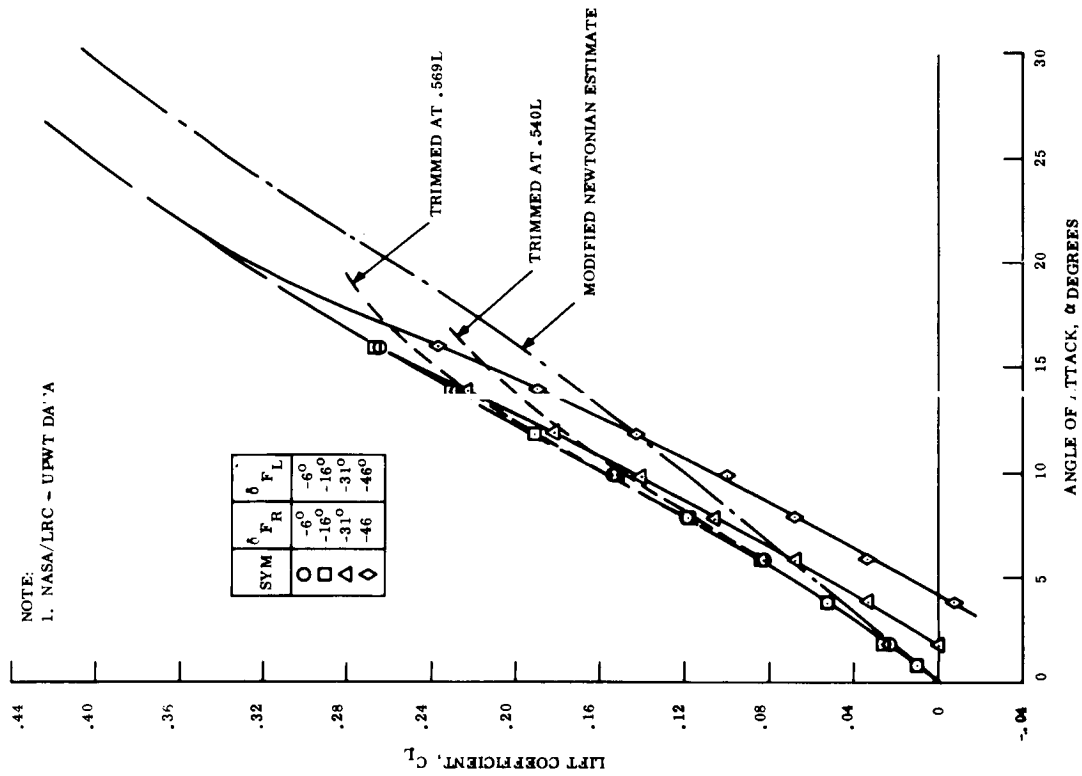


Figure 3. 2-31. - Effect of Center-of-Gravity
Location on Lift-curve, Inboard Flaps
at $M = 4.63$

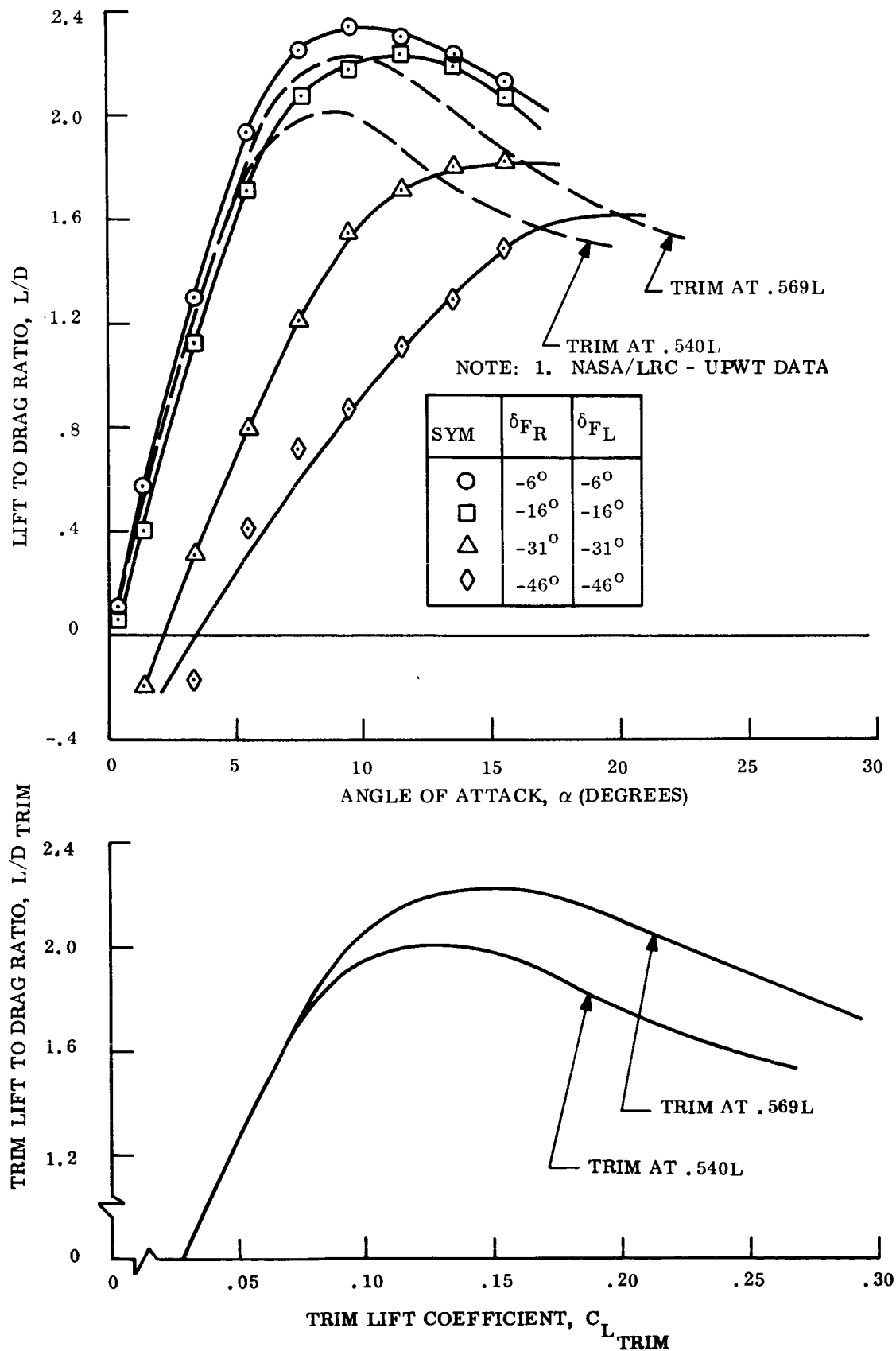


Figure 3.2-32. - Effect of Center-of-Gravity Location on Trim (L/D) Ratio, Inboard Flaps at $M = 3.95$ (Derived from NASA/LRC - UPWT Data)

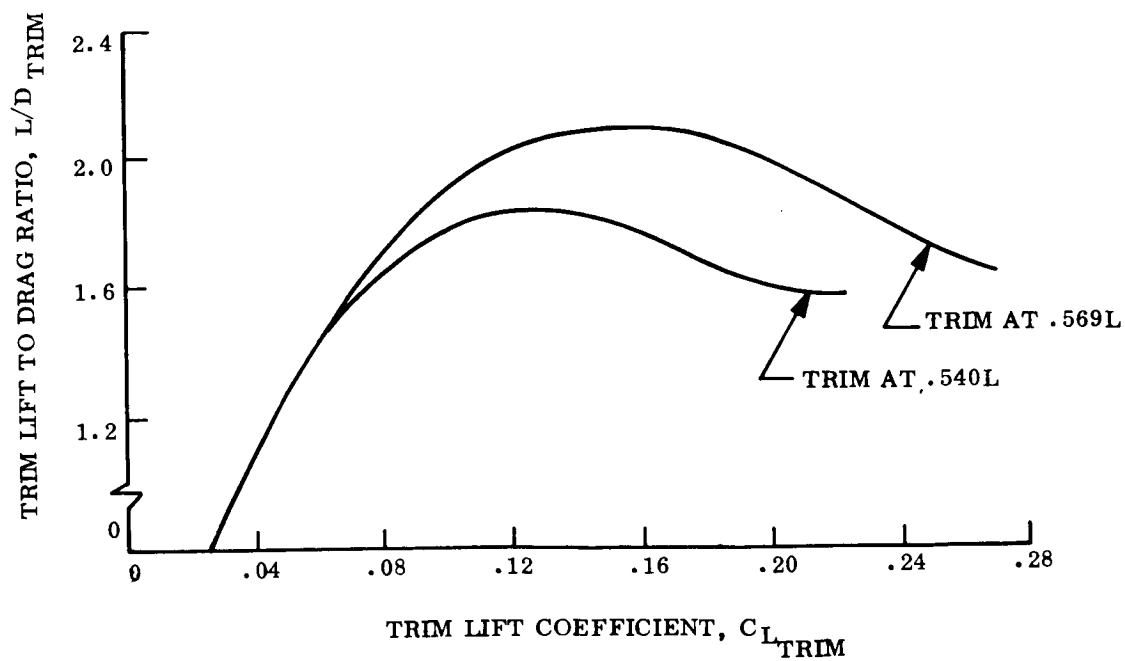
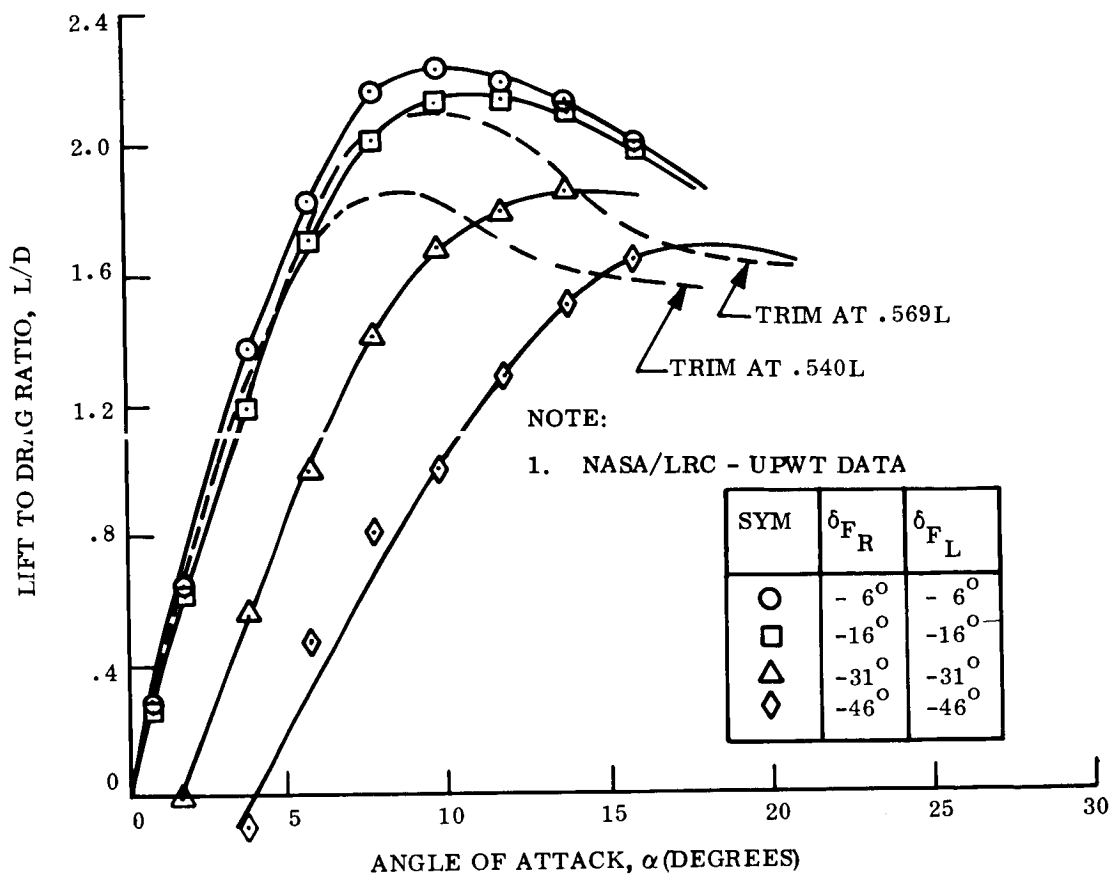


Figure 3.2-33. - Effect of Center-of-Gravity Location on Trim (L/D) Ratio, Inboard Flaps at $M = 4.63$
(Derived from NASA/LRC - UPWT data)

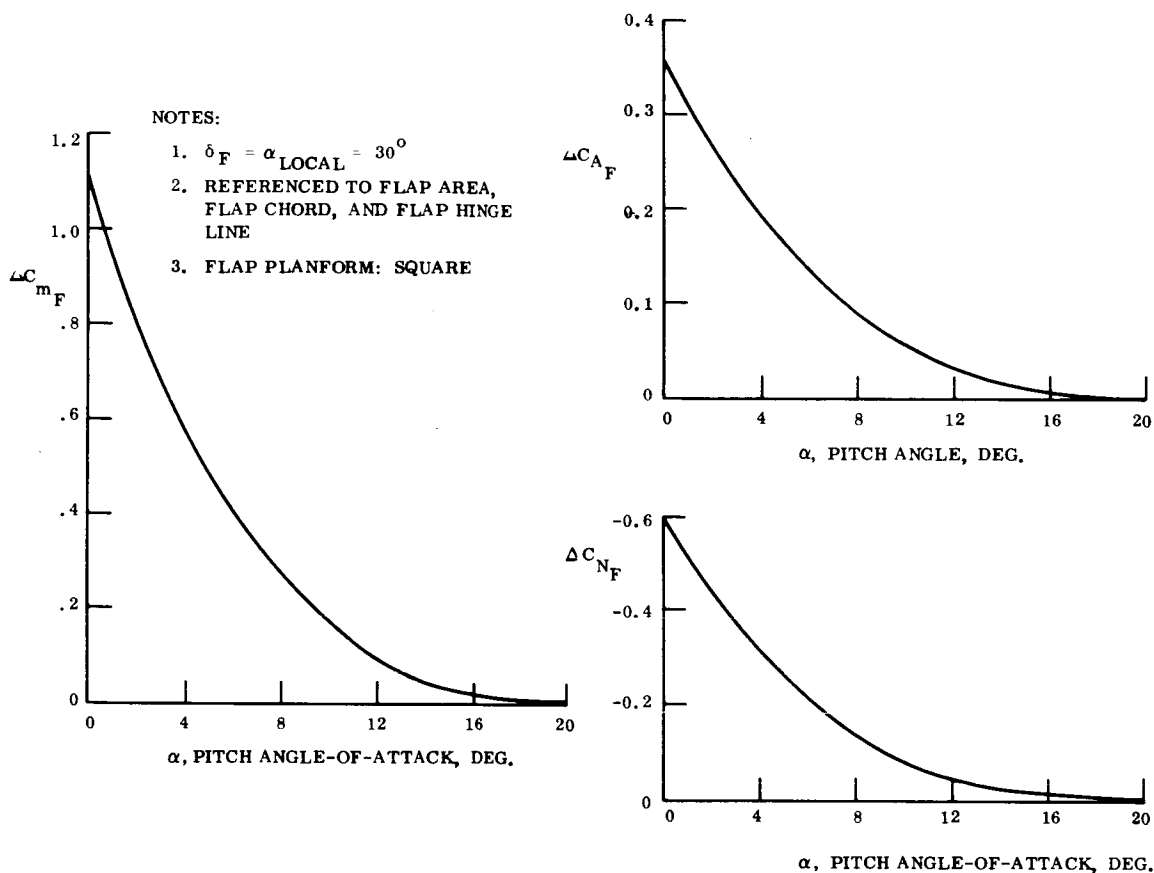


Figure 3.2-34. - Typical Flap Effectiveness at $M = 10$

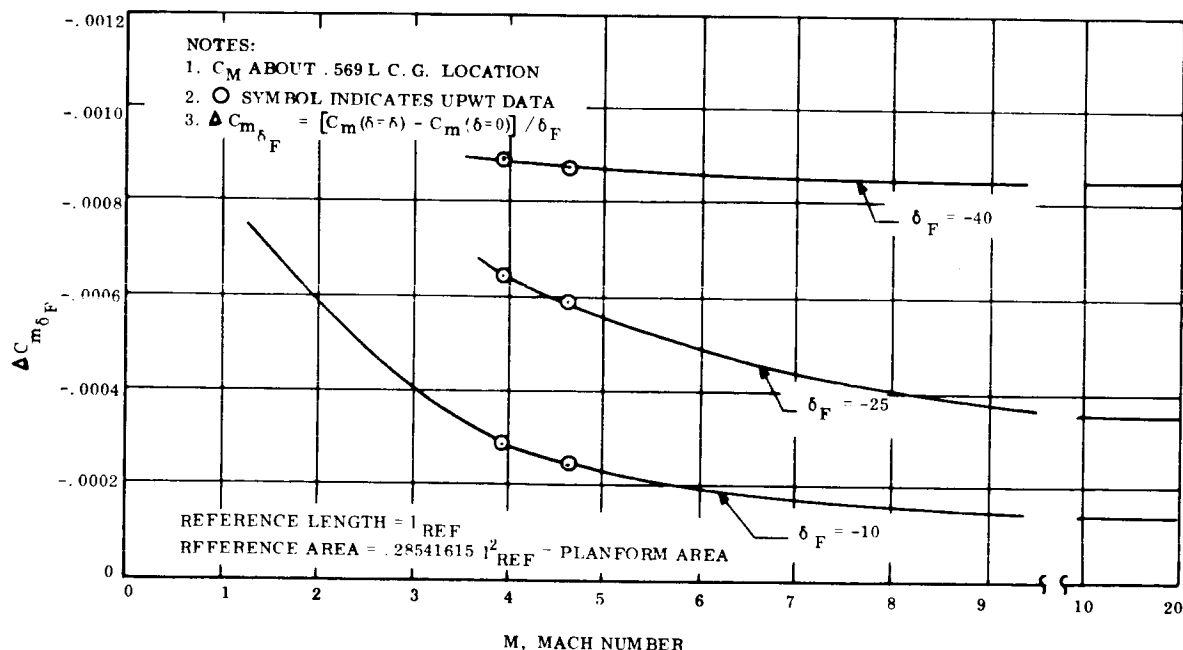


Figure 3.2-35. - Flap Effectiveness at $\alpha = 0$ versus Mach Number

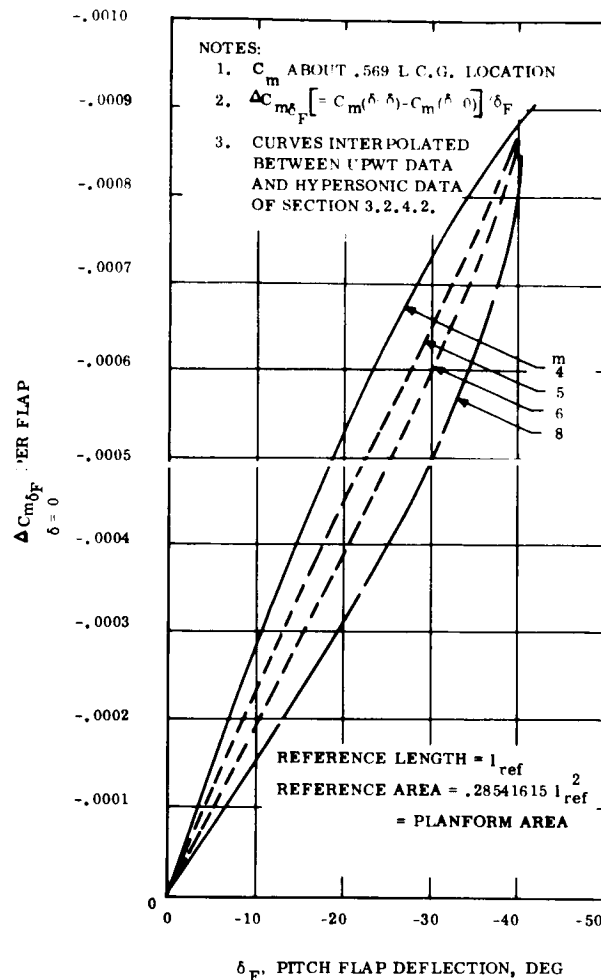


Figure 3.2-36. - Flap Effectiveness versus Deflection at $\alpha = 0$, Selected Mach Number

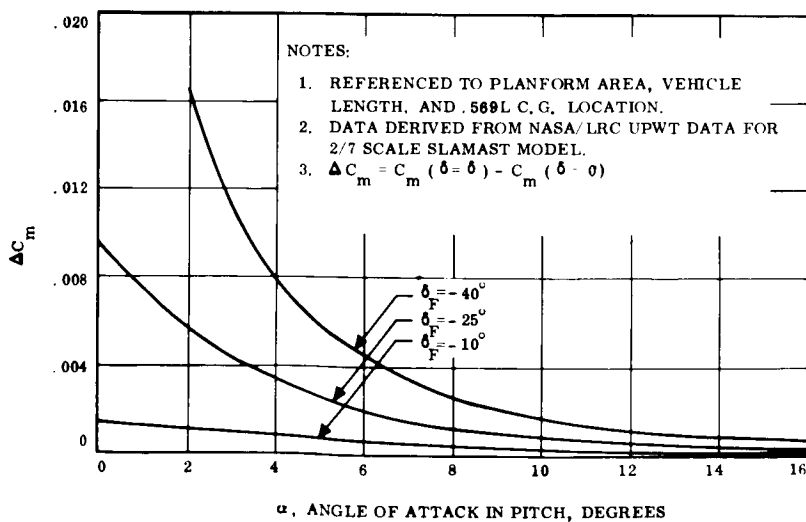


Figure 3.2-37. - Incremental Moment Due to Flap for $10 \leq M \leq 20$

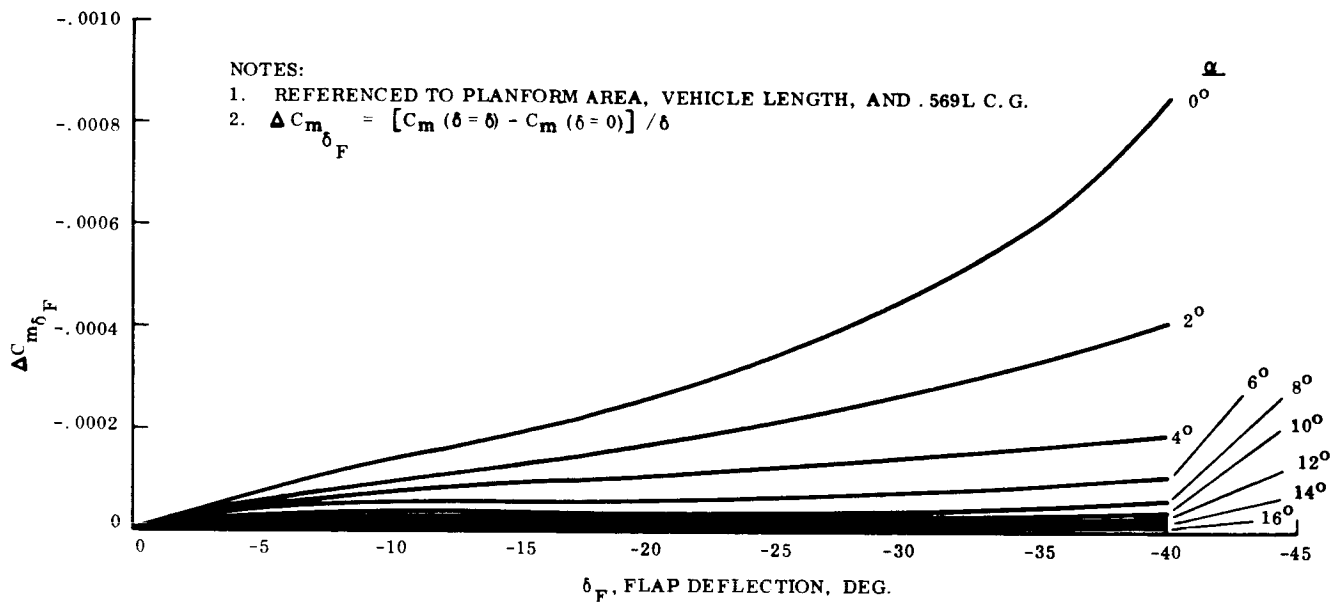


Figure 3.2-38. - Flap Effectiveness for $10 \leq M \leq 20$ versus Flap Deflection

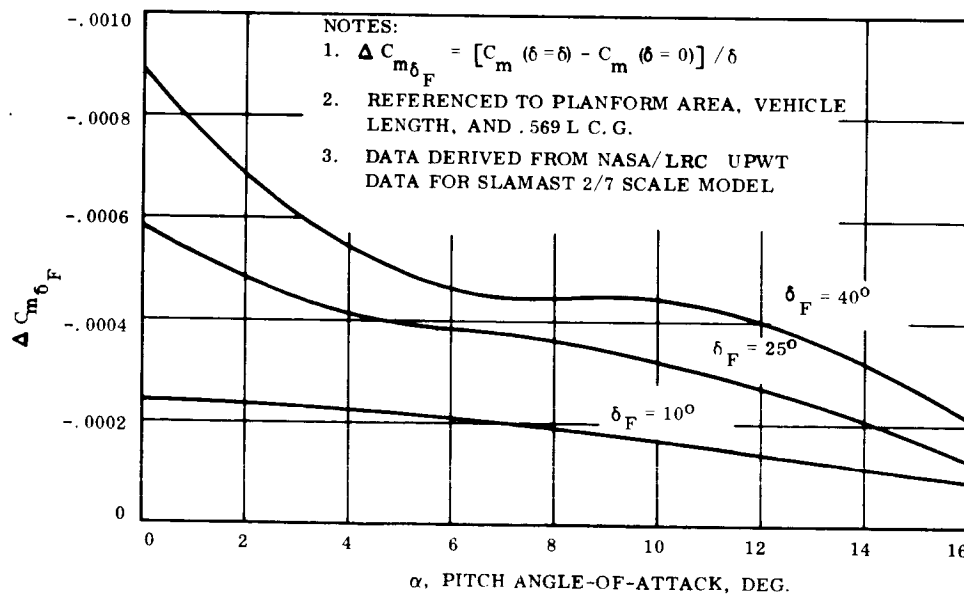


Figure 3.2-39. - Flap Effectiveness at $M = 4.63$ versus Angle-of-Attack

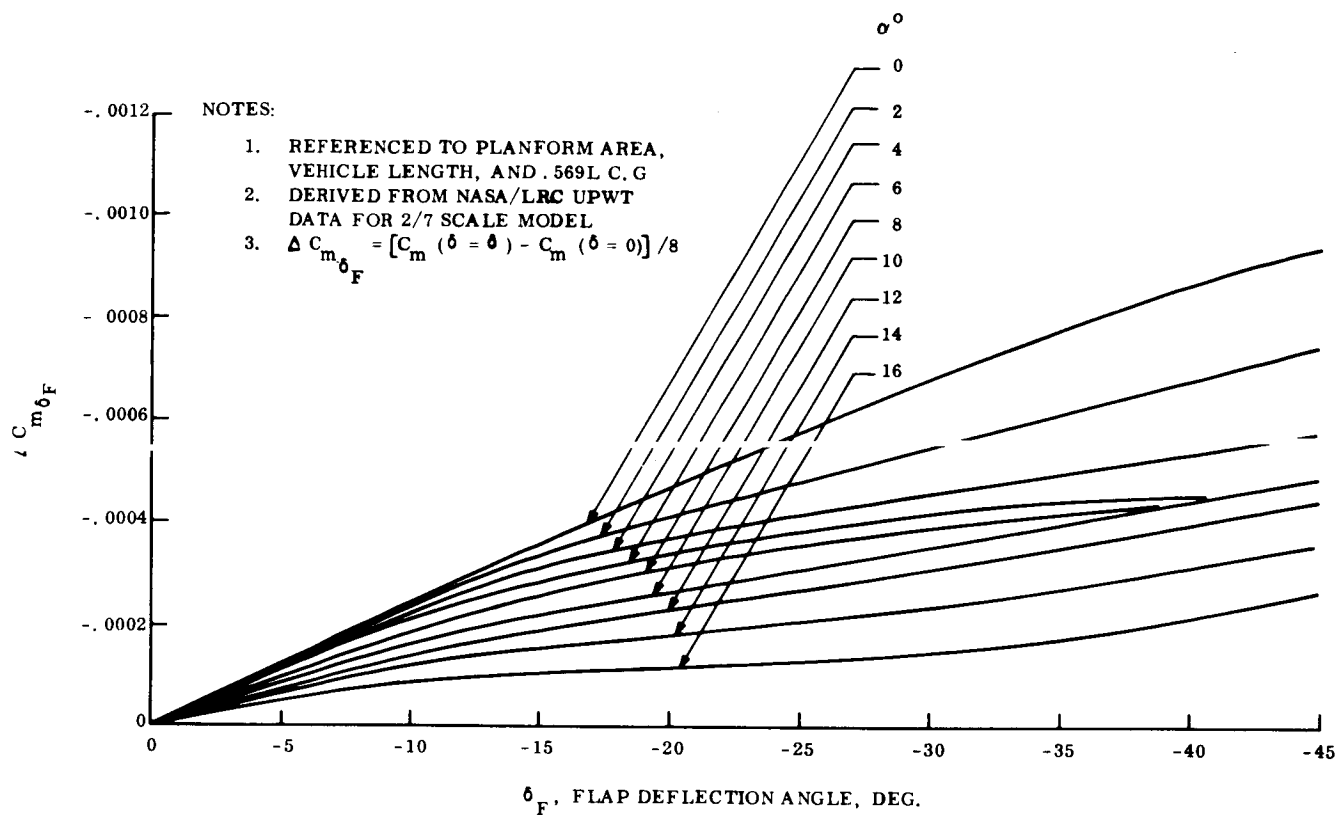


Figure 3.2-40. - Flap Effectiveness at $M = 4.63$ versus Flap Deflection

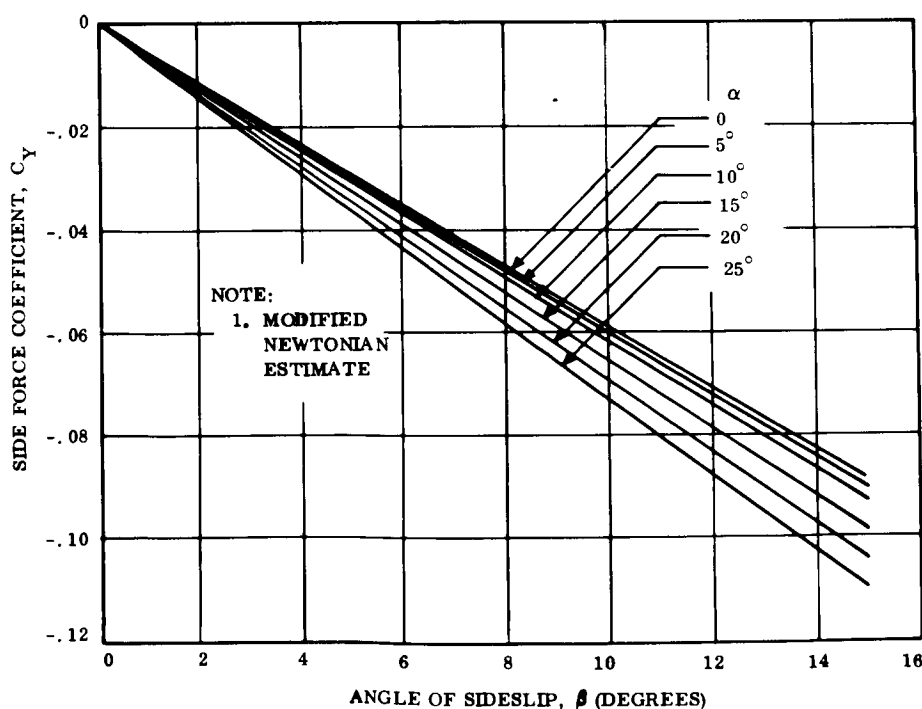


Figure 3.2-41. - Side Force Variation with Sideslip Angle, $10 \leq M \leq 20$.

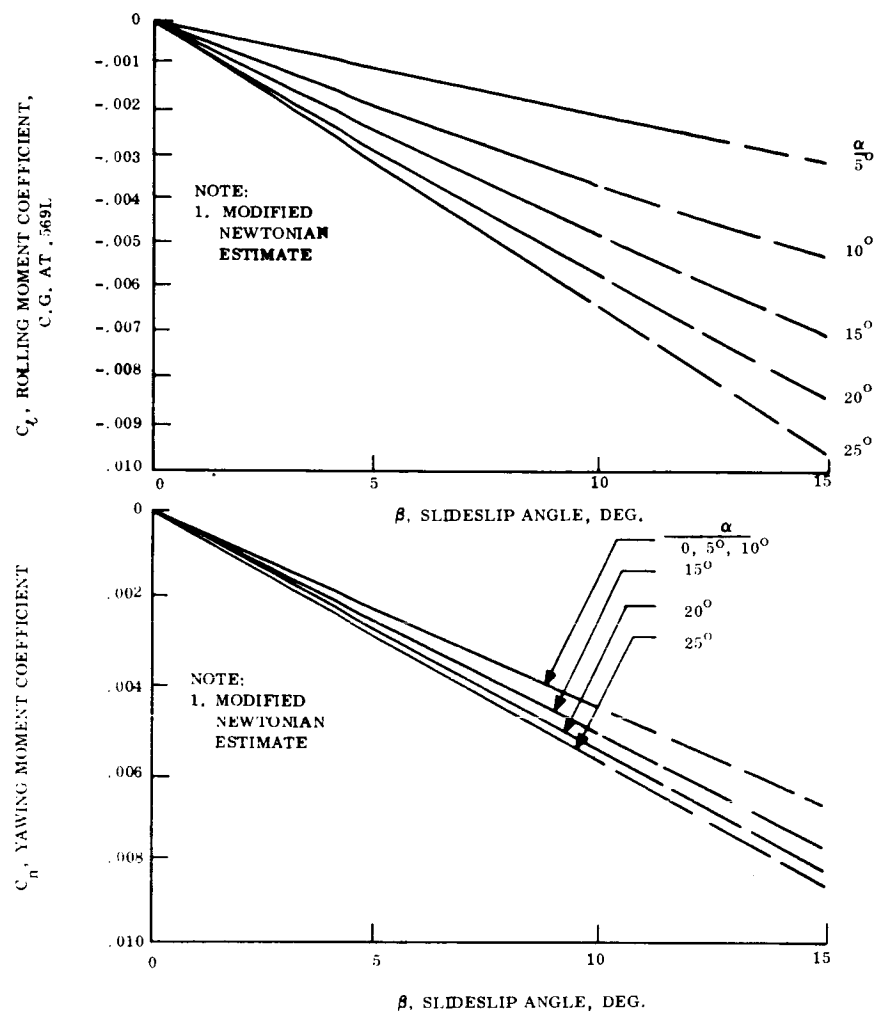


Figure 3.2-42. - Rolling and Yawing Moment Variations with Sideslip Angle, $10 \leq M \leq 20$

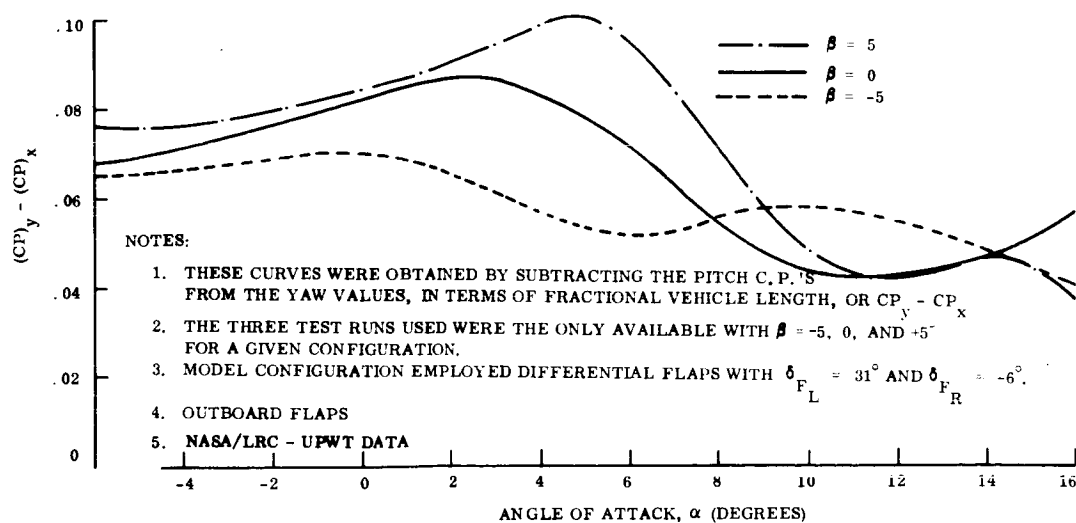


Figure 3.2-43. - Relative Location of Yaw Center-of-Pressure at $M=3.95$

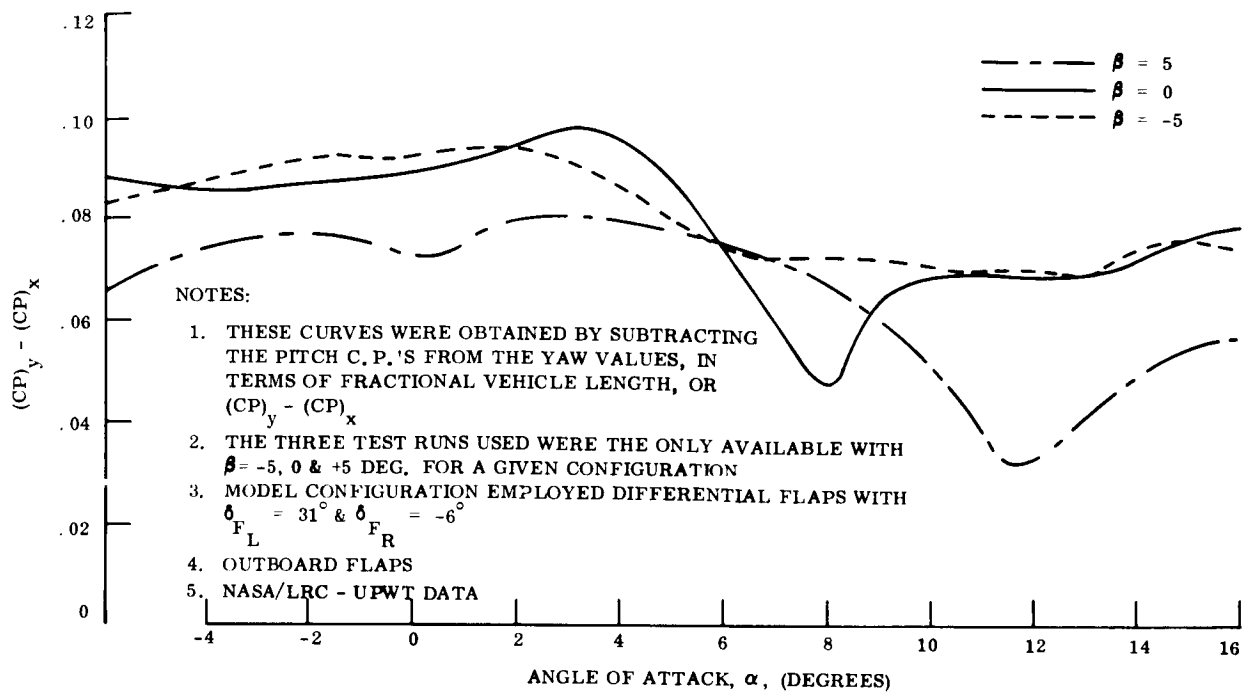


Figure 3.2-44. - Relative Location of Yaw Center-of-Pressure at M=4.63

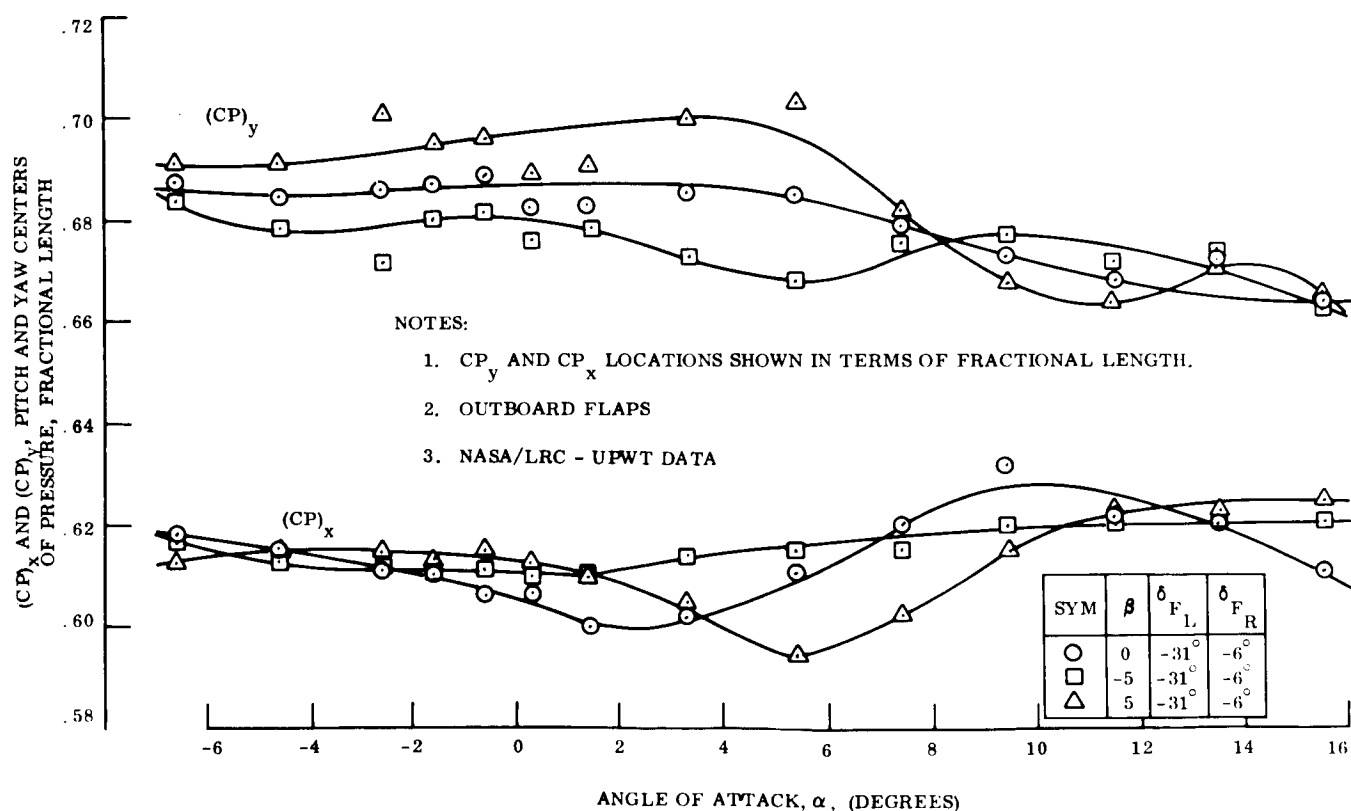


Figure 3.2-45. - Location of Pitch and Yaw Centers-of-Pressure at M=3.95

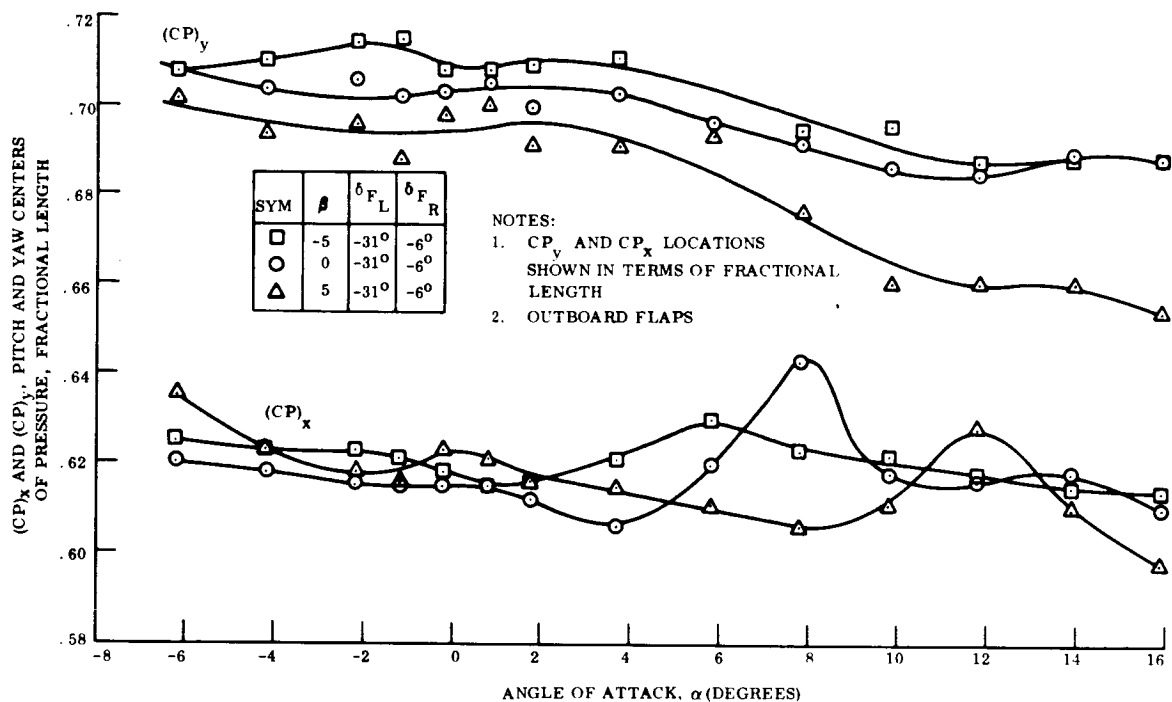


Figure 3.2-46. - Location of Pitch and Yaw Centers-of-Pressure at M=4.63

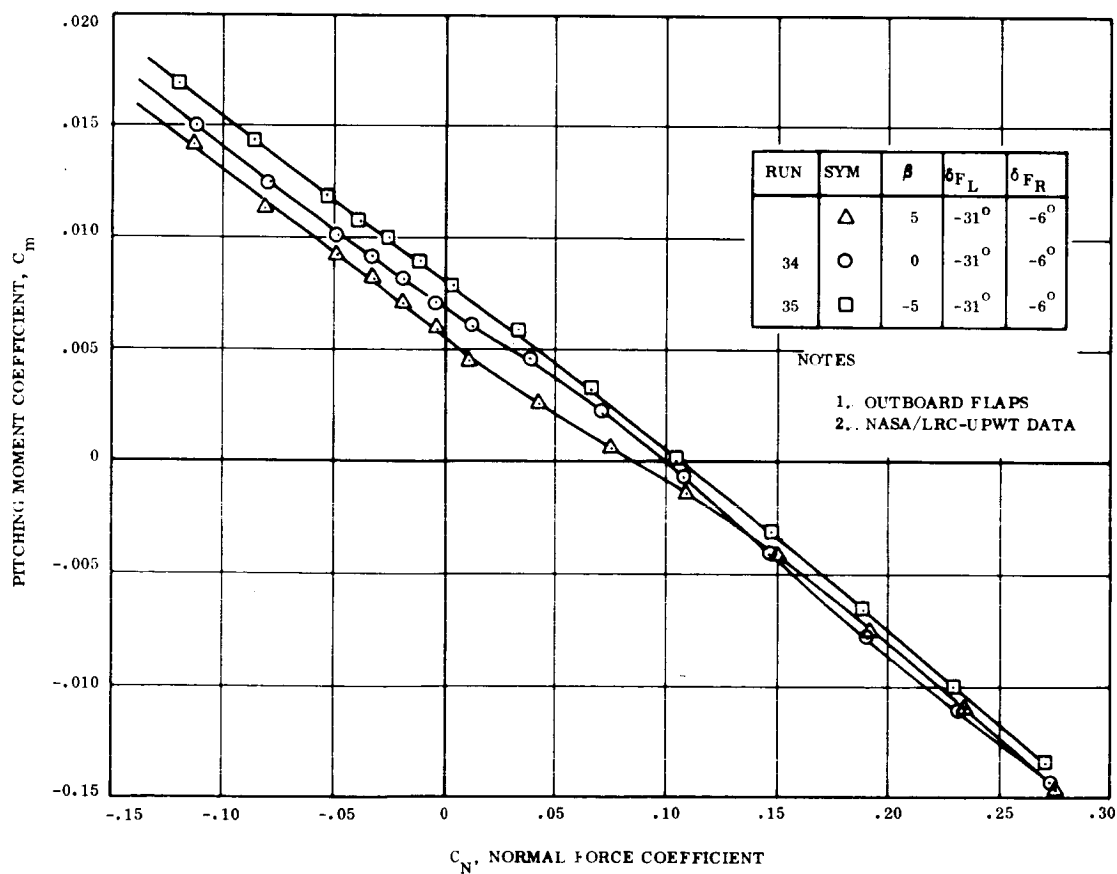


Figure 3.2-47. - Pitch Stability for 25° Differential Flaps at M=3.95

Figures 3.2-47 and 3.2-48 complete the coverage of the lateral-directional aerodynamic characteristics, and present the changes in pitch stability with yaw for the 25° differentially deflected outboard flap model configuration. The figures show very little change of the pitch stability due to slight yaw, even for the most asymmetrical of the model configurations tested.

Further comments on split flaps may be found in paragraph 3.2.2.3.

3.2.3.4 Dynamic stability. - Presented in this section are body alone estimates of the rotary damping derivatives for $10 \leq M \leq 20$. The estimates are presented in Tables 3.2-2 through 3.2-5 and in Figures 3.2-49 through 3.2-52, as obtained under the assumption of modified Newtonian flow through use of the FAB (Force on Arbitrary Bodies) computer program.

The damping derivatives were computed at a $wL/2V$ of 1/1200 in pitch ($w = q$), yaw ($w = r$), and roll ($w = p$). These derivatives were determined by subtracting the static coefficients from those produced during a steady state rotation about each of three axes, and then divided by $wL/2V$, where w is the rotational rate, L the vehicle reference length, and V the freestream velocity vector magnitude.

The presented derivative information is for body alone (flaps at zero deflection), without viscous effects, and for a center-of-gravity location of 56.9 percent of vehicle length.

A comparison of the modified Newtonian predictions for SLAMAST and the SORTIE 1-D shape is presented in Figure 3.2-53, together with SORTIE 1-D dynamic stability test data obtained at 10.18 Mach number and Reynolds' numbers from 0.45 to 3.31 million, based on model length. The comparison of damping-in-pitch information reveals that the two configurations have much the same damping value at zero pitch angle, SORTIE predictions indicating more than SLAMAST with increasing pitch angle of attack. The obtained SORTIE test data indicates approximately half the predicted values over the test ranges of pitch angle and Reynolds number.

In the same figure (Figure 3.2-53) is shown the yaw damping term C_{n_r} comparison. More limited information is shown here, SLAMAST predictions for 0.569L c.g. and SORTIE 1-D test data for 0.5L c.g., this being the extent of the immediately available data. The comparison indicates that SORTIE test values slightly exceed SLAMAST predictions over the cited test ranges, as might be considered reasonable in view of the similarities that are shown in the geometric comparison of Figure 3.2-54.

All the SORTIE test information was obtained at an exciting frequency of eight cycles per second. The model itself was 18.19 inches (0.4620m.) long with a 89.86 square inches (0.05797 sq. m.) planform reference area. The tests were conducted in AEDC's Tunnel C which at $M = 10$ has a test section total temperature of about 1900°R. Forced oscillation of the model was made with a one degree-of-freedom (DOF) balance oriented for pitch and yaw tests, the model being bolted to the balance such that the cross-flexure pivot is centered at the desired model moment reference center (c.g.) about which the model is also mass-balanced.

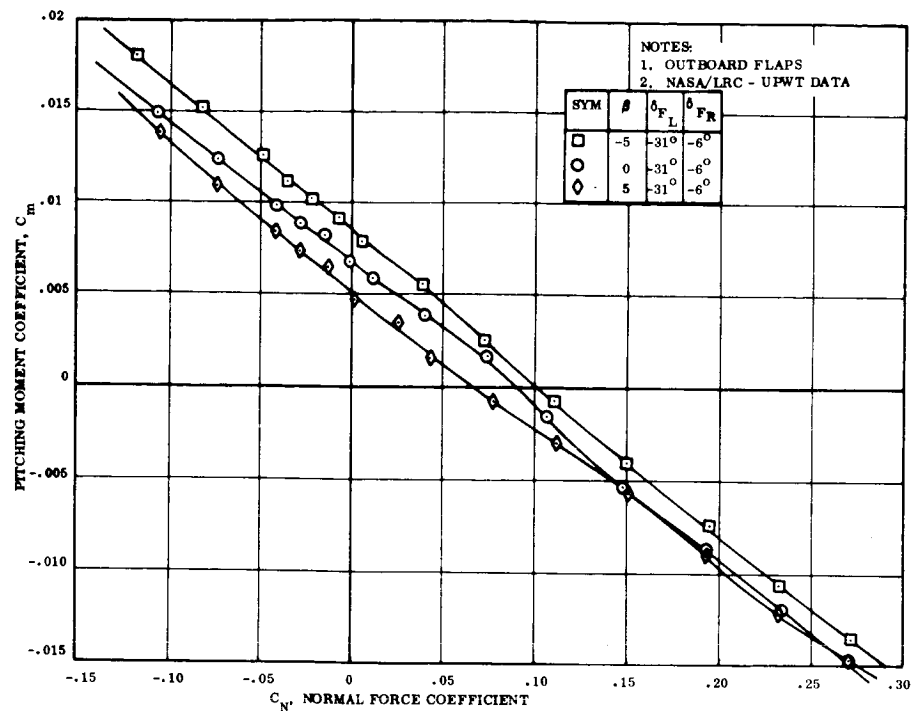


Figure 3.2-48. - Pitch Stability for 25° Differential Flaps at $M=4.63$

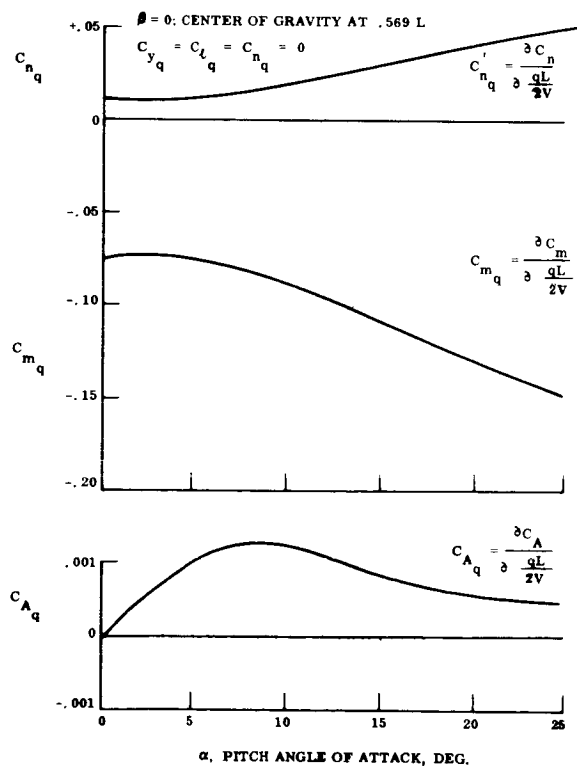


Figure 3.2-49. - Damping In Pitch Derivatives

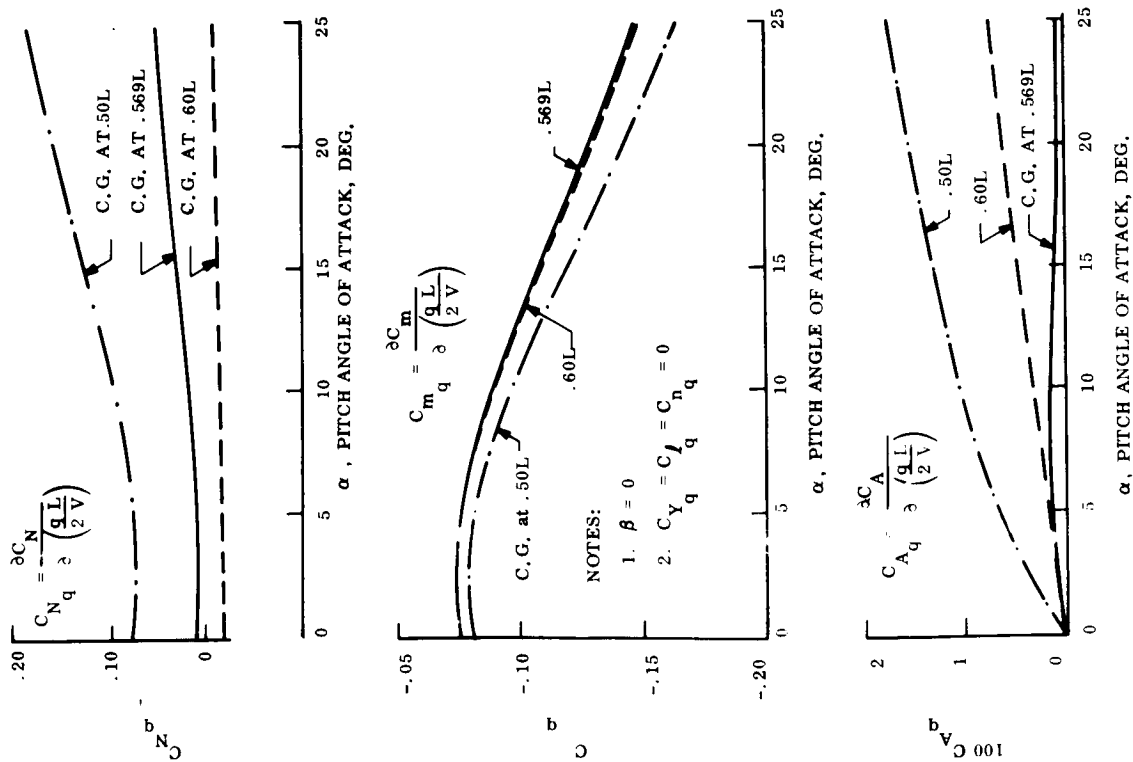


Figure 3.2-50. - Effect of Center of Gravity Location on Pitch Damping Derivative, $10 \leq M \leq 20$

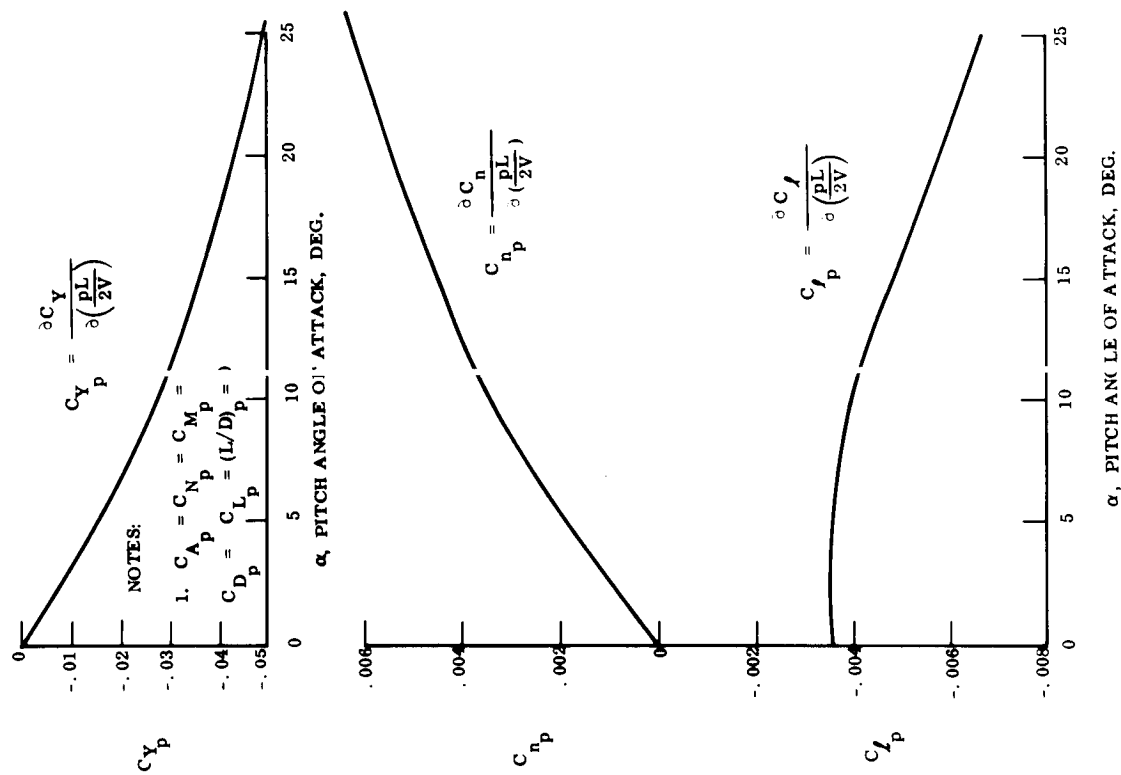


Figure 3.2-51. - Damping In Roll Derivatives $10 \leq M \leq 20$

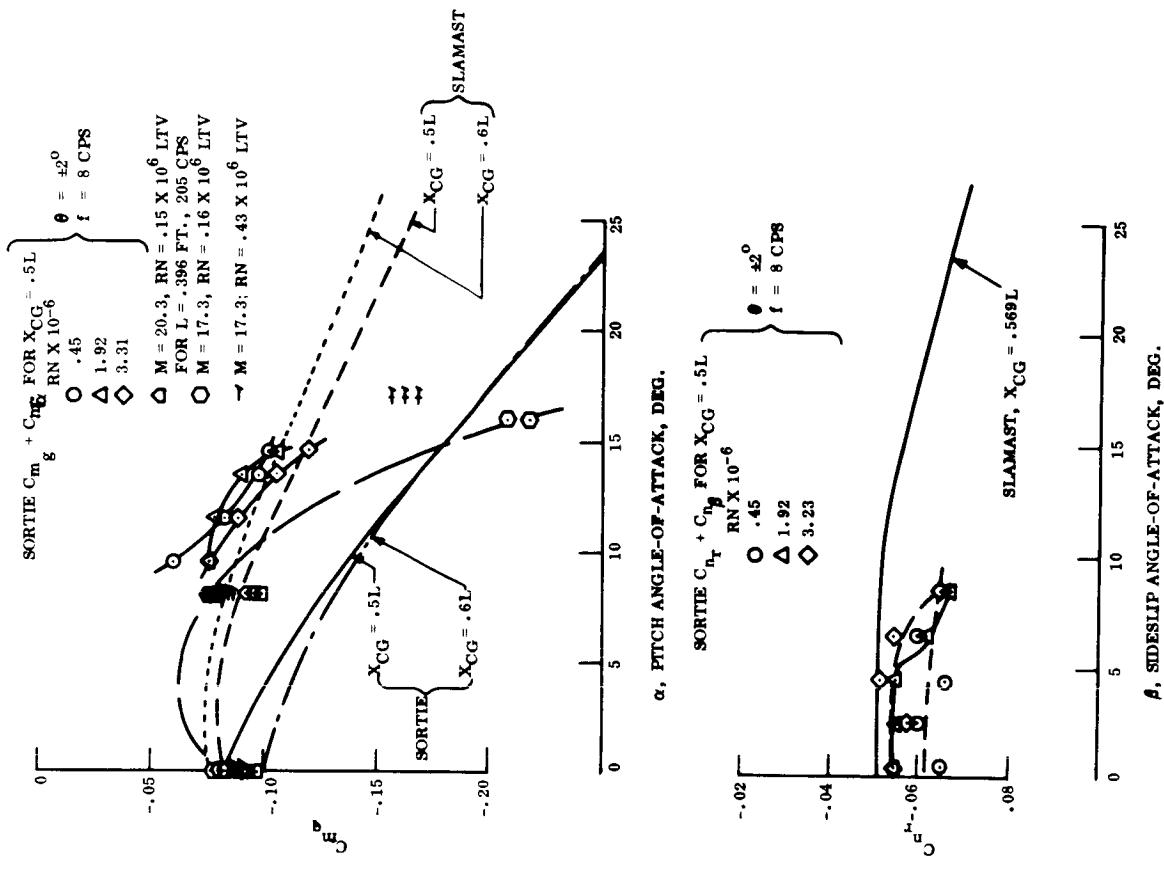


Figure 3.2-53. - Comparison of Estimated SLAMAST Dynamic Stability with SORTIE 1-D Test Data at 10.18 Mach Number

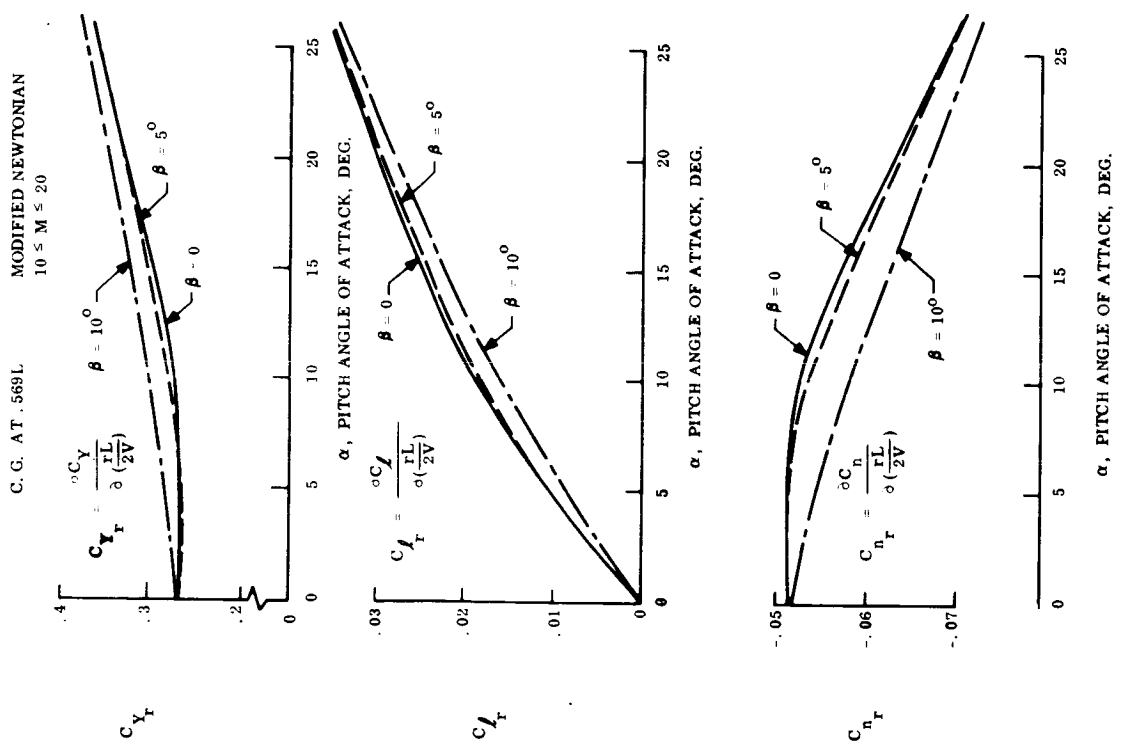


Figure 3.2-52. - Damping In Yaw Derivatives

NOTES:

1. ALL DIMENSIONS IN FRACTIONAL LENGTHS
2. SEE SECTION 3.2.2.1 FOR SLAMAST DIMS.
3. COMPARISON SHOWN IS ON EQUAL PLANFORM AREA BASIS

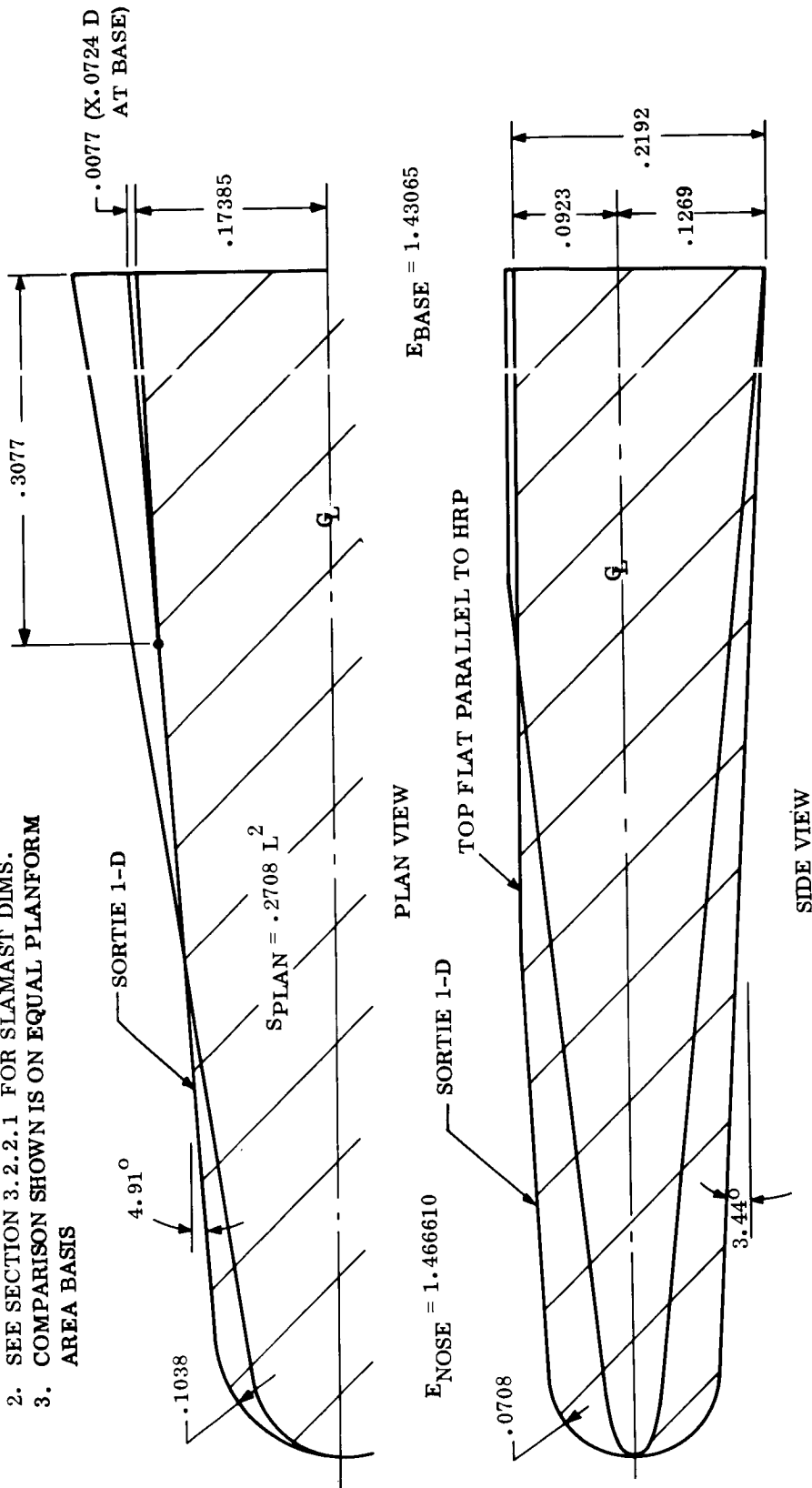


Figure 3.2-54. - Comparison of SLAMAST and SORTIE 1-D Geometric Shape

In forced oscillation testing, an external torque is imposed on the balance in phase with the natural flexure and aerodynamic restoring moment until a constant amplitude oscillation is obtained both wind on and wind off. The difference in torques yields a measure of dynamic damping.

Additional damping-in-pitch data from LTV tests of a 0.396 ft. SORTIE model at 17.3 and 20.3 Mach numbers shown in Figure 3.2-53 indicate agreement with Newtonian predictions at pitch angles near 16° and similar differences at lesser pitch angles as found in the $M = 10.18$ results. The LTV tests were conducted with an excitation frequency of 205 cycles per second at 0.15 to 0.43 million Reynolds number.

TABLE 3.2-2. SLAMAST ROTARY DERIVATIVES IN PITCH FOR MODIFIED NEWTONIAN FLOW, VARYING C.G. LOCATION, AND $\beta = 0$

Pitch Rotary Derivative	X_{cg}	α , Pitch angle-of-attack, deg					
		0	5	10	15	20	25
C_{m_q}	.50	-.08182	-.08148	-.09624	-.11940	-.14244	-.16488
	.569	-.07584	-.07560	-.08856	-.10884	-.12924	-.14892
	.60	-.07602	-.07572	-.08844	-.10836	-.12828	-.14772
C_{N_q}	.50	.07424	.07392	-.09300	.12336	.15288	.18106
	.569	.01176	.01180	.01386	.02943	.03984	.04956
	.60	-.01618	-.01610	-.01518	-.01276	-.01096	-.00951
$100 C_{A_q}$.50	0	.64290	1.0576	1.3044	1.5360	1.7760
	.569	0	.09948	.12384	.08556	.05964	.04690
	.60	0	.14470	.29500	.46200	.60600	.72960

NOTES:

1. $qL/2V$ is 1/1200 for all derivatives shown
2. $C_{\lambda_q} = C_{Y_q} = C_{n_q} = 0$
3. C_{L_q} , C_{D_q} , and $(L/D)_q$ are presented as secondary rotary derivatives in Table 3.2-5.

TABLE 3.2-3. SLAMAST ROTARY DERIVATIVES IN ROLL FOR MODIFIED
NEWTONIAN FLOW AND $\beta = 0$

Roll Rotary Deriv- ative α	0	5	10	15	20	25
C_{Yp}	0	-.01496	-.02736	-.03580	-.04304	-.04966
C_{lp}	-.00358	-.00357	-.00395	-.00482	-.00572	-.00660
C_{nr}	.00002	.00186	.00343	.00448	.00539	.00619

NOTES:

1. $pL/2V$ is 1/1200 for all derivatives shown.
2. $C_{Ap} = C_{Np} = C_{Mp} = C_{Dp} = C_{Lp} = (L/D)_p = 0$
3. Center of gravity at 0.569 vehicle length (design).

TABLE 3.2-4. SLAMAST ROTARY DERIVATIVES IN YAW FOR MODIFIED
NEWTONIAN FLOW AND VARYING SIDESLIP ANGLE

Yaw Rotary Deriv- ative	β	α , Pitch angle-of-attack, deg					
		0	5	10	15	20	25
C_{Yr}	0	.26834	.26732	.27371	.29755	.32726	.35795
	5	.26732	.26616	.28050	.30368	.33045	.35874
	10	.27060	.28308	.30204	.32328	.34752	.37308
C_{lr}	0	0	.01037	.01900	.02486	.02988	.03444
	5	0	.01032	.01809	.02421	.02949	.03426
	10	0	.00840	.01596	.02256	.02820	.03324
C_{nr}	0	-.05141	-.05121	-.05232	-.05679	-.06230	-.06819
	5	-.05120	-.05101	-.05362	-.05803	-.06304	-.06829
	10	-.05184	-.05424	-.05784	-.06180	-.06636	-.07104

NOTES:

1. $rL/2V$ is 1/1200 for all derivatives shown.
2. Center-of-gravity at 0.569 vehicle length (design).
3. Secondary derivatives shown in Table 3.2-5.

TABLE 3.2-5. - SECONDARY SLAMAST ROTARY DAMPING DERIVATIVES

(a) In Pitch, at three C.G. locations, with $\beta = 0$							
Pitch Rotary Derivative	C.G., X/L	α , Pitch angle-of-attack, deg					
		0	5	10	15	20	25
C_{Lq}	.50	.07423	.07311	.08974	.11581	.13839	.15658
	.569	.01185	.01167	.01785	.02821	.03722	.04472
	.60	-.01617	-.01592	-.01444	-.01113	-.00943	-.00747
C_{Dq}	.50	0	.01285	.02656	.04453	.06679	.09261
	.569	0	.00201	.00440	.00843	.01419	.02125
	.60	0	-.00284	-.00554	-.00776	-.00944	-.01064
$(L/D)_q$.50	3.5948	1.5577	.50556	.24096	.12960	.65400
	.569	.57392	.25104	.13920	.11076	.07680	.05328
	.60	-.78324	-.33552	-.02532	+.05232	+.05316	+.04236
(b) In Yaw with $\beta = 0, 5, \text{ and } 10 \text{ deg.}$ and C.G. at 0.569L							
Yaw Rotary Derivative	β	α , Pitch Angle-of-Attack, deg.					
		0	5	10	15	20	25
C_{Lr}	0	0	.00001	-.00008	-.00010	-.00013	-.00013
	5	0	.00199	-.01865	-.02656	-.02777	-.02678
	10	0	-.01378	-.03887	-.05970	-.05424	-.05264
C_{Dr}	-.02348	-.00010	-.00010	-.00010	-.00011	-.00012	-.00014
	5	0	-.02332	-.02335	-.02497	-.02682	-.02828
	10	-.04570	-.04408	-.04494	-.04831	-.05203	-.00520
$(L/D)_r$	0	0	.0080	.0030	.0012	.0008	.0004
	5	0	1.67	.65	.26	.12	.06
	10	0	2.04	1.07	.47	.23	.12

NOTES:

1. Secondary roll derivatives are zero.
2. $pL/2V$ and $rL/2V$ are both $1/1200$ for all derivatives shown.
3. Modified Newtonian flow estimates for $10 \leq M \leq 20$ usc.

3.2.4 AERODYNAMIC PRESSURE DISTRIBUTIONS AND LOADS

3.2.4.1 Pressure distributions. -

3.2.4.1.1 Nose cap: The nose cap pressure distributions presented in Figure 3.2-55 through 3.2-59 were obtained through use of the information contained in references 3.2-2, 3.2-5 and 3.2-12. Reference 3.2-12 contains pressure distributions obtained at a Mach number of seven for a nose similar to that for SLAMAST except in having approximately twice the ellipticity in cross-section.

The data of the reference are presented in terms of pressure coefficient values which were transformed to fractions of the stagnation value to provide basic SLAMAST nose cap pressure distributions. Adjustments to these basic distributions were then made through use of the information contained in references 3.2-5 and 3.2-2 to account for the configuration differences. The resulting nose cap pressure distributions of Figure 3.2-55 through 3.2-59 are considered to be sufficiently representative for the purposes of the SLAMAST feasibility study, but should be replaced with more accurate data as it becomes available.

The nose cap and the other pressure distributions of this section are intended for use only in regions where the assumptions of modified Newtonian flow apply; e. g. , approximately above a Mach number of 10, but may be used for Mach numbers as low as 7 without appreciable error.

3.2.4.1.2 Body: - The body portion aft of the nose cap has a wrapped surface, or one which can be peeled away to form a flat pattern without concavity, except for the body flat (scalloped) areas. The body geometry is defined in considerable detail in paragraph 3.2.2.1. The pressure distribution for the wrapped surface body portion can be described by a single variation of pressure for a given pitch angle-of-attack if plotted with peripheral surface slope and if carry over effects from the nose are neglected. This occurs since pressure is dependent on peripheral slope and not on meridian angle, as pointed out in and confirmed by the test data of reference 3.2-5. The data of that reference and from references 3.2-2 and 3.2-12 were consequently employed to generate the wrapped surface pressure distributions presented here as Figures 3.2-60 and 3.2-61. The associated variation of meridian and peripheral slope angles is found in Figure 3.2-4. These data should, of course, be replaced by test data for the specific SLAMAST shape when those data become available.

3.2.4.1.3 Pitch flap: Pressure distributions for the single-flap of the basic SLAMAST configuration were prepared for flap deflection angles of 0 to -40 degrees and pitch angles-of-attack from -10 to +12, all at zero yaw angle-of-attack. A representation of the shock geometry and a typical flap pressure distribution are shown in Figures 3.2-62 and 3.2-63.

The single-flap estimations were derived from a combination of available in-house test and analytical results, particular calculations for the basic SLAMAST flap, and by comparisons with other available data. The flap geometry employed in the in-house tests was similar to the SLAMAST flap, although the body was a 5°

right circular cone, rather than the SLAMAST modified elliptic conoid shape. The obtained data were then modified to the particular SLAMAST flap geometry for study use. Pressure measurements on the body were limited to a few taps on the body flats just adjacent to the hinge line. Figure 3.2-63 presents a representative example of those flap pressure distributions employed in the study.

The data are believed accurate within an overall $\pm 20\%$ error band for Mach numbers between 10 and 20 at Reynolds numbers less than 2.5 million per foot. Use of the data for Mach numbers from 8 to that at atmospheric entry and for Reynolds numbers less than 5.0 million per foot may increase the possible error to within plus-or-minus 30 percent.

No altitude restrictions were placed on the use of the data during the study, although the extent of separated flow may increase at the higher flight altitudes within SLAMAST performance capability. The consequent decrease in flap effectiveness (with increased separation) would also be reflected in changed pressure distributions, hinge moments, and loads.

Since the vehicle performance depends on trimmed lift capability, and thus on flap effectiveness for a given center-of-gravity location, more accurate knowledge of the flap pressures is required for efficient vehicle design. Flap pressure distribution tests are therefore recommended prior to fixing final flap design for the prototype vehicle. Such tests should be initially at a Mach number of eight or greater with Reynolds number variations encompassing flight conditions (within tunnel capability) to provide an assessment of changed flap performance with Reynolds number and the viscous-interaction parameters, \bar{V} and $\bar{\chi}$. Since flap size, planform geometry, orientation of the hinge line, and sealing are among those parameters that directly affect flap performance, a limited assessment of such factors should be included in the pressure tests.

3.2.4.1.4 Correlation of flap centerline pressures: A simple method coupled with limited available data has provided a correlation of flap centerline pressures as shown in Figure 3.2-62. It appears that the method is a logical step toward analytical prediction of flap pressure distribution that would include the characteristics of the separated region, such as separation angle, Reynolds number at the separation "point", etc.

Past attempts to analytically correlate flap pressures have employed a strip-theory approach. This approach works quite well for vehicles with nose bluntnesses (r_N/r_B) order of or greater than .12, but not as well for sharper nosed configurations. The limits of the approach may be explained by the following:

(1) The shock layer gradients are very small at the base of sharp nosed vehicles while the surface Mach number is very high. This causes the flow over the flat and in the region of the flap to be partly instead of fully expanded as was assumed in the analysis.

(2) Viscous effects are more significant on sharp nosed vehicles as evidenced by localized flow separation noted at the juncture of the flap and the flat in Schlieren photographs of a recent test.

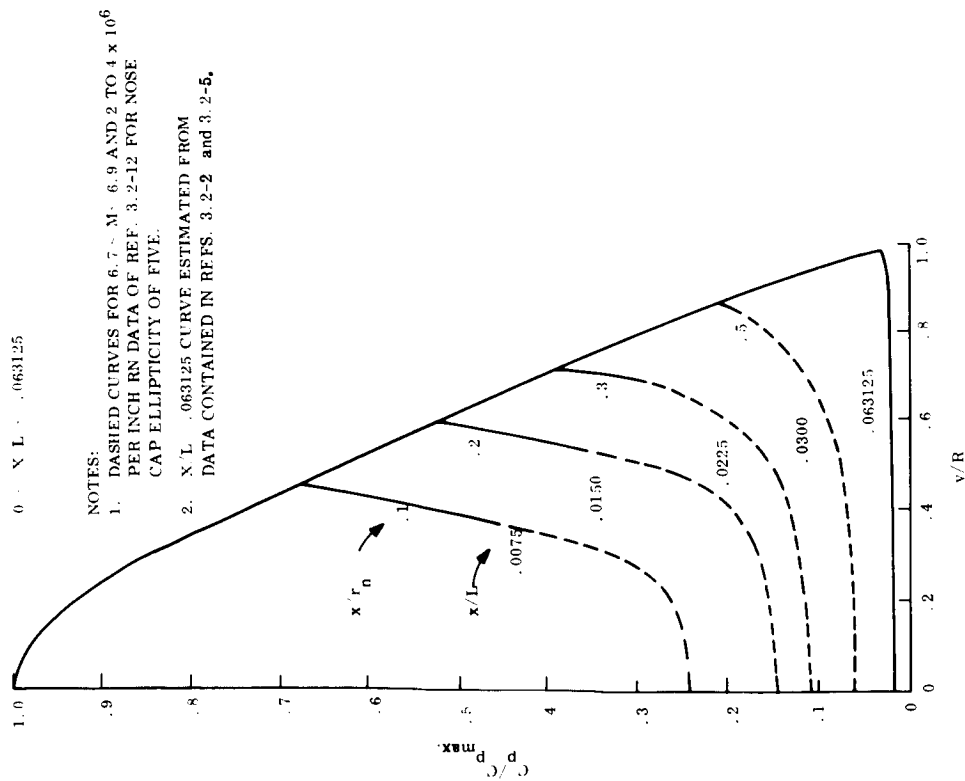


Figure 3.2-55.-Nose Cap Transverse Pressure
Distribution for $\alpha = 0$

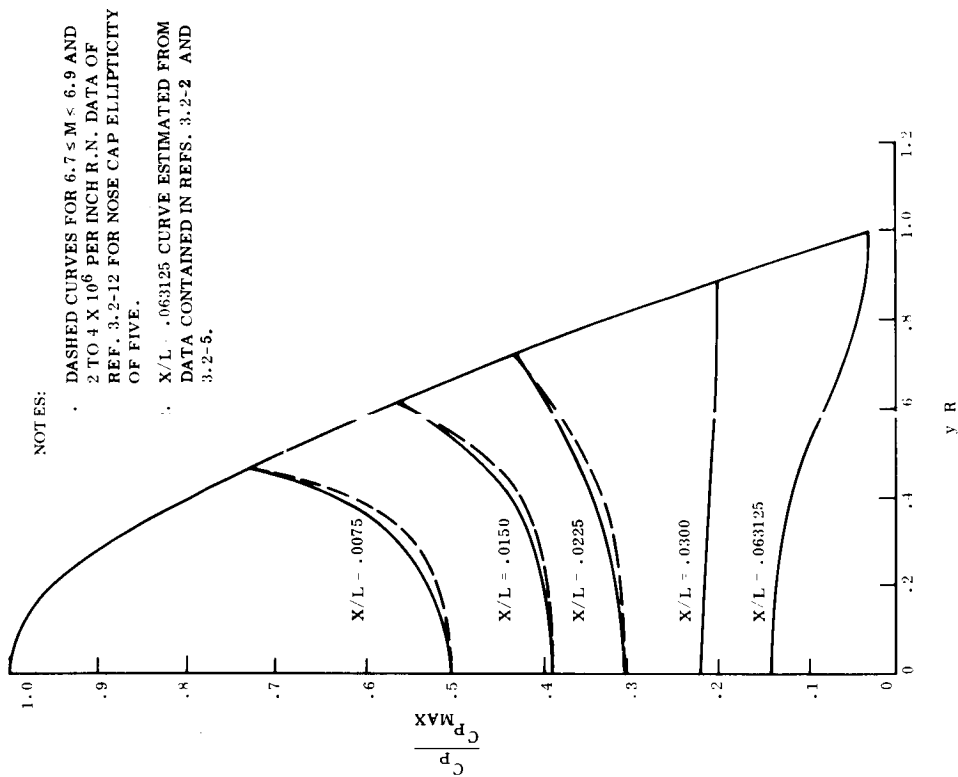


Figure 3.2-56.-Nose Cap Transverse Pressure
Distribution for $\alpha = 150$

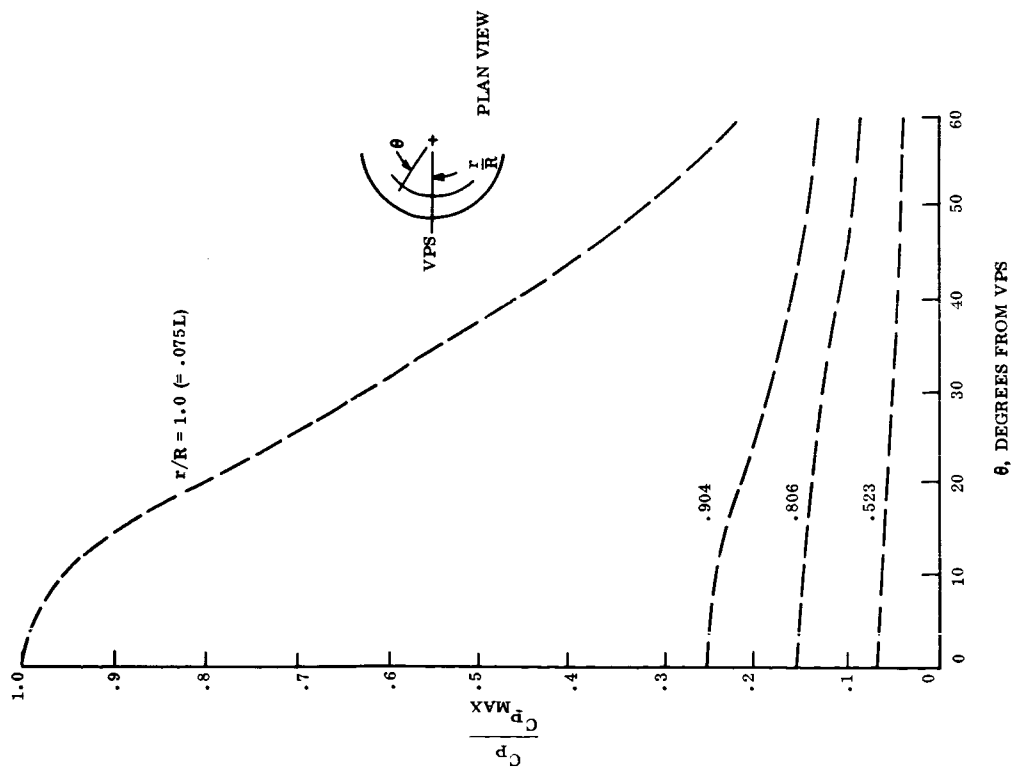


Figure 3.2-57. - Nose Cap Radial Pressure Distribution
for $\alpha = 0$

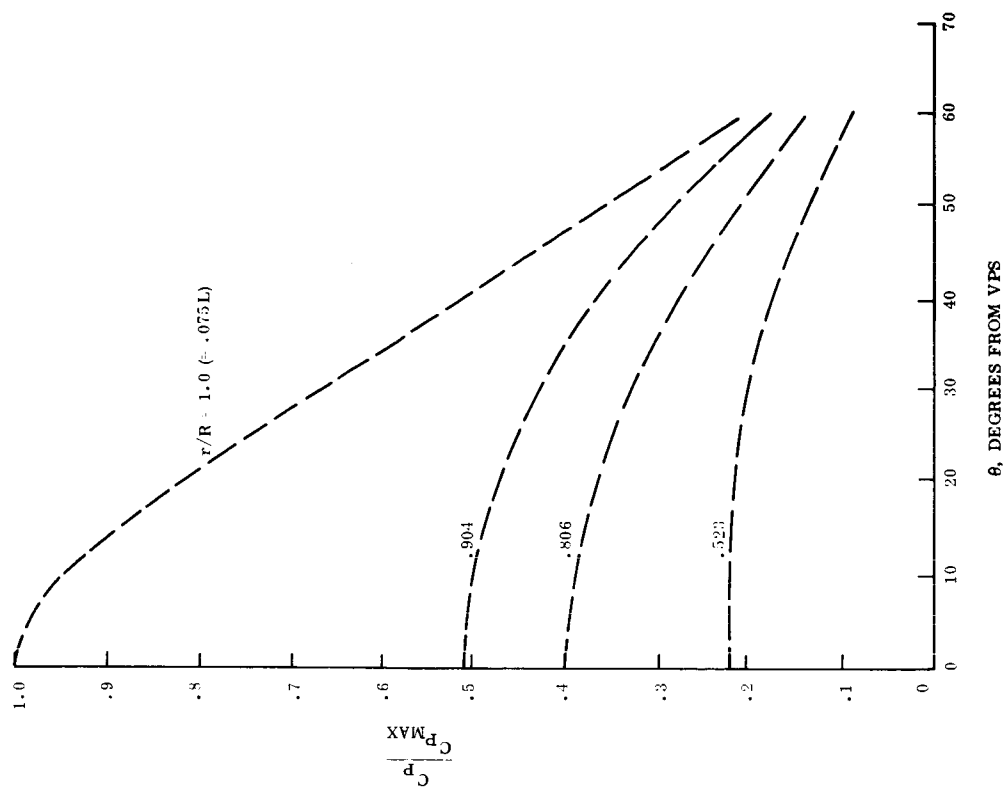


Figure 3.2-58. - Nose Cap Radial Pressure Distribution
for $\alpha = 15^\circ$

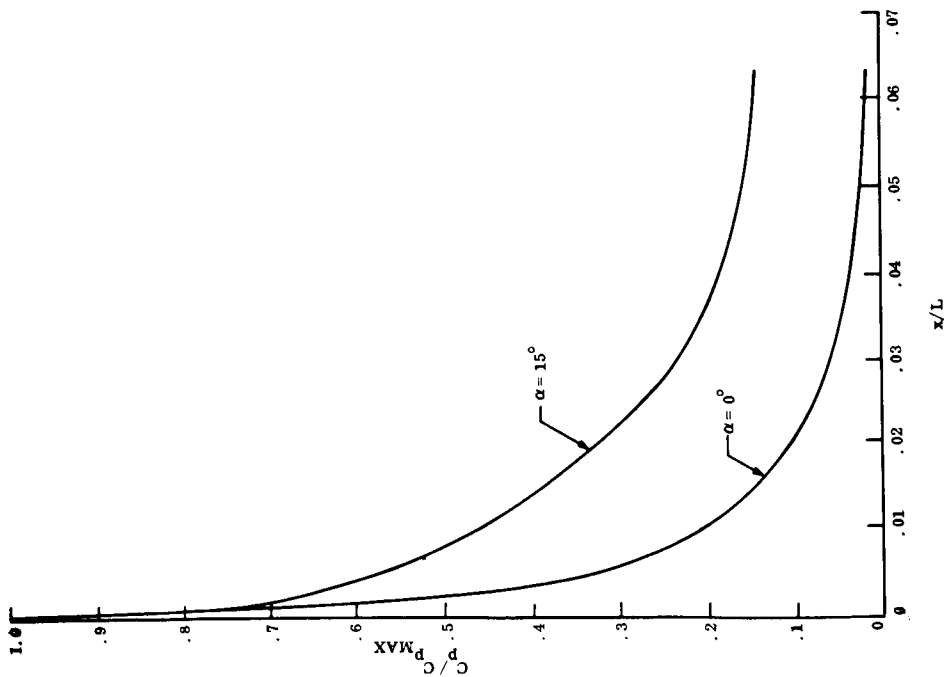


Figure 3.2-59.-Nose Cap Longitudinal Pressure Distribution for $\alpha = 0$ and 15°

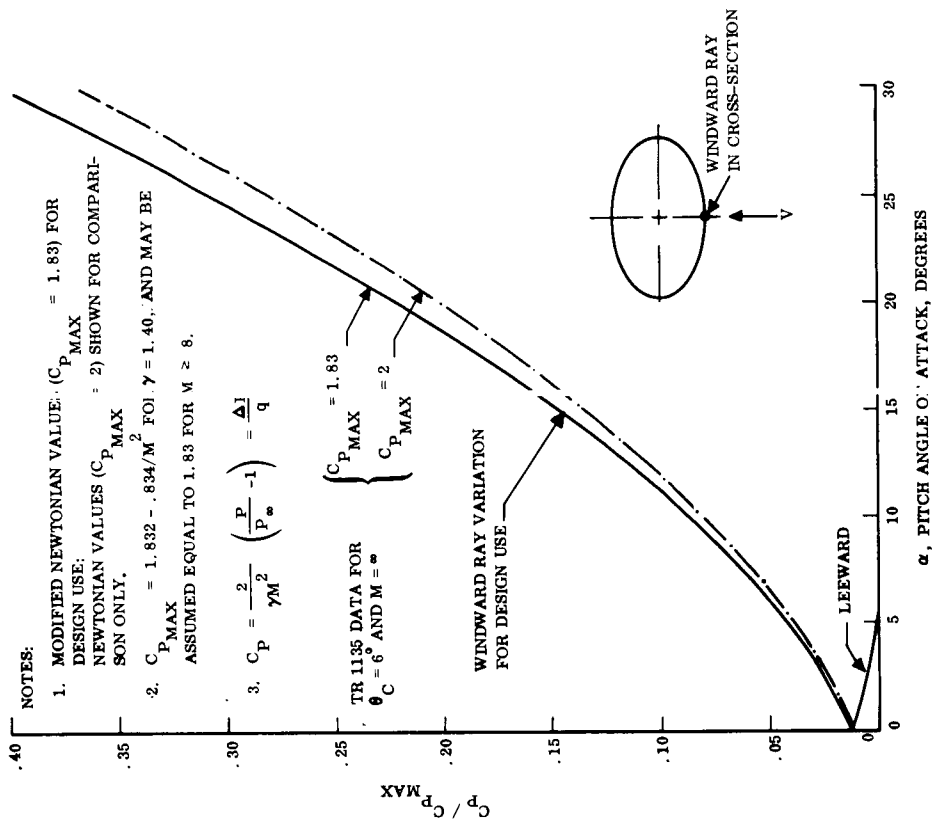


Figure 3.2-60.-Variation of Windward Ray Pressures for Wrapped Surface Regions

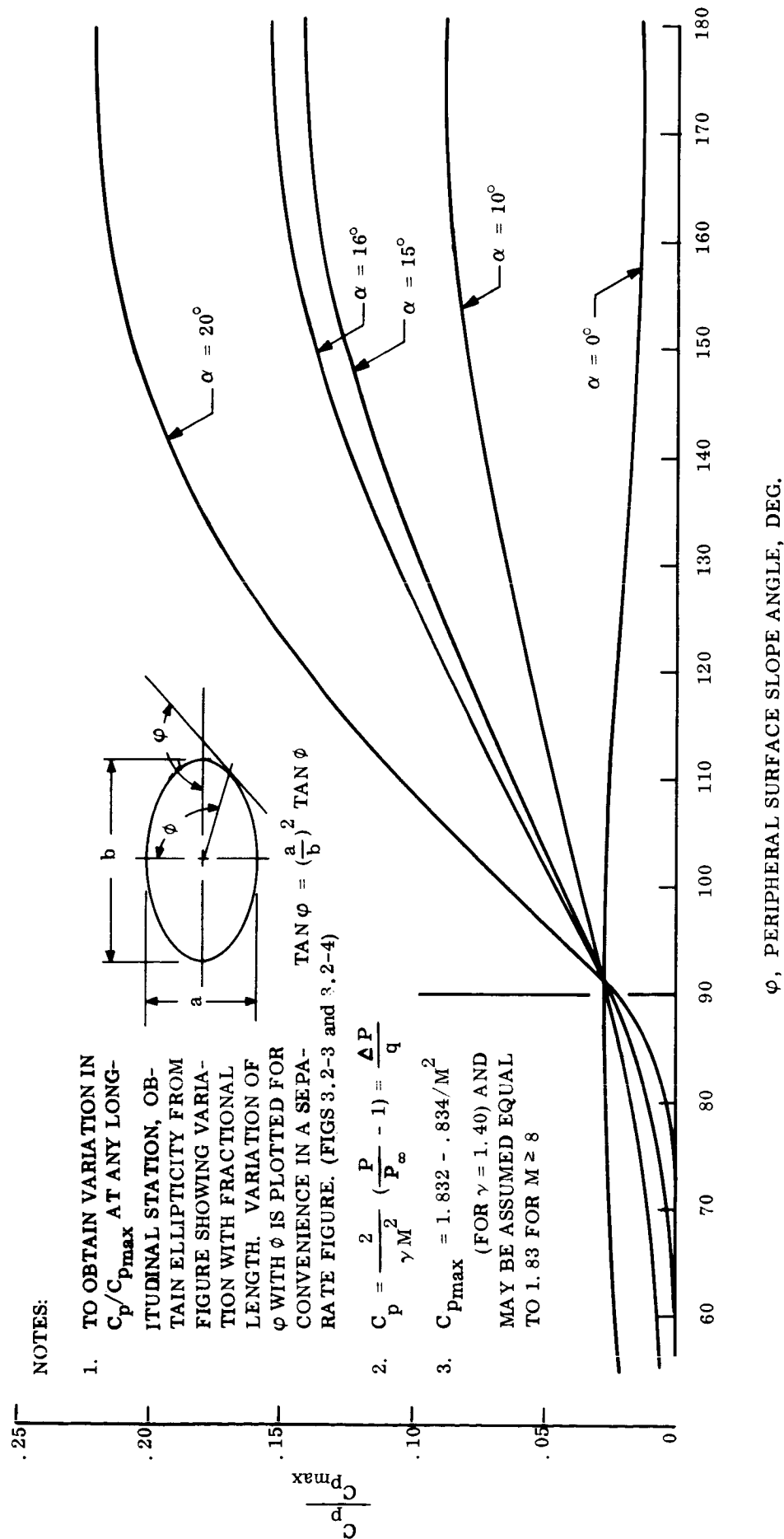


Figure 3.2-61. - Modified Newtonian Pressure Distributions for Wrapped Surface Regions

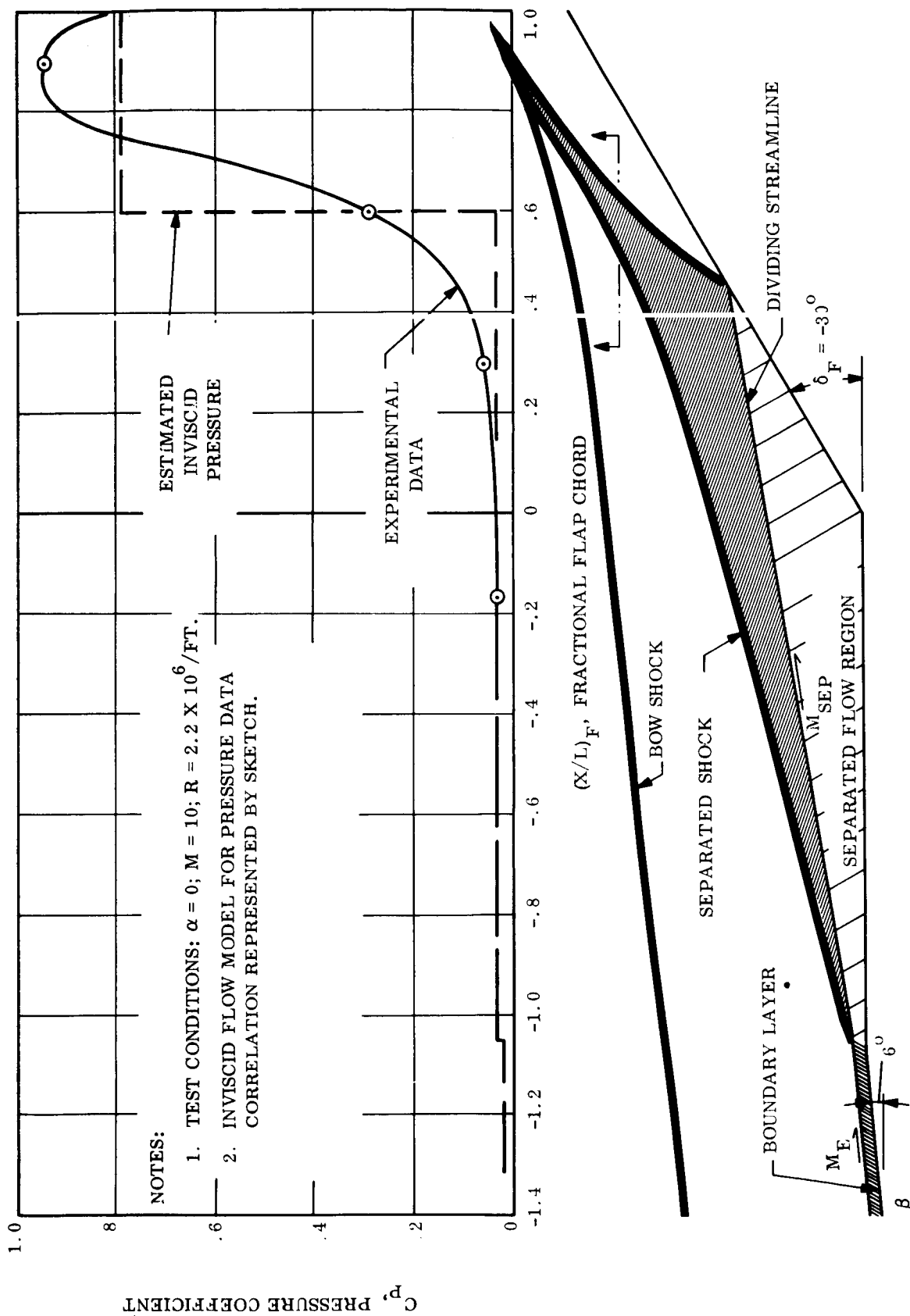


Figure 3.2-62. - Correlation of Flap Centerline Pressure for Laminar Separated Flow

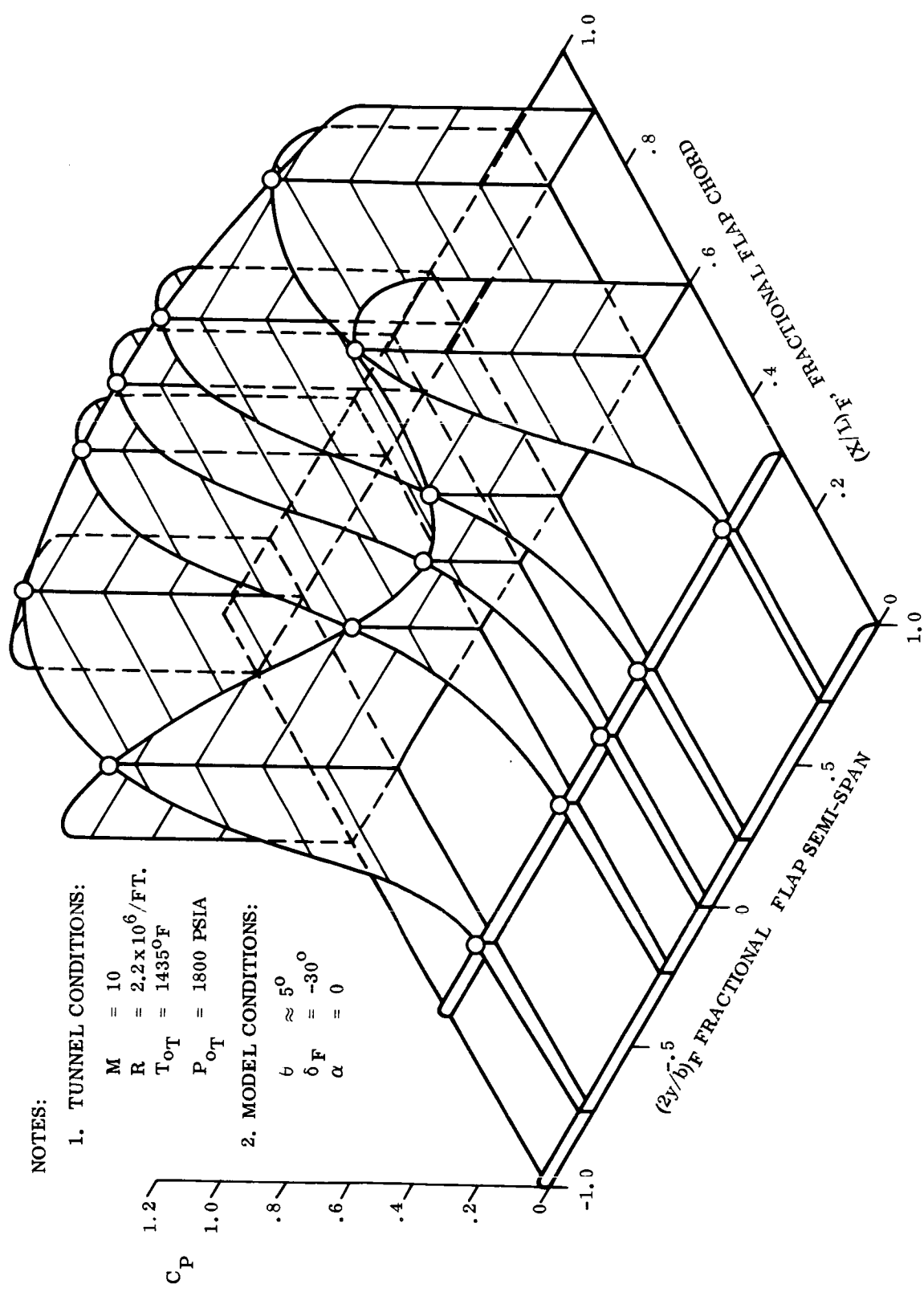


Figure 3.2-63. - Flap Pressure Distribution for Laminar Separated Flow

The strip theory method on the sharper nosed vehicles yielded peak plateau pressures which approximate one-half the measured values. This prompted the present correlation since the only way to increase the pressure recovery on the flap was through a system of weaker shocks (rather than a single strong shock). The resulting inviscid flow model and a comparison of the theory is shown in Figure 3.2-62. It was necessary to assume that the flow separated just before the flap and did not expand onto the flat. This assumption was justified by inspecting a Schlieren flow photograph for this particular test configuration. The flow reaching the upper portion of the flap has gone through the bow shock, the separation shock, and the reattachment shock. The separation is also quite extensive with a low inviscid plateau pressure coefficient, characteristic of laminar flow separation.

3.2.4.2 Loads and hinge moments. - This section presents the body alone cumulative normal force coefficient, cumulative axial force coefficient, incremental moment coefficient, and cumulative moment coefficient distributions with fractional vehicle length in Figures 3.2-64 through 3.2-67, respectively. The data were prepared through use of the pressure distributions of paragraph 3.2.4.1 and the modified Newtonian force and moment results of paragraph 3.2.3.1.

Flap loads and hinge moments are subsequently presented in Figures 3.2-68 through 3.2-74 to complete the configuration load and hinge moment data plots. Inspection of the flap load and hinge moment plots reveals that lower angles-of-attack and higher flap deflections together mean higher loads and moments. Consequently, close examination of transient flight conditions is required to establish the maximum load and hinge moment conditions, which could be higher than the trim values illustrated in Figure 3.2-74.

Figure 3.2-68 presents flap panel load coefficient variation with pitch angle, while Figure 3.2-70 is a cross-plot of the data in Figure 3.2-68. The flap hinge moment coefficient variation with pitch angle-of-attack is presented in Figure 3.2-71; a cross plot of the data of that figure is shown as Figure 3.2-72. Figure 3.2-74 presents the trimmed variation of flap hinge moment determined by Figures 3.2-64 through 3.2-66.

These flap data were obtained by three-dimensionally integrating flap pressures for panel loads and a moment of area of the same for hinge moments. The magnitudes of both are lower than those associated with axisymmetric maneuvering re-entry vehicles, due to the anticipated laminar flow environment. Separated flow is anticipated over as much as 40% of the flap.

Supplementing the flap hinge moment and panel load information of Figures 3.2-68 and 3.2-72 for positive pitch angles-of-attack is the information for negative angles-of-attack up to 20 degrees presented in Figures 3.2-69 and 3.2-73. That information was obtained in this manner: the local flap angle of attack was assumed equal to the free-stream value plus flap deflection into the stream, or $\alpha_{LF} = \alpha_{\infty} - \alpha_F$, where α_F is negative with upward deflection from the body flat, parallel to vehicle centerline. Cross plotting and re-plotting of the referenced data thus provided the curves for negative pitch angle. Data accuracy is estimated at $\pm 25\%$ between Mach numbers of 10 and 20 at Reynolds numbers of less than 2.5 million per ft.

The hinge moment coefficient data are based on flap area and chord length, .7867 sq/ft. (.0731 sq. m.) and .875 ft. (10.57 in. or .2674 m.), for the 63 inches (5.25-ft or 1.600 m.) long SLAMAST vehicle. The load coefficients are based on flap area alone.

NOTE: For other vehicle sizes employing the SLAMAST shape, the reference lengths may be scaled by vehicle length. (e.g., 3.2 m. Vehicle; M. F. = $3.2/1.6 = 2$). For Area, use square of the scale ratio. (e.g., 3.2 m. Vehicle; M. F. = $(3.2/1.6)^2 = 2^2 = 4$).

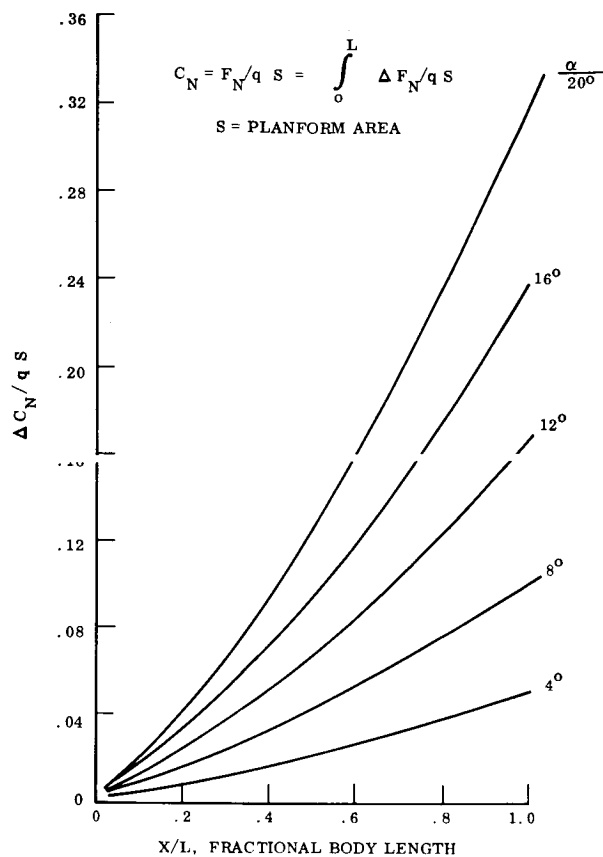


Figure 3.2-64. - Cumulative Normal Force Coefficient Distribution

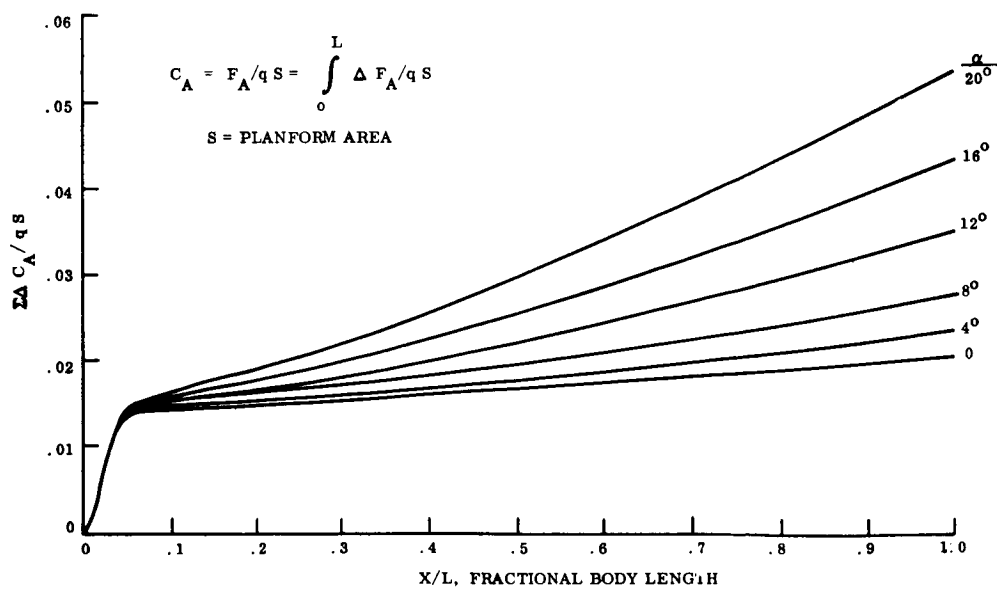


Figure 3.2-65. - Cumulative Axial Force Coefficient Distribution

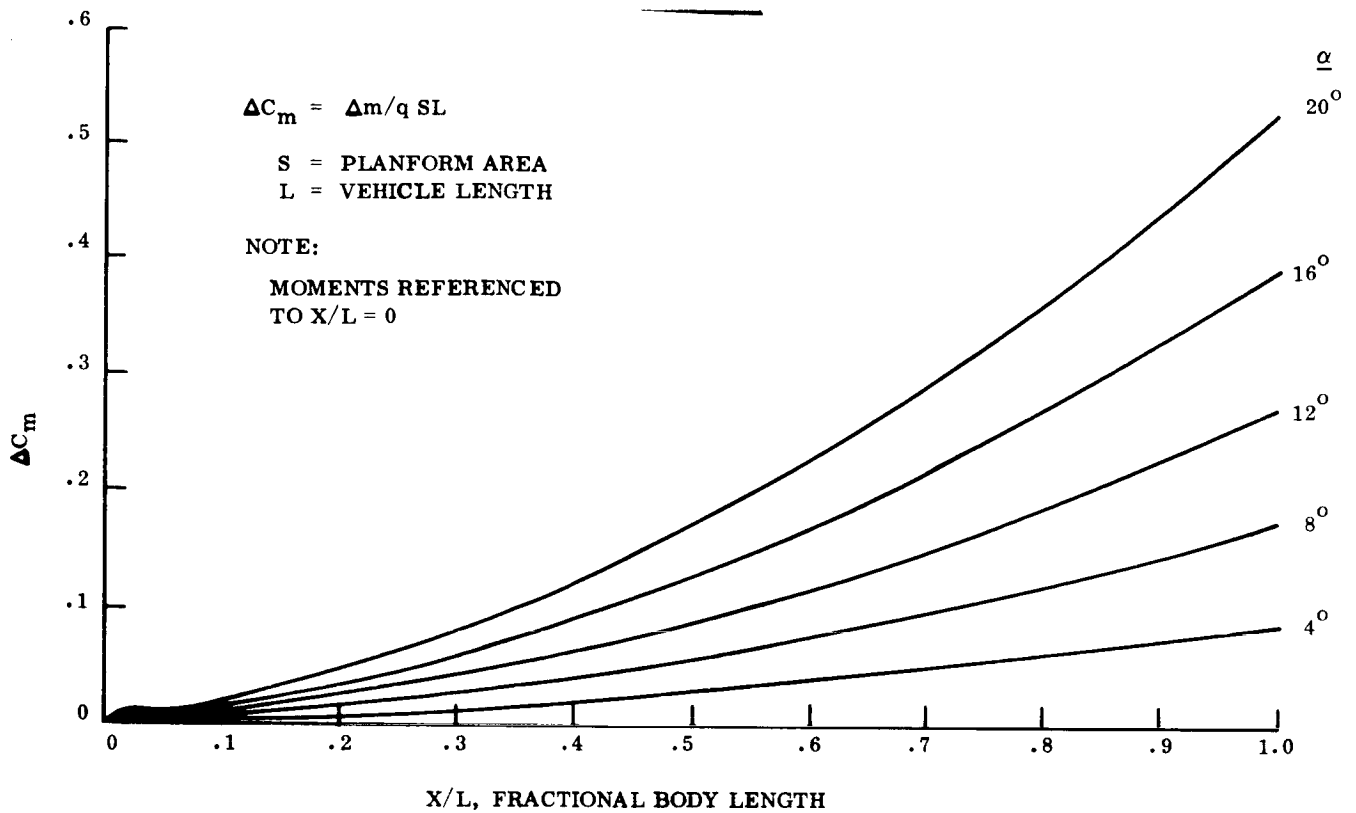


Figure 3.2-66. - Incremental Moment Coefficient Distribution

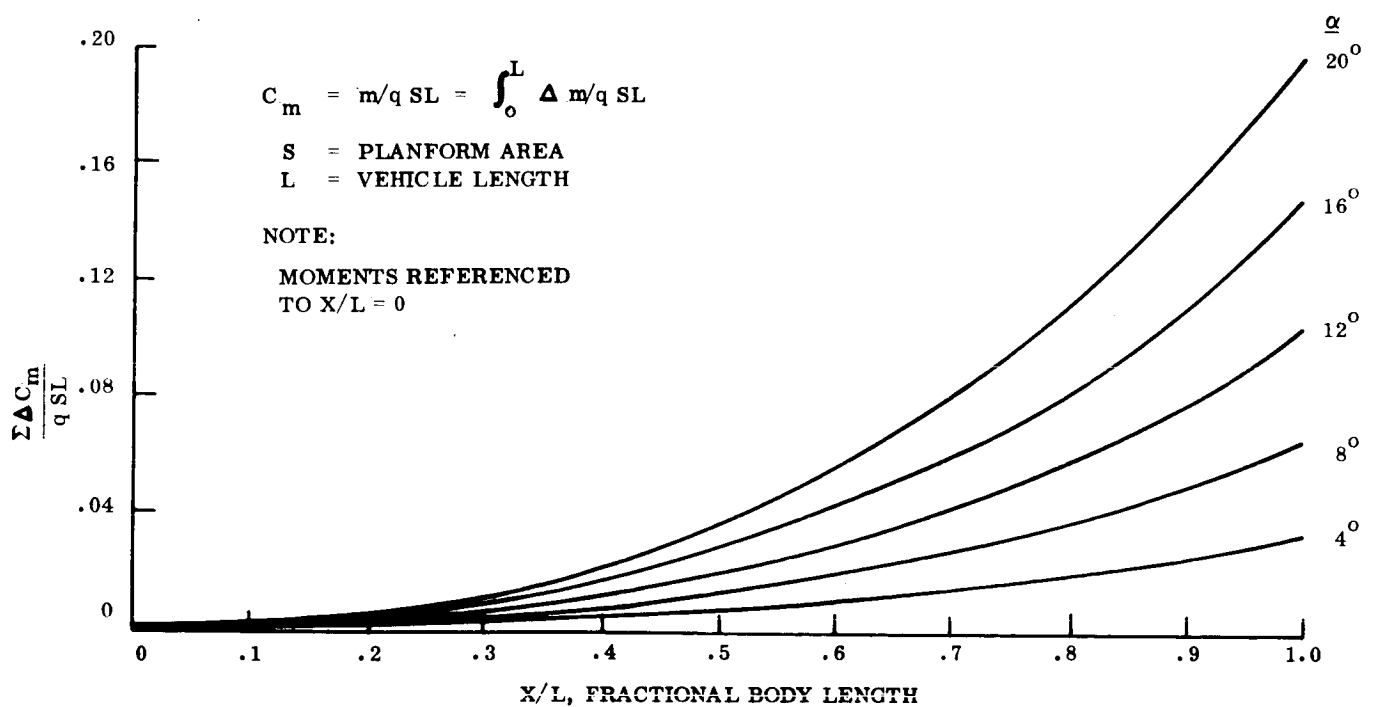


Figure 3.2-67. - Cumulative Moment Coefficient Distribution

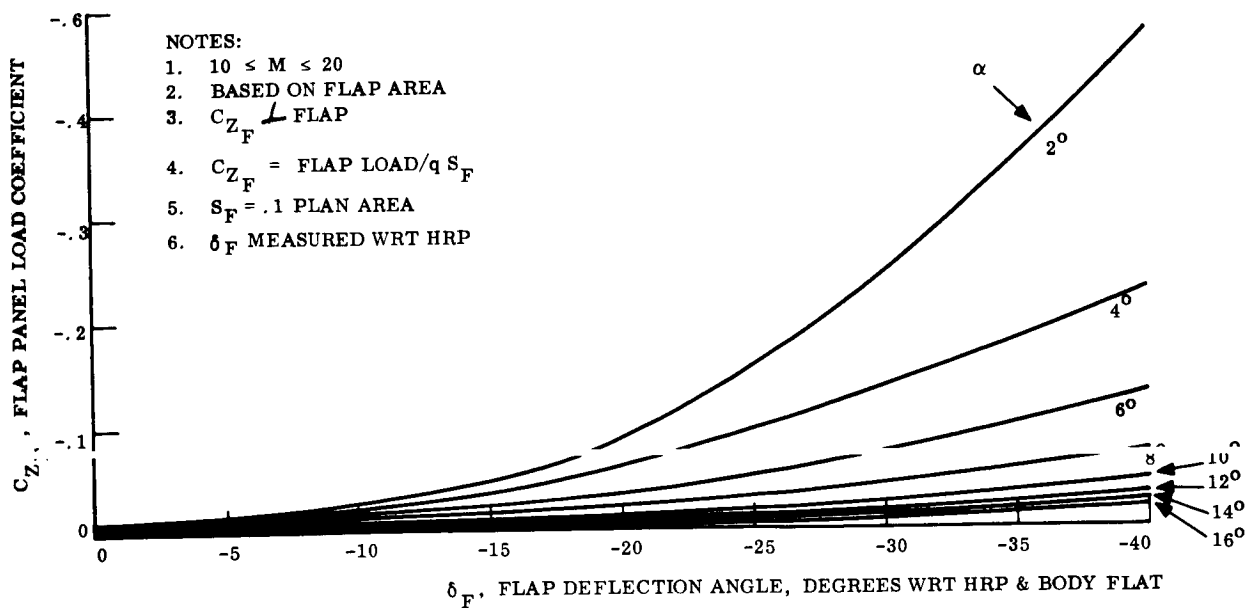


Figure 3.2-68. - Flap Panel Load Coefficient vs Flap Deflection Angle

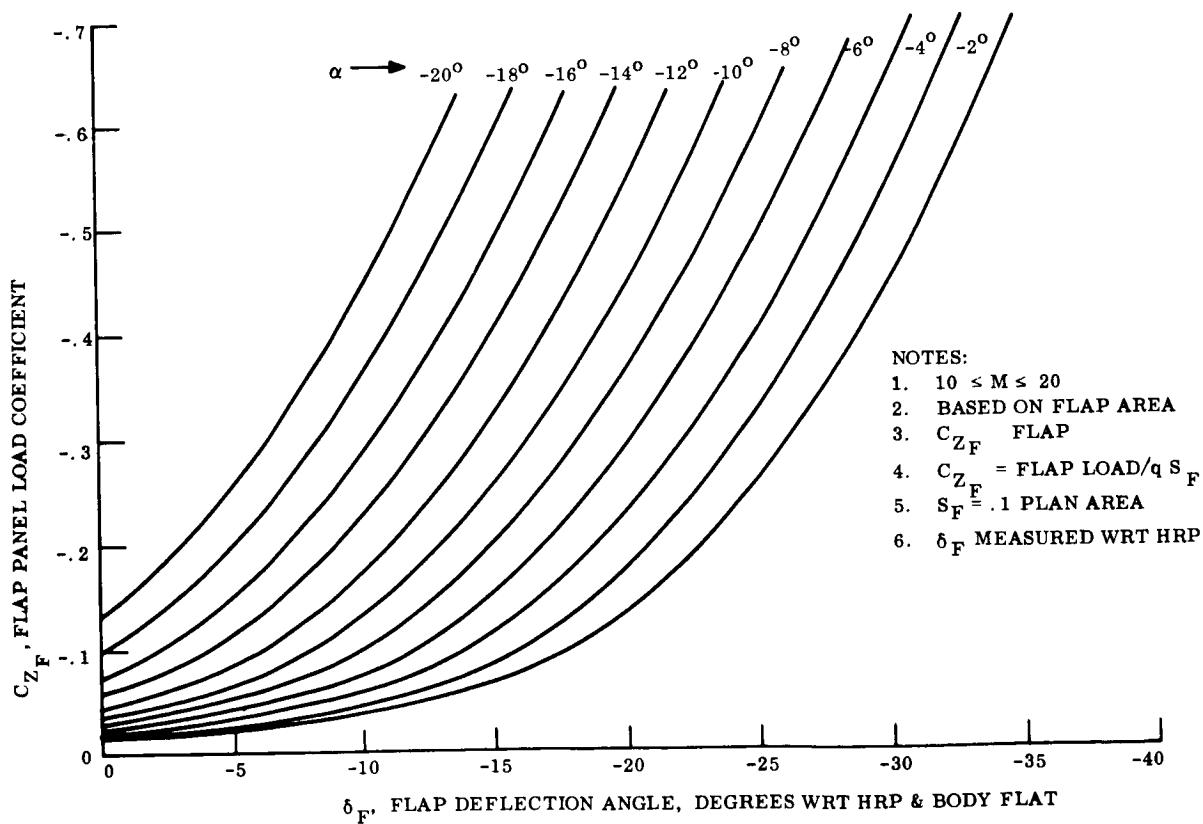


Figure 3.2-69. - Flap Panel Load Coefficient vs Flap Deflection Angle, Negative Angles-of-Attack

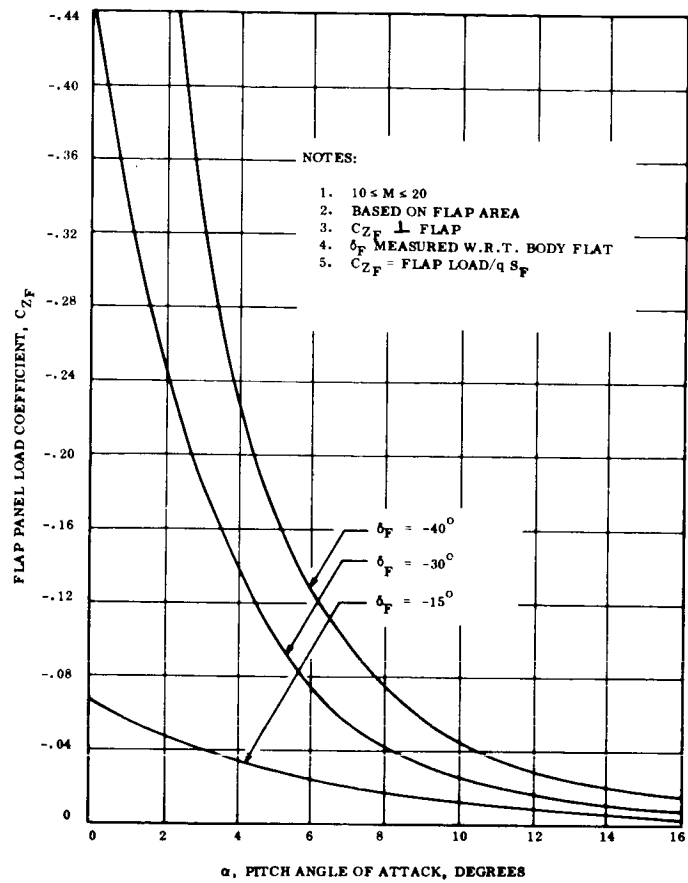


Figure 3.2-70. - Flap Panel Load Coefficient vs Angle-of-Attack

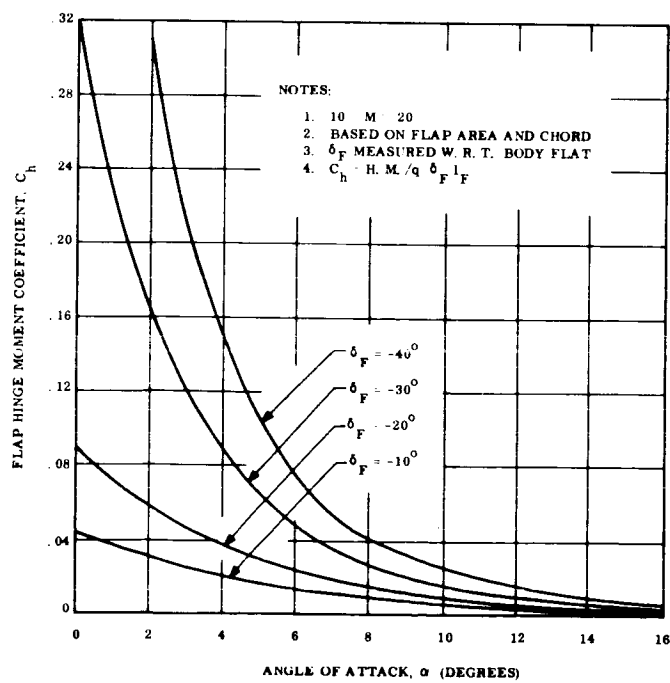


Figure 3.2-71. - Flap Hinge Moment Coefficient vs Angle-of-Attack

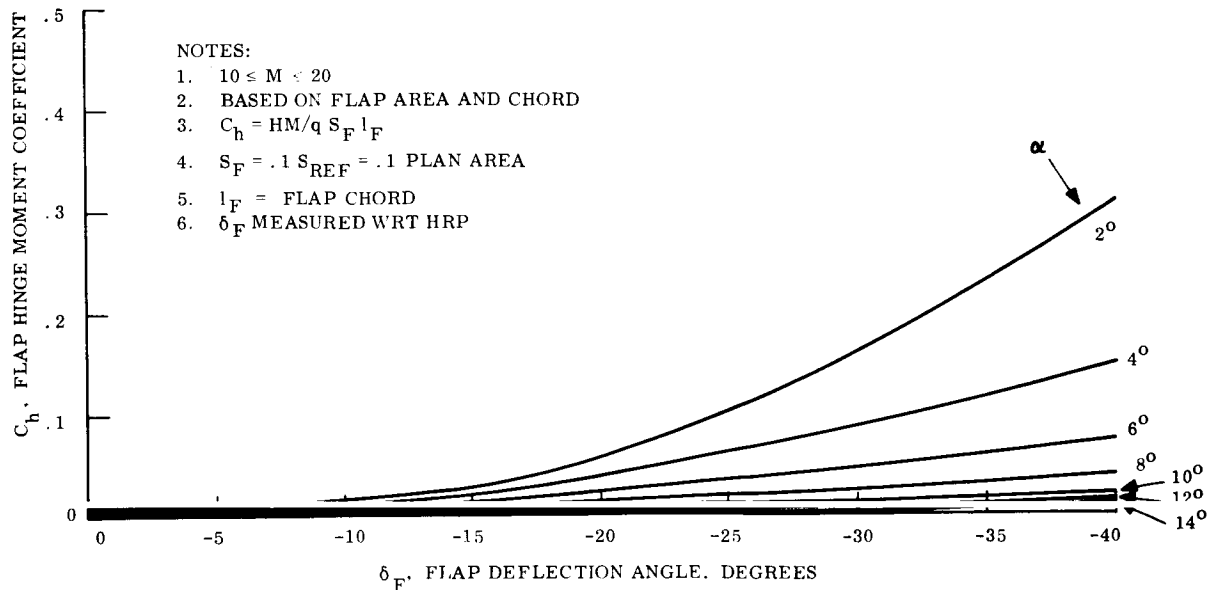


Figure 3.2-72. - Flap Hinge Moment Coefficient vs Flap Deflection Angle

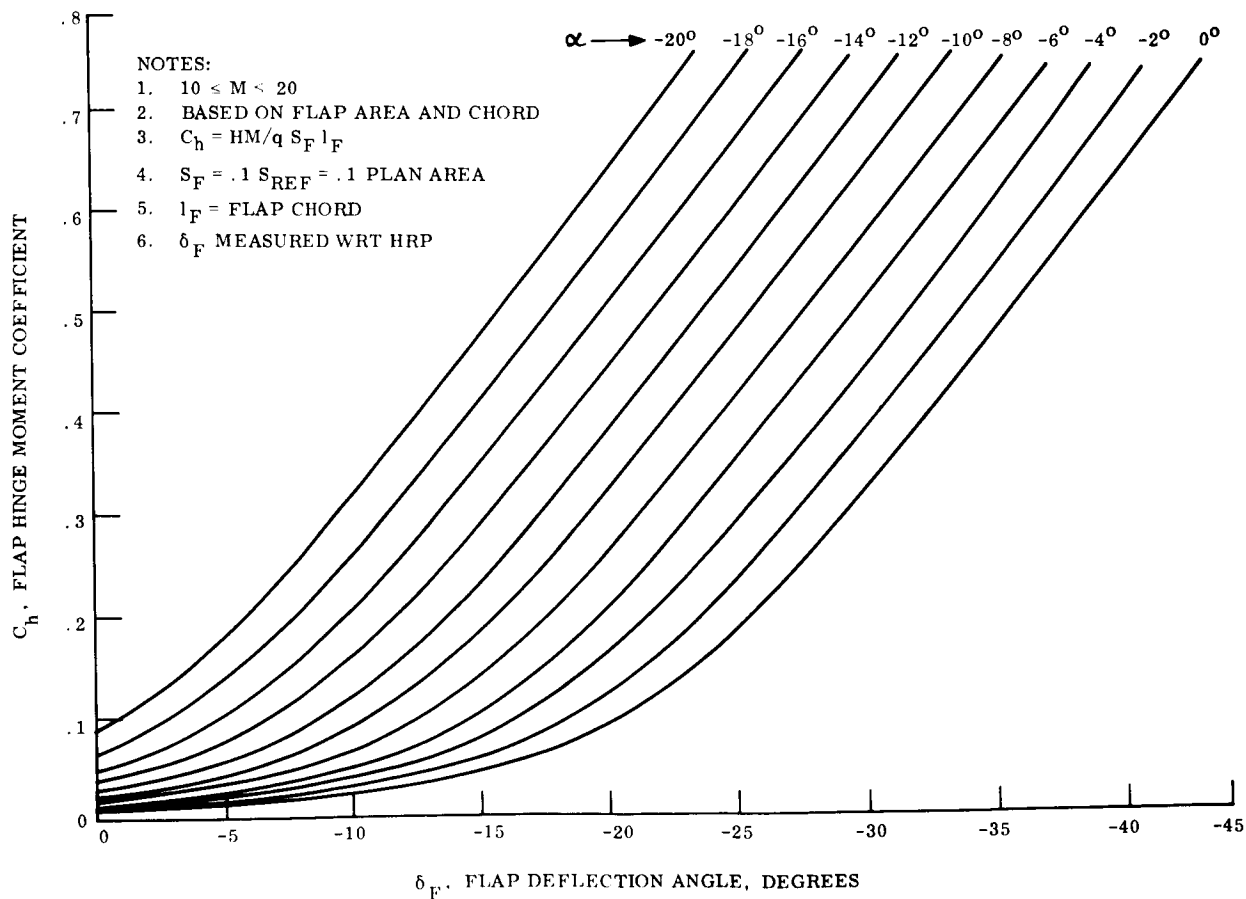


Figure 3.2-73. - Flap Hinge Moment Coefficient vs Flap Deflection Angle, Negative Angles-of-Attack

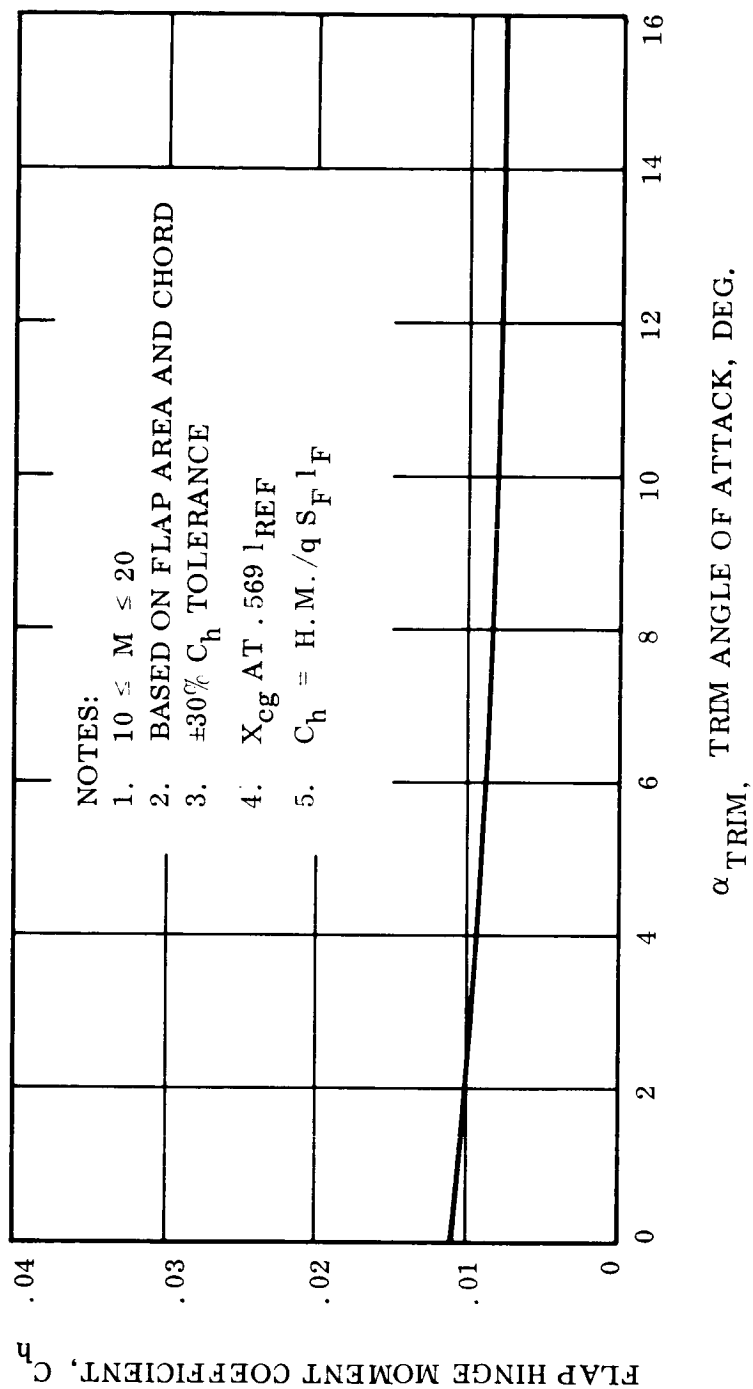


Figure 3.2-74. - Flap Hinge Moment Coefficient Variation with Angle-of-Attack for Trimmed Flight

REFERENCES

- 3.2-1. Dennard, J. S. , and Spencer, P. B. , "Ideal Gas Tables for Oblique-Shock Flow Parameters in Air at Mach Numbers from 1.05 to 12.0", NASA TN D-2221, dated March 1964.
- 3.2-2. Ames Research Staff, "Equations, Tables, and Charts for Compressible Flow", NACA Report 1135, dated 1953 (Supercedes NACA TN 1428).
- 3.2-3. Lewis, C. H. , and Burgess, E. G. III, "Altitude-Velocity Table and Charts for Imperfect Air", Arnold Engineering Development Center Technical Documentary Report No. AEDC-TDR-64-214, dated January 1965.
- 3.2-4. Lees, Lester, "Laminar Heat Transfer Over Blunt-Nosed Bodies at Hypersonic Flight Speeds", Jet Propulsion, April 1956 issue.
- 3.2-5. Burke, G. L. , "Heat Transfer and Pressure Distribution about Sharp and Blunt Elliptic Cones at Angles of Attack and High Mach Numbers", USAF Flight Dynamics Laboratory Report No. AFFDL TR-64-172, dated May 1965.
- 3.2-6. Stivers, L. S. Jr. and Levy, L. L. Jr. , "Longitudinal Force and Moment Data at Mach numbers from 0.60 to 1.40 for a family of Elliptic Cones with Various Semi-apex Angles", NASA TN-1149, dated December 1961.
- 3.2-7. Jorgensen, L. H. , "Elliptic Cones Alone and with Wings at Supersonic Speeds", NACA Report 1376, dated 1958.
- 3.2-8. Flatau, A. , "Low-Speed Wind-Tunnel Study of an Elliptical Cone Glide Shape", U. S. Army Chemical Research and Development Laboratories CRDL Special Publication 1-32, dated October 1961.
- 3.2-9. Spencer, B. Jr. , and Fox, C. H. Jr. , "Hypersonic Aerodynamic Performance of Minimum Wave-Drag Bodies", NASA L-5008, undated.
- 3.2-10. Spencer, B. Jr. , and Phillips, W. P. , "Transonic Aerodynamic Characteristics of a Series of Bodies having Variations in Fineness Ratio and Cross-Section Ellipticity", NASA TN D-2622 dated February 1965.
- 3.2-11. Fournier, R. H. , and Spencer, B. Jr. , "Supersonic Aerodynamic Characteristics of a Series of Related Bodies with Cross-Section Ellipticity", NASA TN D-3539, dated August 1966.
- 3.2-12. Archer, R. D. , Melnik, W. L. , and Herman, R. , "Experimental Pressure and Heat Transfer Distributions on Blunt-Nose Delta Wings for Angles of Attack up to 30° at Mach Number 7", USAF Aerospace Research Laboratory Report No. ARL 63-231, dated December 1963.

3.3 FLIGHT DYNAMICS STUDIES

3.3.1 TRAJECTORY STUDIES

3.3.1.1 Powered flight. - The three stage Scout booster was determined to be adequate to supply the necessary re-entry velocity for the SLAMAST vehicle. To establish the feasibility of the three stage Scout, several powered flight trajectories were generated as a supplement to the Scout boost trajectories supplied by NASA/LRC. This work indicates that the Scout has ample capability and flexibility to provide the re-entry conditions and separation altitude required by the SLAMAST system. For this study, separation was defined to occur nominally at 400,000 ft., and trajectories were generated which achieved the desired burnout altitude as well as the desired re-entry conditions. Table 3.3-1 presents a tabulation of the pertinent trajectory parameters. The runs consist of a "nominal" shallow re-entry and three variations on boost variables to determine re-entry sensitivity for this type of boost profile. Range at re-entry is very sensitive to these boost phase variations and must be considered as a prime parameter in the choice of the boost trajectory from the standpoint of tracking, range safety, and recovery. Path angle is moderately sensitive, while re-entry velocity is quite insensitive. The effect of path angle perturbations on the re-entry trajectory can be desensitized through the use of the flight path control system, and thereby becomes a less prominent effect on the choice of boost trajectory.

3.3.1.2 Re-entry conditions. - Re-entry trajectories were generated for a range of $W/C_L S$ from 150 to 250, re-entry velocities from 15,000 to 25,000 fps, and re-entry path angles from -1.0 to -5.0 degrees in order to supply parametric data for trade-off purposes and to yield the sensitivities of trajectory parameters to the vehicle characteristics and re-entry conditions. The maneuvers are pullouts to constant altitude, in-plane flight using pitch modulation only (zero bank). The maneuvers consist of three phases:

(1) Pullout. - A constant angle of attack providing the specified $W/C_L S$ is maintained from re-entry (400 K feet) until a pullout to horizontal flight is achieved.

(2) Horizontal flight. - The angle of attack is modulated to provide the lift necessary for horizontal flight. The angle of attack increases as the dynamic pressure decreases until the angle of attack for the specified $W/C_L S$ is attained.

(3) Terminal glide. - The angle of attack is held constant and the vehicle glides to impact.

These trajectories were generated for parametric investigation of vehicle environment only and do not incorporate the recovery phase of the SLAMAST mission. Figures 3.3-1 through 3.3-3 show stagnation heating profiles for the 25,000 fps re-entry cases. Figure 3.3-4 shows peak stagnation heating as a function of re-entry path angle, re-entry velocity, and $W/C_L S$. For the high re-entry velocity (25,000 fps) the peak stagnation heating is a strong function of both re-entry path angle and $W/C_L S$ during pullout. For a range of re-entry angle from -1.0 deg. to -5.0 deg., the peak stagnation heating more than doubles, while a range of $W/C_L S$ from 200 to 100 results

TABLE 3.3-1. - PERTINENT TRAJECTORY TABULATIONS

$\dot{\Gamma}_2$ (deg/sec)	Γ_3 (deg)	t_B (sec)	Re-entry range (n. m.)	Re-entry path angle (deg)	$t_E - t_{BO}$ (sec)	Re-entry velocity (fps)	3rd Stage burnout alt. (K ft)
1 -.874	0	200	760	-1.48	127	22754	420
2 -.874	0	200	984	-2.16	189	22741	440
3 -.874	1.0	200	951	-1.85	179	22756	423
4 -.874	0	205	674	-1.36	101	22754	420

$\dot{\Gamma}_2$ = thrust attitude rate during second stage burn

$\dot{\Gamma}_3$ = thrust attitude during third stage burn

t_B = time at start of third stage burn

$t_E - t_{BO}$ = time from third stage burnout to re-entry (400 K feet)

in a peak stagnation heating increase of about 50%. As the re-entry velocity is lowered, however, the peak stagnation heating becomes virtually independent of re-entry path angle. These lower velocities produce a substantially beneficial effect when consideration is given to the path angle dispersions at re-entry that are caused by the boost phase of flight.

3.3.2 DESIGN TRAJECTORIES

The two bounding re-entry trajectories selected for design purposes are pullouts to constant altitude flight for re-entry conditions of $V_0 = 20,000$ fps. and re-entry path angles of 1 and 10 degrees, respectively. These bounds were chosen to obtain a long time thermal soak trajectory for environment simulation (shallow re-entry) and a shorter time, high "g" trajectory to simulate the loading during an abort trajectory (steep re-entry). The pullout angle of attack is 16 degrees. The constant altitude flight is achieved by modulating the angle of attack while holding a zero roll angle. At 700 seconds from re-entry (400 K feet) a drag brake is deployed on the bottom of the vehicle and the pitch flap is deployed to trim the vehicle to a zero lift, high drag condition. The vehicle then performs a ballistic flight down to approximately 25 K feet where the recovery subsystem sequence is initiated with the deployment of a FIST chute. The trajectories were generated using the TRICOP digital simulation of three-degree-of-freedom motion assuming instantaneous trim. The pertinent trajectory parameters are presented in Figures 3.3-5 through 3.3-12. The experiment trajectories are not necessarily confined to horizontal flight but will consist of a pullout to some shallow path angle, either negative or positive, which is required to provide the desired environment history. The re-entry path angle and pullout angle of attack may also be varied for the experiment trajectories, subject to the design constraints.

3.3.3 FOOTPRINT STUDIES

Range safety footprints have been generated for the two design re-entry conditions. These footprints are obtained considering a system malfunction which results in trim to maximum L/D and a fixed roll angle. The footprints comprise Figures 3.3-13 through 3.3-16. The first two footprints correspond to failure at re-entry, while the second two consider failure at 350 seconds from re-entry. The total footprints are extremely large and only 1,200 seconds of flight are shown, since this is the area of concern in the discussion of range safety requirements. The range safety problem is primarily a cross range problem since large downranges can be tolerated and a terminate on time criterion would be sufficient for downrange considerations. A few relatively simple criteria for termination of flight would be sufficient to reduce the footprint to tolerable dimensions. Such termination could be achieved by any of several means such as a 180 degree bank, deactivation of the roll control system to allow spin-up, a commanded spin up with the roll control nozzles, or explosive destruct. The method of flight termination will be chosen to maximize the data recovery probability in the event of a malfunction. The obvious flight termination criterion of time can be used to eliminate a large part of the footprint. For example, if the flight is terminated when the drag brake deployment signal is not sensed by 800 seconds from re-entry (nominal time of deployment plus 100 seconds), the downrange problem is eliminated and some crossrange is eliminated (see Figure 3.3-17). The maximum crossrange

for re-entry failure is still about 1,000 n.mi., however. If a limit on the product of bank angle and time is imposed, the maximum crossrange can be reduced to an acceptable amount. For example, Figure 3.3-17 shows that a limit of 10,500 deg-sec limits the crossrange to 240 n.mi. The two termination criteria together reduce the footprint to the crosshatched area of Figure 3.3-17. Of course, the second criterion is useless if roll reference is lost and a back-up system would probably be necessary.

3.3.4 RECOVERY ENVELOPE

The recovery footprint for nominal tolerances on the primary trajectory influencing variables has been investigated. A $\pm 10\%$ 1σ variation on atmospheric density was assumed for the computation of range uncertainty. The nominal roll reference drift and the yaw angle due to the center of gravity tolerance were considered for the crossrange uncertainty. Under the assumption of independence of these variables the 3σ impact ellipse has a semi-major axis in the range direction of 450 n.mi. and a semi-minor axis in the crossrange direction of 44 n.mi. The compensating effect of control system #2 described in Section 4.1 however, reduces the 3σ range error to ± 170 n.mi. However, the control system mean roll error increases the 3σ crossrange error to ± 110 n.mi. The resulting 3σ recovery area is therefore ± 170 n.mi. in the range direction and ± 110 n.mi. in crossrange.

The deployment conditions for the recovery chute are quite insensitive to the trajectory flown, provided the drag brake deployment functions in a near nominal fashion. For the zero-lift, high drag condition of SLAMAST with a deployed brake flap, the trajectories approach a terminal flight condition at low altitudes and this terminal flight is independent of the prior trajectory history. The conditions at minimum dynamic pressure for a 30 deg flap deployment are:

$$q^* = 200 \text{ psf}$$

$$h = 41,000 \text{ ft.}$$

$$\text{Mach} = 0.88$$

3.3.5 TIP-OFF RATE TOLERANCES

A six degree-of-freedom simulation of the exospheric motion of the SLAMAST vehicle following booster separation was performed in order to define the expected tolerances in angle of attack and body rates at re-entry. The cold gas system defined in paragraph 4.1.1.2 having a dead band of 5° and a transport lag of 0.03 seconds for all three channels was used for this analysis. Initial conditions for body angular rates have been assumed to be $2^\circ/\text{sec}$ about all three axes; these values are typical of the 3σ separation rates obtained from the three-stage Scout-Re-entry F analyses.

Following separation, a one (1) second coast period was assumed prior to initiation of the controller in order to obtain an error signal composed of both angle and rate. This time period is not critical to the successful operation of the controller but should be low enough such that large angular errors are not attained. It has been tacitly

assumed that the platform axes at separation are aligned in such a fashion that the platform longitudinal axis lies along the re-entry velocity vector. Thus, a pitch command value of 14° has been applied to the controller in order that, at re-entry, with the pitch flap deployed at 30° , an aerodynamic trim condition prevails.

Figure 3.3-18 represents a view of the vehicle longitudinal axis angular deviations from an inertially fixed frame. In this figure, the vehicle pitch axis has been commanded to an angle of 14° . The vehicle axis rises from its initial condition, (zero angle and $2^{\circ}/\text{sec}$ about the pitch and yaw axes) until acquired, at which time both axes enter their limit cycle with a deadband of 5° . The motion is completely controlled during all phases of operation. Figures 3.3-19 through 3.3-21 show the phase plane motion of the vehicle about all three axes, which indicate both acquisition and limit cycle operation. Utilizing this data, the re-entry condition tolerances have been tabulated in Table 3.3-2.

3.3.6 VEHICLE INERTIA CHARACTERISTIC TOLERANCES

The effects of products of inertia tolerances on the exospheric motion was investigated in order to determine acceptable values. A principal axis tilt of 0.1 degrees was assumed about each axis, corresponding to a maximum dynamic unbalance of 3,300 oz-in². The results indicate that these values have virtually no effect on the exospheric controller performance.

Since the present system design is launched from the non-spinning 3 stage Scout launch vehicle, spacecraft despin analyses were not performed.

TABLE 3.3-2. -RE-ENTRY CONDITION TOLERANCES

Channel Error	Roll		Pitch		Yaw	
Angle (deg)	± 5	± 5	± 5	± 5	± 5	± 5
Rate (deg/sec)	2.1	-5.8	.7	-.5	.3	-.35

3.3.7 RE-ENTRY DYNAMICS

A six-degree-of-freedom simulation of the atmospheric motion of the SLAMAST vehicle during re-entry and pullout was performed in order to define the complete operation of the vehicle system. In order that the analysis produce characteristics which might severely affect the flight, only those items which are considered to be of prime importance to the vehicle behavior were considered.

The successful operation of a maneuvering vehicle necessitates adequate roll control in regions of high normal loading, primarily the pullout phase. It is during this phase of flight that the normal loading, coupled with a lateral center of

gravity offset, produce the maximum external roll torque which must be successfully countered by the roll control system. Since the pullout altitude is a function of the vehicle bank angle, the trajectory is unstable from the point of view of roll angle and could not perform a pullout maneuver if the roll control is inadequate. While design analyses are based on this fact, a simulation brings out effects which are generally not included in the preliminary design cycle; aerodynamic coupling effects caused by dynamic motion is an example of unaccounted for-torques.

The trajectory shown is one in which a lateral center of gravity offset of 0.02 inch was applied to the system along with an initial angle-of-attack error (from the desired trim value) of 1.0 degrees. The trajectory is shown in Figure 3.3-22, which indicates a successful pullout and a slight climb thereafter. Since the flight path control was not completely tuned to a constant altitude flight, the perturbation in altitude was not unexpected. The angle-of-attack history, shown in Figure 3.3-23, exhibits a well-damped oscillation in attempting to reach the required trim value prior to pullout. At pullout (90 seconds), the flap backs off in order to reduce the angle of attack such that a skip-type flight is not obtained. The angle-of-attack motion exhibits rapid reduction due to flap reduction followed by a damped oscillation as the flap moves slowly upward to maintain virtually constant altitude.

Figure 3.3-24 shows the bank angle history throughout re-entry with the cold gas system in operation at a 5 degree deadband. The initial oscillation in bank angle is caused by the roll torque produced by aerodynamic coupling through the torque produced by sideslip oscillations. As the lateral motion becomes damped, the vehicle assumes a biased roll angle which is caused by the roll torque produced by vehicle normal g's and a lateral center of gravity offset of 0.02 inch. Following pullout (90 seconds), the reduction in normal g's causes the roll angle limit cycle to increase as shown. This limit cycle is biased in the positive direction which is produced by the nominal one 'g' flight required to fly constant altitude, and the sideslip oscillations attendant to the coupling caused by the angle-of-attack change. The bank angle motion, viewed in toto, while cyclic nature, has been adequately controlled by the cold gas system.

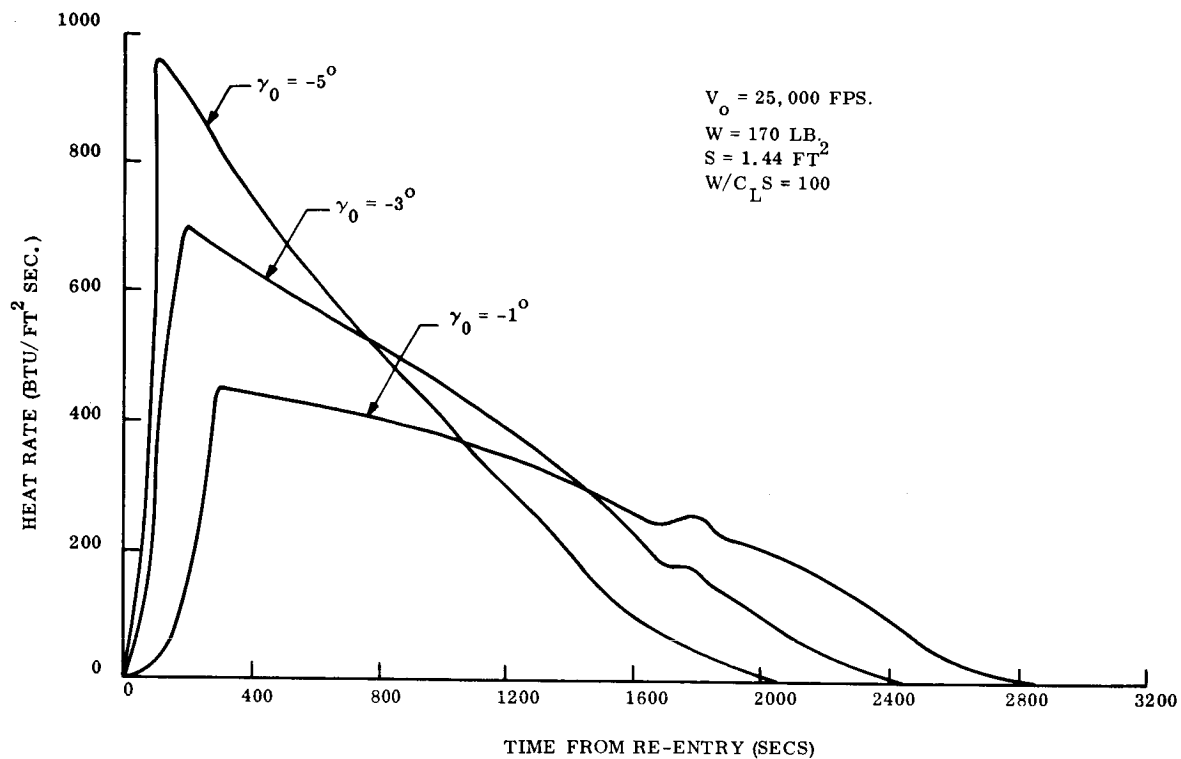


Figure 3.3-1. - SLAMAST Stagnation Heating, $\alpha_o = 25.3^\circ$

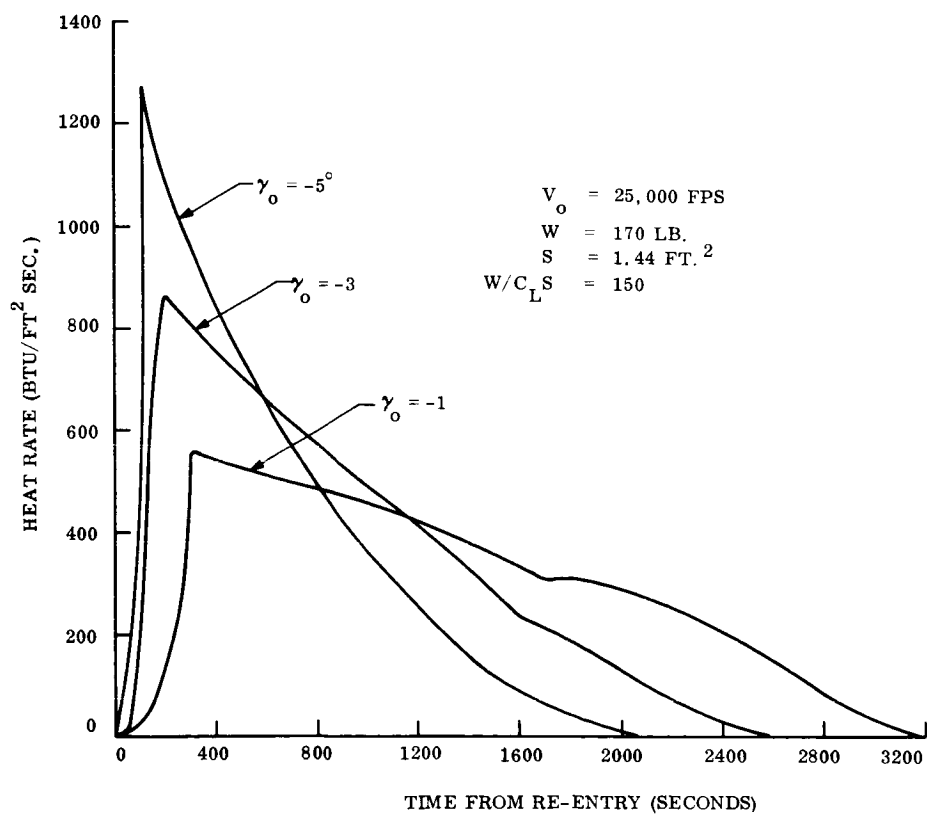


Figure 3.3-2. - SLAMAST Stagnation Heating, $\alpha_o = 17.9^\circ$

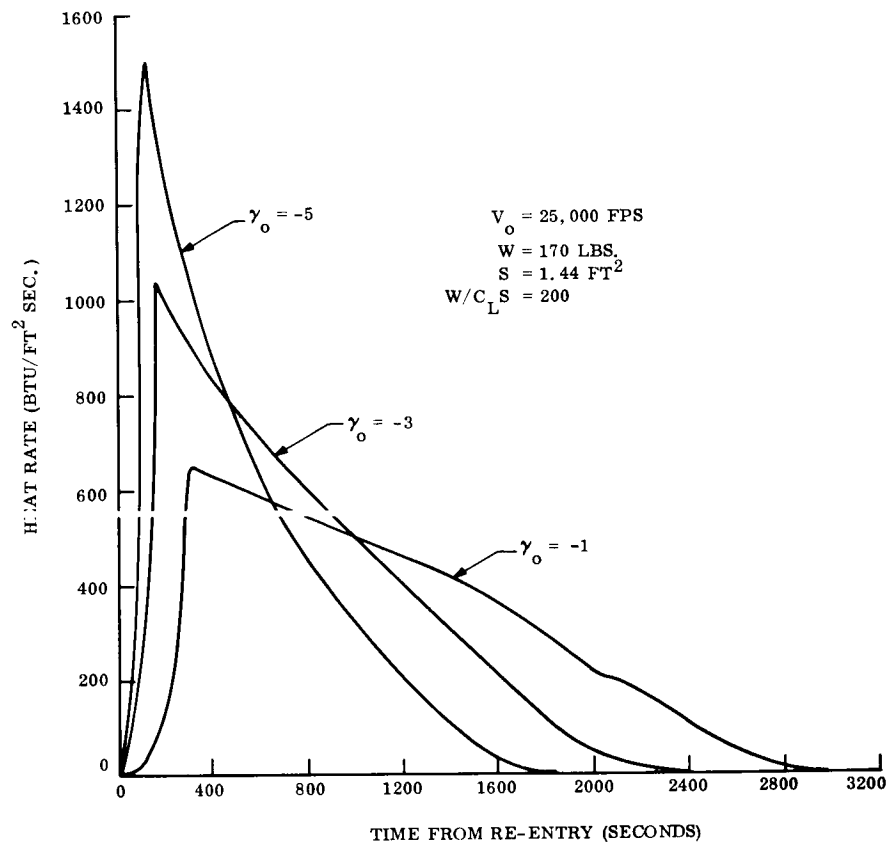


Figure 3.3-3. - SLAMAST Stagnation Heating, $\alpha_o = 13.9^\circ$

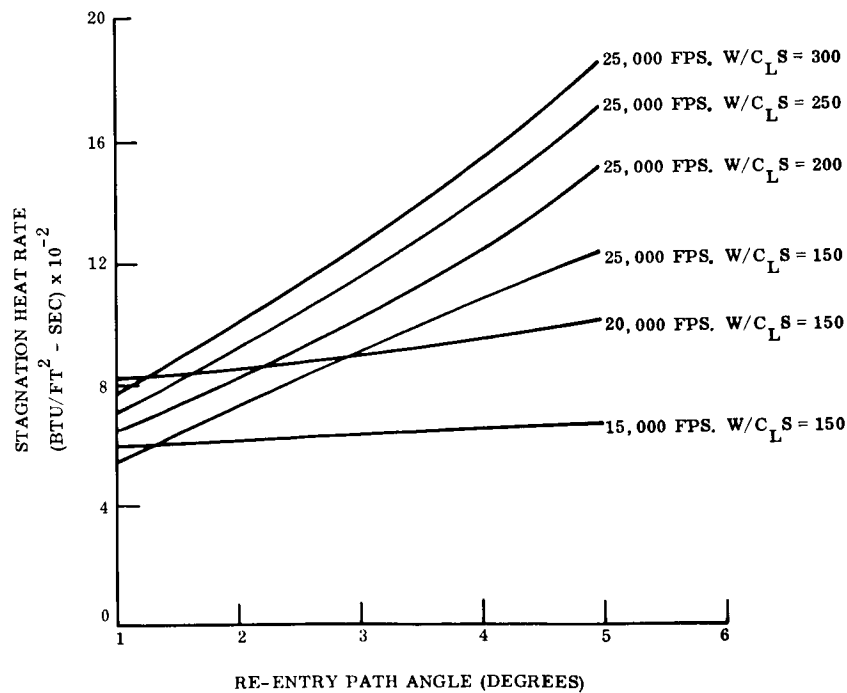


Figure 3.3-4. - SLAMAST Maximum Stagnation Heat Rate

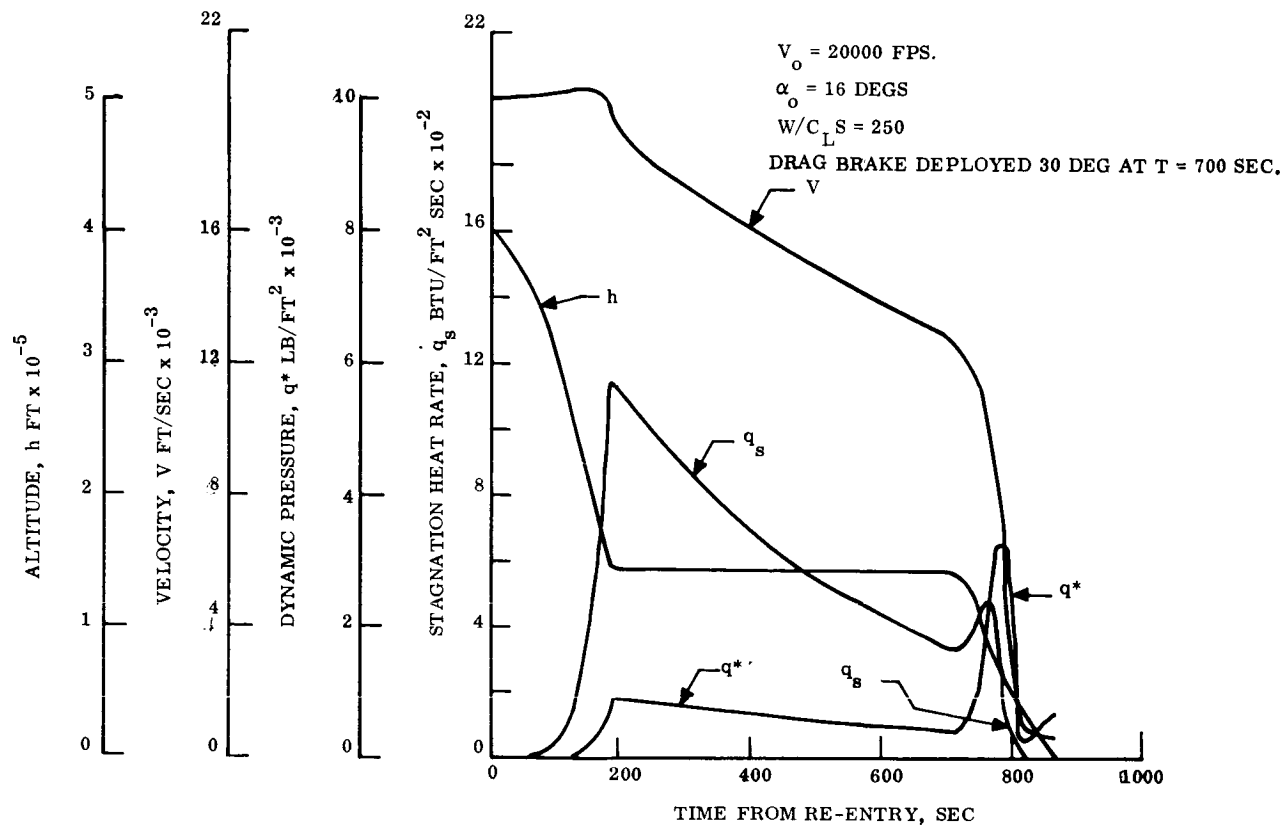


Figure 3.3-5. - SLAMAST Re-entry, $\gamma_o = -1^\circ$

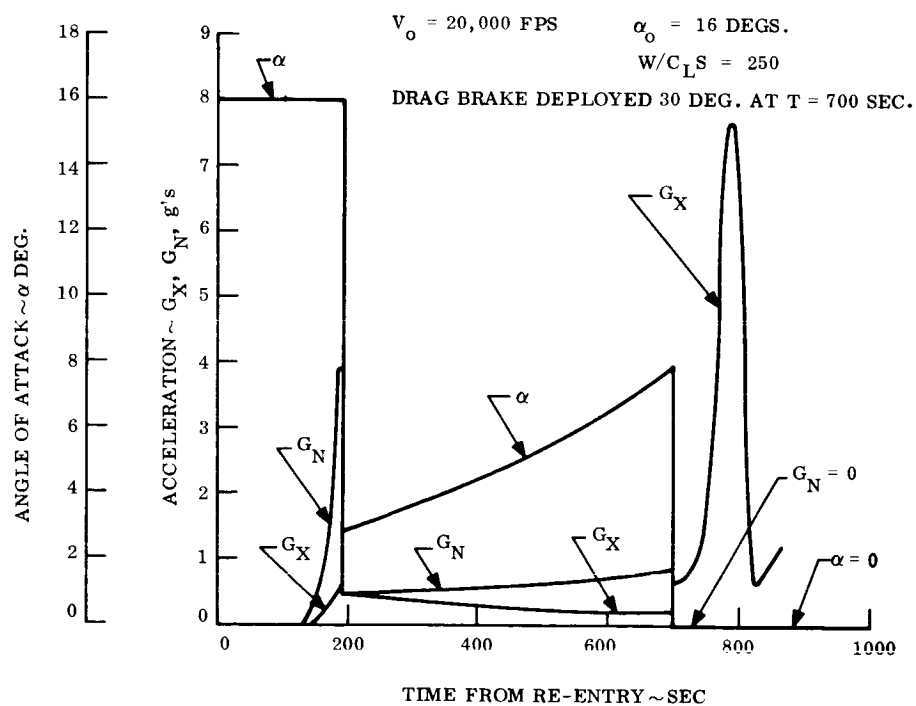


Figure 3.3-6. - SLAMAST Re-entry, $\gamma_o = -1^\circ$

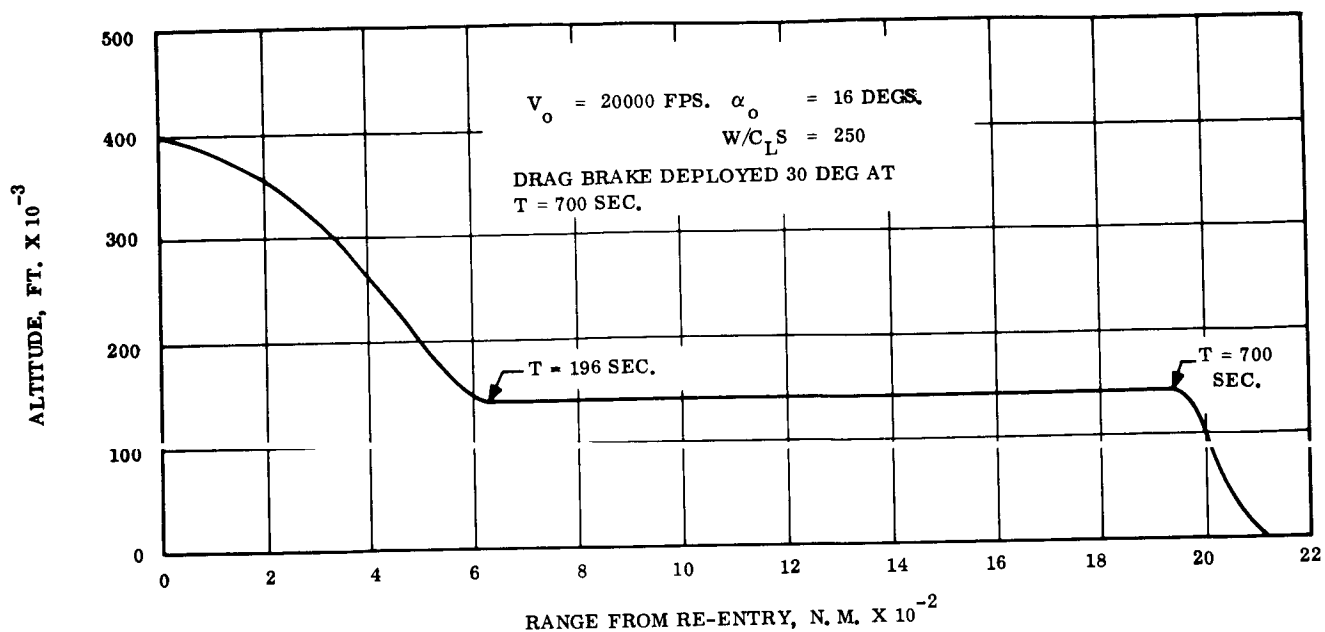


Figure 3.3-7. - SLAMAST Re-entry, $\gamma_o = -1^\circ$

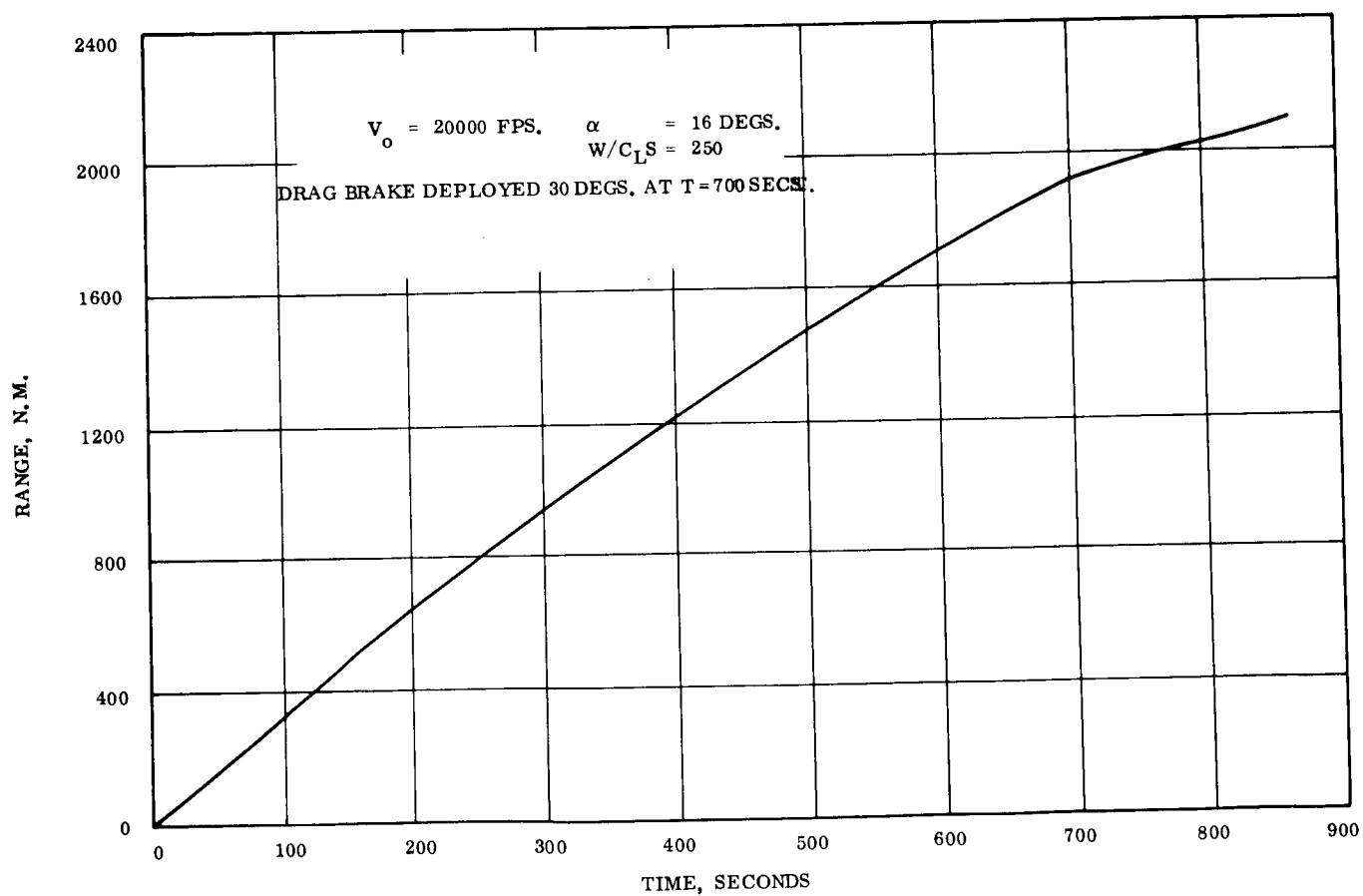


Figure 3.3-8. - SLAMAST Re-entry, $\gamma_o = -1^\circ$

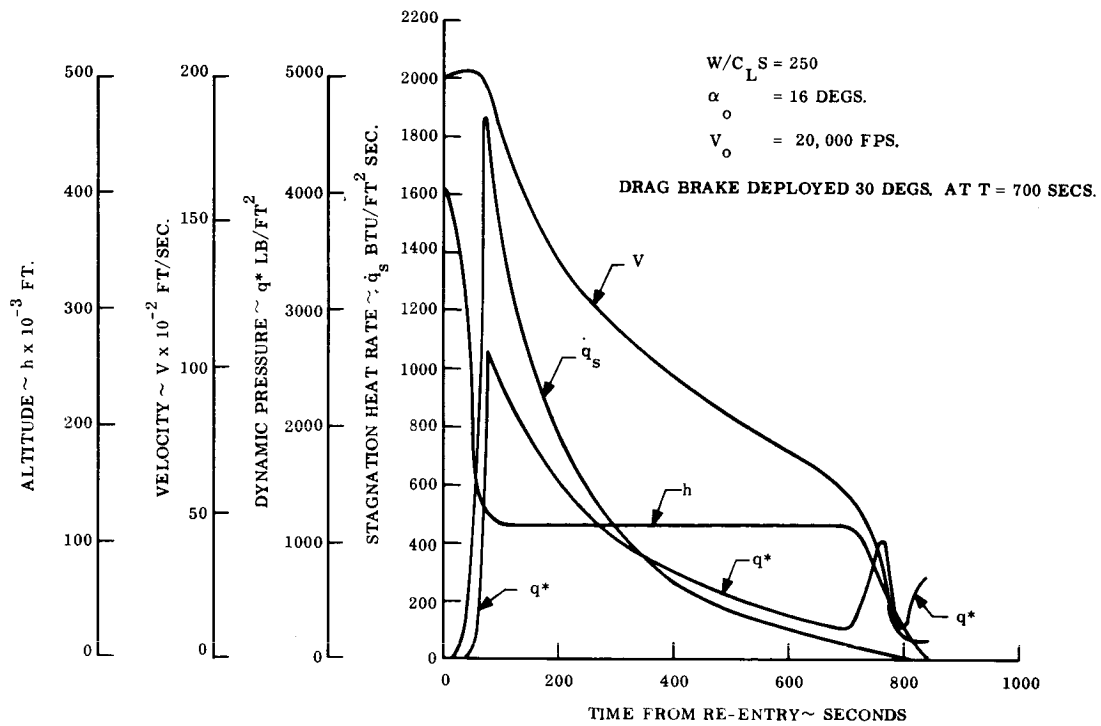


Figure 3.3-9. SLAMAST Re-entry, $\gamma_o = -10^\circ$

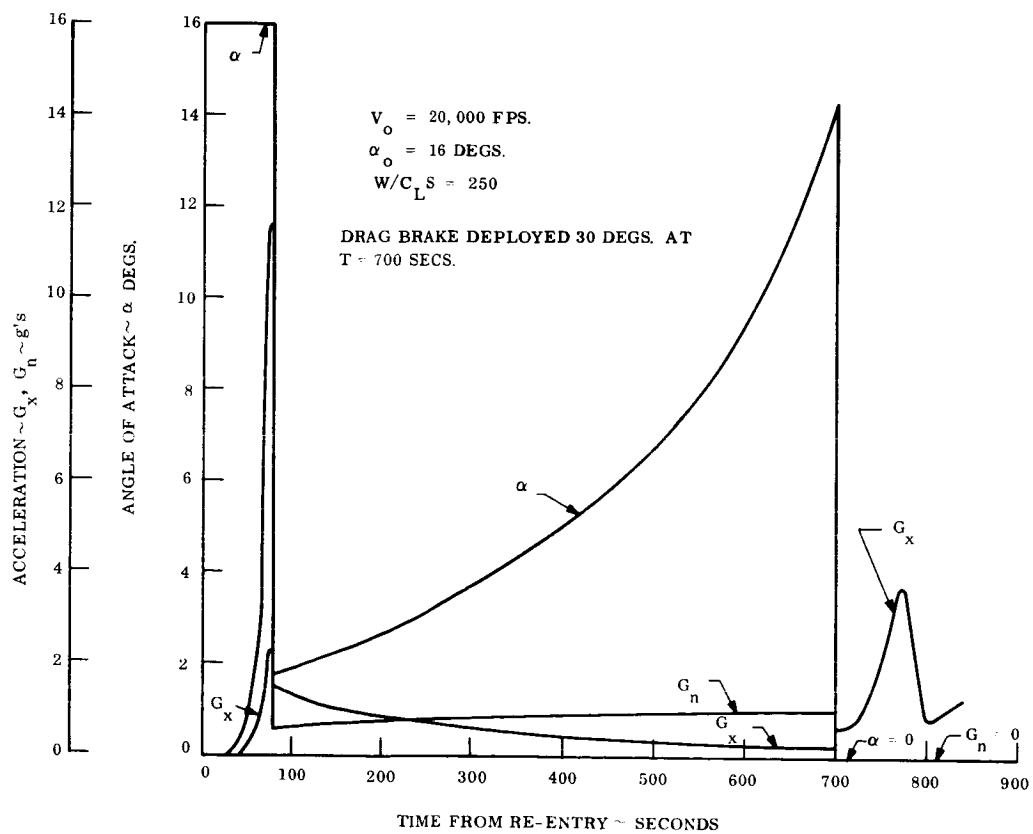


Figure 3.3-10. - SLAMAST Re-entry, $\gamma_o = -10^\circ$

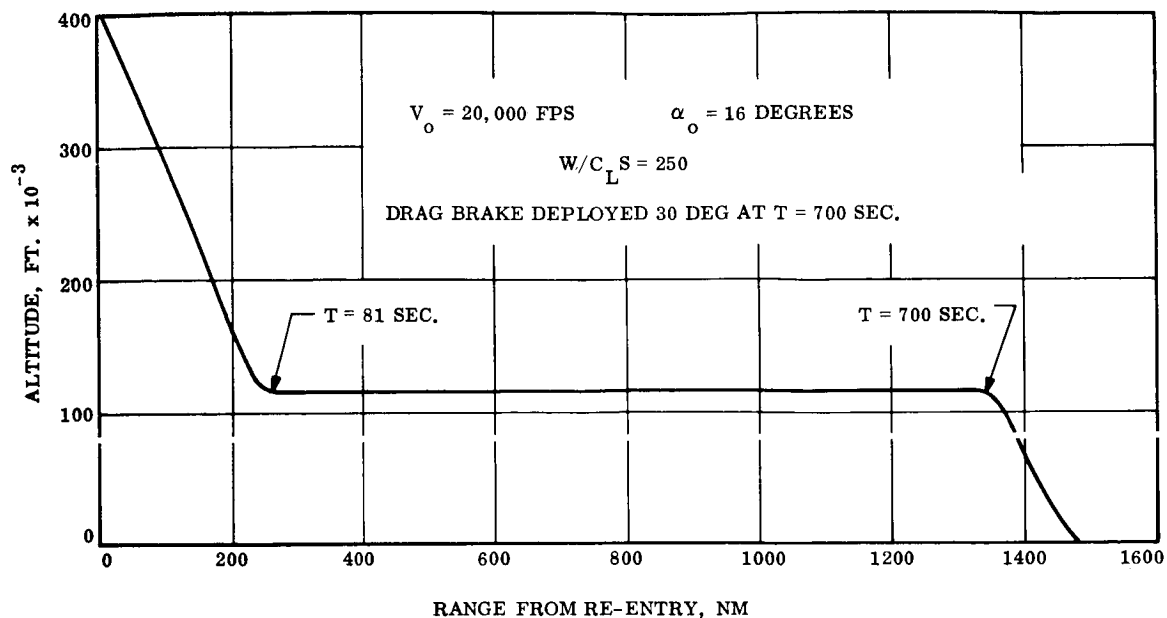


Figure 3.3-11. - SLAMAST Re-entry, $\gamma_o = -10^\circ$

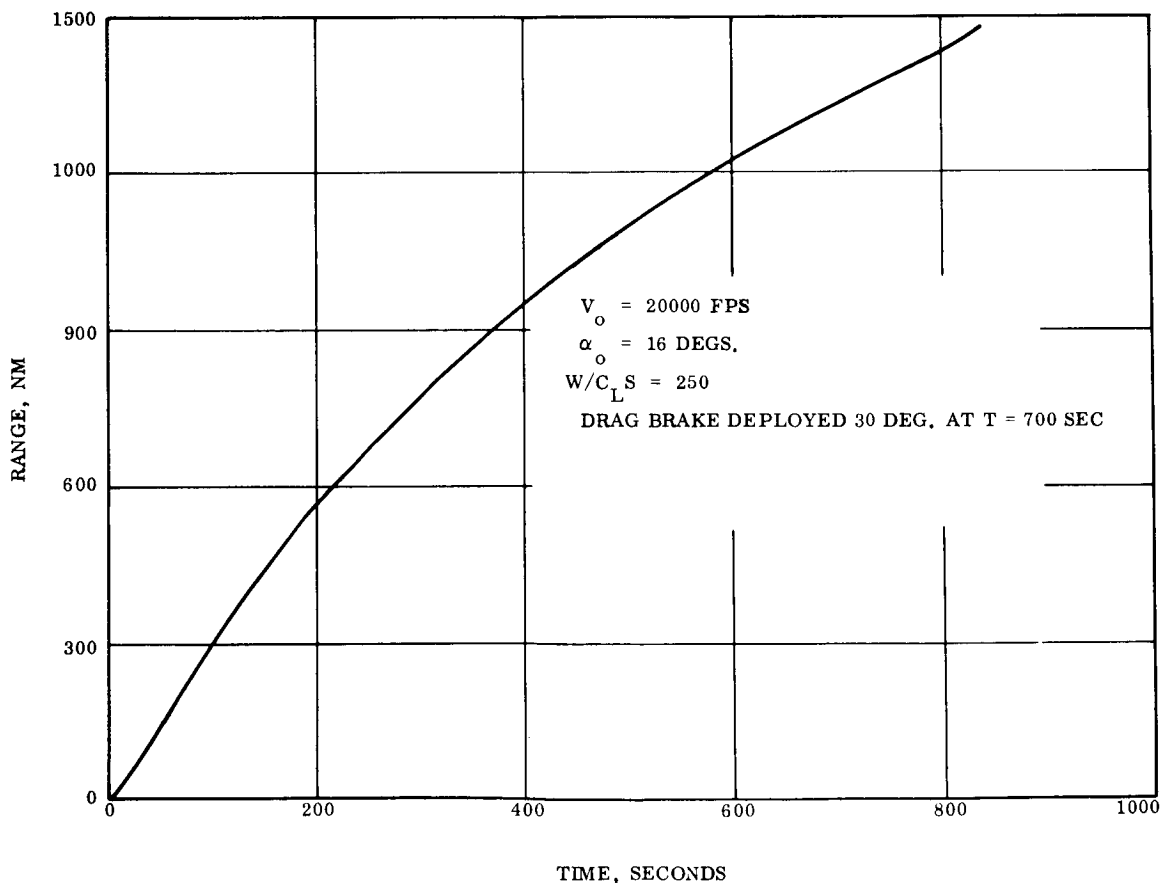


Figure 3.3-12. SLAMAST Re-entry, $\gamma_o = -10^\circ$

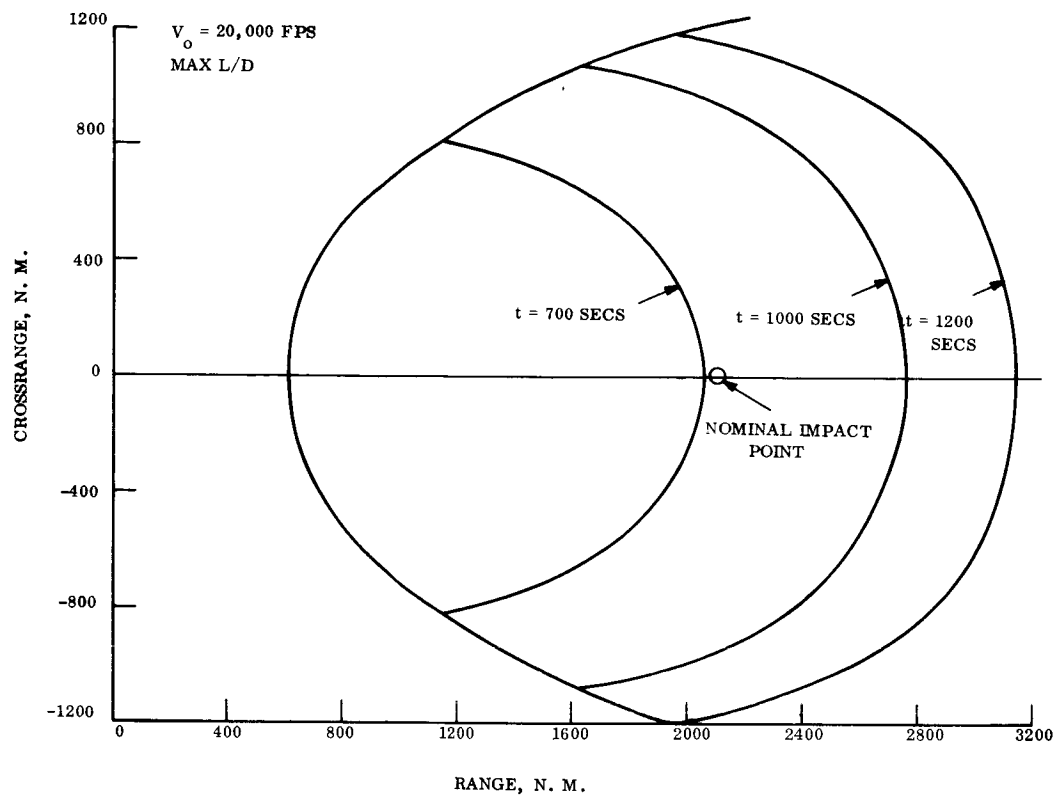


Figure 3.3-13. - SLAMAST Range Safety Footprint, $\gamma_0 = -1^\circ$, Failure at Re-entry

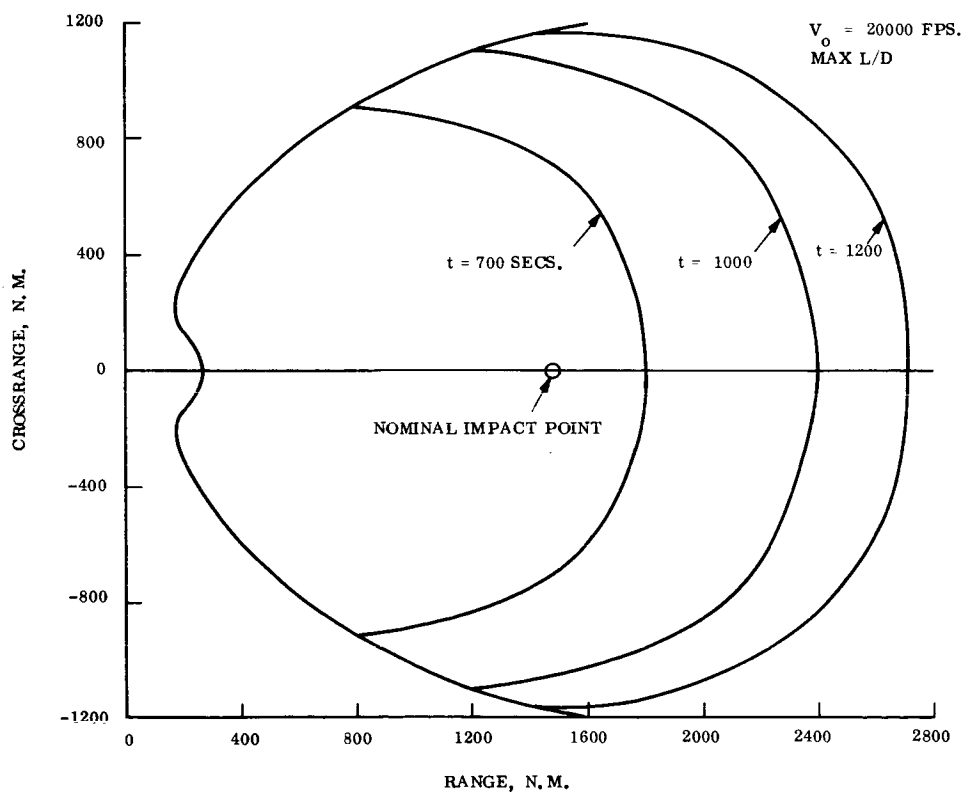


Figure 3.3-14. SLAMAST Range Safety Footprint, $\gamma_0 = -10^\circ$, Failure at Re-entry

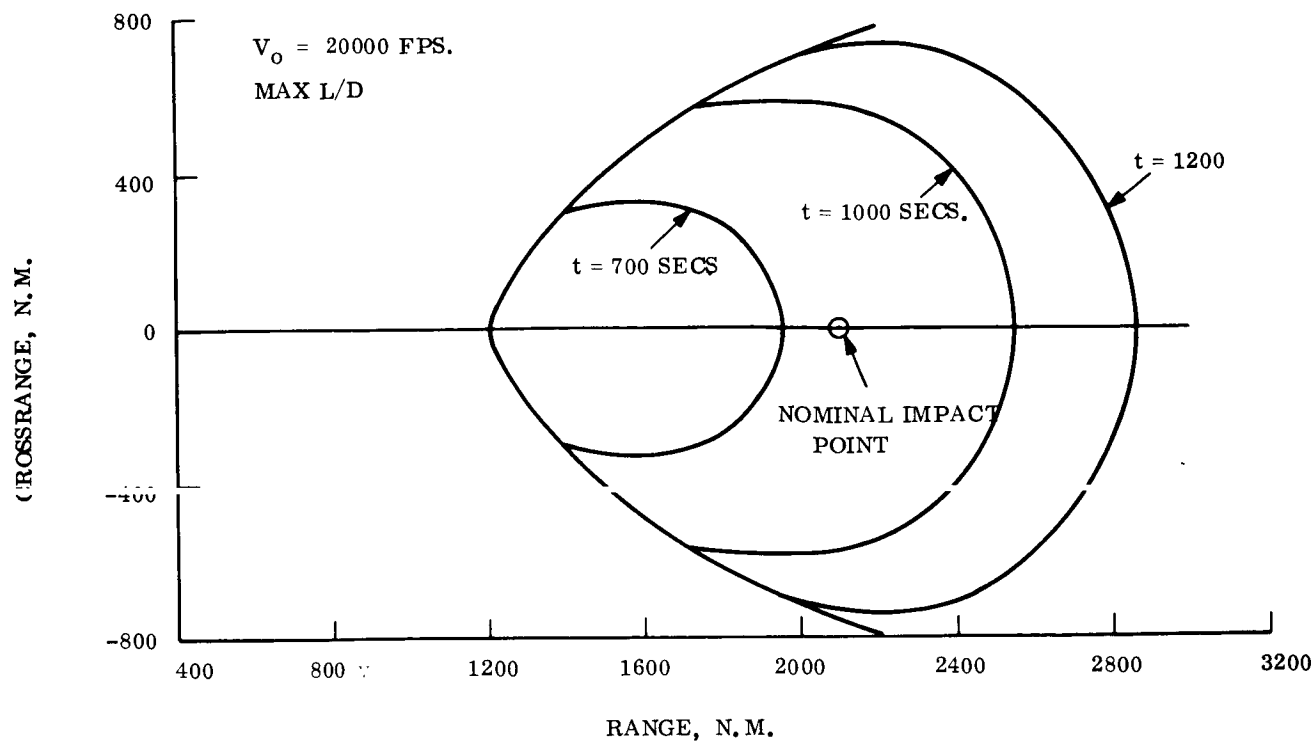


Figure 3.3-15. SLAMAST Range Safety Footprint,
 $\gamma_o = -1^\circ$, Failure at 350 Sec. from Re-entry

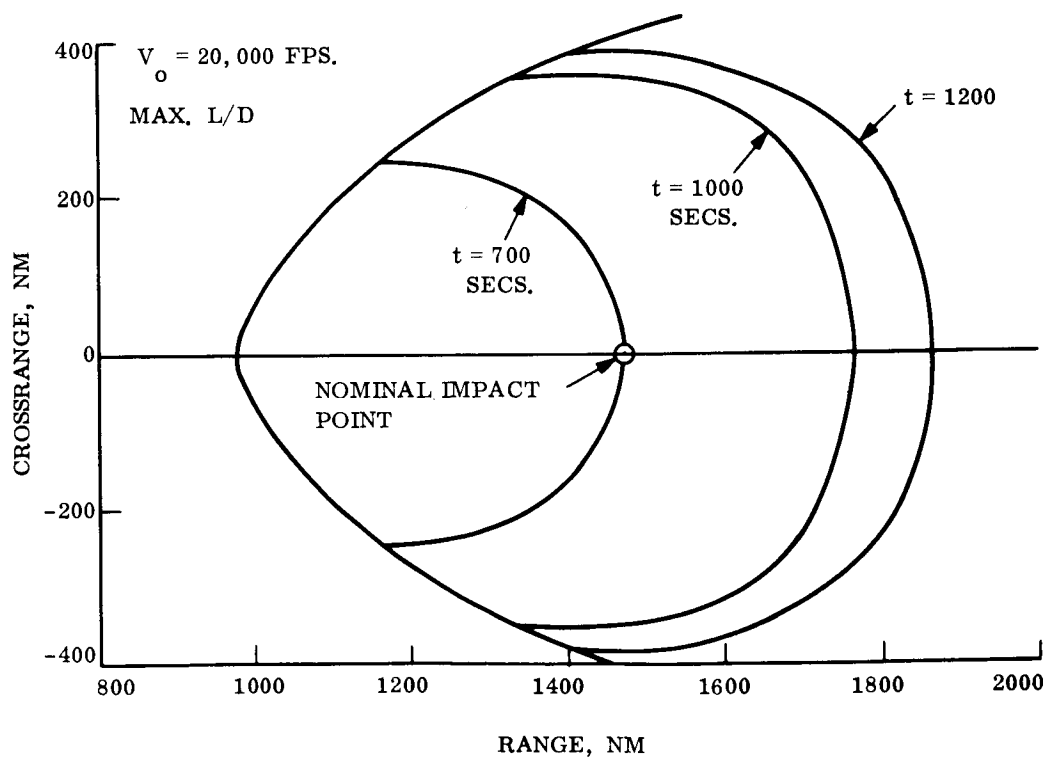


Figure 3.3-16. SLAMAST Range Safety Footprint
 $\gamma_o = -10^\circ$, Failure at 350 Sec. from Re-entry

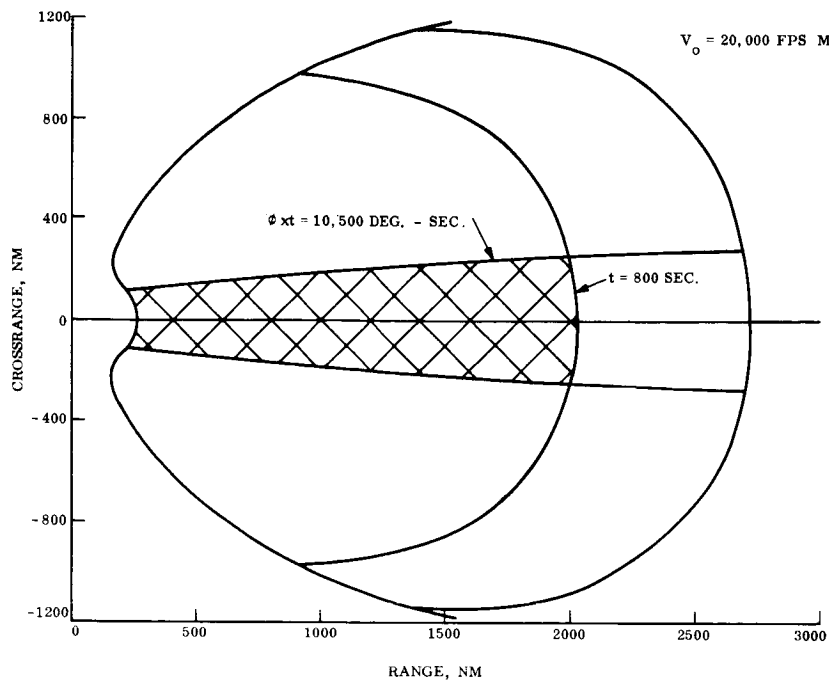


Figure 3.3-17. - SLAMAST Range Safety Footprint, $\gamma_0 = 10^\circ$, Failure at Re-entry

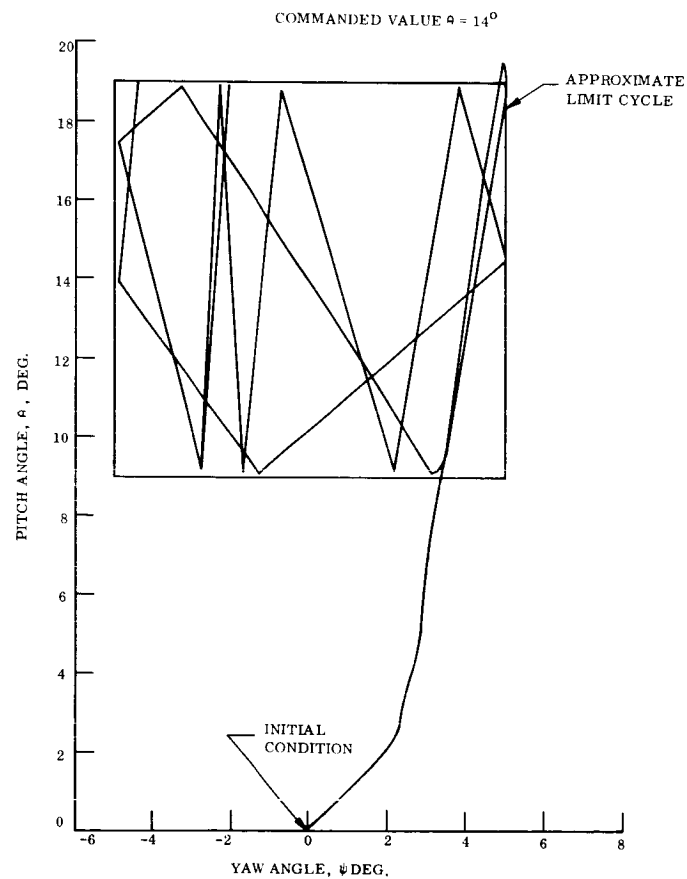


Figure 3.3-18. SLAMAST Exospheric Motion, Longitudinal Axis Motion in Inertial Space

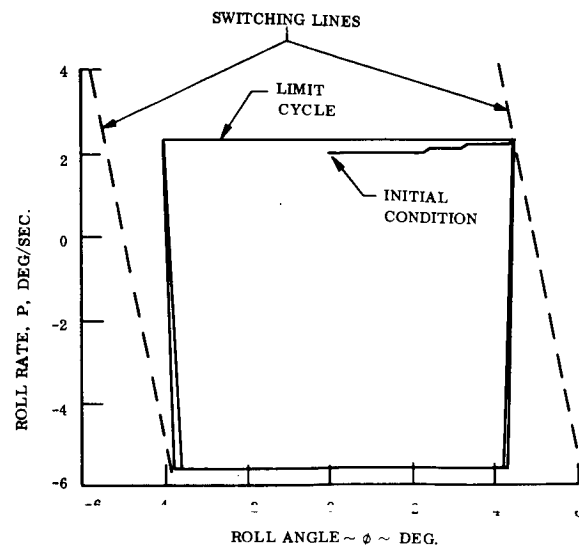


Figure 3.3-19. SLAMAST Exospheric Motion, Roll Phase Plane

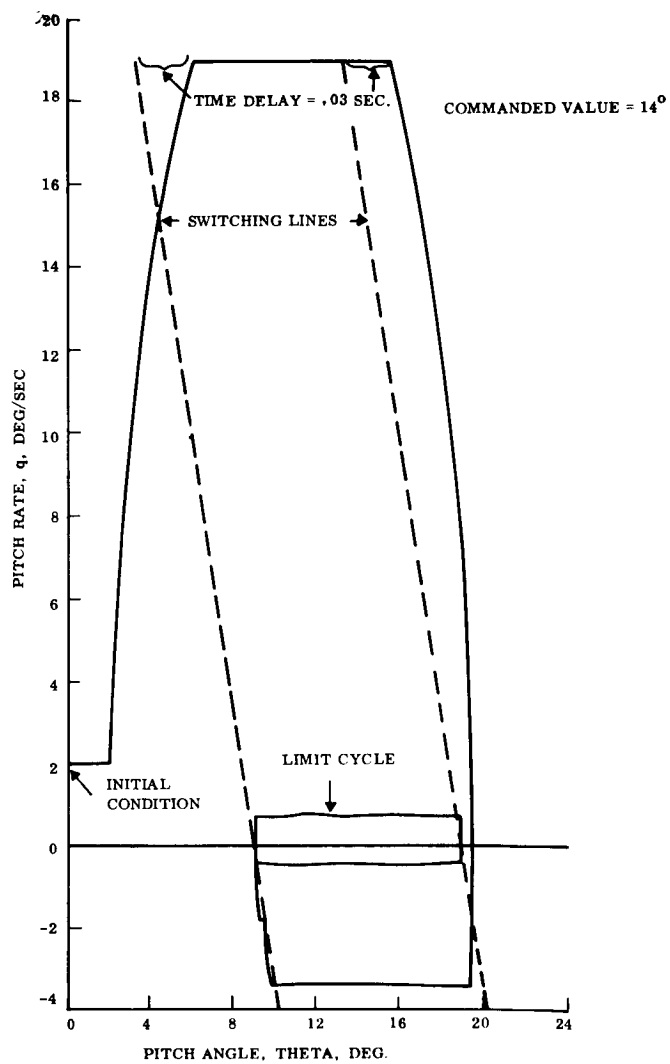


Figure 3.3-20. SLAMAST Exospheric Motion, Pitch Phase Plane

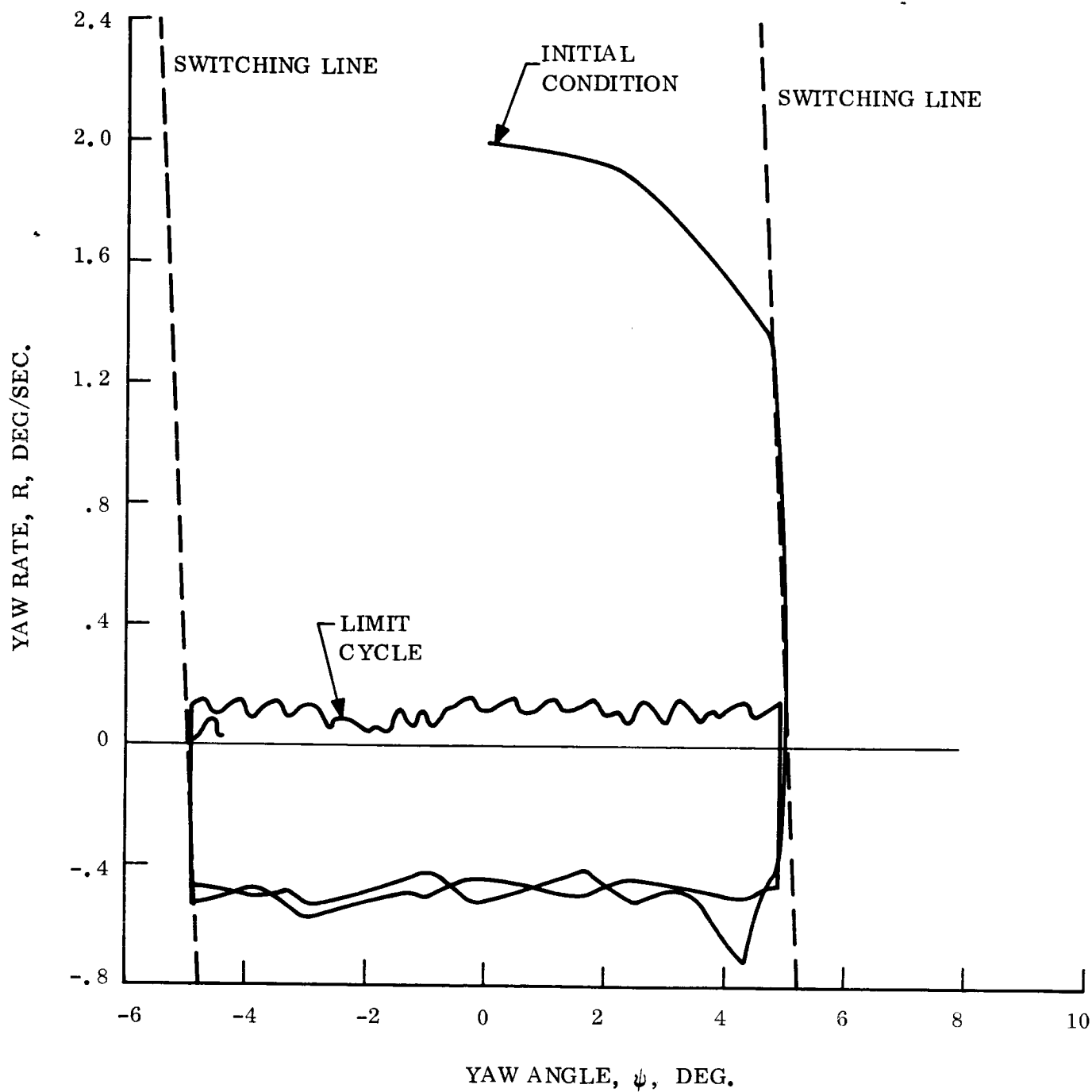


Figure 3.3-21. - SLAMAST Exospheric Motion, Yaw Phase Plane

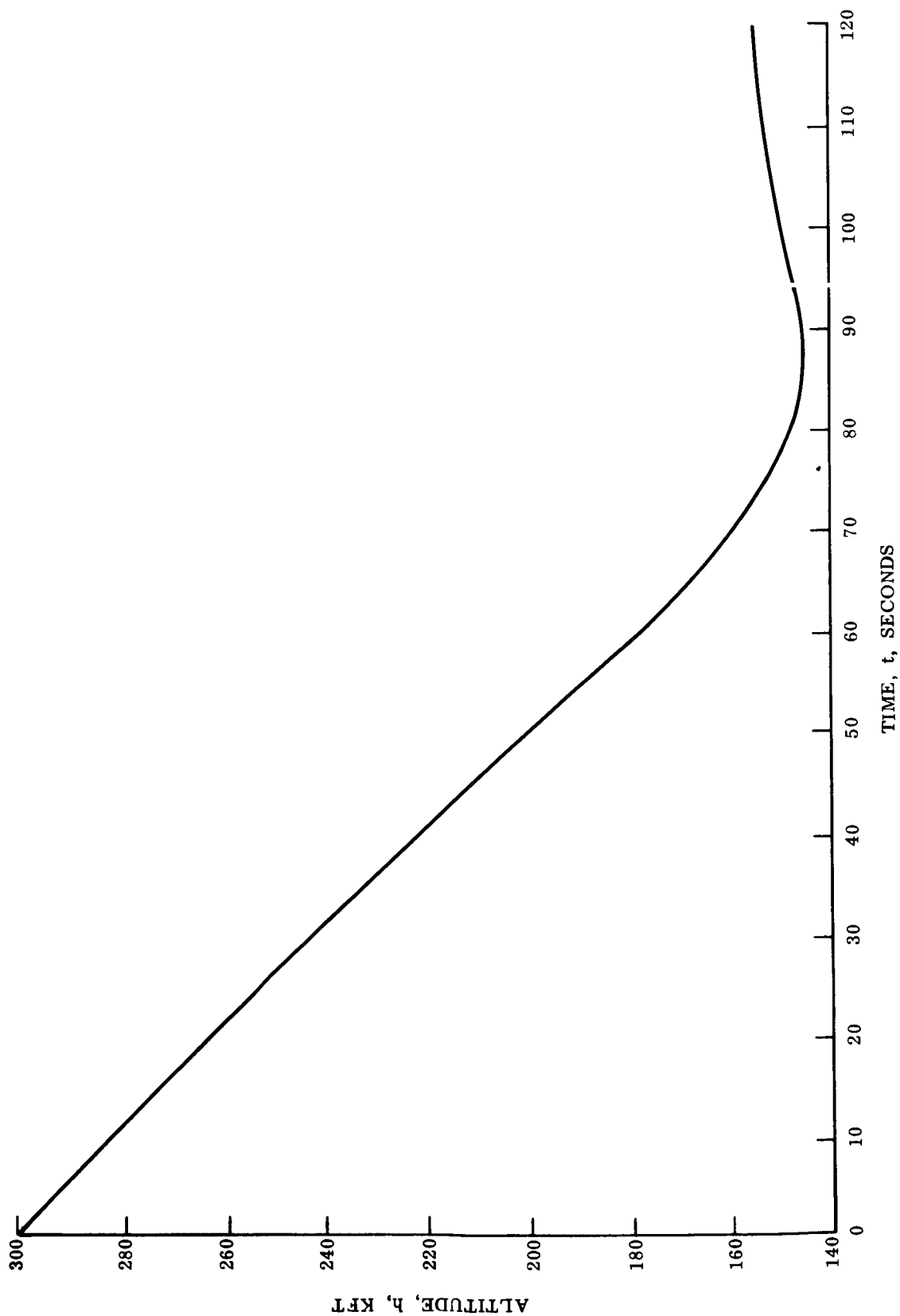


Figure 3.3-22. - Altitude vs. Velocity

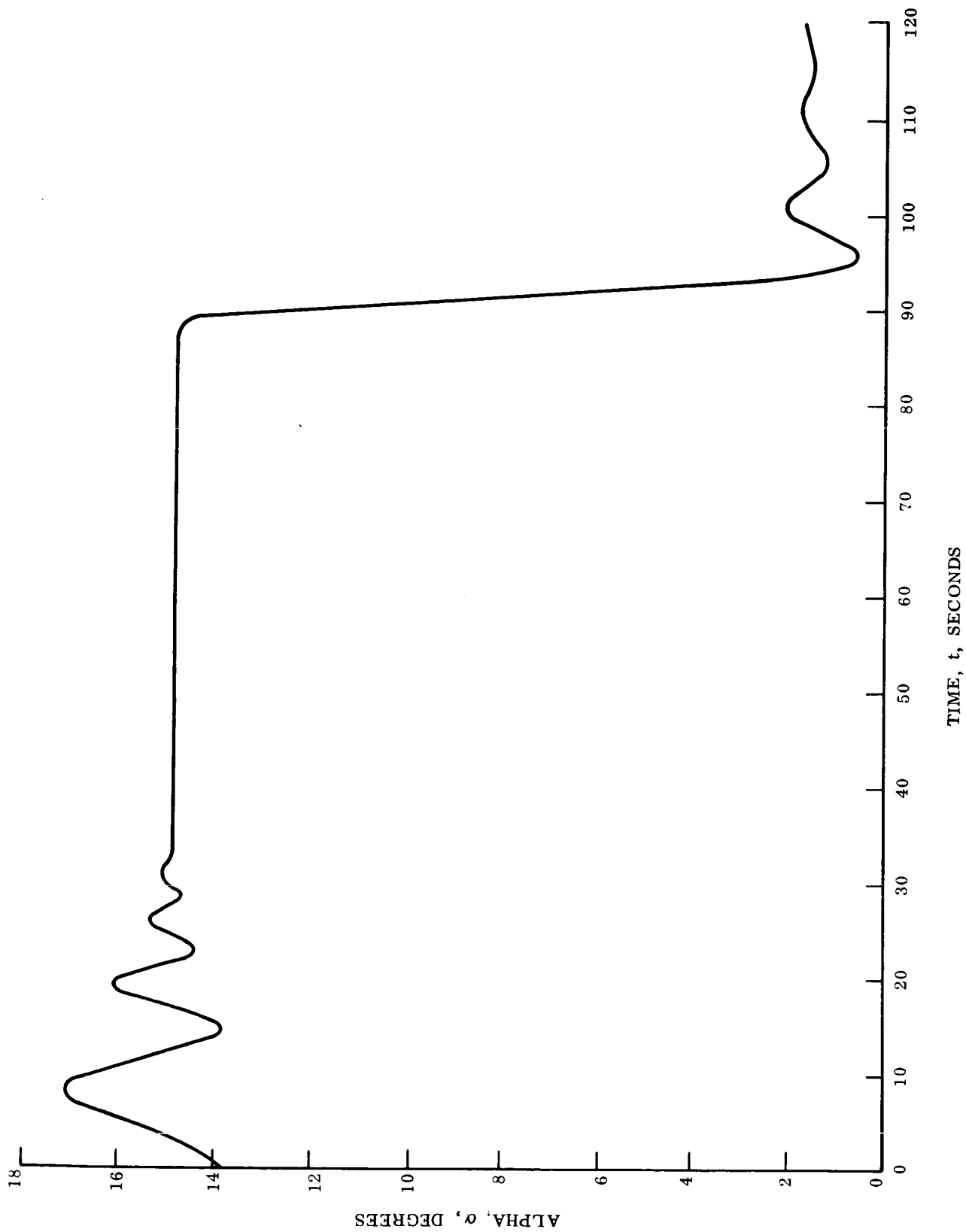


Figure 3.3-23. - Angle of Attack History

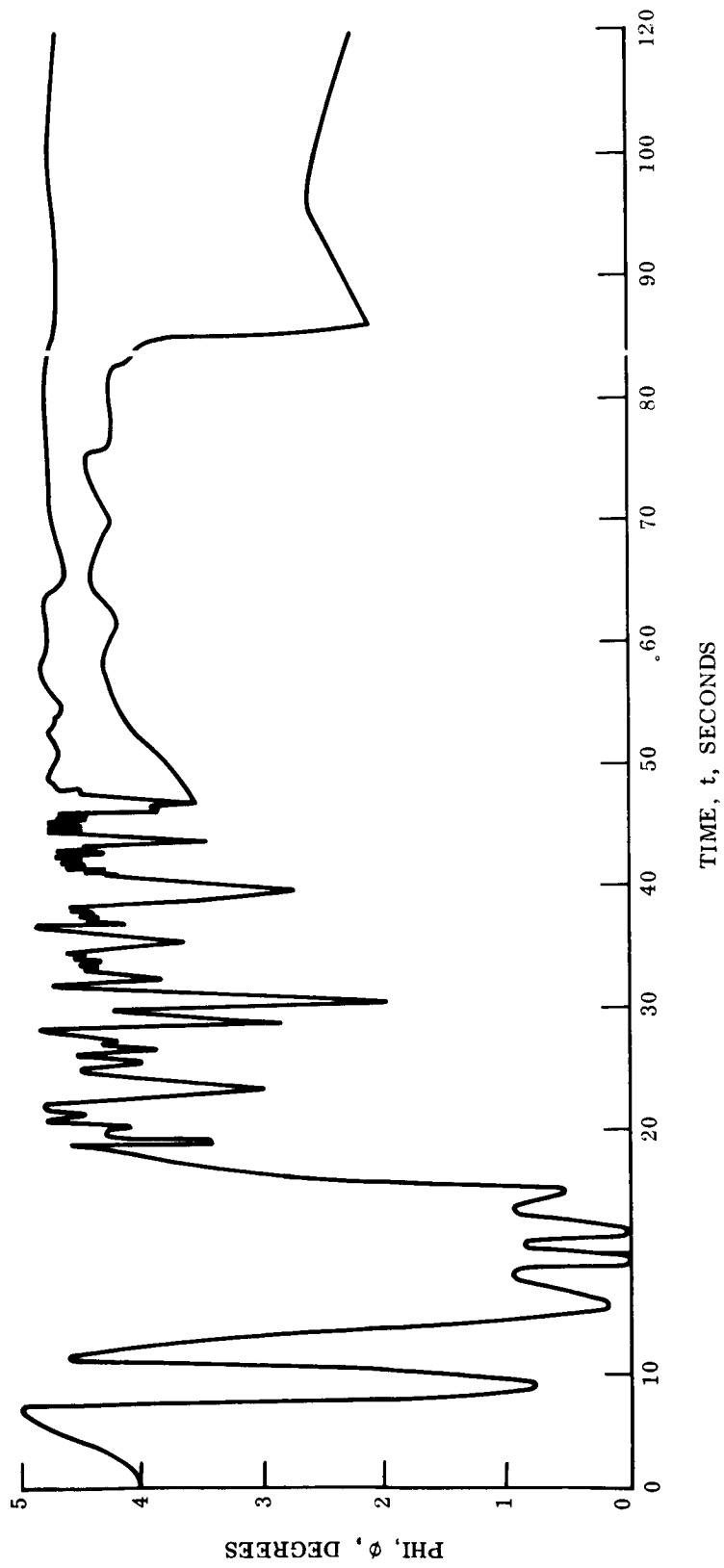


Figure 3.3-24. - Bank Angle History

3.4 THERMODYNAMIC STUDIES

3.4.1 AERODYNAMIC HEATING

All thermodynamic calculations have been determined for the SLAMAST configuration as illustrated in Figure 3.4-1.

The trajectories considered have the following initial entry conditions

	<u>1⁰ Entry</u>	<u>10⁰ Entry</u>
Altitude (feet)	400,000	400,000
Velocity (feet per second)	20,000	20,000
Entry angle (degrees)	1	10
W/C _L S (lbs. per foot square)	250	250
Pull-out altitude (feet)	142,000	115,500

and are shown in Figures 3.4-2 and 3.4-3. Note that in Figure 3.4-2 (the 1⁰ entry case) the dotted lines represent an additional 70 seconds of glide time to the actual trajectory. This additional 70 seconds is carried throughout in all 1⁰ entry calculations. The effect of this is a small percentage (approximately 5%) increase in total integrated heating since the additional time occurs just prior to drag brake deployment. As a result temperatures and degradation would be negligibly changed.

Pressure distribution used in evaluating the skirt - windward, leeward, and side - elliptical heating correlations are shown in Figures 3.4-4 and 3.4-5. Figure 3.4-6 shows the pressure distribution used in evaluating the pitchflap and dive break.

3.4.2 NOSE CAP HEATING

Stagnation point convective heating (to an axisymmetric stag point) was calculated through use of the "Planetary Aerodynamic Heating Program" (PAHP) reference 3.4-1, which uses Lees' theory reference 3.4-2 modified through use of Eckert's reference enthalpy technique, reference 3.4-3.

In Lees' equation,

$$\dot{q}_{\text{stag}} = \frac{.778}{Pr^{2/3}} (\rho e^* \mu e^*)^{0.5} \left(\frac{dUe}{dS} \right)^{0.5} (h_s - h_w)$$

where the coefficient has been adjusted to produce agreement with Mark 2 and X-17 flight test data. The velocity gradient, $\frac{dU_e}{ds}$ is given by

$$\frac{dU_e}{ds} = \frac{U_\infty}{R_n} \left[\frac{\rho_\infty}{\rho_2} \left(2 - \frac{\rho_\infty}{\rho_2} \right) \right]^{0.5}$$

For evaluation of convective heating to a non-axisymmetric stagnation point (as exists for the SLAMAST vehicle) Reshotko has suggested in reference 3.4-4 that the above relationships are applicable if an effective nose radius, $R_{n_{eff}}$ is employed where

$$R_{n_{eff}} = R_{n_x} \left[\frac{1 + \left(\frac{R_{n_x}}{R_{n_z}} \right)^{0.5}}{2} \right]^{0.5}$$

For the 63-inch long SLAMAST vehicle, as shown in Figure 3.4-1 $R_{n_x} = 4.725''$, $R_{n_z} = 0.656''$ and $R_{n_{eff}} = 0.956''$.

Employing these relations, stagnation heating histories for both the 1° and 10° entry trajectories are shown in Figure 3.4-7. Figure 3.4-8 shows the stagnation point pressure and enthalpy histories for both 1° and 10° entry cases.

An important consideration in evaluating the heating off the stagnation point is the determination of whether the flow is laminar or turbulent. Employing the SLAMAST configuration as an axisymmetric body, laminar and turbulent heat transfer rates were obtained through use of the "Planetary Aerodynamic Heating Program". The following equations are used in determining the laminar and turbulent heating. Local laminar heat transfer is calculated for an axis symmetric cone by the compressible reference enthalpy equations of reference 3.4-5 where

$$\dot{q}_{lam} = \frac{0.389}{Pr^{2/3}} \frac{\rho_e^* \mu_e^* U_e r (h_r - h_w)}{\left[\int_0^S \rho_e^* \mu_e^* U_e r^2 ds \right]^{0.5}}$$

For the turbulent boundary layer a relationship derived by Walker, reference 3.4-6, which satisfies both the momentum and energy integral equation and includes the affect of a finite pressure gradient is employed. The solution to these equations is obtained by use of Blasius incompressible flat plate skin friction coefficients modified for compressible flow by use of Eckert's reference enthalpy, reference 3.4-3 and is given by

$$\dot{q}_{\text{TURB}} = \frac{0.0296}{P_R^{2/3}} \frac{\rho_e \mu_e^{0.25} U_e (\mu_e^* / \mu_e)^{0.2} (\rho_e^* / \rho_e)^{0.8} r^{0.25} (h_R - h_w)}{\left[\int_0^s \rho_e U_e \mu_e^{0.25} r^{1.25} ds \right]^{0.2}}$$

Figure 3.4-9 shows (for 1° entry) the ratio of local heating to stagnation heating (at time of maximum heating) as a function of x/L considering both laminar and turbulent values. It can be seen from this axisymmetric distribution that turbulence will increase the laminar heating on the skirt by factors ranging from two to three times the laminar value.

A transition Reynolds number of 150,000 on the nose and 1,500,000 on the skirt was used, based on analytical studies of reference 3.4-8, to be the criteria for transition of laminar to turbulent flow. Figure 3.4-10 shows this transition correlation with both the 1° and 10° entry trajectories superimposed. Since local Reynolds number is a function of both pressure and wetted length,

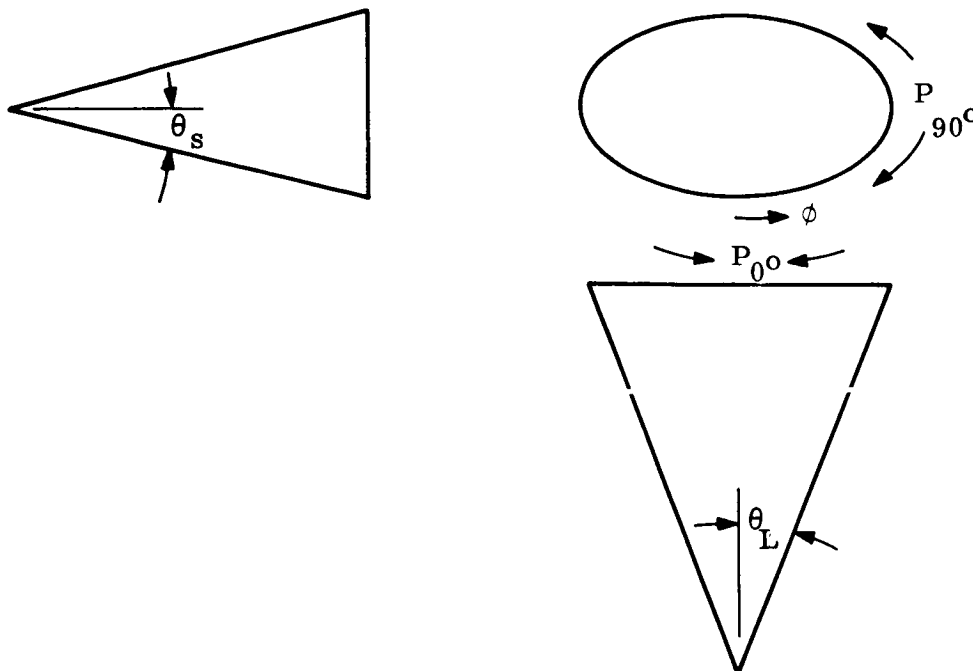
$$R_{e_s} = \frac{\rho_e U_e S}{\mu_e}$$

transition lines as a function of altitude and Mach number are shown for both a nose and end point of the SLAMAST vehicle. From this figure it can be seen that both the 1° and 10° entry trajectories will experience laminar flow. Transition to turbulent flow will occur just prior to chute deployment. In our analysis this occurrence of transition was neglected since convective flow at this altitude and Mach number is small.

3.4.3 SKIRT HEATING

Local aerodynamic heating predictions for the SLAMAST configuration are complicated by the elliptical geometry and angle-of-attack motion. Semi-empirical methods have been developed for the prediction of laminar heat flux for cones of elliptical cross-section in references 3.4-9 and 3.4-10. From reference 3.4-9, the following procedure has been adapted for calculating the local windward, leeward, and side heating to the elliptical SLAMAST vehicle:

- (1) Heating to the SLAMAST vehicle is simulated by heating on axisymmetric cones of varying half-angles and angles-of-attack.
- (2) The zero angle-of-attack case is first considered. The ellipse at zero angle-of-attack:



Since the 90° ray is at a higher angle-of-incidence (with respect to the free stream) than the 0° ray, the pressure is higher there thus inducing a circumferential velocity gradient. The flow characteristics may be compared to that which exists for a circular cross-section (cone) vehicle. The boundary layer at $\phi = 90^\circ$ is thinned over what the cone would experience there of equal half-angle and thickened at $\phi = 0^\circ$. The result is to increase or decrease the heating depending upon the peripheral angle.

The heating on a particular ray of the ellipse may be calculated by representing the geometry by a circular cone of some half-angle and at some angle-of-attack. The combination of half-angle and angle-of-attack must be such that the same incidence angle results as for the ellipse.

These angles may be determined by the following considerations. The cone pressures at $\phi = 0^\circ$ and 90° are the same as on the ellipse. P_{90} is unaffected by α . Thus, the cone half-angle for $\phi = 0^\circ$ heating is θ_L . To give the same incidence angle as the ellipse at $\phi = 0$ this requires that $\alpha = \theta_s - \theta_L$ i.e. $\theta_L + (\theta_s - \theta_L) = \theta_s$. This assumes that the effect of cross flow on the heating to the ellipse is exactly simulated by the cone at angle-of-attack. At $\phi = 90^\circ$, the opposite is true. The cone to simulate heating here is $\theta_c = \theta_s$, $\alpha = \theta_L - \theta_s$.

For the ellipse at angle-of-attack, the approach is to obtain the ratio, h/h_0 , for a circular cone at the same angle-of-attack as the ellipse. The cone half-angle for windward ray heating is θ_s . The 90° ray is assumed to be unaffected by the angle-of-attack.

Then, for the SLAMAST;

$$\theta_s = 6^\circ$$

$$\theta_L = 9^\circ$$

$$0 \leq \alpha \leq 20^\circ$$

with:

SLAMAST heating at zero angle-of-attack is given by an equivalent cone

$$\phi = 0^\circ : \theta_c = 9^\circ, \quad \alpha = -3^\circ$$

$$\phi = 90^\circ : \theta_c = 6^\circ, \quad \alpha = 3^\circ$$

For instance, to the windward or leeward rays

$h_{j\phi, \alpha}$ heat transfer coefficient where $j = E, C, SP$

$E \sim$ elliptical cross-section body (SLAMAST)

$C \sim$ circular

$SP \sim$ stagnation point

$\phi \sim$ cone half-angle

$\alpha \sim$ angle-of-attack

The desired quantity is h_E

$$h_{E6, \alpha} = \left(\frac{h_{E6, \alpha}}{h_{E6, 0}} \right) \left(\frac{h_{E6, 0}}{h_{C9, -3}} \right) \left(\frac{h_{C9, -3}}{h_{C9, 0}} \right) \left(\frac{h_{C9, 0}}{h_{SP}} \right) h_{SP}$$

$$\frac{h_{E6, \alpha}}{h_{E6, 0}} = \frac{h_{C6, \alpha}}{h_{C6, 0}}$$

Therefore, the ratio of convective heat transfer coefficient on the SLAMAST at angle-of-attack over the zero angle-of-attack case is the same as for a cone

$$\frac{h_{E6,0}}{h_{C9,-3}} = 1.0 \quad \text{a conclusion from reference 3.4-9}$$

$$\frac{h_{C9,-3}}{h_{C9,0}} = \quad \text{evaluated from references 3.4-9 and 3.4-10}$$

$$\frac{h_{C9,0}}{h_{SP}} \quad \text{calculated with program of reference 3.4-1}$$

In a similar manner, the heating to the side ray is given by

$$h_{E9,\alpha} = \left(\frac{h_{E9,\alpha}}{h_{E9,0}} \right) \left(\frac{h_{E9,0}}{h_{C6,+3}} \right) \left(\frac{h_{C6,+3}}{h_{C6,0}} \right) \left(\frac{h_{C6,0}}{h_{SP}} \right) h_{SP}$$

$$\frac{h_{E9,\alpha}}{h_{E9,0}} = 1.0 \quad \text{i. e., the heating to the side ray of the SLAMAST vehicle is independent of angle-of-attack}$$

$$\frac{h_{E9,0}}{h_{C6,+3}} = 1.0 \quad \text{a conclusion from reference 3.4-9}$$

$$\frac{h_{C6,+3}}{h_{C6,0}} \quad \text{evaluated from reference 3.4-9 and 3.4-10}$$

$$\frac{h_{C6,0}}{h_{SP}} \quad \text{calculated with program of reference 3.4-1}$$

Employing the above techniques, local laminar convective heat flux distribution have been generated for a range of applicable free stream Mach numbers, and angles-of-attack for both the windward, leeward, and sideward vehicle meridians. These distributions are presented in Figures 3.4-11, 3.4-12, and 3.4-13.

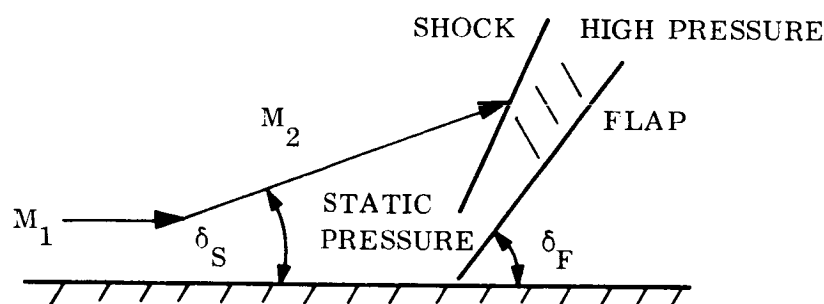
Combining the local heat flux distribution and the stagnation heating history, local heat flux histories for both the windward, leeward, and side meridians have been generated. These histories are presented in Figures 3.4-14, 3.4-15 and 3.4-16. Note that the generic shape of the sideward ray heat flux history is similar to the stagnation point heat flux history, while the windward and leeward rays have

similar generic shapes. This is due to the stagnation point and side ray being relatively unaffected by the angle-of-attack history, whereas the windward and leeward rays are strongly effected by the angle-of-attack history.

3.4.4 PITCH FLAP AND DRAG BRAKE HEATING

Aerodynamic heating to both the pitch flap and drag brake was calculated using basically the same techniques employed in the skirt heating analysis.

3.4.4.1 Pitch flap. - The pitch flap is on the leeward meridian and located at the end of the vehicle. Local laminar heating rates for the leeward ray were modified to account for the maximum pressure change. Based upon the data of references 3.4-11 and 3.4-12, there will be regions of separated and attached flow (see sketch) when there is a large flap deflection.



Reference 3.4-12, which is an analytical correlation for turbulent heat flux to flaps indicates a factor of three should be applied to the local heating at the reattachment point. A factor of five times the local laminar heating was employed for our particular pitch flap analysis where:

- (1) The flow is laminar to just after drag brake deployment.
- (2) The elliptical geometry will cause some interaction effects.
- (3) There is not currently available any applicable correlation or test data.

3.4.4.2 Drag brake. - The drag brake is located on the windward meridian towards the end of the vehicle. It is used only in terminating the glide trajectory in a shorter time interval. When the drag brake is employed the same procedure used in calculating the pitch flap heating is applied to the drag brake calculations.

Figure 3.4-17 shows the heat flux histories for both the pitch flap and drag brake. Note at the time of drag brake deployment, the heating to both the pitch flap and drag brake is similar since there is no longer a windward or leeward meridian, that is, the angle-of-attack (α) = 0.

3.4.5 NOSE CAP, SKIRT, PITCH FLAP, AND DRAG BRAKE SHEAR STRESS

Aerodynamic shear stress histories for the nose cap, skirt, pitch flap, and drag brake are shown in Figures 3.4-18, 3.4-19, 3.4-20, and 3.4-21. The x/L and meridian location of these histories correspond to the heating rate histories. The following relationship was used in the shear stress calculation

$$\text{Shear Stress } (\tau) = \frac{(\text{Pr})^{0.667}}{g} \times U_e \left(\frac{\dot{q}_C}{h_r - h_w} \right)$$

The maximum shear stress calculated does not exceed 7 lbs/ft² on the nose cap, pitch flap, or drag brake; and on the skirt the maximum value does not exceed 3 lbs/ft².

3.4.6 THERMAL DESIGN RESULTS

The heat transfer rates calculated in paragraphs 3.4.2 and 3.4.3 for the 1° entry trajectory were employed in the one dimensional Reaction Kinetics Ablation Program (REKAP), reference 3.4-13, to analyze the temperature and degradation response of typical materials for use in a SLAMAST vehicle design.

The REKAP program solves the charring ablator transient heat conduction problems by solving simultaneously the governing differential equation and the surface and backface boundary conditions.

These are:

$$\dot{q}_{\text{net}} = \dot{q}_C + \dot{q}_{\text{HGR}} - \dot{q}_{\text{RR}} - \dot{q}_{\text{BLOCK}}$$

where:

$$\dot{q}_C = H (h_R - C_{P_{BL}} T_w)$$

$$\dot{q}_{\text{HGR}} = \dot{q}_{\text{HGR}}(\text{time})$$

$$\dot{q}_{\text{RR}} = \sigma \epsilon T_w^4$$

$$\dot{q}_{\text{LAMINAR BLOCKING}} = \dot{q}_C \left[0.69 \frac{\bar{M}_{\text{AIR}}}{\bar{M}_{\text{GAS}}} \frac{\phi_o^{1/3}}{P_R^{1/3}} \right]$$

$$\dot{q}_{\text{TURBULENT BLOCKING}} = \dot{q}_C \left[1 - e^{-0.38 \frac{C_{P_{GAS}}}{C_{P_{BL}}} \phi_o} \right]$$

$$\phi_o = \left[\int_{\text{frontface}}^{\text{backface}} \dot{m} g \, dx \right] \left[\frac{h_r - h_w}{\dot{q}_C} \right]$$

$$\dot{m} g = \rho_v \left[\frac{\rho - \rho_C}{\rho_v} \right]^\eta \sum_{i=1}^{\dot{m}} A_i e^{-\frac{\Delta E_i}{RT}}$$

$$\frac{\partial}{\partial x} \left[K \frac{\partial T}{\partial x} \right] = \rho C_p \frac{\partial T}{\partial t} + H_{gf} \dot{m} g -$$

$$\left(C_g + \frac{\partial H_K}{\partial T} \right) \frac{\partial T}{\partial x} \int_{x=x'}^{x=\text{BACKFACE}} \dot{m} g \, dx K \frac{\partial T}{\partial x} = 0$$

The shield structure composites which were analyzed with the REKAP program are shown in Table 3.4.1.

The analytical results, that is, temperature and degradation histories, temperature profiles, mass addition histories, and shield requirements, obtained from the REKAP analysis of the above shield structure composites are shown in Figures 3.4-22 through 3.4-52 (see list of illustrations). A brief discussion of these results where the figures themselves are not self explanatory follows.

3.4.6.1 Nose cap thermal results. - The nose cap design for which thermodynamic studies were conducted is sketched below.

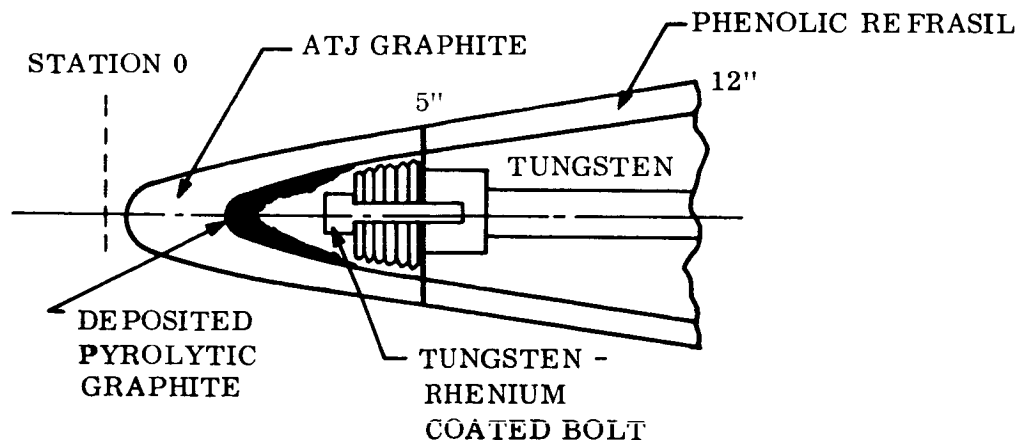
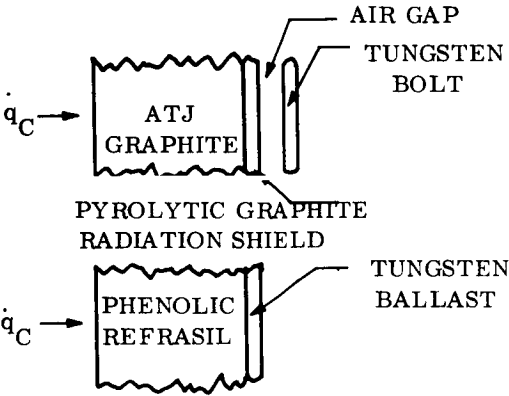
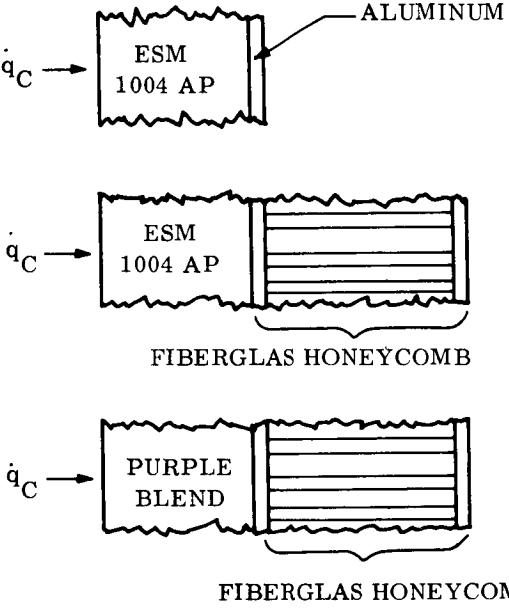



TABLE 3.4-1. - SHIELD STRUCTURE COMPOSITES ANALYZED

<p>(1) <u>NOSE CAP</u></p>  <p>ATJ GRAPHITE</p> <p>PYROLYTIC GRAPHITE RADIATION SHIELD</p> <p>PHENOLIC REFRASIL</p> <p>AIR GAP</p> <p>TUNGSTEN BOLT</p> <p>TUNGSTEN BALLAST</p> <p>q_C</p> <p>q_C</p>	<p>ATJ GRAPHITE REKAP MODEL REFERENCES 3.4-14 AND 3.4-15 SEE TABLES 3.4-2 AND 3.4-3 INPUTS</p> <p>PHENOLIC REFRASIL REKAP MODEL REFERENCE 3.4-16 SEE TABLES 3.4-2 AND 3.4-3 INPUTS</p>
<p>(2) <u>SKIRT</u></p>  <p>ESM 1004 AP</p> <p>ALUMINUM</p> <p>ESM 1004 AP</p> <p>FIBERGLAS HONEYCOMB</p> <p>PURPLE BLEND</p> <p>FIBERGLAS HONEYCOMB</p> <p>q_C</p> <p>q_C</p> <p>q_C</p>	<p>ESM 1004 AP REKAP MODEL REFERENCE 3.4-17 SEE TABLES 3.4-2 AND 3.4-3 INPUTS</p> <p>PURPLE BLEND REKAP MODEL REFERENCE 3.4-18 SEE TABLES 3.4-2 AND 3.4-3 INPUTS</p>
<p>(3) <u>PITCH FLAP & DIVE BRAKE</u></p>  <p>PHENOLIC NYLON</p> <p>BERYLLIUM</p> <p>q_C</p>	<p>PHENOLIC NYLON REKAP MODEL REFERENCE 3.4-19 SEE TABLES 3.4-2 AND 3.4-3 INPUTS</p>

Figures 3.4-22 to 3.4.25 show the typical temperature and degradation histories and temperature profiles for a typical graphite nose tip. Pyrolytic graphite is deposited behind the ATJ graphite and is used as an insulator to reduce the temperature. Original analyses indicated that without this the bolt would exceed its maximum allowable temperature ($>3000^{\circ}\text{R}$) as a result of the high radiation heat exchange between the ATJ Graphite and the tungsten-rhenium bolt.

In order that the high temperatures in the stagnation region are not conducted directly to the low temperature skirt ablator material; an intermediate nose cap shield structure of phenolic refrasil material was designed. Figures 3.4-26 and 3.4-27 show typical phenolic refrasil temperature and degradation results.

For the entire nose cap, note that the shield thicknesses shown are nominal thicknesses that adequately (thermally) protect the structure. Actual design thicknesses would vary depending on the thermal safety margin and the structural stress analysis results.

Mass addition rates for the entire nose cap are shown in Figure 3.4-28. The differences in shape between the graphite and refrasil curves is that the graphite material experiences mass loss only due to oxidation and sublimation where the phenolic refrasil experiences no surface melting but only in depth phenolic resin decomposition.

Preliminary structural analysis indicates that a potential problem exists if the temperature gradient between the stag point and $x/L = 0.0208$ is as great as the 2000°R shown. For the feasibility study only a one-dimensional analysis was conducted. However, for the final design a multidimensional analysis would be performed which would take into account the high conductivity of the graphite material. It is anticipated that this analyses would show that a large temperature gradient along the nose cap region would not exist.

3.4.6.2 Skirt thermal results. - Skirt shield structure composites were evaluated for heating rates beginning at an $x/1$ location of 0.0208 and proceeding to an $x/1 = 1.0$ for the windward, leeward, and side meridians. The shield structure combination analyzed were for both thermal design and experimental simulation.

A summary of the temperature studies made for both the ESM and Purple Blend shield composites are shown in Figures 3.4-29 and 3.4-30. Figures 3.4-29 and 3.4-30 show nominal shield requirements as a function of $x/1$ and integrated heating respectively for both materials. Shield requirements are shown for design temperatures of 750°R (300°F) and 1060°R (600°F). It should be noted that these are nominal shield requirements and that actual design thicknesses would include a 30 percent safety margin.

These results are for a 1° entry trajectory with chute deployment occurring at time = 900 seconds from 400K feet. Shield requirements for a 10° entry would be slightly less.

3.4.6.2.1 Typical ESM shield structure results: Figures 3.4-31 through 3.4-38 show 1° entry temperature and degradation* histories, and temperature profiles for various locations along the windward, leeward, and side meridians. Figures 3.4-39 and 3.4-40 show windward meridian temperature and degradation results for a 10° entry trajectory. Figure 3.4-41 shows 1° entry total mass addition rates for an ESM shield structure composite for all meridians. For comparison, the 10° entry mass addition rate is also shown.

3.4.6.2.2 Typical purple blend shield structure results: Figures 3.4-42 through 3.4-45 show 1° entry temperature and degradation* histories, and temperature profiles for an $x/1 = 1.0$ on the windward and leeward meridians. Figures 3.4-46 and 3.4-47 show windward meridian temperature and degradation results for a 10° entry trajectory. Figure 3.4-48 shows 1° entry total mass addition rates for a Purple Blend shield structure composite for the windward and leeward meridians. For comparison, the 10° entry mass addition rate is also shown.

3.4.6.3 Pitch flap and dragbrake thermal results. - Heating rates calculated in paragraphs 3.4.2 and 3.4.3 were employed in the calculation of the temperature and degradation response of the Phenolic Nylon thermal protection material for the pitch flap and drag brake. Figure 3.4-49 shows the results of a parametric study presenting nominal Phenolic Nylon pitch flap and dragbrake thicknesses as a function of maximum backface temperature. Note that the actual design thickness would be dependent on both the thermal safety margin and the structural stress analysis.

3.4.6.3.1 Typical phenolic nylon thermal results for pitch flap and drag brake: Figures 3.4-50 through 3.4-53 show typical 1° entry temperature and degradation histories and temperature profiles for both the pitch flap and drag brake. Figure 3.4-54 shows the 1° entry total mass addition rates that can be expected for both the pitch flap and drag brake.

*Char thickness is defined as the depth (from the surface) at which the material density is equal to 97% of the virgin material density.

3.4.7 INTERNAL ENVIRONMENTAL CONTROL

A preliminary thermal analysis was conducted to determine what methods of thermal control would be required to maintain the electronic equipment within their operating temperature limits.

3.4.7.1 Summary. - Two structural temperature response profiles were considered, a hot structure with a maximum temperature of 1060°R and a cold structure with a maximum temperature of 760°R . It was found that the electronic components could be maintained within required limits for either case by the following means:

(1) Control component launch temperature by appropriate ground air conditioning.

(2) Cover vehicle backface with a low emissivity tape.

(3) Isolate components from the structure by using Textolite or equivalent mounting brackets and shelves. Insulating washers and bushings are sufficient for some components.

(4) Use low emissivity coatings on some of the electronic equipment boxes.

The analysis indicates that insulating washers and bushings between the equipment packages and vehicle structure are sufficient thermal isolation for the cold structure cases. Therefore, special low conductivity brackets and shelves are not required. This will result in a less sophisticated mounting scheme for this case.

No special thermal control system is required for either design. It is quite probable that a more detailed analysis of an actual internal configuration would result in elimination of some of the above requirements for various components.

3.4.7.2 Discussion. - The temperature history of the components during the flight will depend upon initial launch temperature, backface temperature history, component power profile, and the thermal resistance between the components and the vehicle skin.

The electronic components receive heat from two separate sources. Heat is generated internally by the power supplied to the electronics, and heat is transmitted from the vehicle skin to the components by conduction, convection and radiation.

Two backface temperature responses as shown on Figure 3.4-55 were considered. They are typical responses of ESM 1004 AP and NASA 602 Ablator during a trajectory such as that shown on Figure 1 of Reference 3.4-20. One curve is based on a heat shield thickness that would result in a maximum design temperature of 1060°R , or a hot structure, and the other a shield thickness that reaches a maximum of 760°R for a cold structure.

Without air conditioning, it is expected that a maximum launch temperature of 125°F could occur on the electronic equipment assuming a low solar absorptivity paint on the outside of the vehicle. With sufficient air conditioning, which is readily available at the Wallops Island launch site, this lift off temperature could be reduced to 72°F. The effect of these two extremes were investigated.

The internal heat dissipation histories of the various components is given on Figure 3.4-55. These were obtained from the power profiles given in references 3.4-21, 3.4-22, and 3.4-23. They are during flight only and assume no ground checkout time.

Because of the high backface temperatures encountered during the flight, it was apparent that the components would have to be mounted in a manner in which thermal conduction from the vehicle skin would be at a minimum. Two methods were considered: first, that the components were attached to the vehicle structure through mounting brackets or shelves made of Textolite or equivalent, with a resulting conductance from vehicle to component of 0.04 BTU/HR-°F or less; second, that the equipment packages were mounted directly to the structure, whose temperature equalled that of the skin, by insulating washers and bushings with a total conductance of 0.40 BTU/HR-°F.

In addition, because of the high skin temperatures, a vehicle backface with a surface of low emissivity is necessary to reduce the effect of thermal radiation to the equipment. It was assumed that the backface was covered with a low emissivity tape with emissivity equal to 0.15. The components were assumed to have a surface with emissivity equal to 0.80.

The maximum operating temperature of the electronic equipment is +160°F. The upper limit of the silver oxide-zinc batteries is +120°F.

Since this is a preliminary analysis preceeding a final design of the vehicle internals, the analysis was performed on a component by component basis. With this method each component is considered individually and assumed to be a single mass alone inside the vehicle. In doing this, the thermal interaction between components is disregarded, and the view factor from each component to the vehicle skin is assumed to be equal to unity when considering radiant heat transmission. Since heat is being transfered from the vehicle to the components, this method of analysis yields higher component temperatures than will actually occur and is thus conservative.

Figures 3.4-56 through 3.4-59 show the various component temperature histories from launch to splashdown for both hot and cold structure, air conditioned and not air conditioned. The data composing these figures was calculated as described above assuming a Textolite mounting structure with backface surface having an emissivity equal to 0.15 and component emissivities equal to 0.80. These figures show that for both the hot and cold structure cases investigated, component launch temperatures will have to be controlled in order to keep some of the components from exceeding their maximum allowable temperatures during operation. Thus,

some ground air conditioning will be required. The analysis showed that within the range of launch temperatures investigated, a shift in initial temperature results in an equal shift in final temperature. On this basis, the maximum allowable launch temperature of each component can be found from the figures presented. Thus, the effect of any ground check out can be considered.

Further study of Figure 3.4-56 shows that two components, the transmitter and signal conditioner, exceed the maximum allowable temperature of 160°F even if their launch temperature is equal to 72°F. However, if the cases of these components are treated with Alodine 1200 or equivalent, resulting in a surface emissivity of 0.15 or less, their maximum temperatures will not exceed the allowable limit. It is also highly probable that the temperatures will remain below 160°F even without the low emissivity coating when actual view factors are used.

Figures 3.4-60 and 3.4-61 show the component temperature profiles assuming the insulating washer mounting technique. Although this method is less effective than the Textolite structure in limiting the amount of heat transfer by conduction, the figures show it to be adequate for many of the components.

3.4.7.3 Recommendations. - Ground air conditioning should be provided to control component launch temperatures. The vehicle backface should be covered with a low emissivity coating. The components should be isolated from the structure. This can be accomplished by using Textolite or equivalent mounting brackets; or, in some cases as shown by the data, insulating washers and bushings alone would be sufficient.

3.4.8 MATERIAL SELECTION

3.4.8.1 Introduction. - Microballooned phenolic nylon (MPN) and ESM 1004 P have been evaluated as the prime thermal protection materials over major portions of this vehicle. ESM 1004 P has been selected as the prime material for the following reasons: available property data, thermal performance, thermostructural compatibility, available analytical techniques, established manufacturing and quality control procedures, flight experience, and cost.

Those portions of the vehicle that will be exposed to a peak heat flux of greater than 100 BTU/ft² - sec. (e.g., nose, leading edges, flaps, etc.) will be thermally protected by a material selected from the class of higher density, high performance shield materials such as graphite, phenolic reffrasil, phenolic nylon, etc.

3.4.8.2 Property data. - ESM 1004 P is an unsupported, foamed methyl phenyl silicone containing low concentrations of aluminum silicate fibers. This material is completely characterized with existing thermal, mechanical, ablative and environmental property data required for design on both the virgin and char materials (reference 24 and 25).

Protective coatings for ESM (a white rutile Titania filled RTV-511 designated PD-147) which seal the foam surface if desired, have been qualified to air-to-air missile specifications of ten cycles to five minutes exposure at 360°F to 370°F, ten days at 120°F at 100 percent relative humidity and prelaunch environmental soak conditions of -65°F and +160°F.

ESM 1004 P did not support fungus growth as per MIL-STD 810, Method 508 and was unaffected by exposure to salt fog, MIL-STD 810, Method 509. There was no significant effect on tensile properties in the humidity test exposure of MIL-STD 810, Method 507.

3.4.8.3 Thermal performance. - A number of independent investigators have reported that the low density silicones are particularly suited for these design and heating conditions.

In a study conducted by Langley Research Center (reference 3.4-26), the following conclusion was made:

"In the 2500-kilowatt jet stream of low oxygen content, the performance of low-density silicone resin is superior to that of low-density phenolic-nylon at heating rates from 80 to 150 BTU/ft²-sec. and at shear stresses near 4.7 lbs/ft²; however, phenolic-nylon is superior to silicone resin in a low-oxygen content stream at heating rates outside this range."

After a personal communication with the author concerning this conclusion, Mr. Clark said that although tests were not run at heating rates below 80 BTU/ft²-sec., it was his opinion that the low density silicones would be superior also at heating rates below this value. This opinion has been further substantiated by the Aerospace survey (reference 3.4-27) in which they report:

"It is apparent that the charring ablator materials are more efficient for the high heat flux, short re-entry times, while the silicone elastomers are more efficient for the milder heat fluxes and longer re-entry times."

In a study conducted for the Office of Advanced Research and Technology of NASA, the ablative concept was the lightest weight system for lifting entry vehicles using allowable backface temperature of 600°F and the low-density silicone elastomeric type material was considerably lighter than a material representative of the class of low density rigid ablators (reference 3.4-25).

Comments from other investigators include:

"The silicone materials do not recede until the heat flux exceeds about 90 BTU/ft²-sec. -----." (reference 3.4-27)

"Under the low pressures of these simulated environmental test conditions, silicone materials form a protective melt layer below 60 BTU/ft²-sec., but not at the higher heat fluxes." (reference 3.4-27)

"..... it was concluded from these plasma tests that the silicone elastomer ablation materials are a good choice for present and future mission requirements for ablative lifting bodies. This conclusion is based on thermal performance, insulation efficiency, recession characteristics, cold soak properties, manufacturing simplicity, materials availability, reliability for the mission requirement, and process and quality control procedures." (reference 3.4-27)

"Most of the interest to date has been focused on the silicone polymers, because of their low thermal conductivity, high thermal efficiency at low to moderate heat fluxes, low temperature properties, elongation of several hundred percent at failure, oxidative resistance, low density and compatibility with other structural substrate materials." (reference 3.4-28)

"In the area of re-entry thermal protection, elastomers are acquiring new importance. They are suitable for long-time exposure to the cryogenic temperatures of space and are now being used in primary heat shields. They minimize the accumulation of thermal and mechanical stresses in composite structures by yielding under stress." (reference 3.4-29)

Significant studies have been conducted on the development, fabrication and qualification of this class of material. (reference 3.4-30) Other studies have reported:

"The addition of phenyl groups to the basic methyl silicone elastomer permits attainment of good shield-structural compatibility on large scale structures down to low orbit temperatures of -290°F to -300°F. The chemical foaming processes, both supported and unsupported, permit density variations between 20 and 80 lb/ft³; the material provides highly effective thermal insulation for the long-time re-entries associated with lifting vehicles. Thermal shield weight is significantly decreased (by factor of 2.0-2.5) by allowing the maximum structural temperature to go to 600°F rather than 300°F." (reference 3.4-24)

3.4.8.4 Thermostructural compatibility. - Experiments have been conducted in a thermal simulator to determine the thermostructural capability of the ESM 1004 P material bonded to aluminum and laminated phenolic fiberglass for the cold temperature extremes occurring in orbit. The material has been successfully cycled between - 300°F and +300°F. The 1004 material has a coefficient of thermal

expansion approximately that of the metallic structure at temperatures below -180°F (ductile-brittle transition temperature). Thus, this material provides shield-structure compatibility at low temperatures as demonstrated by successful large scale tests down to -300°F . At temperatures above about -70°F , the material has a high coefficient of expansion compared with the substructure. However, ESM has high strain capability at these temperatures and no stresses are induced in the system (reference 3.4-24).

3.4.8.5 Available analytical techniques. - Measured temperature data for a number of heat fluxes in several plasmajet tests have been compared with analytical predictions (reference 3.4-24). The analytical data were obtained by using a Reaction Kinetics Ablation Program (REKAP) which has been developed for ESM 1004 P. This program computes the temperature distribution within a plastic material undergoing thermal decomposition. The rate of decomposition is controlled by an Arrhenius type of relation obtained from thermogravimetric data. It includes the effect of density change during the decomposition process. The gases formed by the decomposition of the gas flow through the char material that is formed are assumed to be in thermal equilibrium with the char. The reduction in heat transfer caused by mass injection into the boundary layer is evaluated by semi-empirical relations derived from experimental data. The surface recession or char removal mechanisms included in the program are those of oxidation, sublimation, melting, and vaporization.

3.4.8.6 Manufacturing and quality control procedures

3.4.8.6.1 Manufacturing experience: ESM sheet stock and molded parts are fabricated as standard production items. Their manufacture and bonding are controlled by material, processing, and quality control specifications including complete in-process inspection. In addition to fabrication and application to the leading edge, ventral fin, and speed brakes for flight test on the X-15, an ESM thermal shield has been fabricated in sheet and molded sections for a full scale re-entry satellite vehicle.

The spray application of ESM was demonstrated in the field by coating the ventral fin and lower speed brakes on X-15-1 on September 3, 1965. Solid propellant rocket cases have also been coated with spray ESM both in-house and in the field.

3.4.8.6.2 Quality control: All raw materials are qualified through extensive acceptance testing. Since the shield is fabricated before bonding, ablation, mechanical and thermal acceptance tests are made on the shield material before application for total quality assurance. Material, engineering, quality control and manufacturing specifications have been issued and are official documents controlling the fabrication of ESM (reference 3.4-32). The material has been fabricated and qualified in the production operation.

3.4.8.7 Flight experience. - In addition to the X-15, ESM has been flown on the aft covers of the AMDT vehicle and two current classified programs. Two modifications designed for higher flux and shear conditions have also been applied and flown on the aft portion of the skirt of the STV (TVX-PRESS) vehicle. It is currently being fabricated as the thermal protection for the aft shield of an operational satellite re-entry vehicle.

3.4.8.8 Cost. - It is estimated that due to the extensive molds and tooling required for MPN and the manufacturing experience with ESM, the cost of an ESM heat shield would be approximately one-third of a MPN shield of comparable weight (reference 3.4-24).

3.4.8.9 Nose tip materials. - The SLAMAST nose tip design involves the use of several materials:

- (1) a structural graphite (ATJ) nose tip and threaded insert,
- (2) a tungsten-rhenium retaining nut and bolt,
- (3) pyrolytic graphite insulating washers, and
- (4) a boron-alloyed pyrolytic graphite (BPG) lining for the inside of the nose tip.

The PG washers are available commercially from several vendors and present no problems. This report outlines the present state-of-the-art for the other materials involved and estimates the amount of development effort, if any, that would be required prior to their successful fabrication.

3.4.8.9.1 Graphite nose tip technology: Graphite base materials have great potential for use on slender, small nose radius vehicles of the TVX, RMV-A and SLAMAST type. This form of carbon has high thermal shock resistance, good high temperature strength, excellent machinability, high thermal conductivity, a high sublimation temperature, and a relatively low oxidation rate. The available manufactured graphites are not one specific material, but a family of materials which are essentially pure carbon. They differ from each other from the standpoint of degree of preferred orientation of the crystallites, the grain and/or crystallite size, the density, the size and number of pores or voids, the degree of graphitization and the level of impurities. Thus, a wide variation can be produced in the physical and chemical properties of graphites, depending upon the choice of starting materials and the conditions used in processing the graphites during the manufacturing cycle.

Excellent review of many aspects of graphite technology exist both in the trade and published literature. Examples are (a) the graphite handbook published by the National Carbon Company, (b) Proceedings of the 7 Carbon Conferences sponsored by the American Carbon Committee and the R and T Division of the Air Force Systems Command, and (c) a book by Ubbelohde and Lewis.

The Re-entry Systems Department has shown through flight test of vehicles such as TVX and RMV-A that manufactured graphites such as the National Carbon Company's ATJ grade of graphite can be used satisfactorily for nose tips on slender, small nose radius vehicles.

Synthetic or manufactured graphites are, in general, made by the same basic process. Graphite is formed in bulk by heating organic cokes at high temperatures in the absence of air. This material is subsequently mixed with coal tar pitch and the mixture is consolidated, shaped, and heated. Processing details vary with individual producers, but the basic operations described are standard throughout the industry. To obtain graphite of highest purity, the bars are heated in an atmosphere containing gases such as chlorine and fluorine. This removes impurities including the rare earths, vanadium and boron and, if carried out properly, is reported to reduce the total ash content to values under 20 parts per million. *

ATJ Graphite is covered by General Electric Specification NCS3146B. The specification requirements for this material are:

Bulk Density	1.73 gm/cm ³ minimum
Compressive Strength (RT)	
With Grain	7300 psi
Against Grain	7300 psi
Tensile Strength	
With Grain	2900 psi
Against Grain	2900 psi
Purity	
Type I Ash	150 ppm
Radiographic Requirements	
Density	Uniform
Voids, Cracks, Inclusions	None
Grain Size	.007 maximum
Specific Resistance	
With Grain	13.6×10^{-4} ohm/cm
Against Grain	17.0×10^{-4} ohm/cm

For the SLAMAST program ATJ graphite appears best suited to meet the program requirements. The material will withstand the extended heating rate for the long re-entry times involved. There is no thermal shock or serious application problem with this material and the oxidation resistance of commercial available ATJ appears adequate. If further oxidation resistance is required the material can be purified which will enhance its oxidation resistance or a silicon carbide coating could be applied.

* The standard procedure in the carbon industry is to measure impurity content on the basis of residual ash from a known weight of combusted sample.

3.4.8.9.2 Pyrolytic graphite insulative lining: The SLAMAST nose tip, constructed of ATJ graphite, has an internal cavity to accommodate the head of the tungsten-rhenium retaining bolt. To provide thermal insulation protection for this bolt head, it has been proposed that this cavity be lined with boron-alloyed pyrolytic graphite (BPG).

The deposition of BPG on the inside surfaces of ATJ graphite nose tips has been successfully accomplished on numerous occasions on study contracts currently being conducted at the General Electric Co. No major problems are expected so long as the ATJ/BPG thickness ratio (radially) is 2.0 or more. When the thickness to radius (t/r) ratio of deposited BPG exceeds 0.06, tight delaminations are likely to appear in the BPG. However, when present they will not cause any problems since the BPG lining is not a structural member. In fact, by creating additional interfaces in the material, they enhance the thermal insulation properties of the BPG lining material.

After deposition of the BPG lining, machining would be required to remove the BPG from surfaces where it is not desired. At this time female threads would be machined to accommodate the threaded ATJ insert.

In summary, the BPG lining concept appears to be applicable to the SLAMAST program without extensive development. One or two development runs might be needed to establish process parameters such as nozzle position, length of run, and deposition temperature. However, no difficulties are expected if the lining thickness ratio and the thickness to radius ratio previously mentioned are not exceeded. The thermal insulative properties of the BPG will maintain the temperature. The tungsten rhenium bolt will "see" below the critical temperature of the alloy.

3.4.8.9.3 Tungsten rhenium nose bolt material: The bolt temperature during re-entry will rise into the 3000° F range. The primary requirement for the bolt material is the maximum margin of safety on strength at 3000° F. However, the bolt must also have adequate ductility at ambient temperatures to withstand machining without serious surface damage, assembly and handling loads, and powered flight vibration.

Several materials, all refractory metal alloys, have been considered for nose bolt applications, for example:

Tungsten - 25% Rhenium

Tantalum - 10% Tungsten

Tungsten - 2% Molybdenum

T 222 Tantalum Alloy

Compared with Tungsten-25% Rhenium, Tantalum-10% Tungsten is weaker above 3000° F, Tungsten-2% Molybdenum has no ductility below 250°C, and T22 has usable properties to 3500° F but poses a serious availability problem. The most advantageous combination of high temperature strength, ambient temperature ductility, adequate machinability, and commercial availability was provided by wrought

Tungsten-25% Rhenium produced by powder metallurgical methods. Mechanical properties of @-25 Re as determined by several laboratories are as follows:

<u>Temp °F</u>	<u>Ult. Tensile (psi)</u>
R. T.	177,000
3000	30,000
4000	11,000
4500	5,000

Although tungsten alloys oxidize rapidly at temperatures in the 4000°F area, oxidation is not a consideration in this application because of the low oxygen partial pressures that can exist within the graphite nose tip assembly.

3.4.9 SYMBOLS AND SUBSCRIPTS

Symbols

V	Velocity	Ft/sec.
C	Specific heat at constant pressure	BTU/lb °R
h ^p	Enthalpy or altitude	BTU/lb or ft
H	Heat of gas formation	BTU/lb
H ^{gf}	Heat of cracking	BTU/lb
k ^K	Thermal conductivity	BTU/ft-sec °R
M _∞	Mach number	
m	Mass loss rate	lb/ft ² -sec
n	Reaction order	
P	Pressure	lb/ft ²
q	Heat transfer rate	BTU/ft ² -sec
R	Universal gas constant	BTU/lb mole °R
R _N	Nose radius	feet
r _N	Local vehicle radius, normal to roll axis	feet
s	Surface wetted length, from stagnation point	feet
s	Boundary layer gas-char interface velocity	ft/sec
t	Time	seconds
T	Temperature	°R
w	Weight	pounds
ρ	Density	lbs/ft ³
γ	Flight path angle	degrees
μ	Gas viscosity	lb-sec/ft ²
M	Molecular weight	Lb _m /Mole
E	Emissivity	
a	Stephan-Boltzmann Constant	(0.476x10 ⁻¹² BTU/sec-ft ²)
Re	Reynolds number	

Subscripts

B	Mass transfer effect	
e	Edge of boundary layer conditions	
c	Char, also aerodynamic convective heating rate	
g	Decomposition gas	
L	Laminar flow conditions	
o	Uncharred or virgin state	
r	Recovery conditions	
W	Surface or wall conditions	
Δ	Distance from dividing stream line	feet
T	Turbulent flow condition	
RR	Re-radiation	
HGR	Hot gas radiation	
OO	Free-stream conditions	

TABLE 3.4-2. THERMOPHYSICAL PROPERTIES AND REACTION KINETICS CONSTANTS OF
OUTER SHIELD MATERIALS EMPLOYED IN REKAP

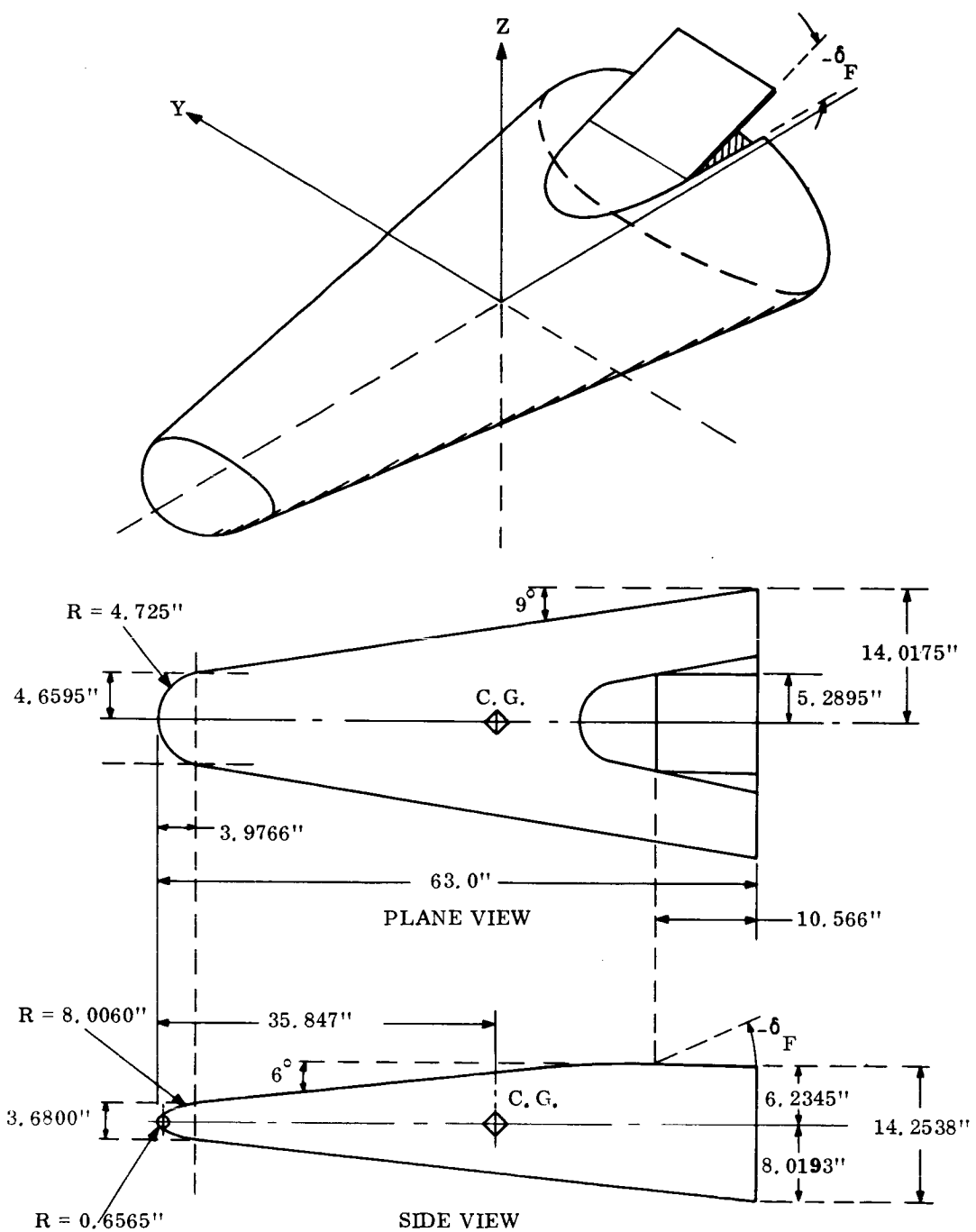
Quantity	Symbol	Units	Phenolic Nylon	Phenolic Refrasil	ATJ Graphite
Virgin Density	P_V	LB/FT ³	75	104	108
Char Density	P_C	LB/FT ³	18.75	87.6	
Char Surface Emissivity	ϵ		0.86	0.80	
Prolysis Gas Specific Heat	C_{pg}	BTU/LB ⁰ R	1.3 to 6.7	.6	
Molecular Weight of Injected Species	\overline{Mg}		28	34	
Order of Reaction	η		3	2	
Pre-exponential Factor	Z	Sec ⁻¹	44, 500, 000	.001 to 1300	
Activation Energy	ΔE	BTU/LB Mole	57, 000	1200 to 33500	
Heat of Decomposition	Hg_f	BTU/LB	1000	400	$K_1 = 0$
			1000	400	$K_2 = 5.88$
			1000	400	
			1000	400	
Specific Heat	C_p	BTU/LB ⁰ R	600 ⁰ R 0.378 710 ⁰ R 0.42 1210 ⁰ R 0.49 2075 ⁰ R 0.52	600 ⁰ R 0.22 710 ⁰ R 0.24 1210 ⁰ R 0.35 2075 ⁰ R 0.5	500 ⁰ R 0.13 800 ⁰ R 0.25 1000 ⁰ R 0.31 2000 ⁰ R 0.44
Conductivity	K_v	BTU/FT-SEC ⁰ R	610 ⁰ R .000038 860 ⁰ R .000038 1335 ⁰ R .000038 1710 ⁰ R .000039 1335 ⁰ R .000456 1710 ⁰ R .0000468	610 ⁰ R .00009 860 ⁰ R .00009 1335 ⁰ R .00009 1710 ⁰ R .00009 1335 ⁰ R .000126 1710 ⁰ R .000126	500 ⁰ R .0181 800 ⁰ R .0165 1000 ⁰ R .0154 2000 ⁰ R .0099
Virgin					
Char	K_c	BTU/FT-SEC ⁰ R	2200 ⁰ R .0000576	2210 ⁰ R .000126	

TABLE 3.4-2. THERMOCOPHYSICAL PROPERTIES AND REACTION KINETICS CONSTRAINTS OF
OUTER SHIELD MATERIALS EMPLOYED IN REKAP Concluded

Quantity	Symbol	Units	ESM 1004 AP	NASA E4A1
Virgin Density	P_v	LB/FT ³	36	41.8
Char Density	P_c	LB/FT ³	14.4	16.7
Char Surface Emissivity	ϵ		0.9	0.62
Pyrolysis Gas Specific Heat	Cpg	BTU/LB °R	0.384	0.4
Molecular Weight of Injected Species	$\overline{M_g}$		24.5	29.2
Order of Reaction	n	Sec ⁻¹	2	1
Pre-exponential Factor	Z		30,000	390,000
Activation Energy	ΔE	BTU/LB Mole	47,500	39,760
Heat of Decomposition		BTU/LB		
1335°R			50	1000
1460°R			450	1000
1710°R			1000	1000
2610°R			1960	1000
Specific Heat	c_p	BTU/LB °R		
600°R			600°R 0.305	600°R 0.34
710°R			710°R 0.360	710°R 0.34
1210°R			1210°R 0.440	1210°R 0.34
2075°R			2075°R 0.440	2075°R 0.34
Conductivity	K_v	BTU/FT-SEC°R		
Virgin				
610°R			610°R .0000237	500°R .0000208
860°R			860°R .0000220	900°R .0000208
1335°R			1335°R .0000210	1300°R .0000274
1710°R			1710°R .0000231	1800°R .00004
Char	K_c	BTU/FT-SEC°R		
1335°R			1335°R .0000777	1300°R .0000274
1710°R			1710°R .0000855	1800°R .000040
2210°R			2210°R .0000104	2250°R .000050

TABLE 3.4-3. THERMOPHYSICAL PROPERTIES OF STRUCTURAL MATERIALS EMPLOYED IN REKAP

Quantity	Symbol	Units	Fiberglass Face	Honeycomb Core	Aluminum
Virgin Density	ρ_v	LB/FT ³	119	1.74	169
Specific Heat	C_p	BTU/LB ⁰ R	0.247 0.247 0.247 0.247	600 ⁰ R 0.28 710 ⁰ R 0.28 1210 ⁰ R 0.28 2075 ⁰ R 0.28	500 ⁰ R 0.212 800 ⁰ R 0.238 1000 ⁰ R 0.25 1500 ⁰ R 0.284
Conductivity	K_v	BTU/FT-SEC ⁰ R	0.00064 0.00064 0.00064 0.00064	500 ⁰ R 0.0001134 800 ⁰ R 0.0001134 1000 ⁰ R 0.0001134 2000 ⁰ R 0.0001134	500 ⁰ R 0.0365 800 ⁰ R 0.0339 1000 ⁰ R 0.0322 2000 ⁰ R 0.0297
Quantity	Symbol	Units	Tungsten	Pyrolytic Graphite	Beryllium
Virgin Density	ρ_v	LB/FT ³	1210	108	113.6 to 104.7
Specific Heat	C_p	BTU/LB ⁰ R	760 ⁰ R 0.0327 960 ⁰ R 0.0335 1460 ⁰ R 0.0346 1960 ⁰ R 0.0360	500 ⁰ R 0.13 800 ⁰ R 0.25 1000 ⁰ R 0.31 2000 ⁰ R 0.44	560 ⁰ R 0.473 860 ⁰ R 0.56 1260 ⁰ R 0.628 1860 ⁰ R 0.7
Conductivity	K_v	BTU/FT-SEC ⁰ R	760 ⁰ R 0.0236 960 ⁰ R 0.0224 1460 ⁰ R 0.02037 1960 ⁰ R 0.01897	500 ⁰ R .000145 800 ⁰ R .000135 1000 ⁰ R .000128 2000 ⁰ R .000095	560 ⁰ R .0288 860 ⁰ R .0266 1260 ⁰ R .0168 1860 ⁰ R .0122



NOTES:

1. ALL CROSS-SECTIONS ARE ELLIPTICAL
2. \diamond CENTER OF GRAVITY.
3. VEHICLE REFERENCE AREA = 7.8661 FT²

Figure 3.4-1. - Basic Dimensional Configuration

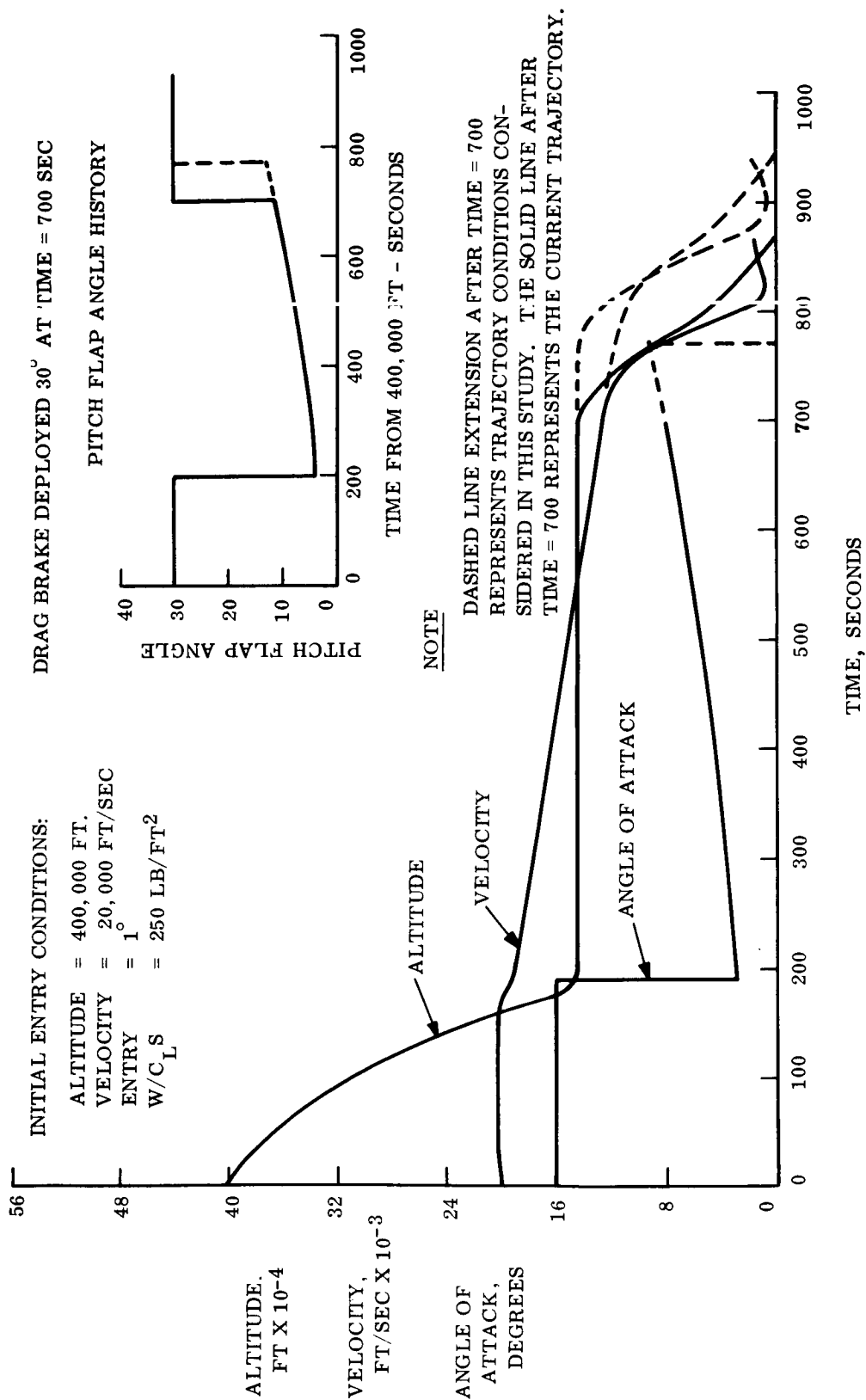


Figure 3.4-2. - One-Degree Entry Trajectory and Angle of Attack History

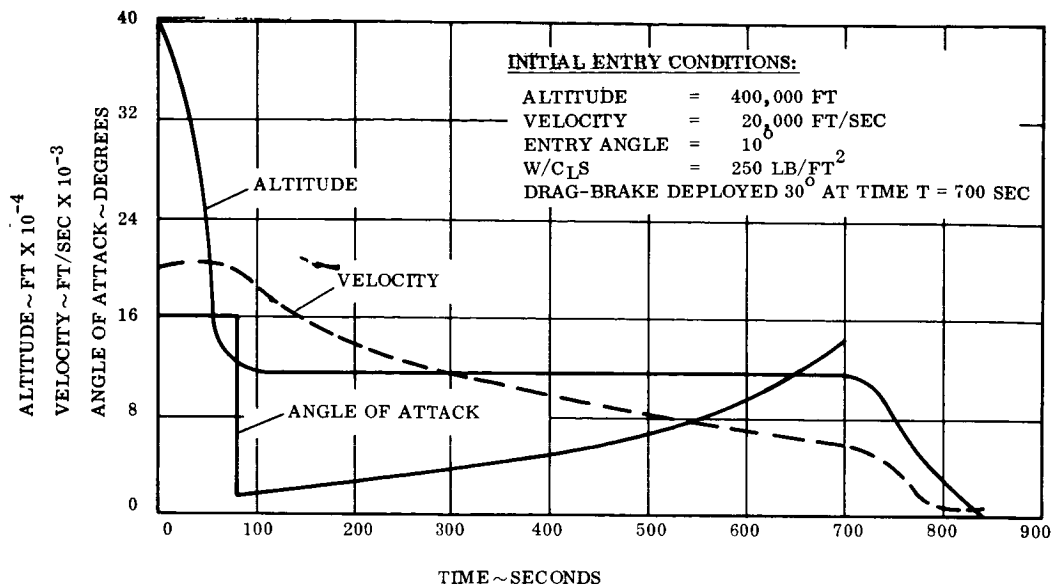


Figure 3.4-3. - Ten-Degree Entry Trajectory and Angle of Attack History

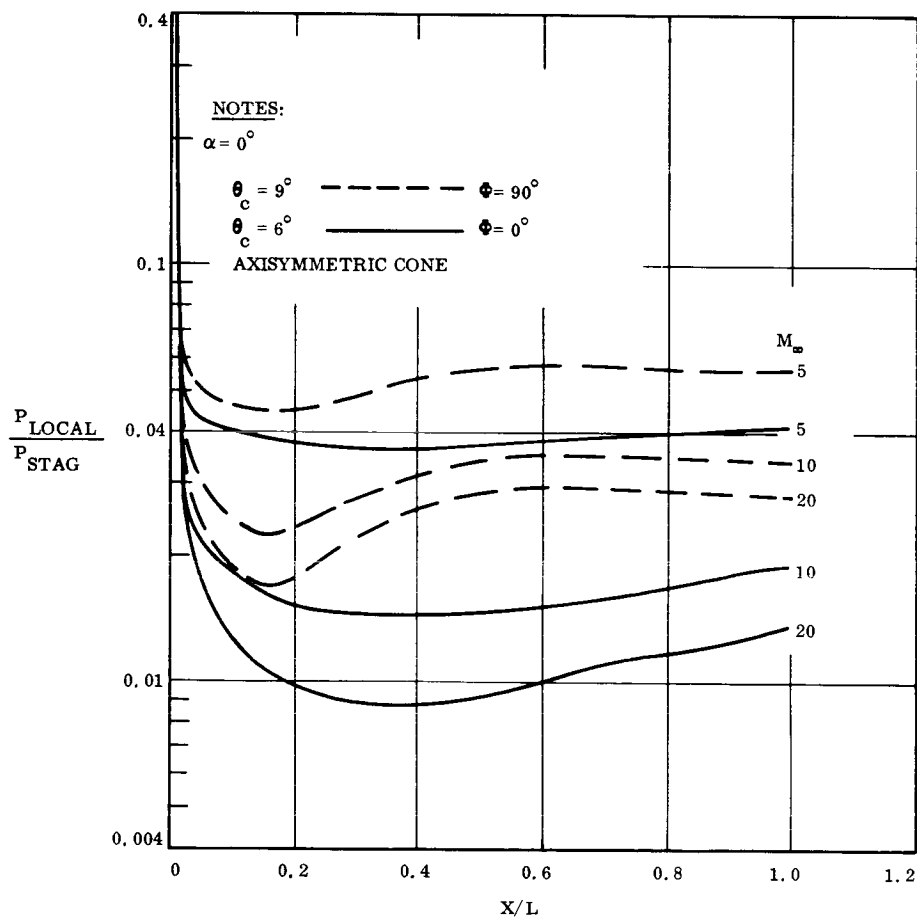


Figure 3.4-4. Pressure-Ratio Distribution for Zero Angle of Attack

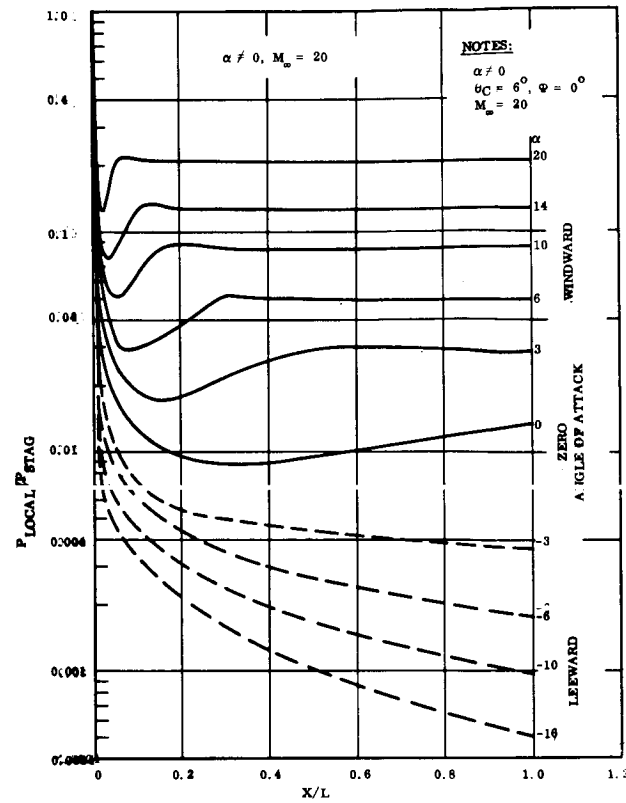


Figure 3.4-5. - Pressure-Ratio Distribution for Angle of Attack Not Equal to Zero at Mach 20

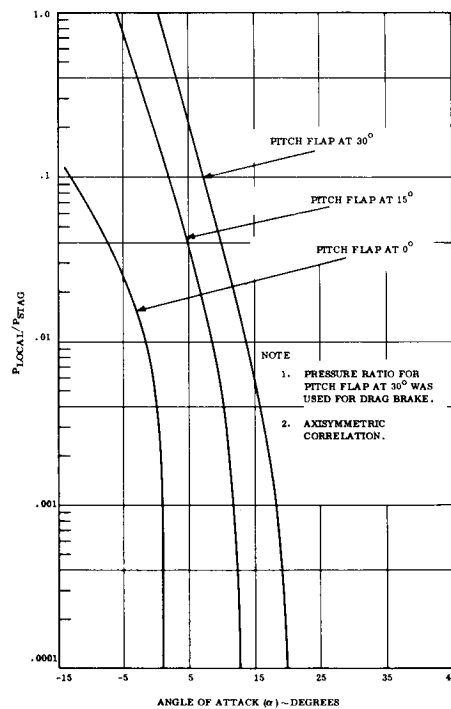


Figure 3.4-6. - Pitch-Flap and Drag-Brake Pressure-Ratio Distribution at Mach 20

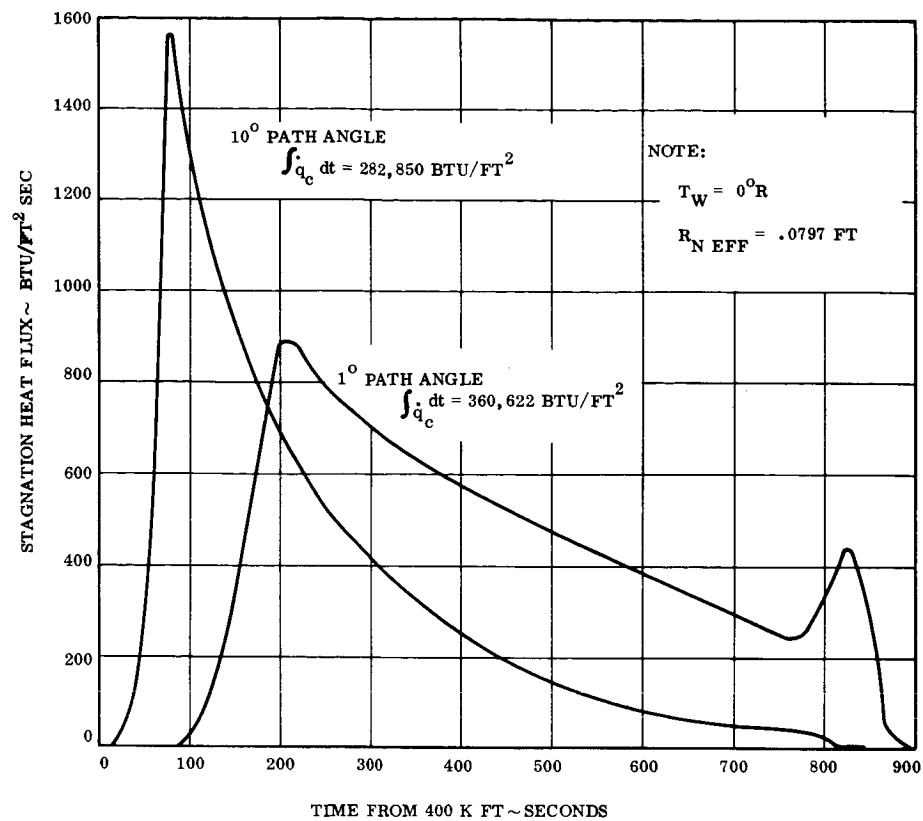


Figure 3.4-7. - Stagnation Point Convective Heating Histories

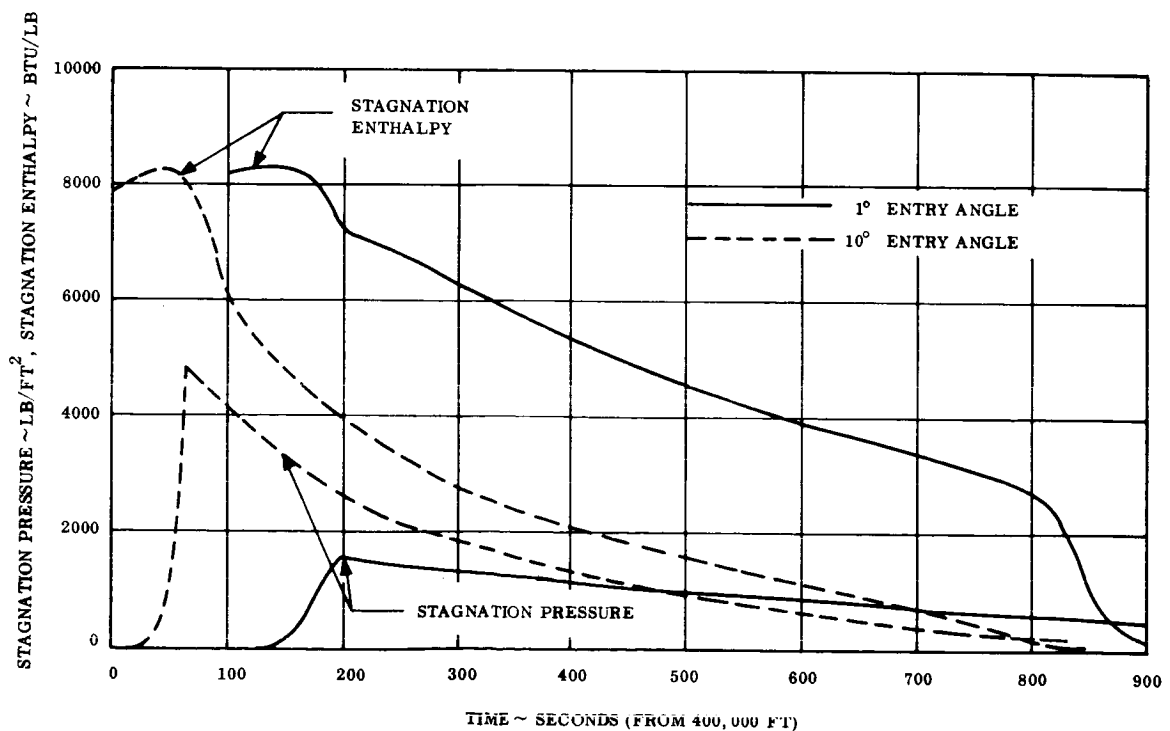


Figure 3.4-8. Stagnation Point Pressure and Enthalpy Histories

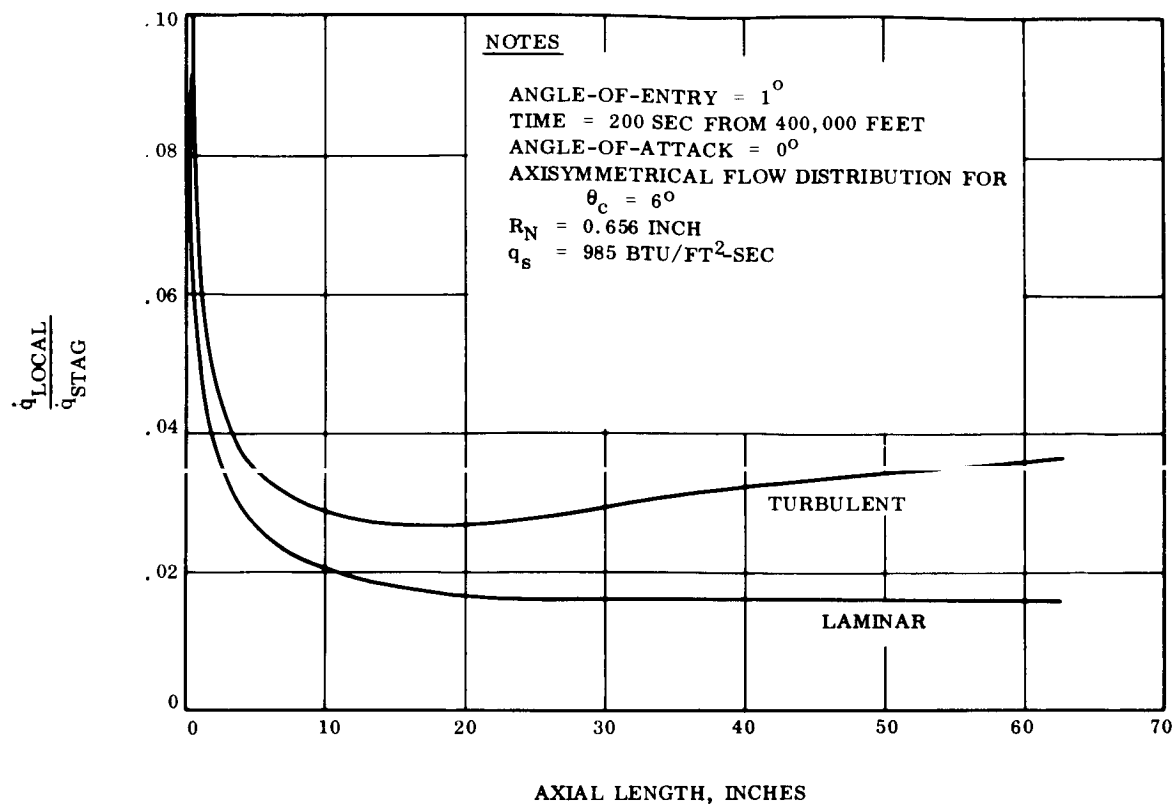


Figure 3.4-9. - Laminar and Turbulent Convective Heat Flux Distribution at Time of Maximum Heating

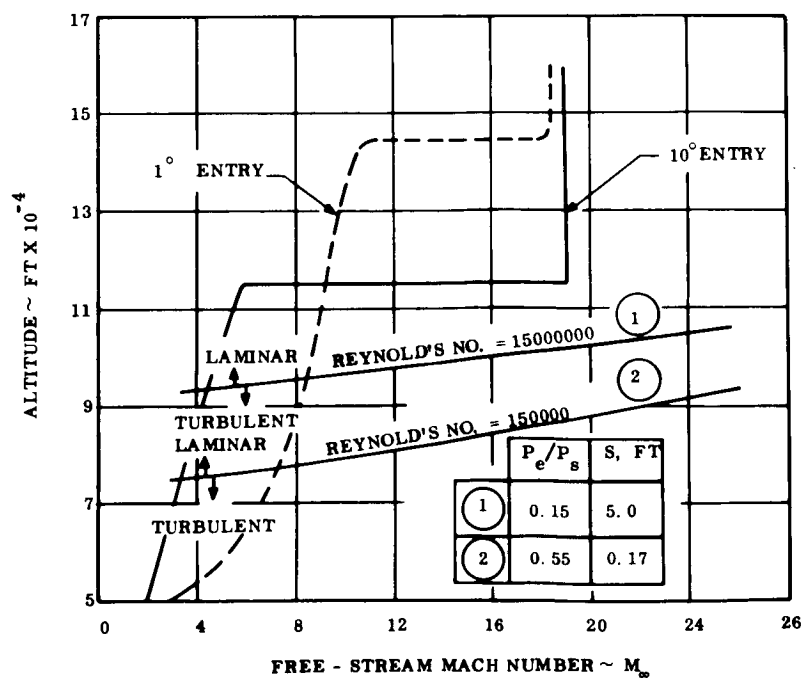


Figure 3.4-10. - Boundary Layer Transition Criteria

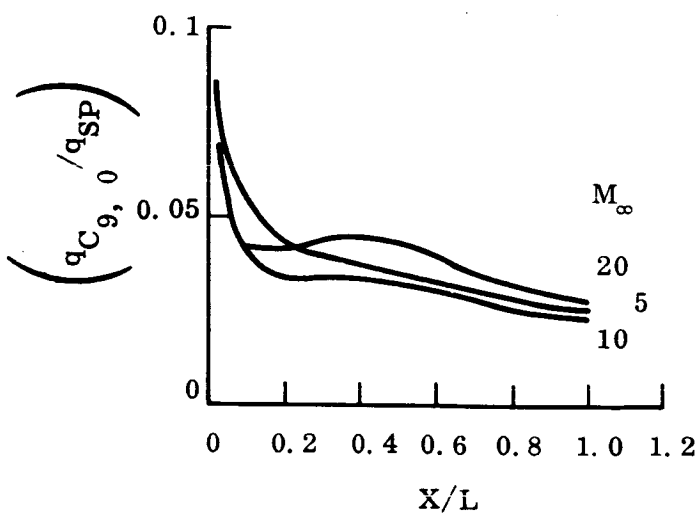
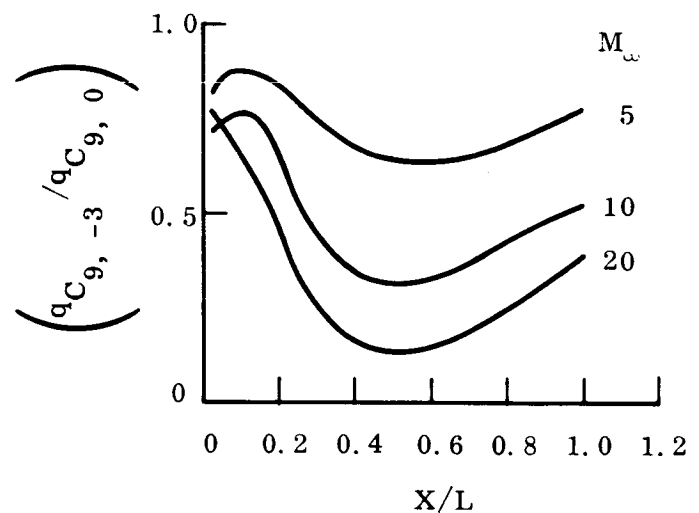
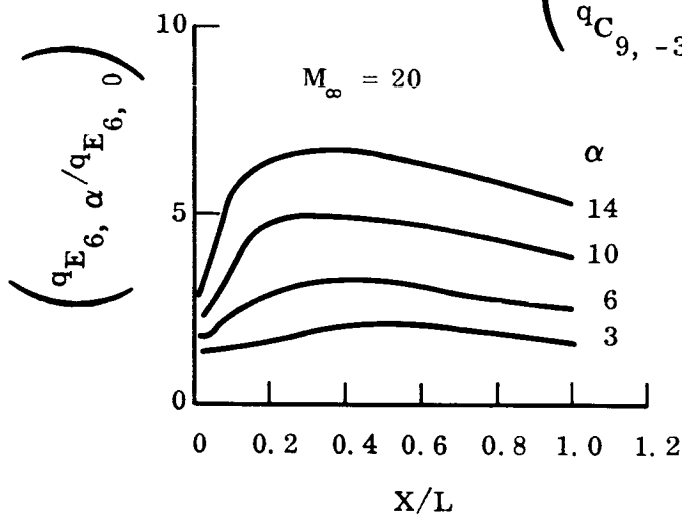
NOMENCLATURE:

$q_{j_e, \alpha} \sim$ HEAT TRANSFER RATE TO A BODY OF
HALF-ANGLE, θ , AT ANGLE-OF-ATTACK, α
 $j \sim E, C, SP$

$E \sim$ ELLIPTICAL CROSS-SECTION BODY (SLAMAST)
 $C \sim$ CIRCULAR CROSS-SECTION BODY (CONE)
 $SP \sim$ STAGNATION POINT

$$q_{E_6, \alpha} = \left(\frac{q_{E_6, \alpha}}{q_{E_6, 0}} \right) \left(\frac{q_{E_6, 0}}{q_{C_9, -3}} \right) \left(\frac{q_{C_9, -3}}{q_{C_9, 0}} \right) \left(\frac{q_{C_9, 0}}{q_{SP}} \right) q_{SP}$$

WHERE $\left(\frac{q_{E_6, 0}}{q_{C_9, -3}} \right) = 1.0$



$q_{SP} \sim$ OBTAINED FOR A GIVEN
TRAJECTORY AND NOSE RADIUS
 $L = 63$ INCHES, TOTAL LENGTH

Figure 3.4-11. - Heating Correlations to the Windward Meridian, 1° Entry

NOMENCLATURE:

$q_{j\theta,\alpha} \sim$ HEAT TRANSFER RATE TO A BODY OF HALF-ANGLE, θ , AT ANGLE-OF-ATTACK, α

$j \sim$ E, C, SP

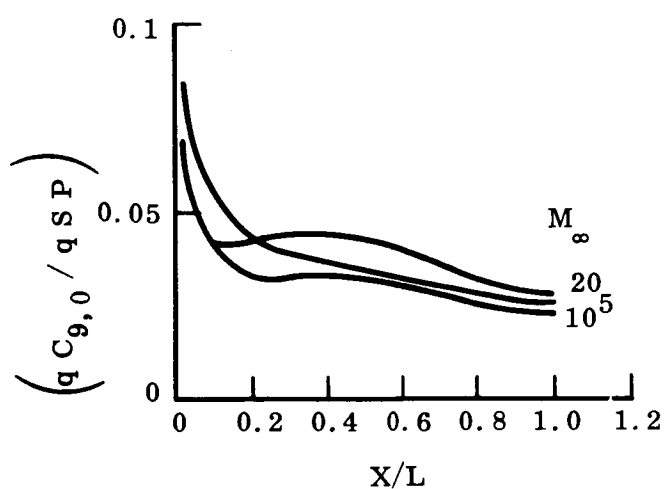
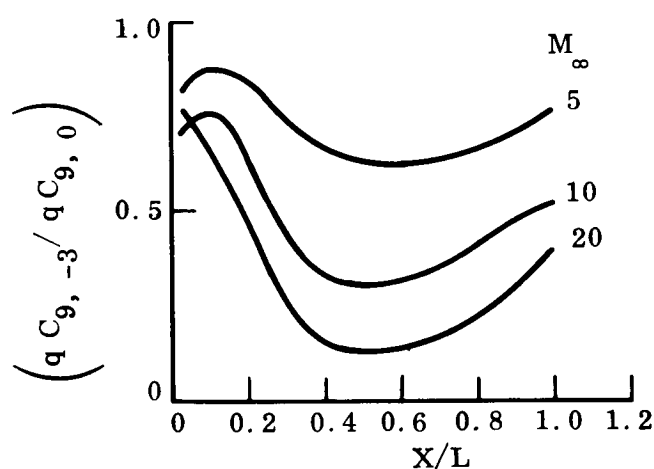
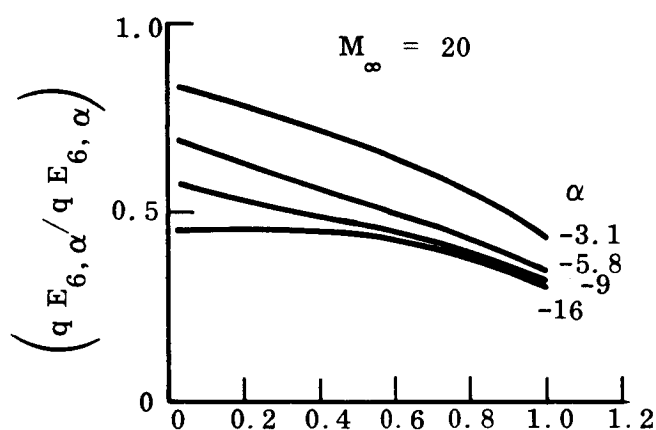
E \sim ELLIPTICAL CROSS-SECTION BODY (SLAMAST)

C \sim CIRCULAR CROSS-SECTION BODY (CONE)

SP \sim STAGNATION POINT

$$q_{E,6,\alpha} = \left(\frac{q_{E,6,\alpha}}{q_{E,6,0}} \right) \left(\frac{q_{E,6,0}}{q_{C,9,-3}} \right) \left(\frac{q_{C,9,-3}}{q_{C,9,0}} \right) \left(\frac{q_{C,9,0}}{q_{SP}} \right) q_{SP}$$

WHERE $\left(\frac{q_{E,6,0}}{q_{C,9,-3}} \right)$



$q_{SP} \sim$ OBTAINED FOR A GIVEN TRAJECTORY & NOSE RADIUS

L = 63 INCHES, TOTAL LENGTH

Figure 3.4-12. Heating Correlations to the Leeward Meridian, 1° Entry

NOMENCLATURE:

$q_{j\theta, \alpha} \sim$ HEAT TRANSFER RATE TO A BODY OF
HALF-ANGLE, θ , AT ANGLE-OF-ATTACK, α
 $j \sim E, C, SP$

$E \sim$ ELLIPTICAL CROSS-SECTION BODY (SLAMAST)

$C \sim$ CIRCULAR CROSS-SECTION (CONE)

$SP \sim$ STAGNATION POINT

$$q_{E9, \alpha} = \left(\frac{q_{E9, \alpha}}{q_{E9, 0}} \right) \left(\frac{q_{E9, 0}}{q_{C6, +3}} \right) \left(\frac{q_{C6, +3}}{q_{C6, 0}} \right) \left(\frac{q_{C6, 0}}{q_{SP}} \right) q_{SP}$$

$$\text{where } \left(\frac{q_{E9, 0}}{q_{C6, +3}} \right) = \left(\frac{q_{E9, \alpha}}{q_{E9, 0}} \right) = 1.0$$

$q_{SP} \sim$ OBTAINED FOR A GIVEN
TRAJECTORY AND NOSE RADIUS

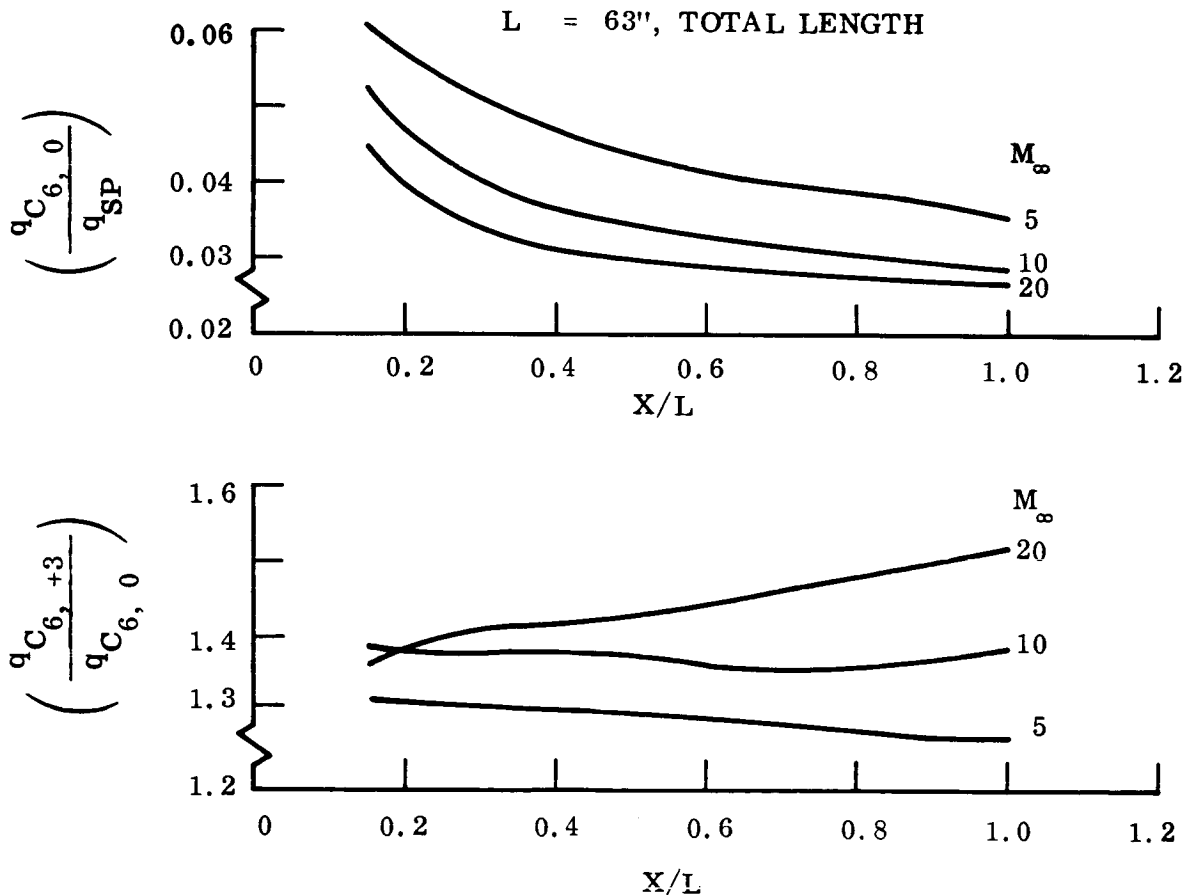


Figure 3.4-13. - Heating Correlations to the Sideward Meridian, 1° Entry

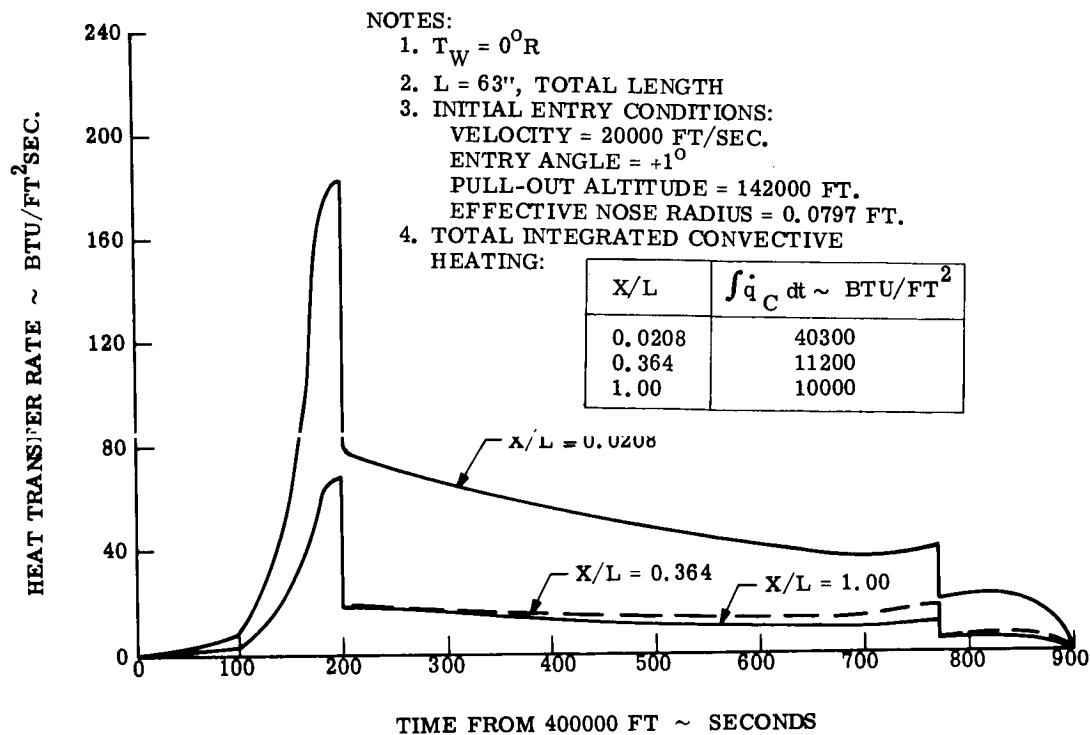


Figure 3.4-14. - Convective Heat Transfer Rates, 1° Entry, Windward Ray

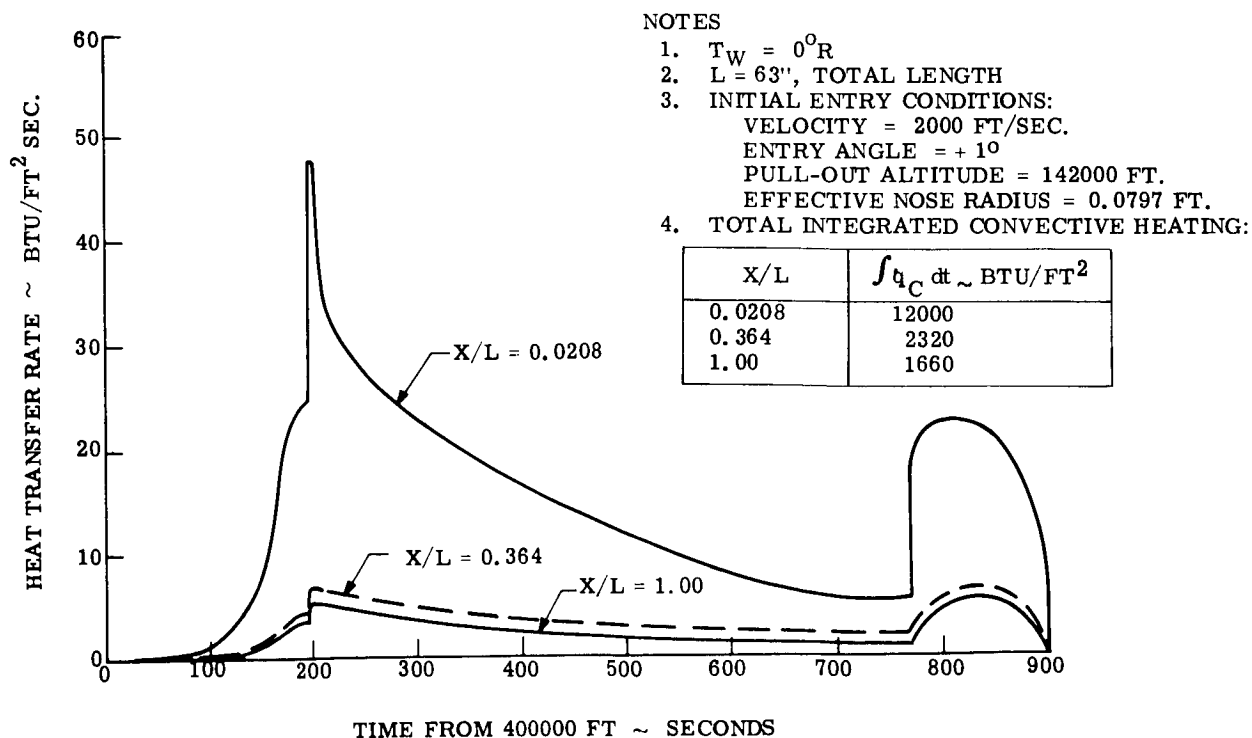


Figure 3.4-15. - Convective Heat Transfer Rates, 1° Entry, Leeward Ray

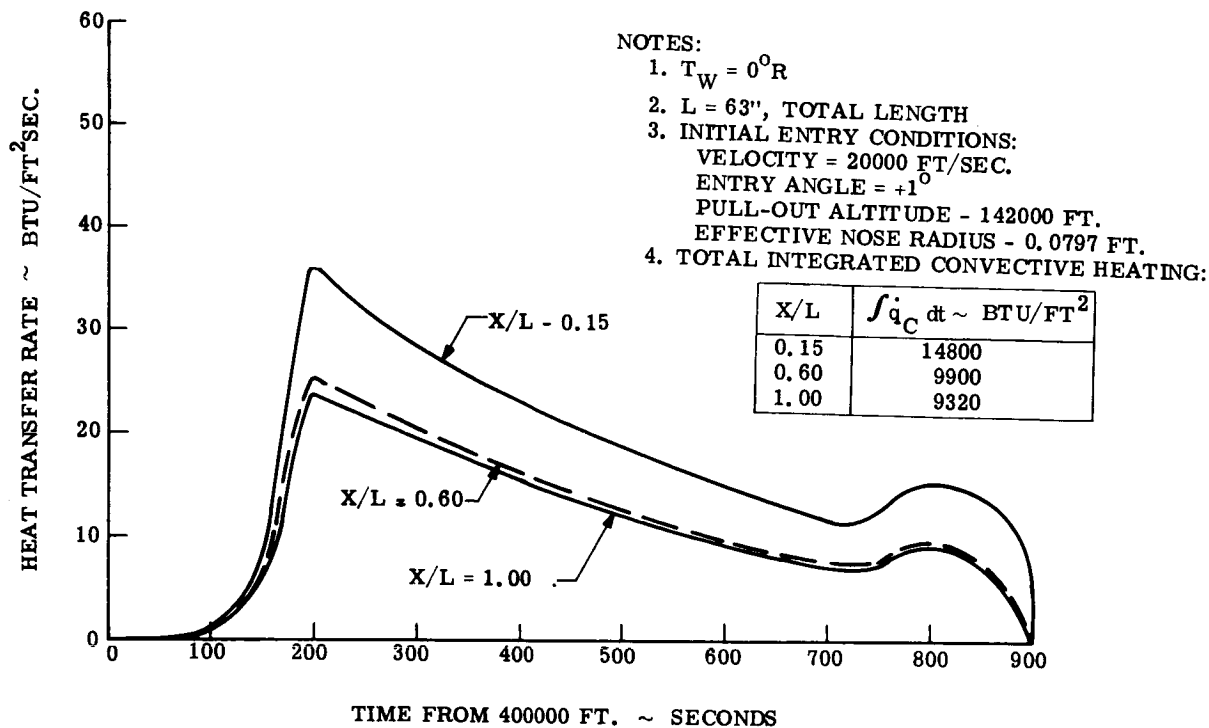


Figure 3.4-16. - Convective Heat Transfer Rates, 1° Entry, Sideward Ray

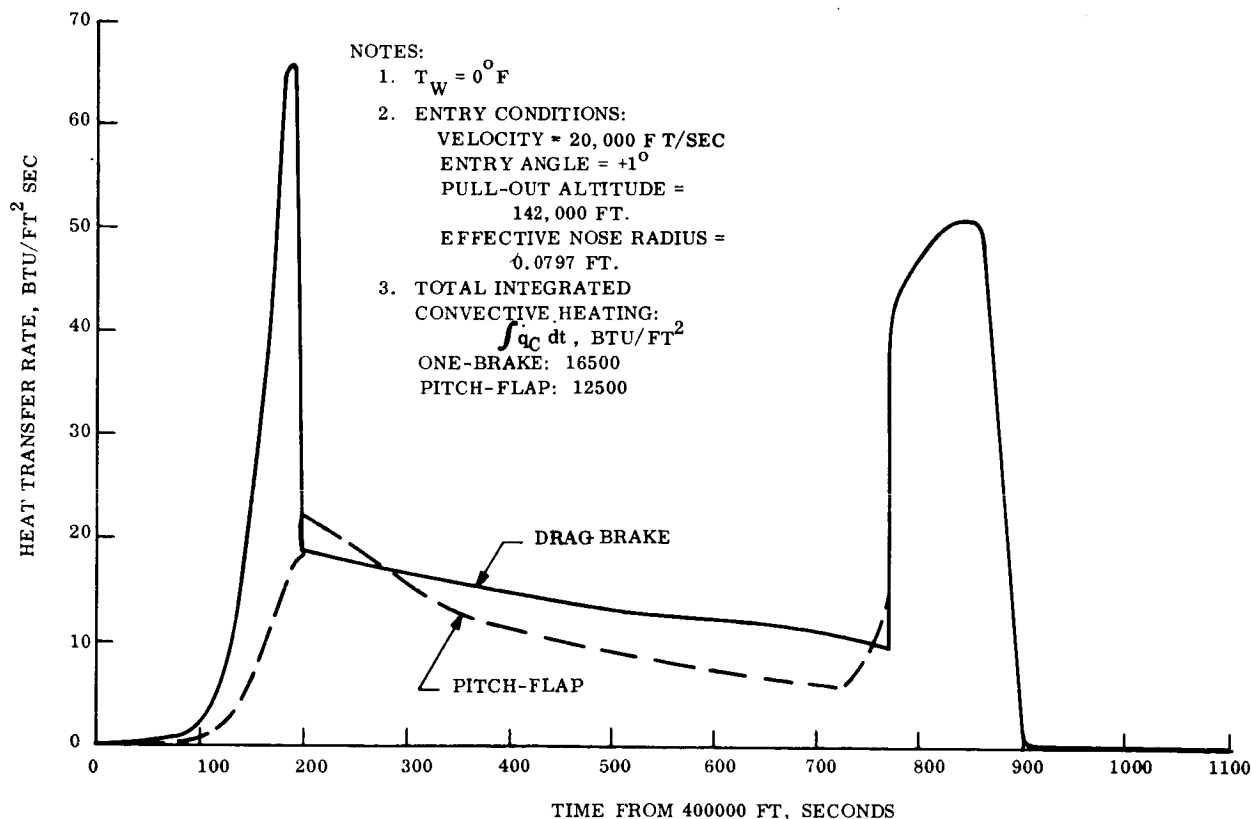


Figure 3.4-17. - Convective Heat Transfer Rates, 1° Entry, Drag Brake and Pitch Flap

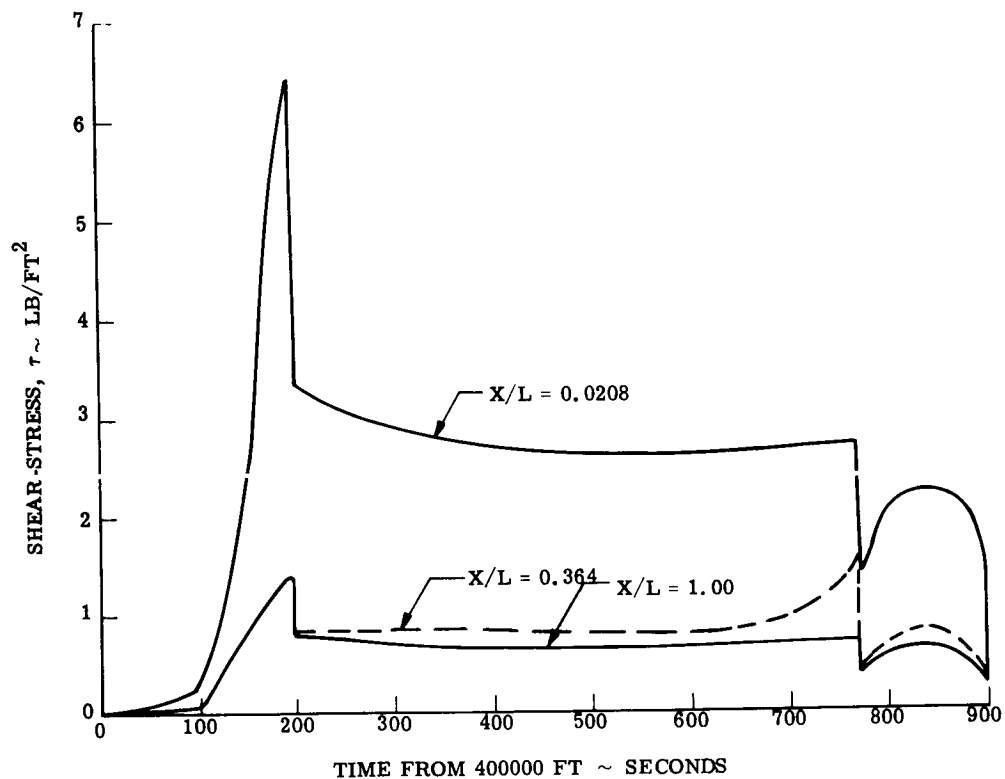


Figure 3.4-18. - Windward Ray Shear-Stress Histories, 1° Entry

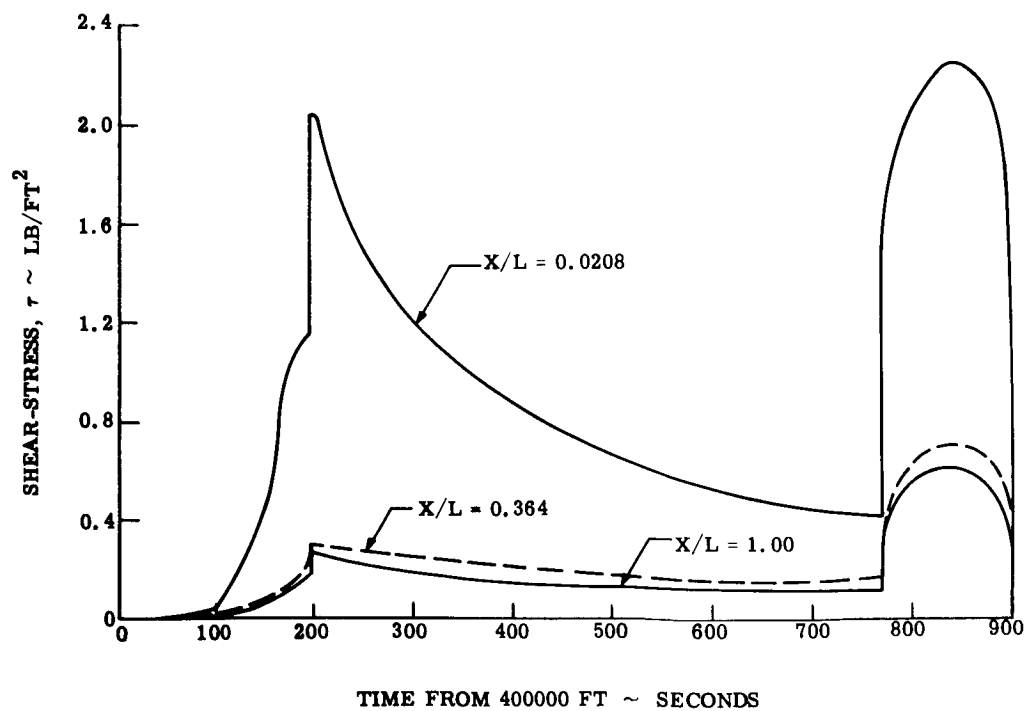


Figure 3.4-19. - Leeward Ray Shear-Stress Histories, 1° Entry

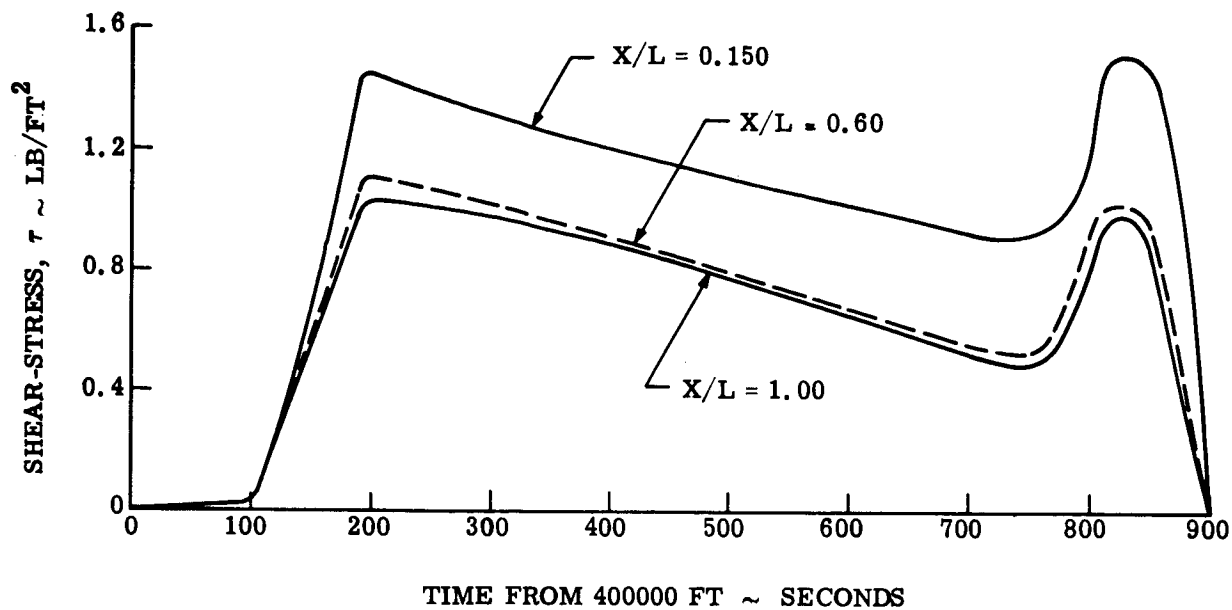


Figure 3.4-20. - Sideward Ray Shear-Stress Histories, 1° Entry

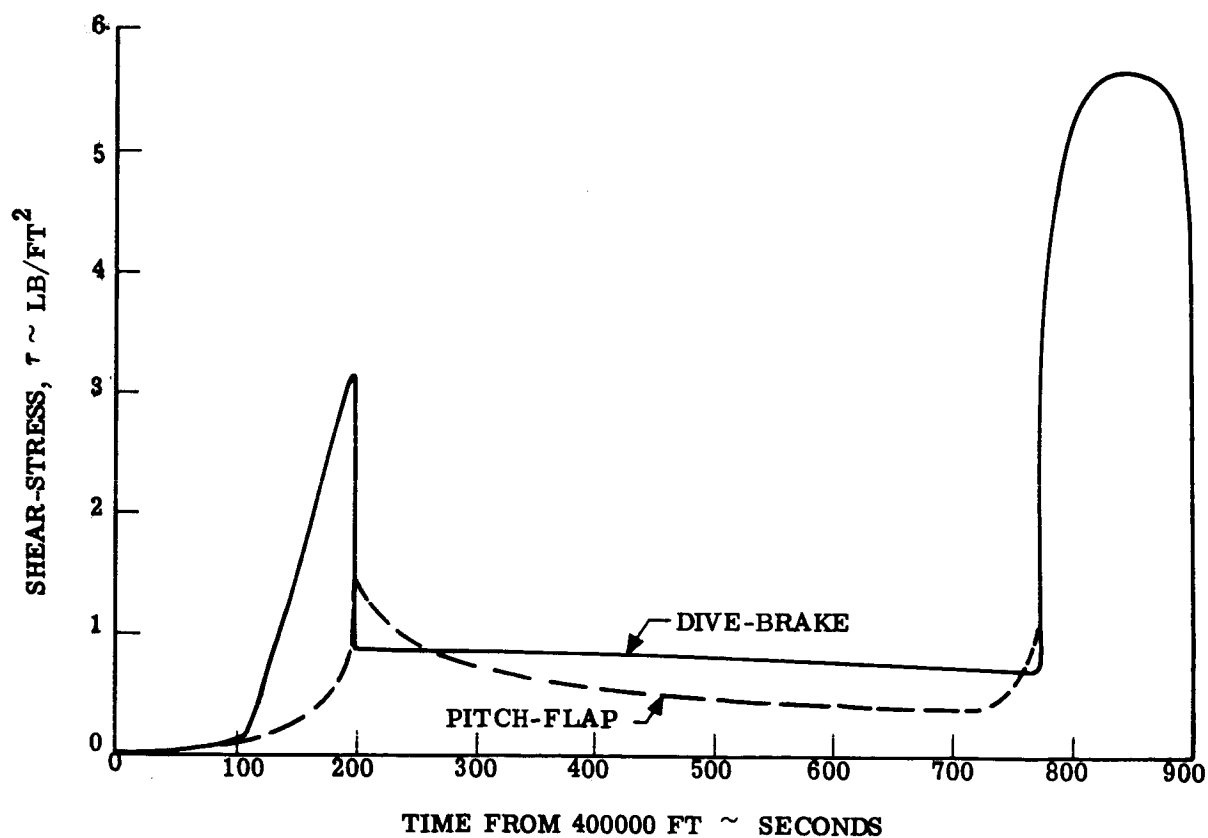


Figure 3.4-21. - Drag Brake and Pitch Flap Shear-Stress Histories, 1° Entry

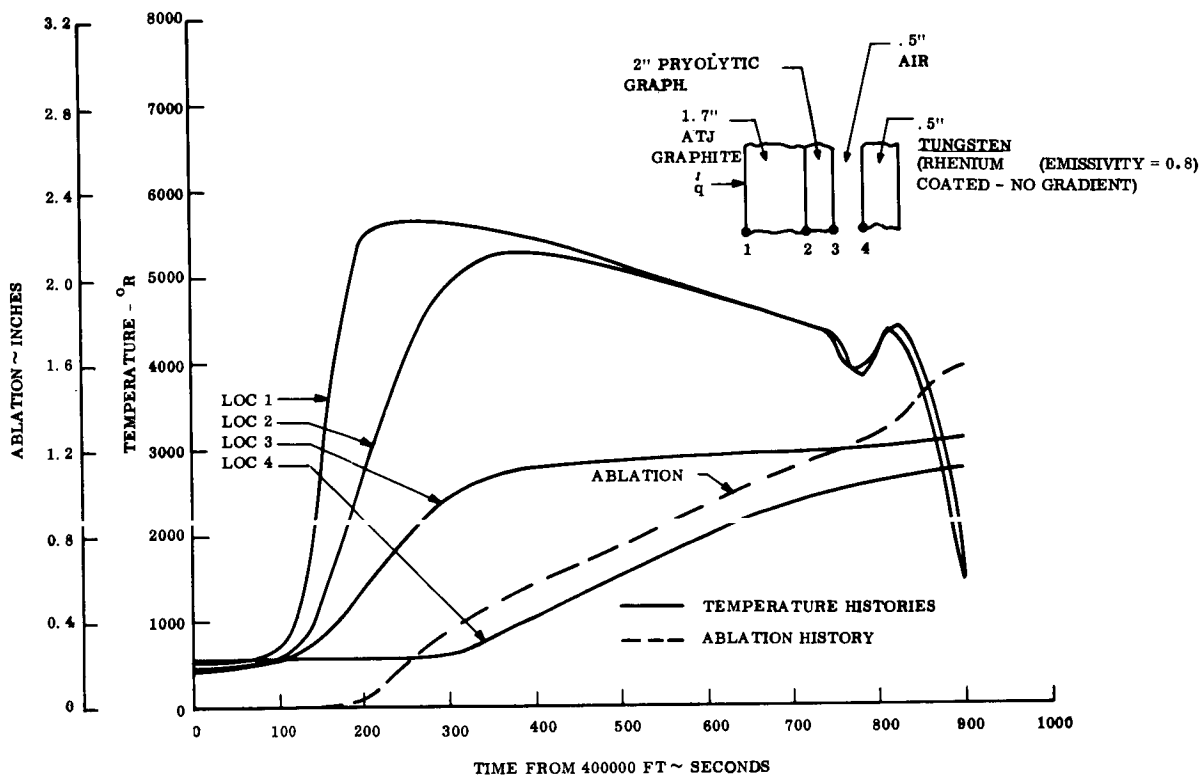


Figure 3.4-22. - Nose Cap Stagnation Point ATJ Graphite Temperature and Ablation Histories, 1° Entry

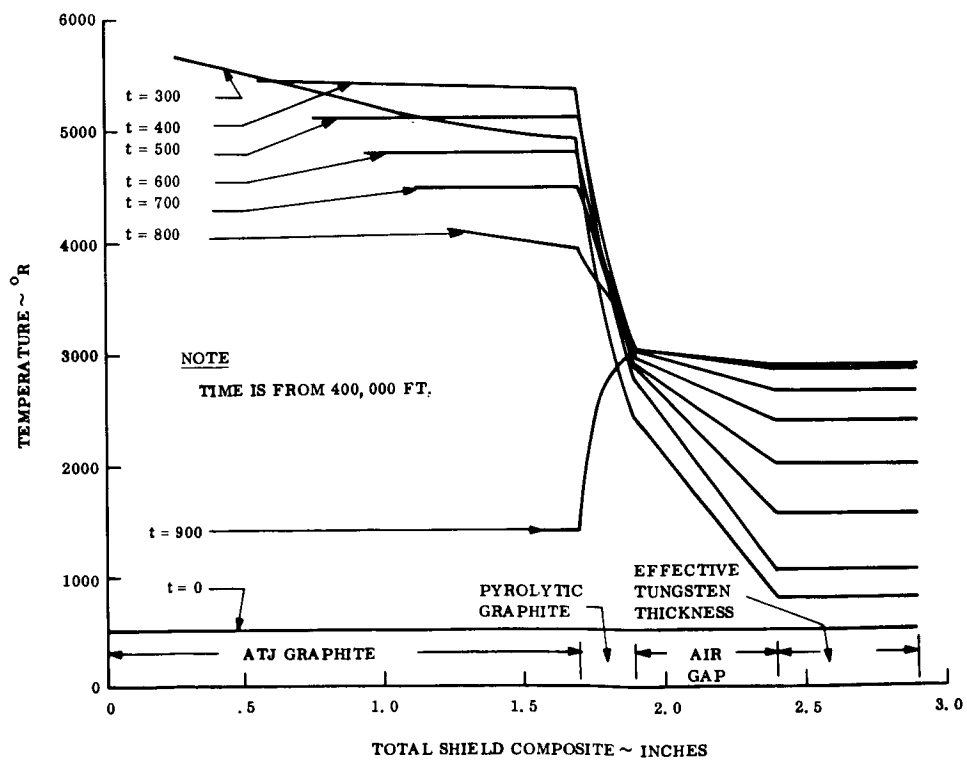


Figure 3.4-23. - Nose Cap Stagnation Point ATJ Graphite Temperature Profiles, 1° Entry

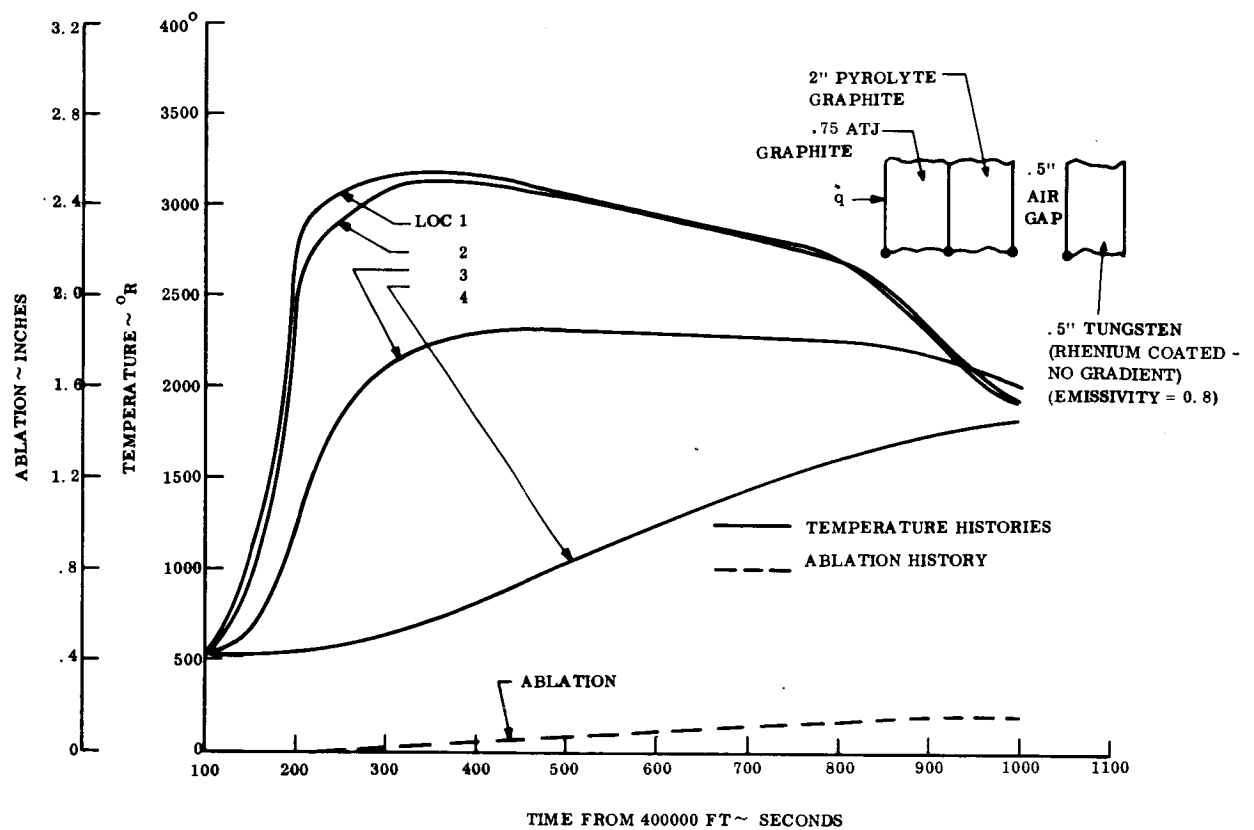


Figure 3.4-24. - Nose Cap ATJ Graphite Temperature and Ablation Histories, $x/l = 0.0208$, Windward, 1° Entry

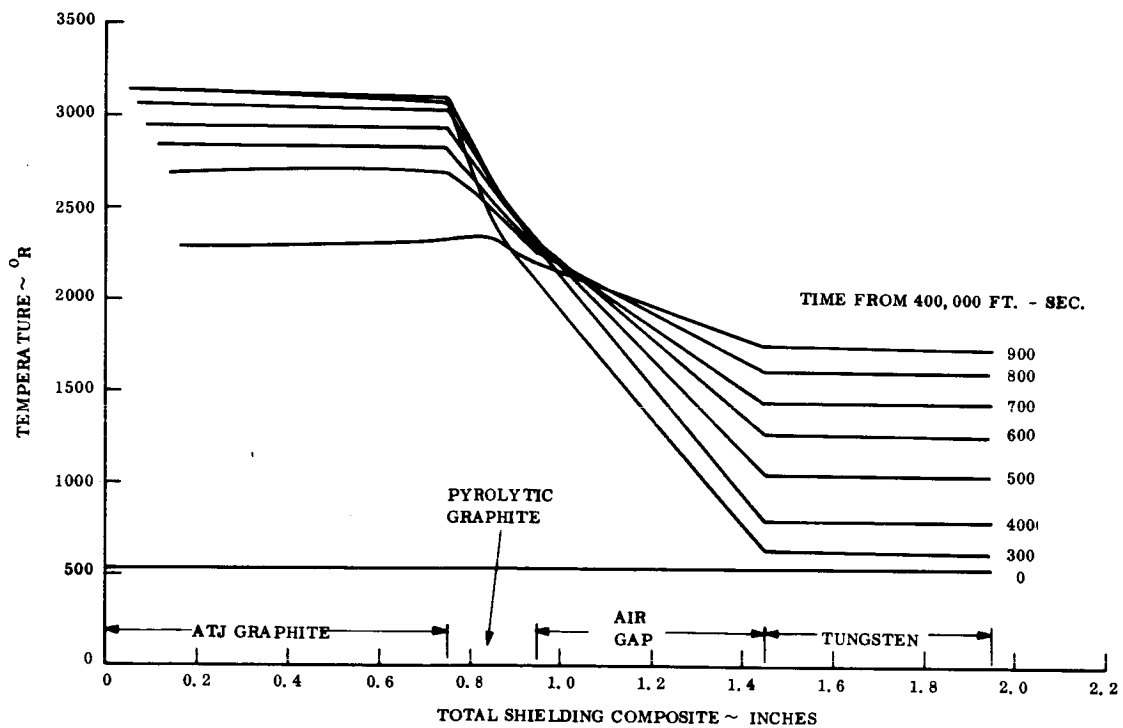


Figure 3.4-25. - Nose Cap ATJ Graphite Temperature Profiles, $x/l = 0.0208$, Windward 1° Entry

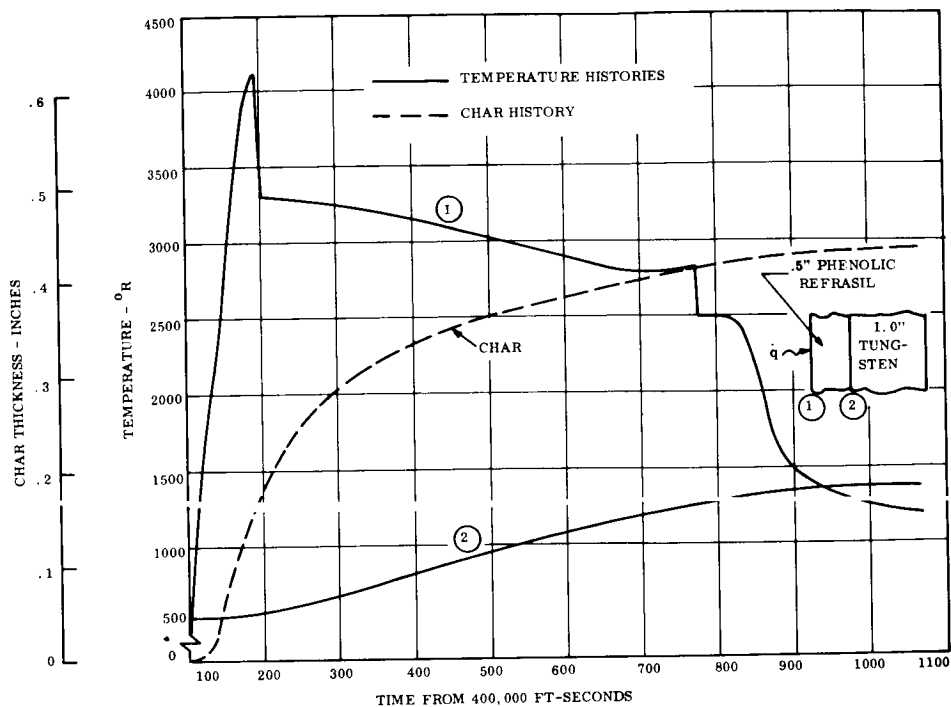


Figure 3.4-26. - Nose Cap Phenolic Refrasil Temperature and Degradation Histories, $x/l = 0.0208$, Windward 1° Entry

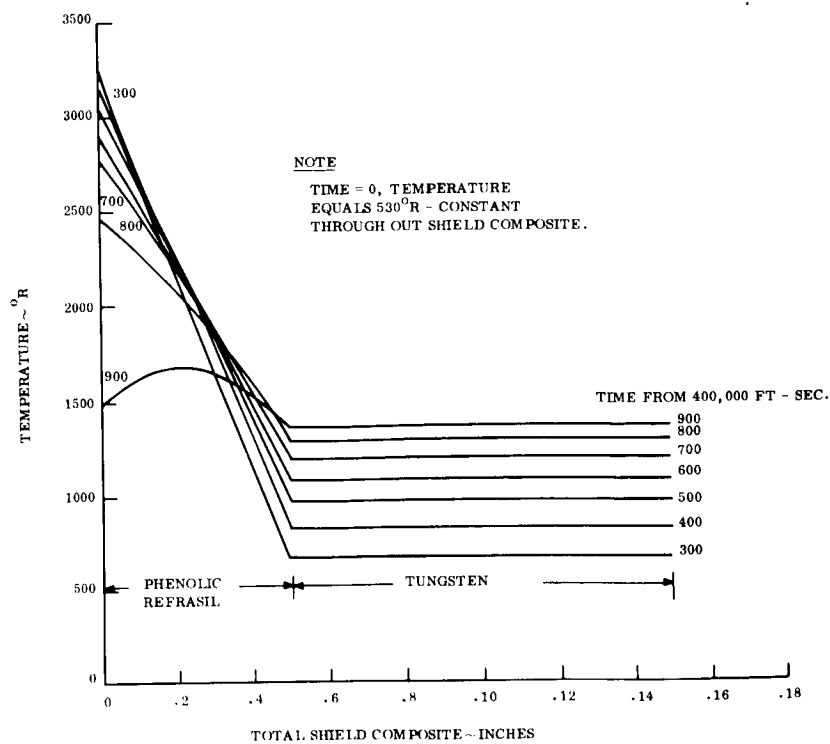


Figure 3.4-27. - Nose Cap Phenolic Refrasil Temperature Profiles, $x/l = 0.0208$, Windward 1° Entry

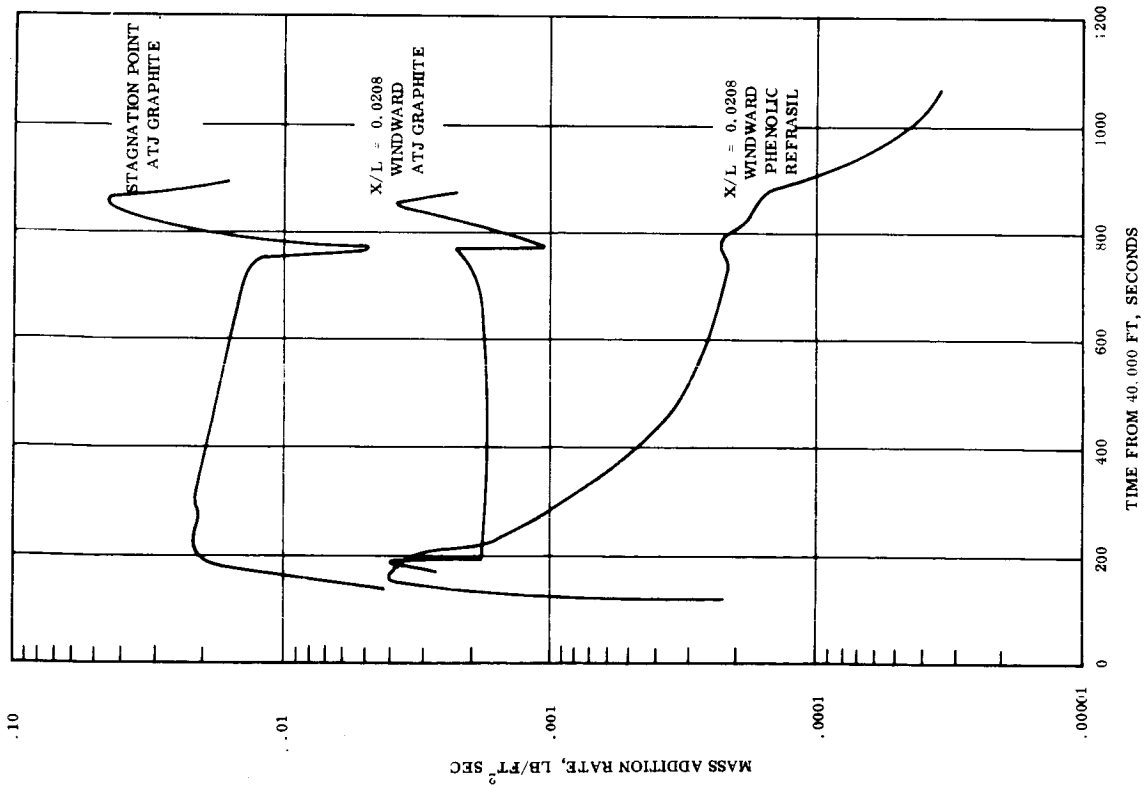


Figure 3.4-28. - Nose Cap ATJ Graphite and Phenolic Refrasil Total Mass Addition Histories, 1° Entry

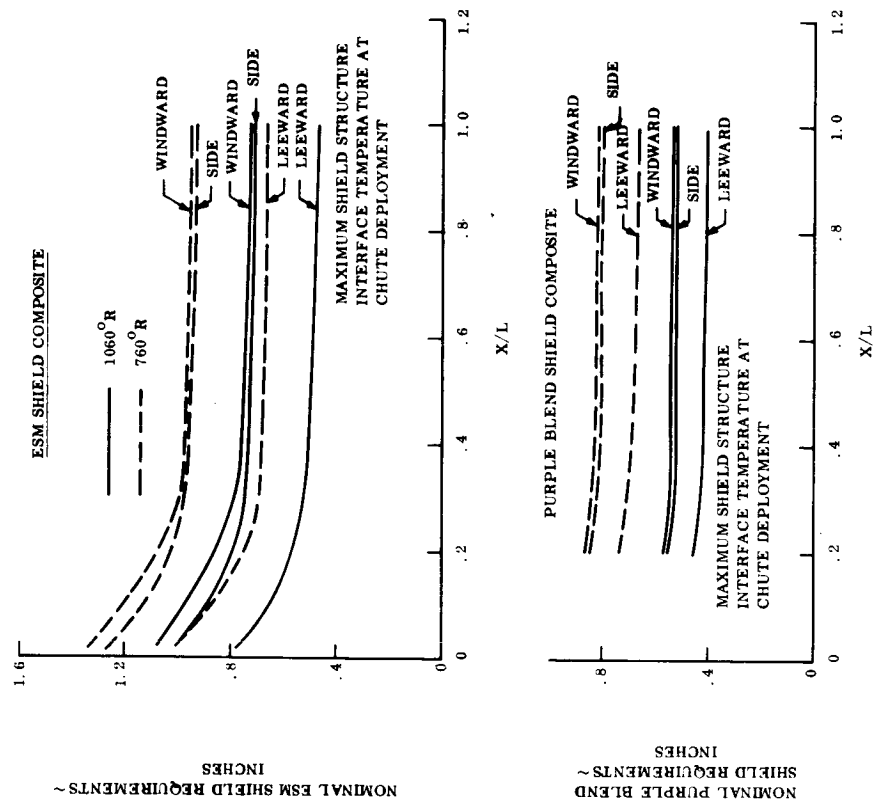


Figure 3.4-29. - Skirt-Nominal Shield Requirements for ESM and Purple Blend as a Function of x/l , 1° Entry

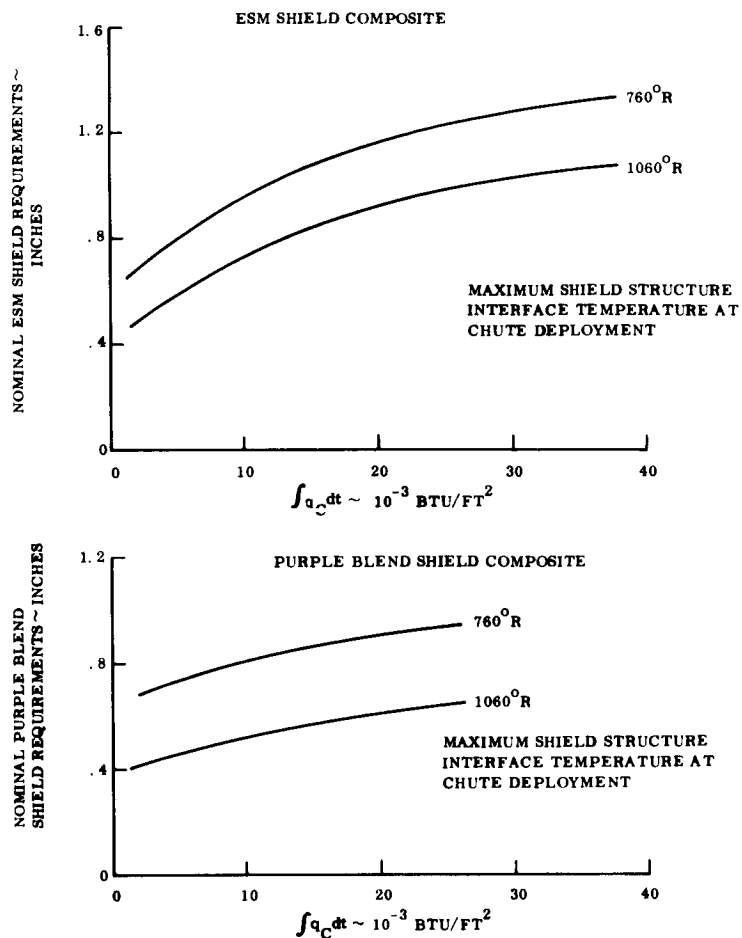


Figure 3.4-30. - Skirt-Nominal Shield Requirements for ESM and Purple Blend as a Function of Total Integrated Convective Heating, 1° Entry - Windward, Leeward, and Side

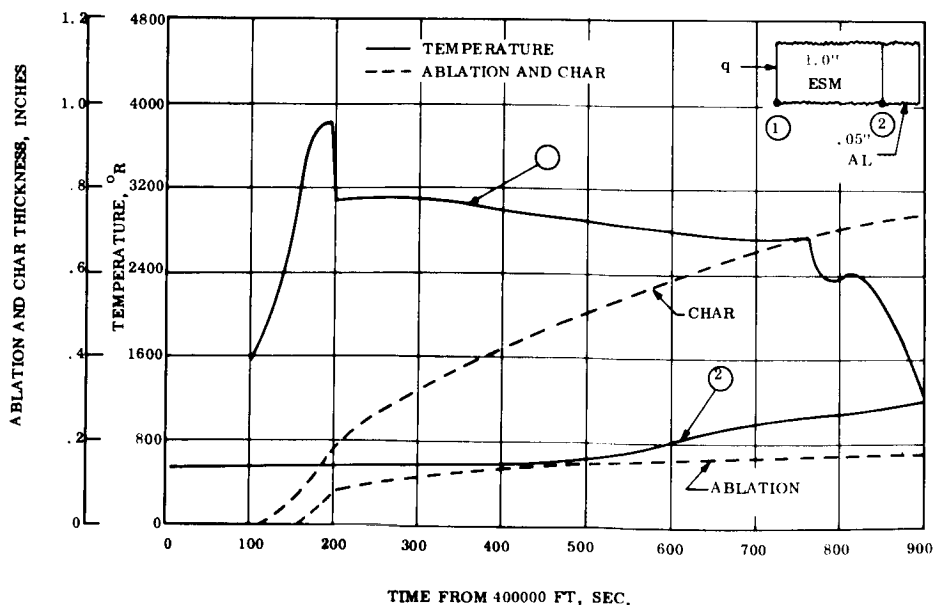


Figure 3.4-31. - Skirt-ESM-Temperature and Degradation Histories, $x/l = 0.0208$, Windward, 1° Entry

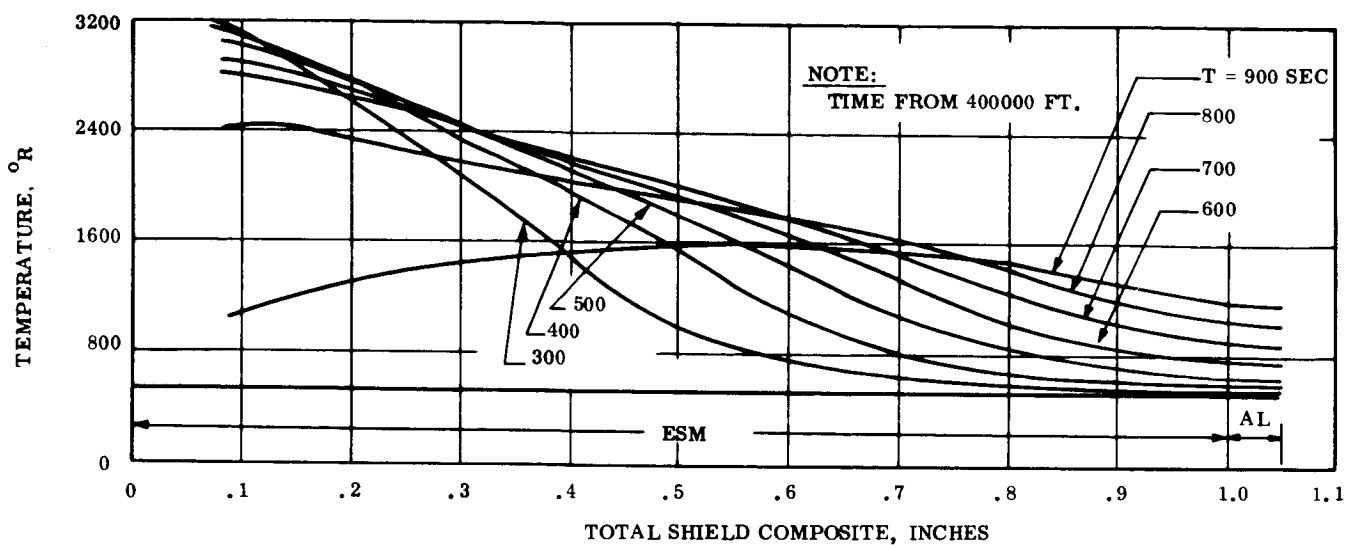


Figure 3.4-32. - Skirt-ESM- Temperature Profiles, $x/l = 0.0208$, Windward, 1° Entry

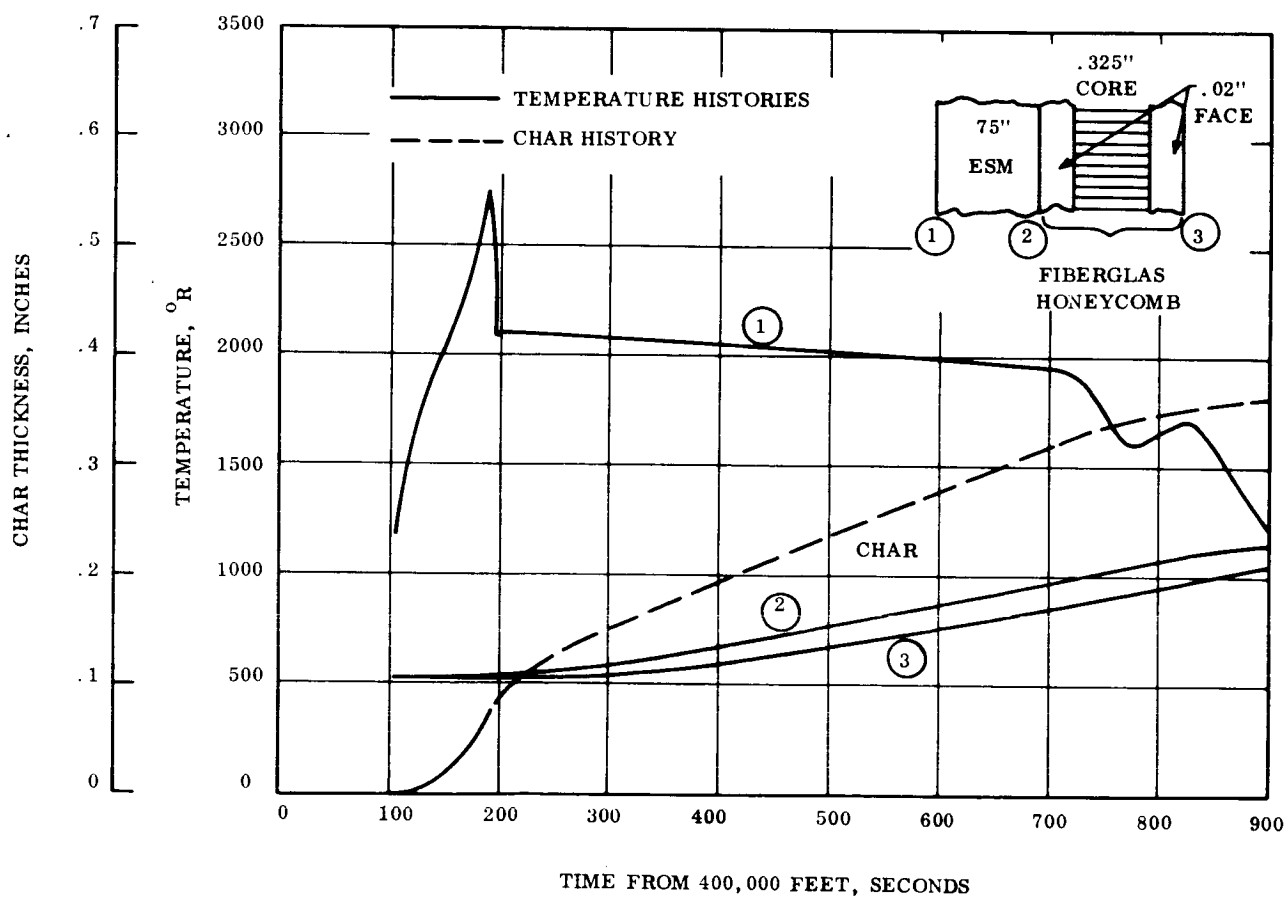


Figure 3.4-33. - Skirt-ESM-Temperature and Degradation Histories, $x/l = 1.0$, Windward, 1° Entry

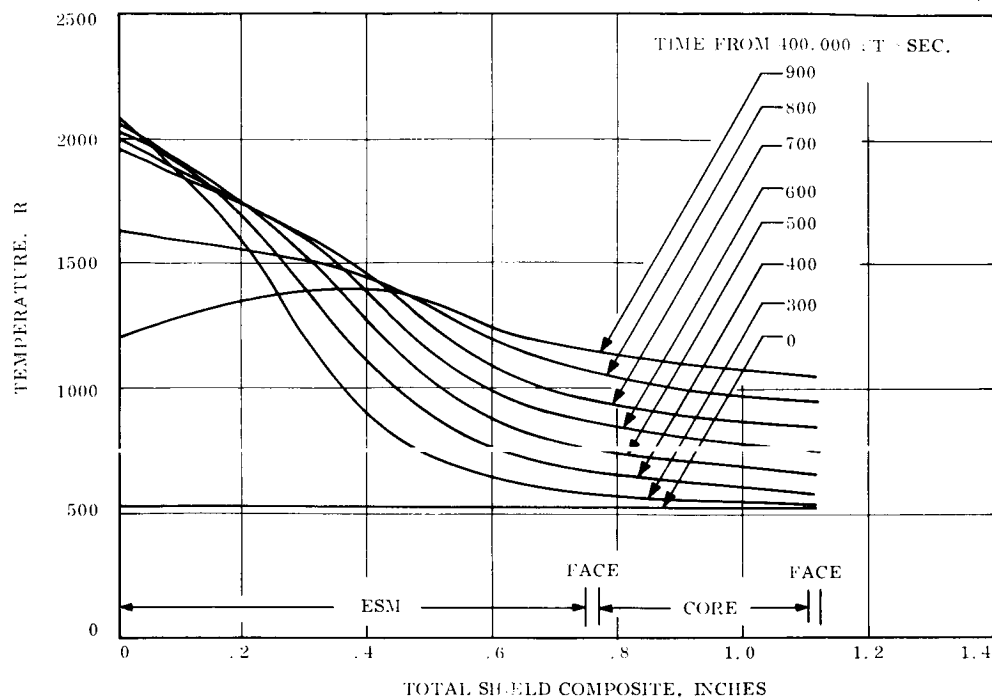


Figure 3.4-34. - Skirt-ESM-Temperature Profiles, $x/l = 1.0$, Leeward, 1° Entry

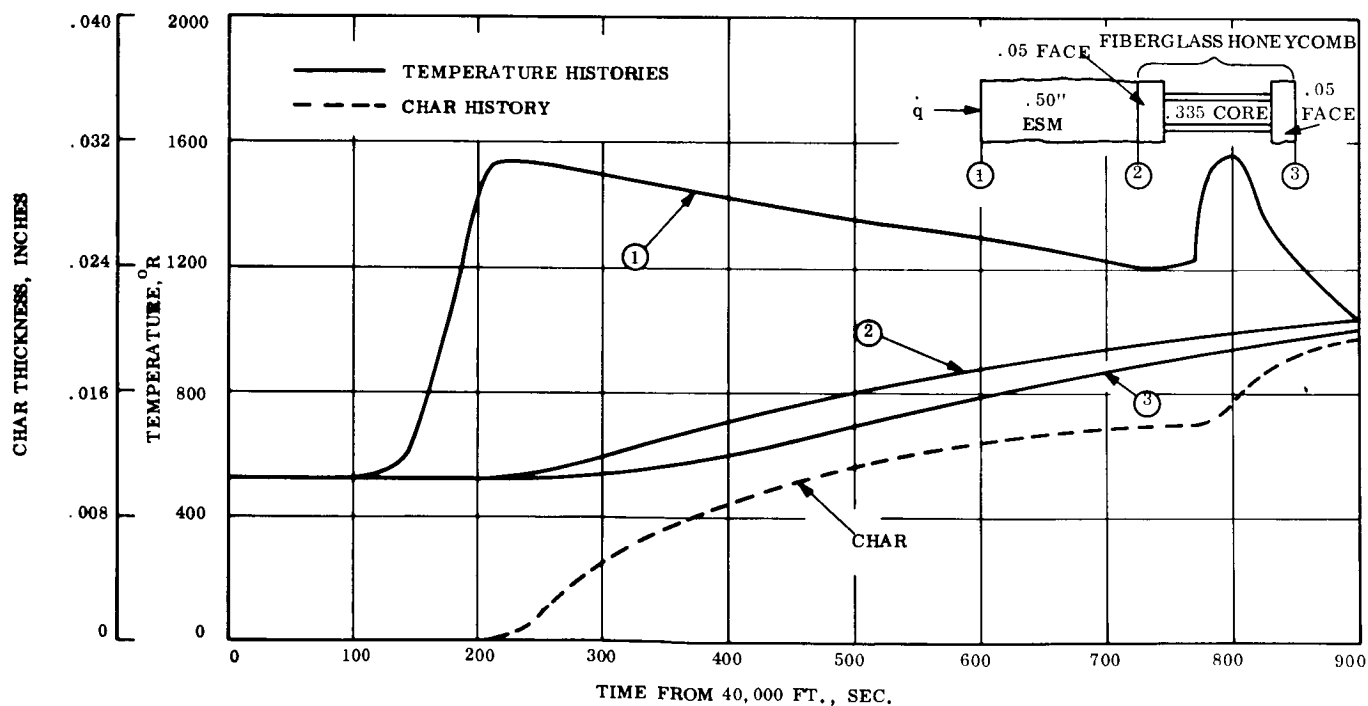


Figure 3.4-35. - Skirt-ESM-Temperature and Degradation Histories, $x/l = 1.0$, Windward, 1° Entry

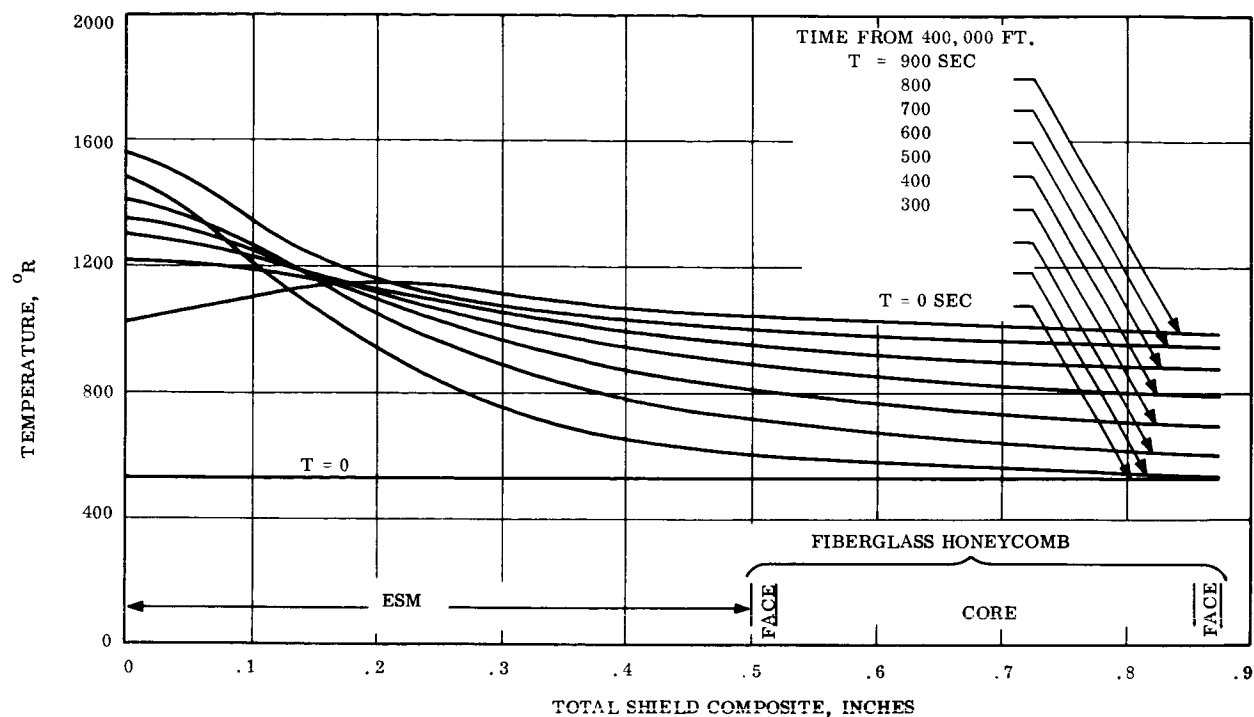


Figure 3.4-36. - Skirt-ESM-Temperature Profiles, $x/l = 1.0$, Leeward, 1° Entry

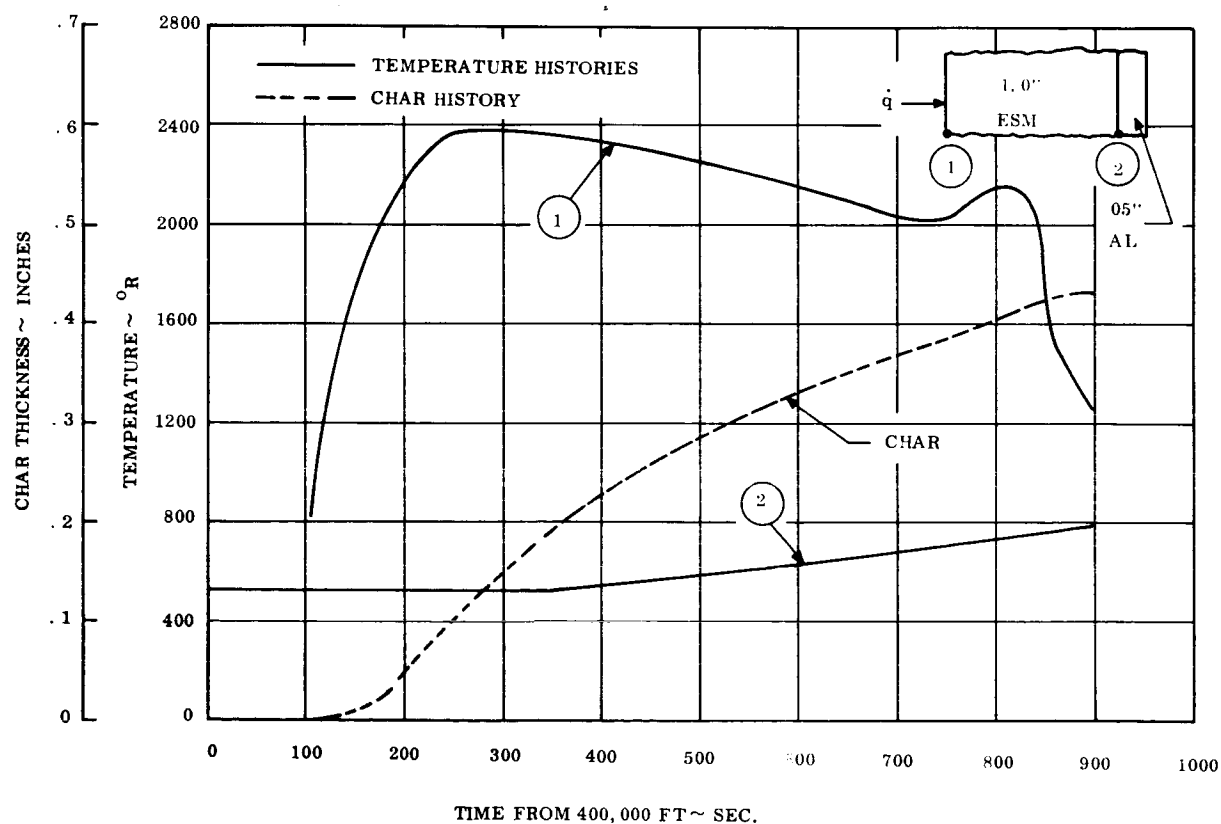


Figure 3.4-37. - Skirt-ESM-Temperature and Degradation Histories, $x/l = 0.15$, Side, 1° Entry

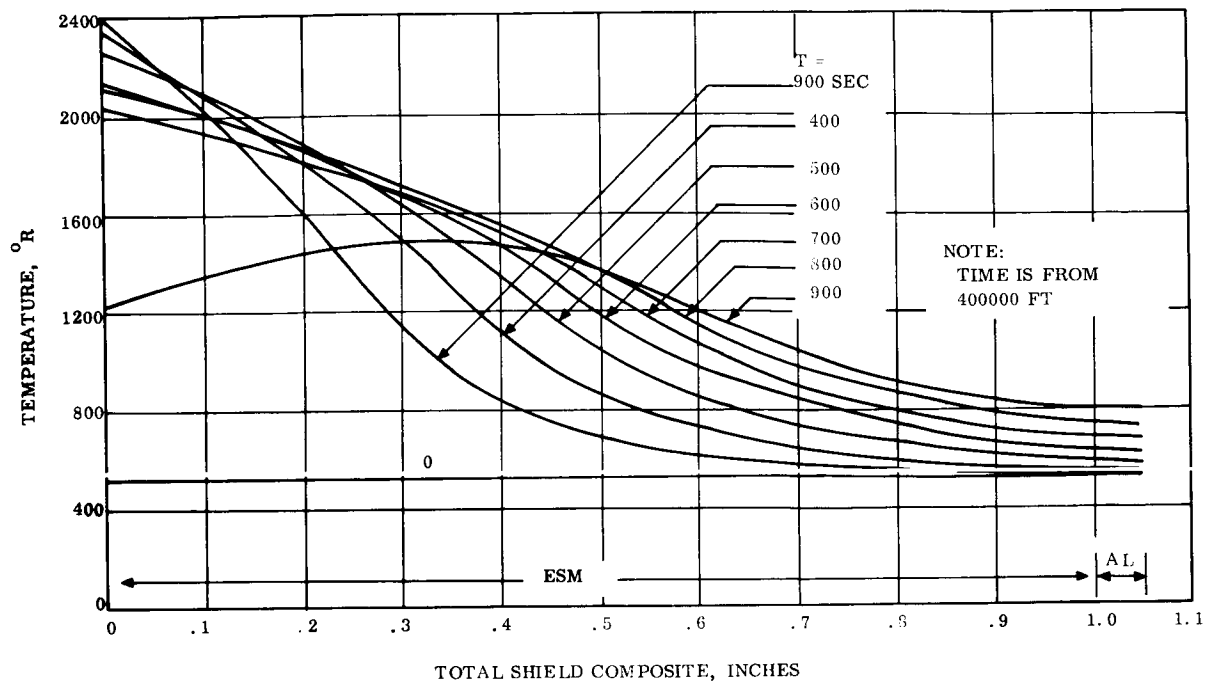


Figure 3.4-38. - Skirt-ESM-Temperature Profiles, $x/1 = 0.15$, Side, 1° Entry

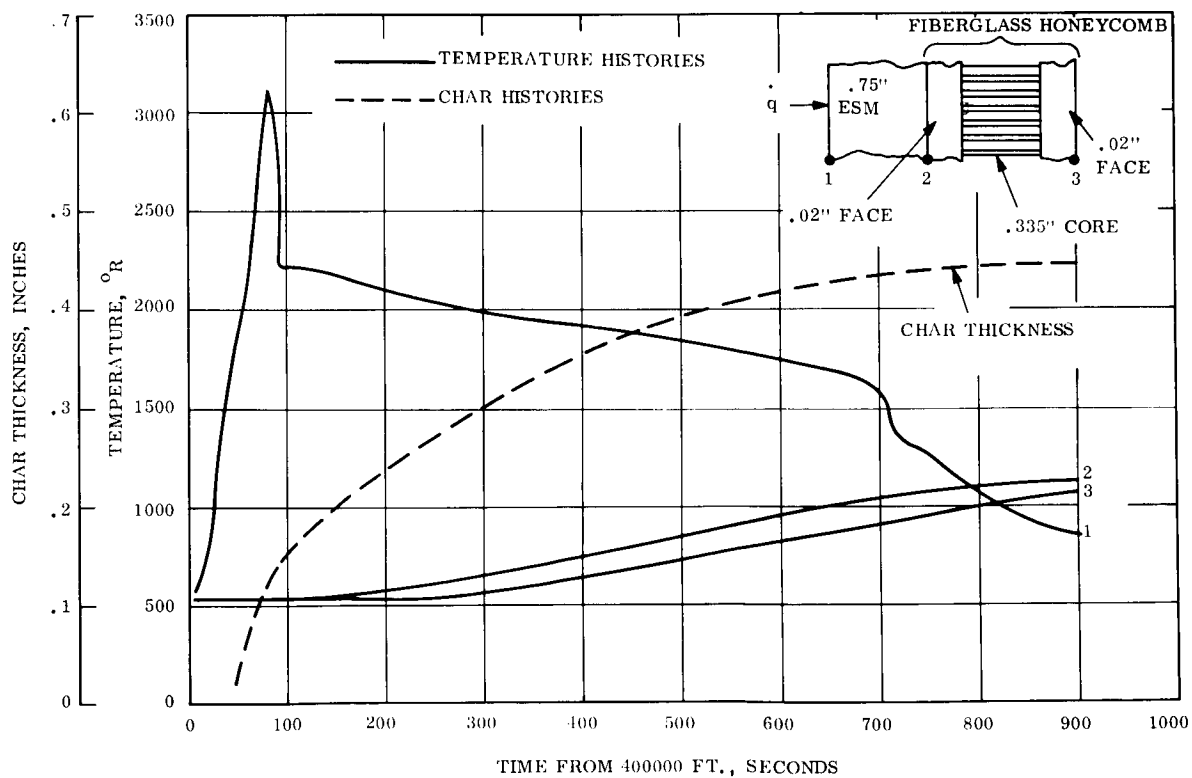


Figure 3.4-39. - Skirt-ESM-Temperature and Degradation Histories, $x/1 = 0.364$, Windward, 10° Entry

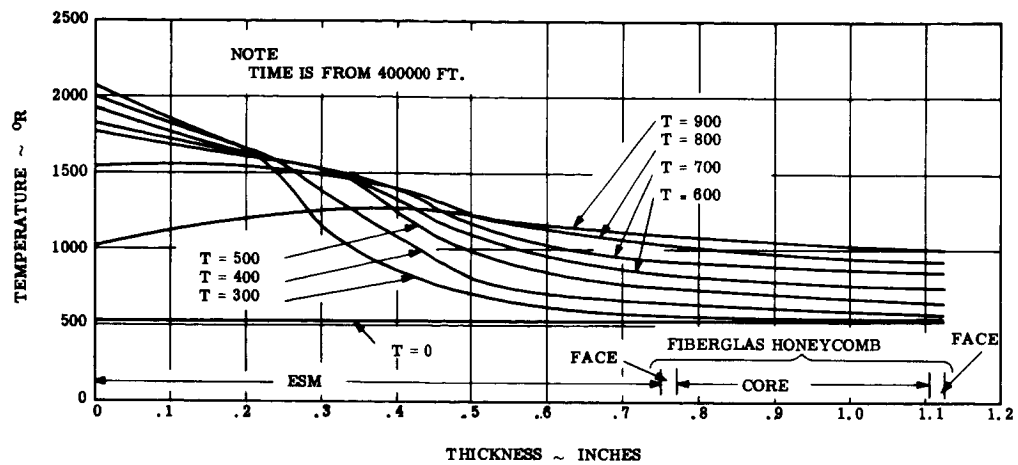


Figure 3.4-40. - Skirt-ESM-Temperature Profiles, $x/l = 0.364$, Windward, 10° Entry

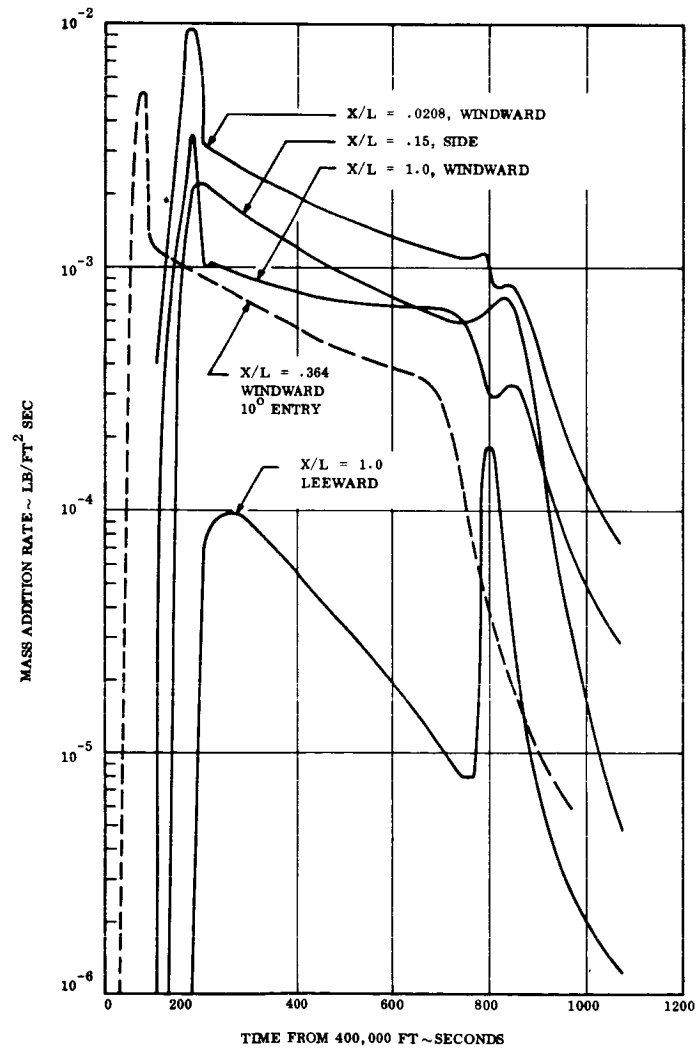


Figure 3.4-41. - Skirt-ESM Total Mass Addition Histories, Windward, Leeward, and Side, 1° Entry

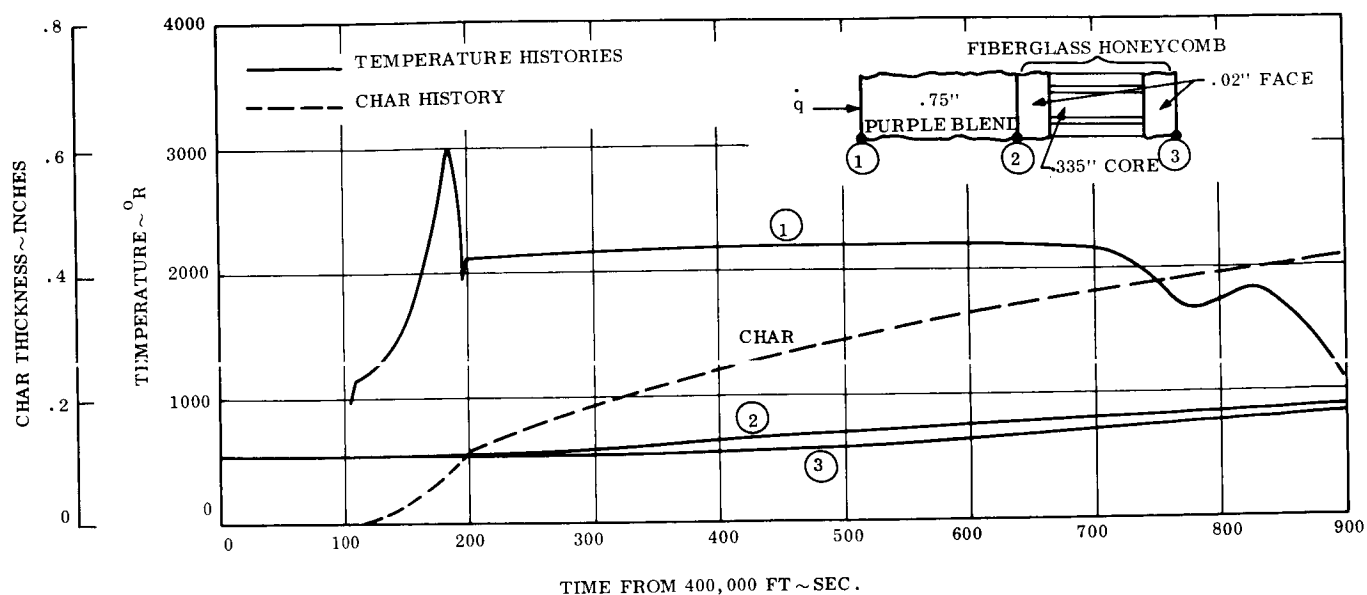


Figure 3.4-42. - Skirt-Purple Blend-Temperature and Degradation Histories, $x/l = 1.0$, Windward, 1° Entry

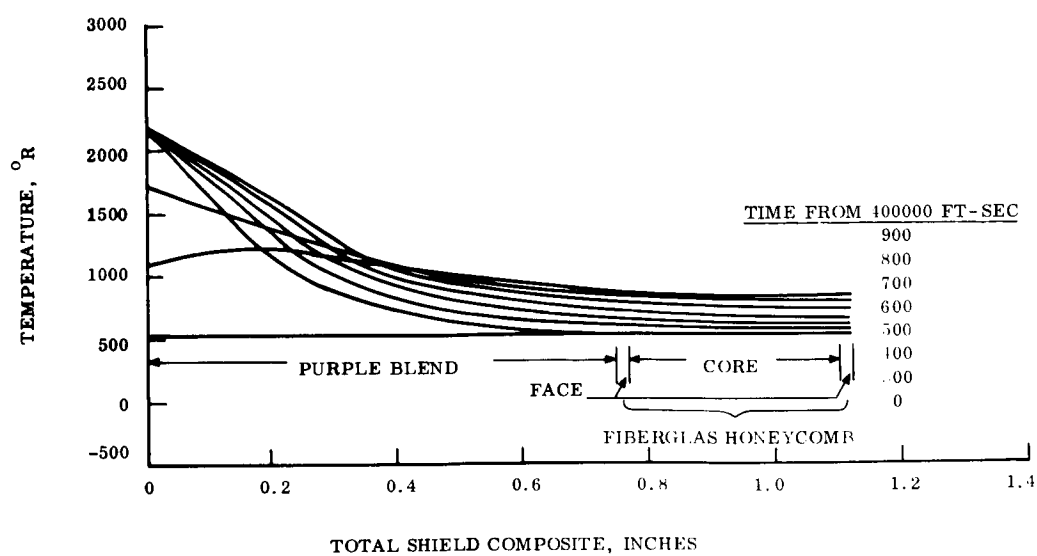


Figure 3.4-43. - Skirt-Purple Blend-Temperature Profiles, $x/l = 1.0$, Windward, 1° Entry

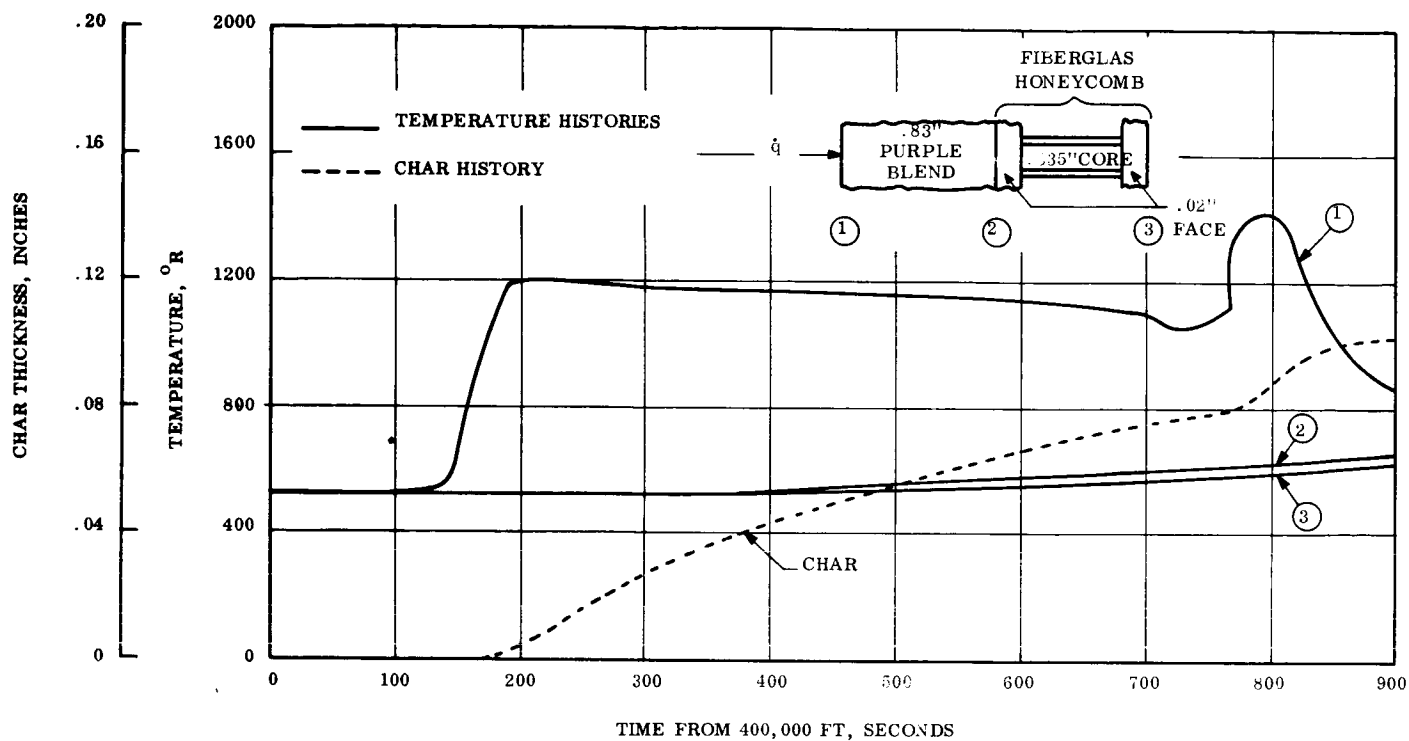


Figure 3.4-44. - Skirt-Purple Blend- Temperature Degradation Histories, $x/l = 1.0$, Leeward, 1° Entry

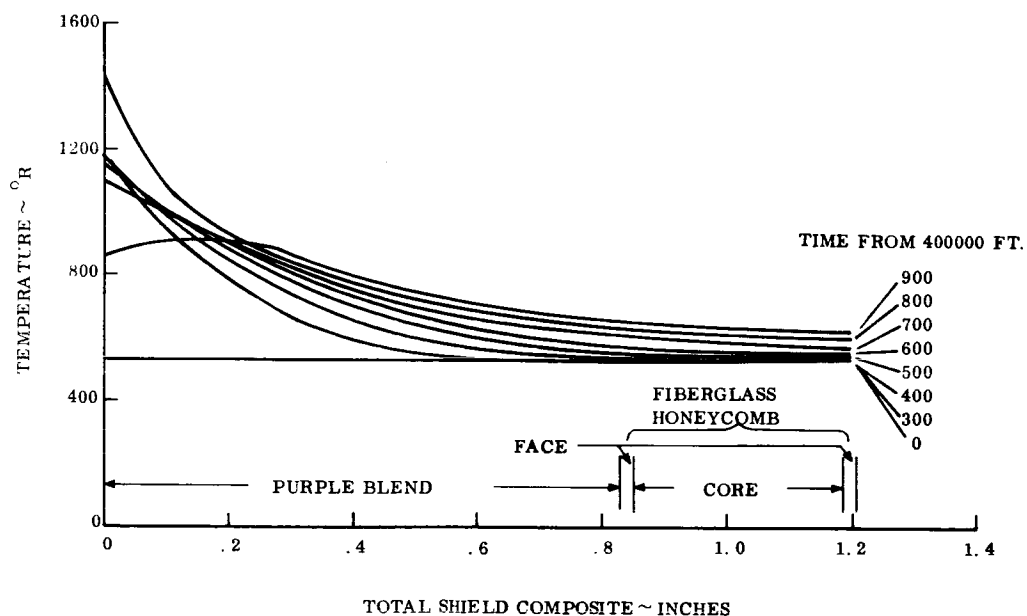


Figure 3.4-45. - Skirt-Purple Blend-Temperature Profiles, $x/l = 1.0$, Leeward, 1° Entry

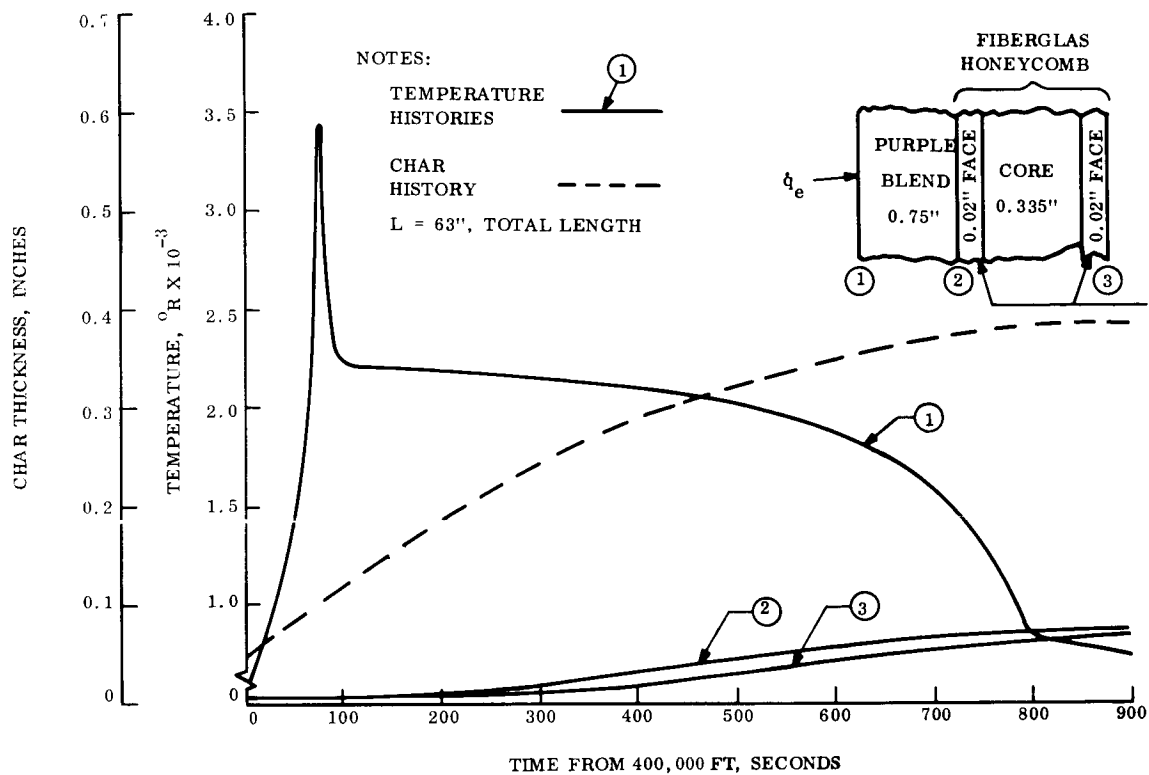


Figure 3.4-46. - Skirt-Purple Blend-Temperature and Degradation Histories,
 $x/l = 0.364$, Windward, 10^0 Entry

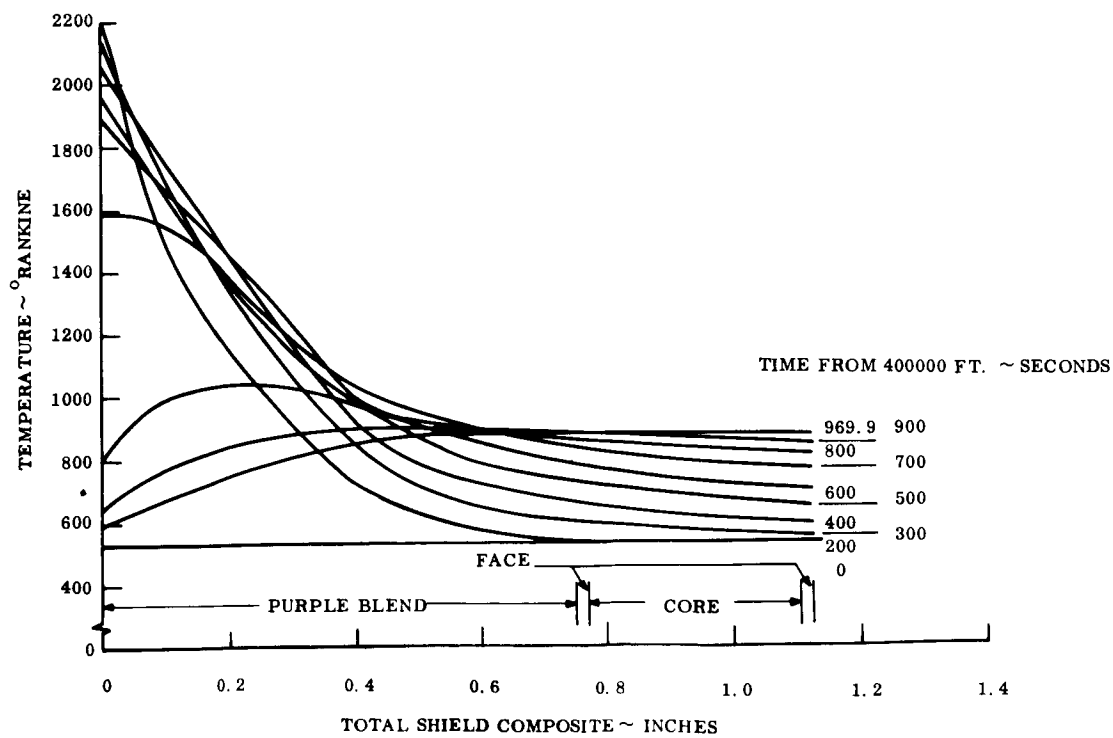


Figure 3.4-47. - Skirt-Purple Blend-Temperature Profiles,
 $x/l = 0.364$, Windward, 10^0 Entry

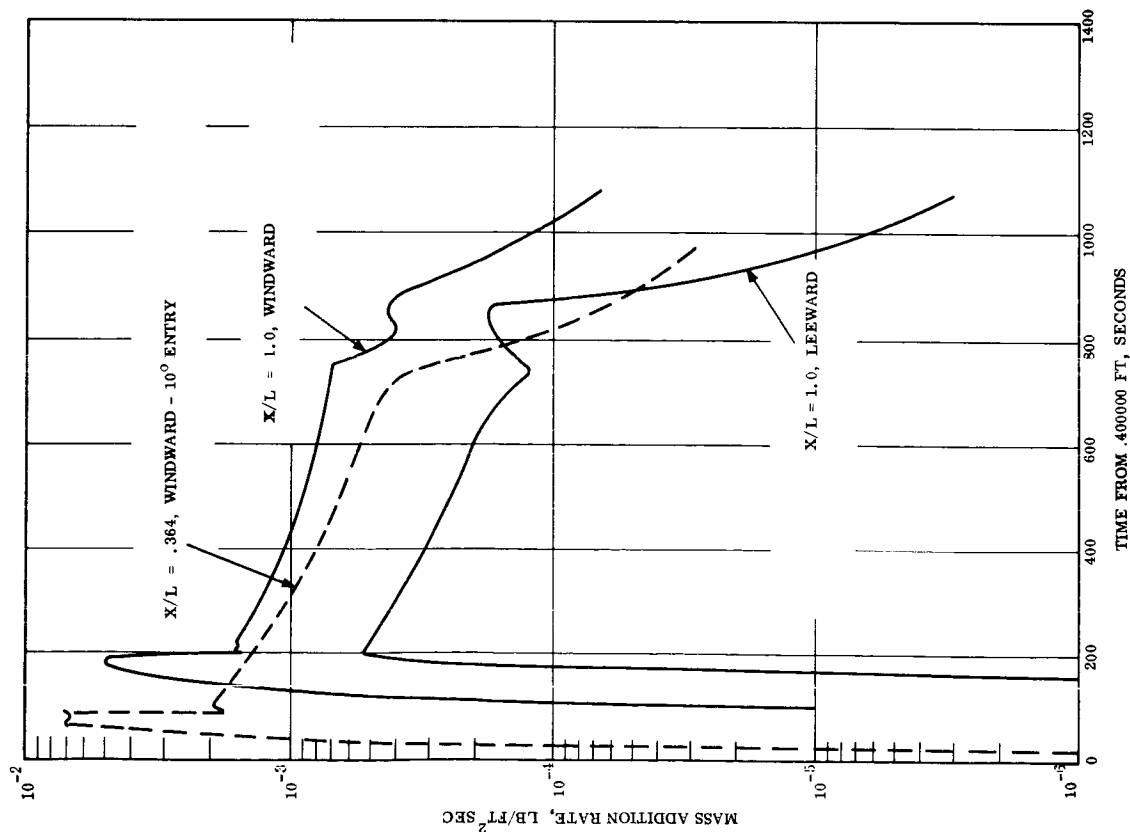


Figure 3.4-48. - Skirt-Purple Blend-Total Mass Addition Histories, Windward and Leeward, 1° Entry

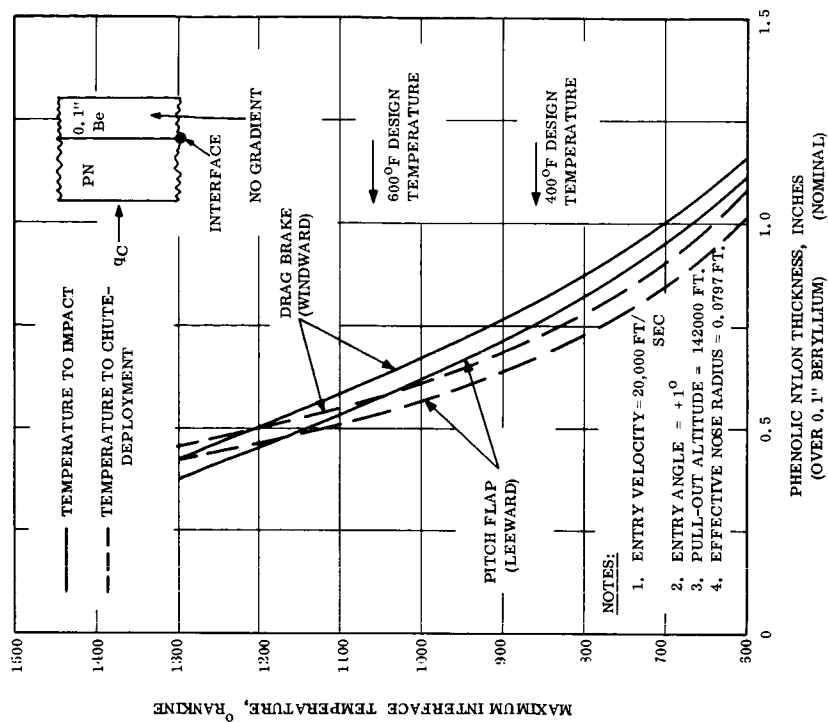


Figure 3.4-49. - Pitch-Flap and Drag-Brake Phenolic Nylon Nominal Heat-Shield Requirements 1° Entry

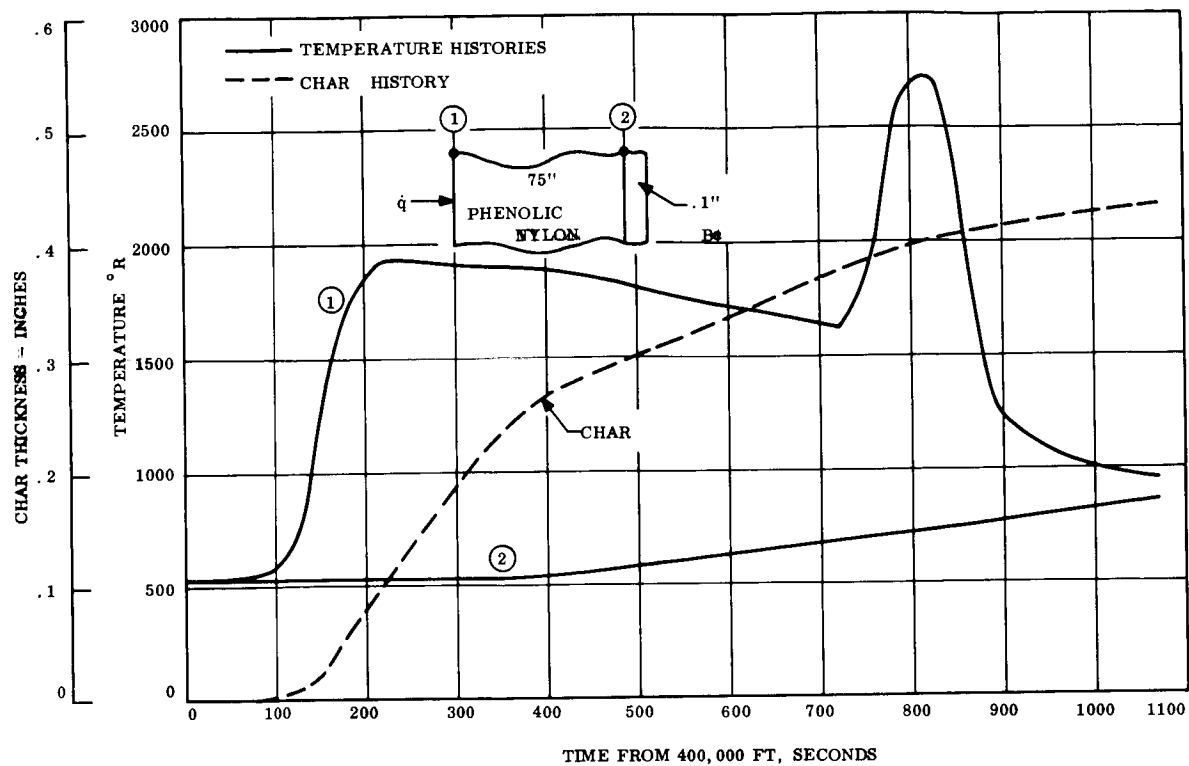


Figure 3.4-50. - Pitch Flap Phenolic Nylon Temperature and Degradation Histories, $x/l = 1.0$, Leeward, 1° Entry

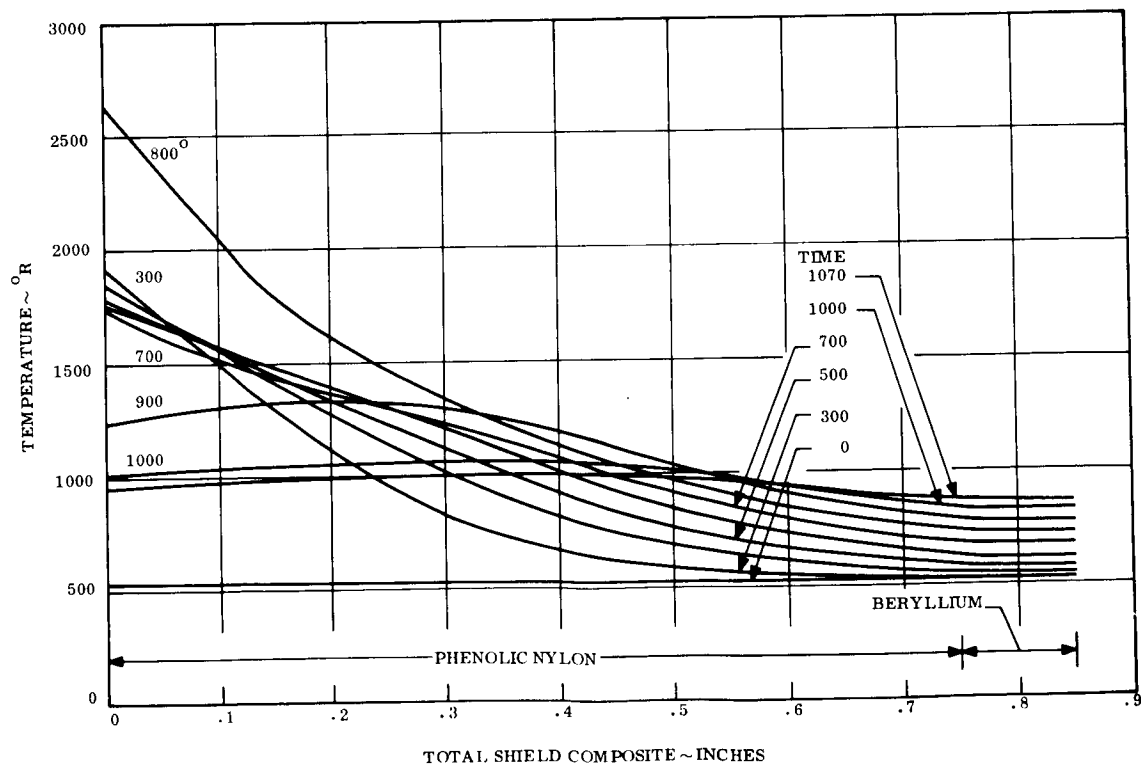


Figure 3.4-51. - Pitch Flap Phenolic Nylon Temperature Profiles, $x/l = 1.0$ Leeward, 1° Entry

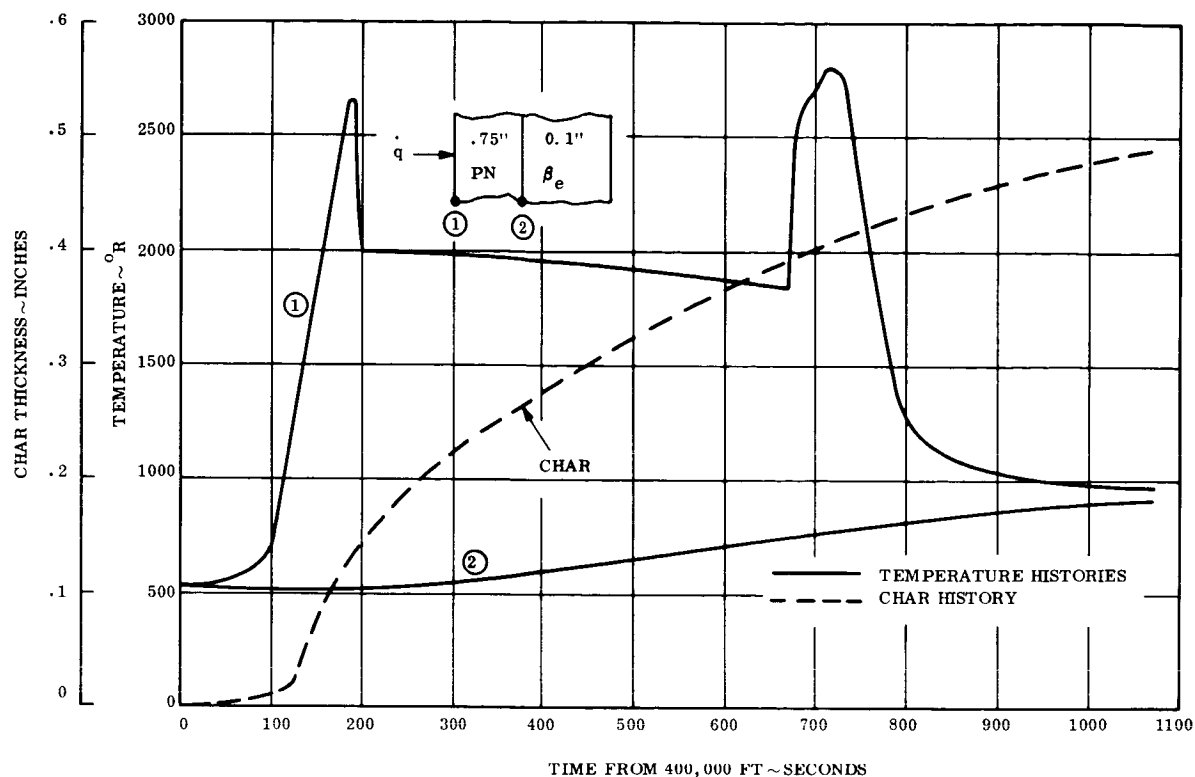


Figure 3.4-52. - Drag Brake Phenolic Nylon Temperature and Degradation Histories, $x/l = 1.0$, Windward, 1° Entry

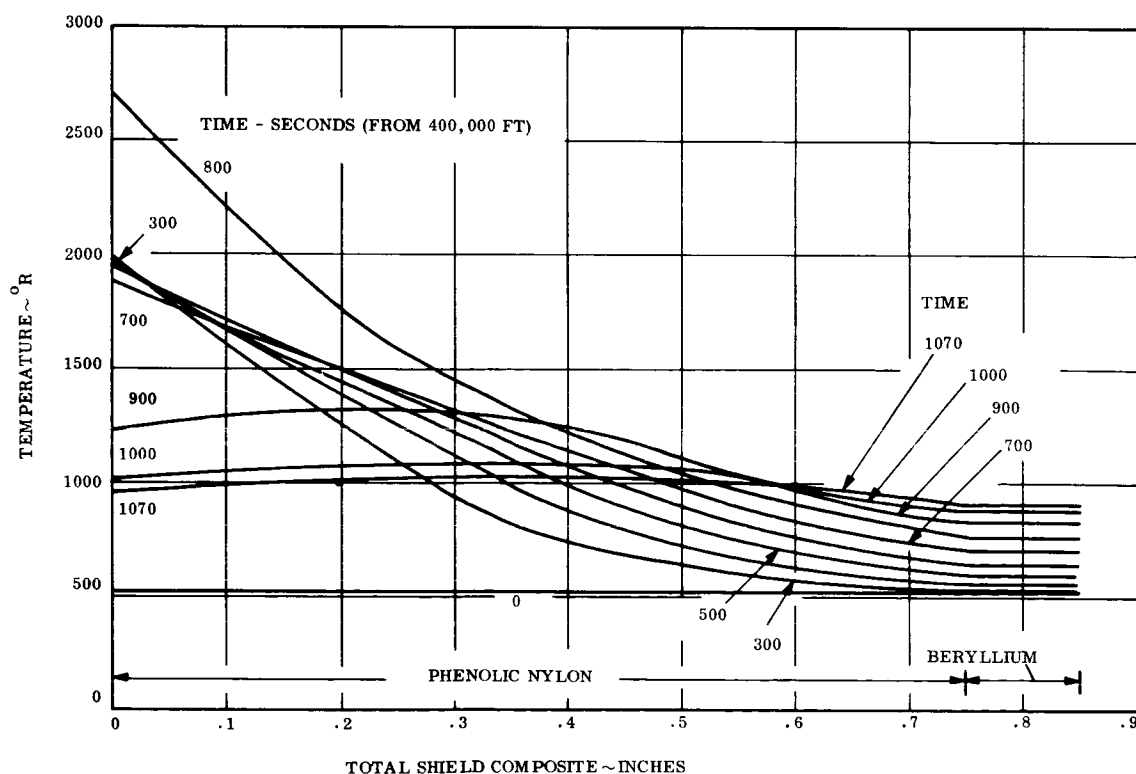


Figure 3.4-53. - Drag Brake Temperature Profiles, $x/l = 1.0$, Windward, 1° Entry

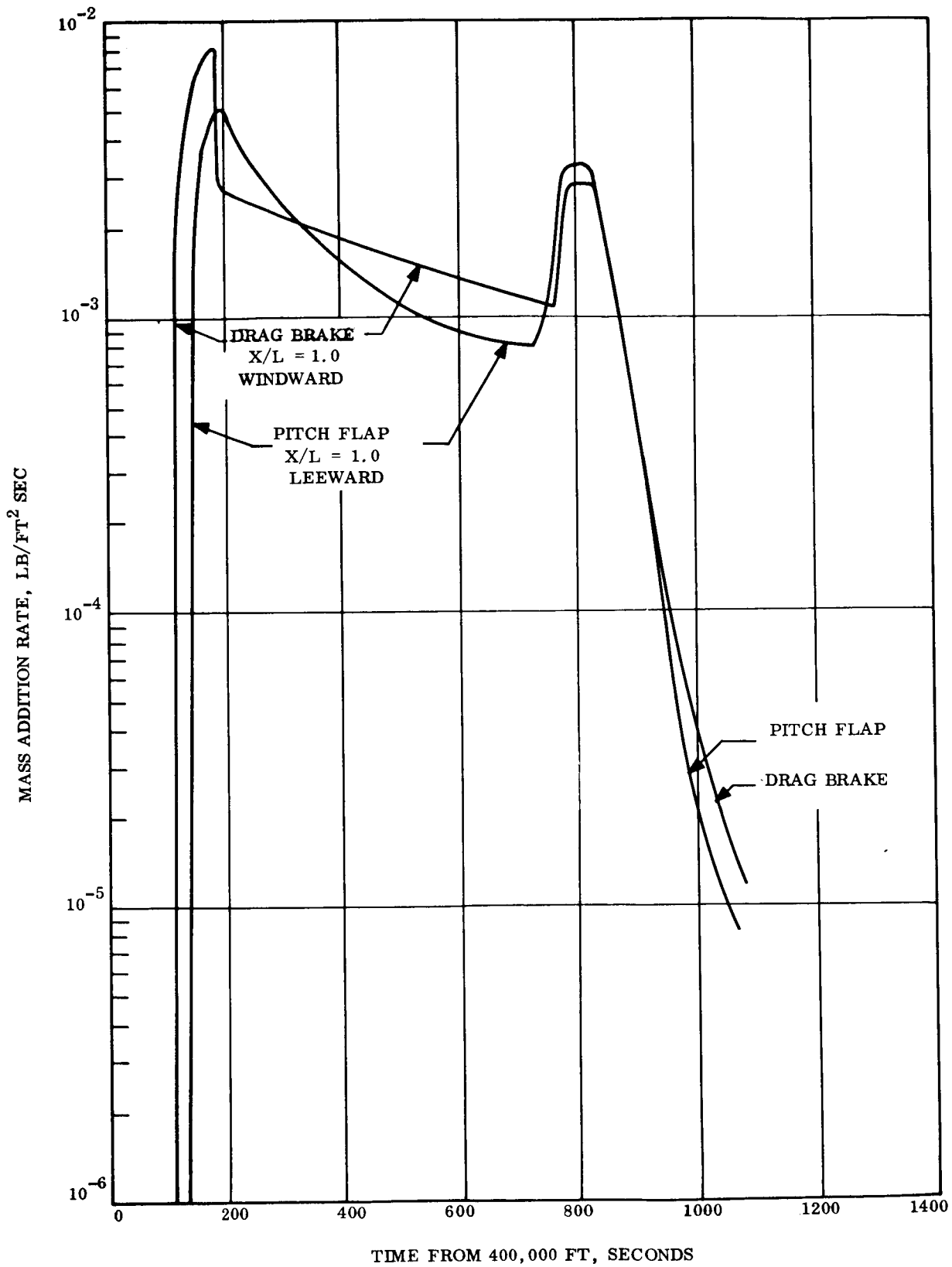


Figure 3.4-54. - Drag Brake and Pitch Flap Phenolic Nylon Total Mass Addition Histories

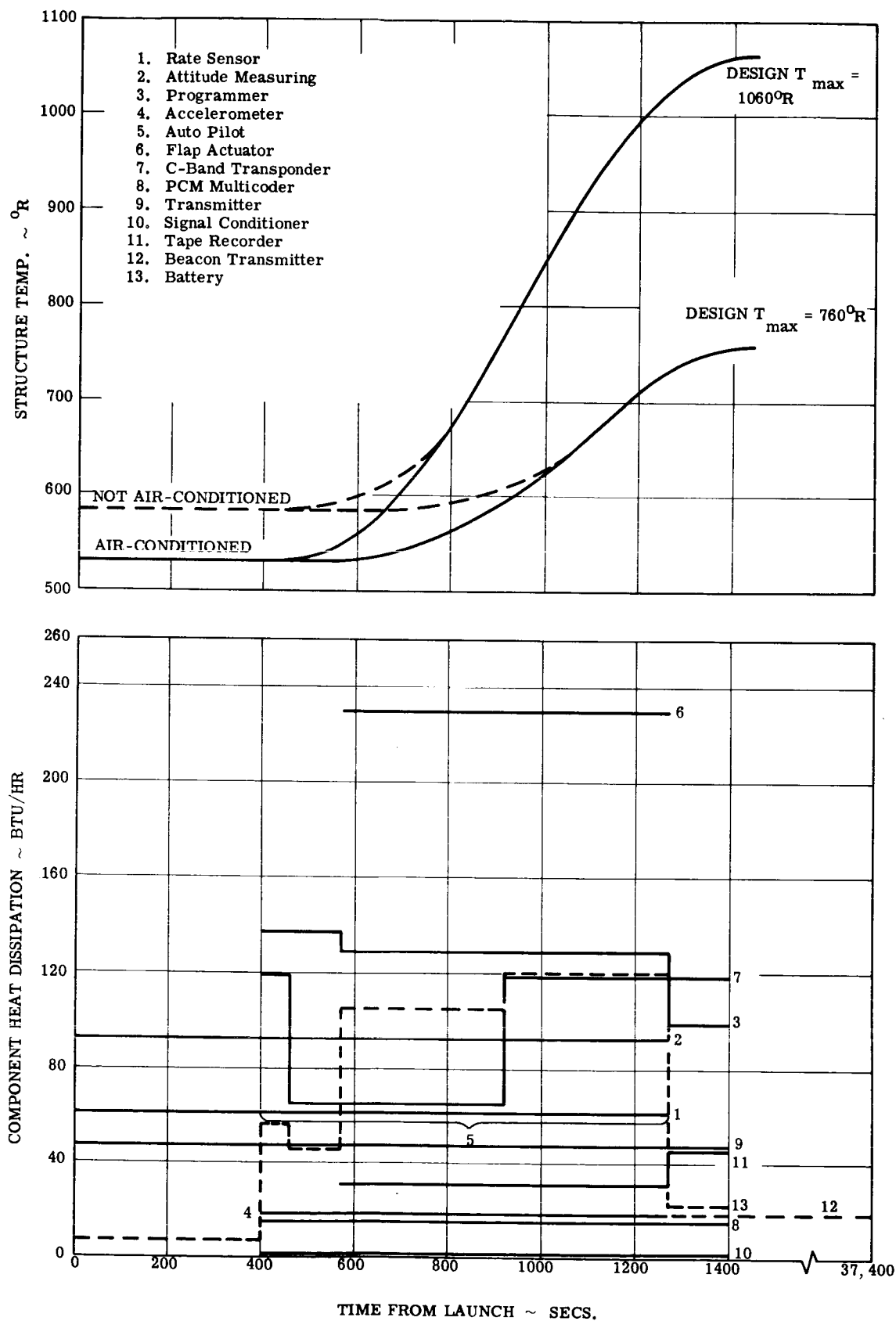


Figure 3.4-55. - Backface Temperature and Heat Dissipation Profiles

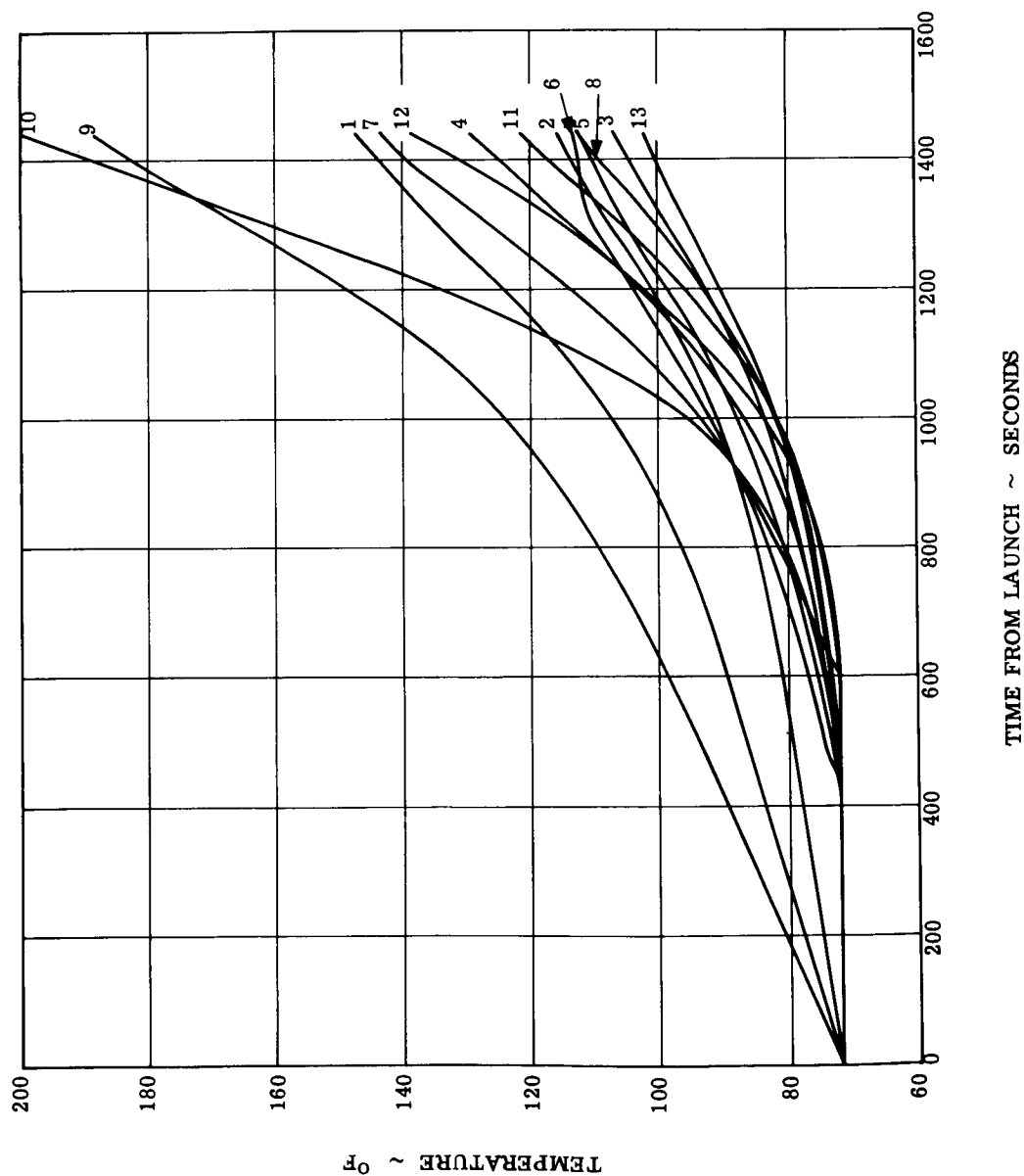
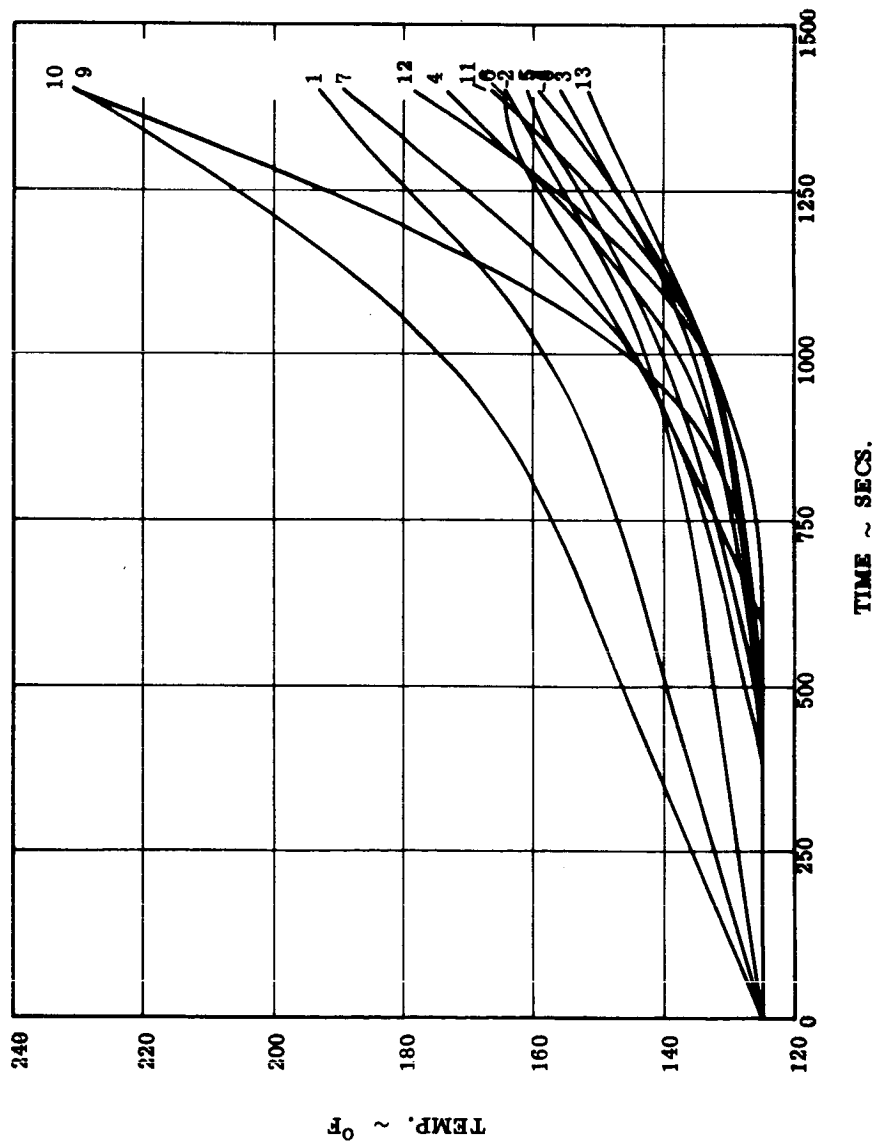


Figure 3.4-56. - Component Temperature Histories for Hot Structure, Air Conditioned, Textolite Structure



1. Rate Sensor
2. Attitude Measuring Sensor
3. Programmer
4. Accelerometer
5. Auto Pilot
6. Flap Actuator
7. C-Band Transponder
8. PCM Multicoder
9. Transmitter
10. Signal Conditioner
11. Tape Recorder
12. Beacon Transmitter
13. Battery

Backface $f = 0.15$
 Component $f = 0.80$
 Conductance from Vehicle to Component =
 0.04 BTU/HR- $^{\circ}$ F

Figure 3.4-57. - Component Temperature Histories for Hot Structure, Not Air Conditioned, Textolite Structure

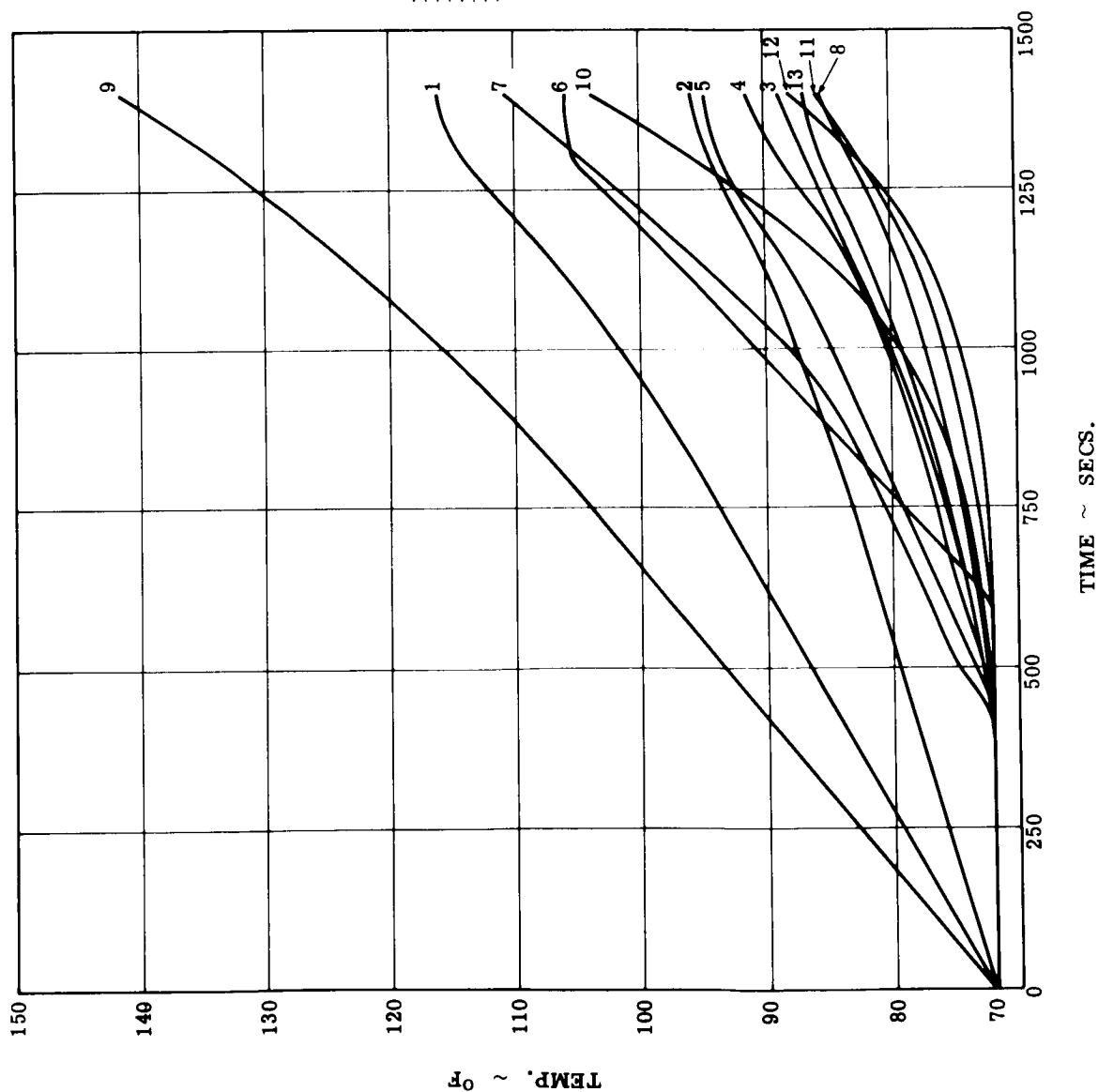


Figure 3.4-58. - Component Temperature Histories for Cold Structure, Air Conditioned, Textolite Structure

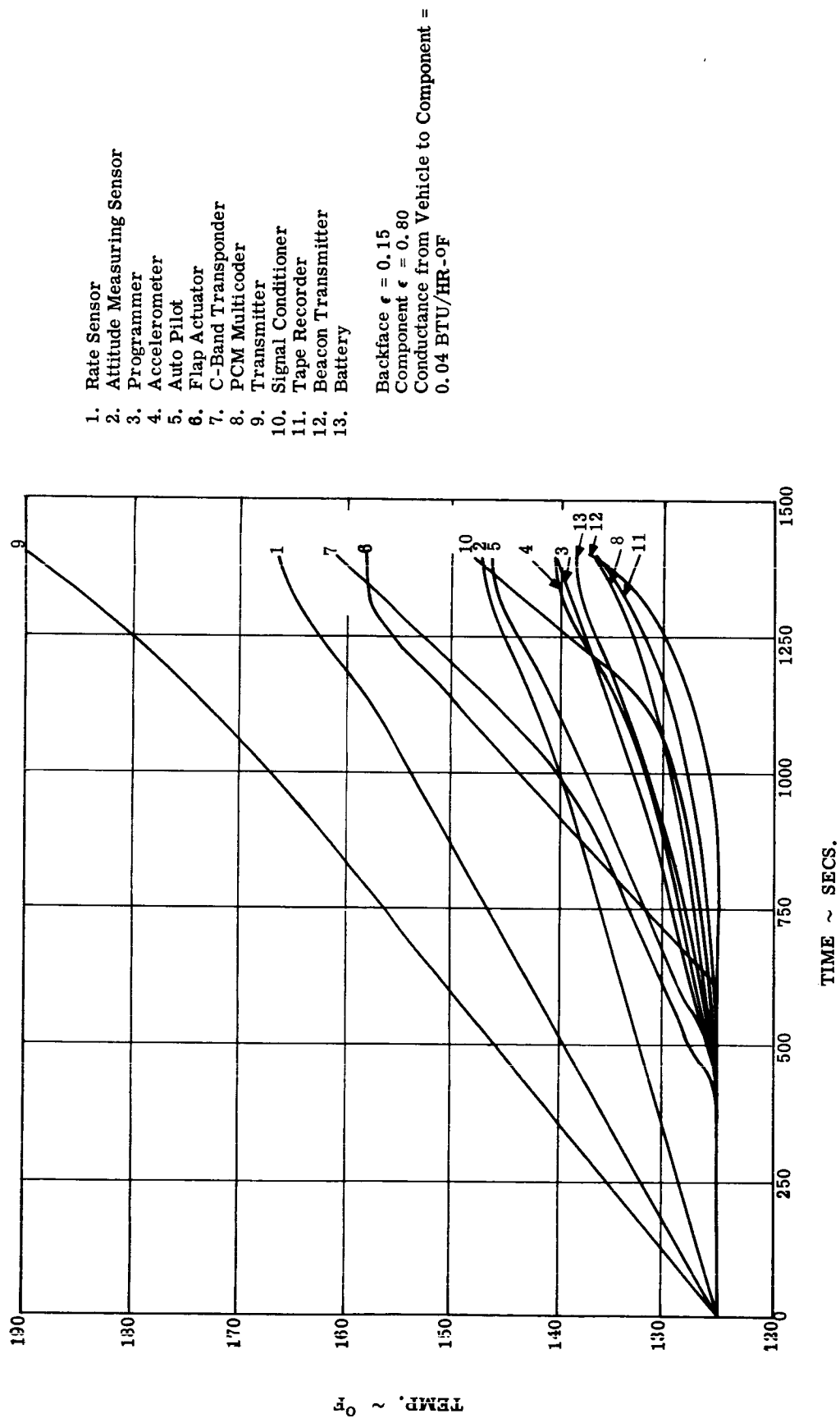


Figure 3.4-59. - Component Temperature Histories for Cold Structure, Not Air Conditioned, Textolite Structure

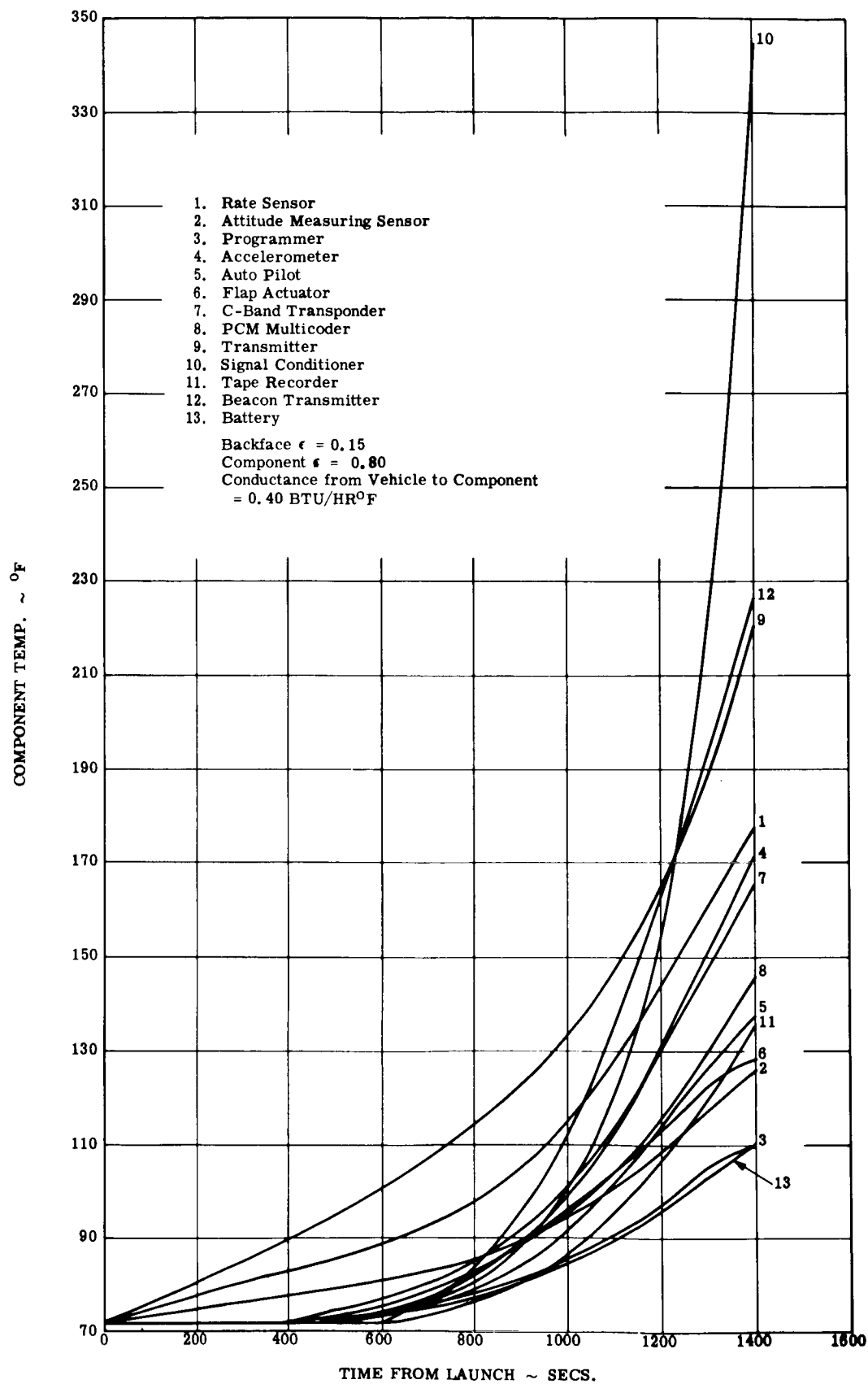


Figure 3.4-60. - Component Temperature Histories for Hot Structure, Air Conditioned, With Insulating Washers

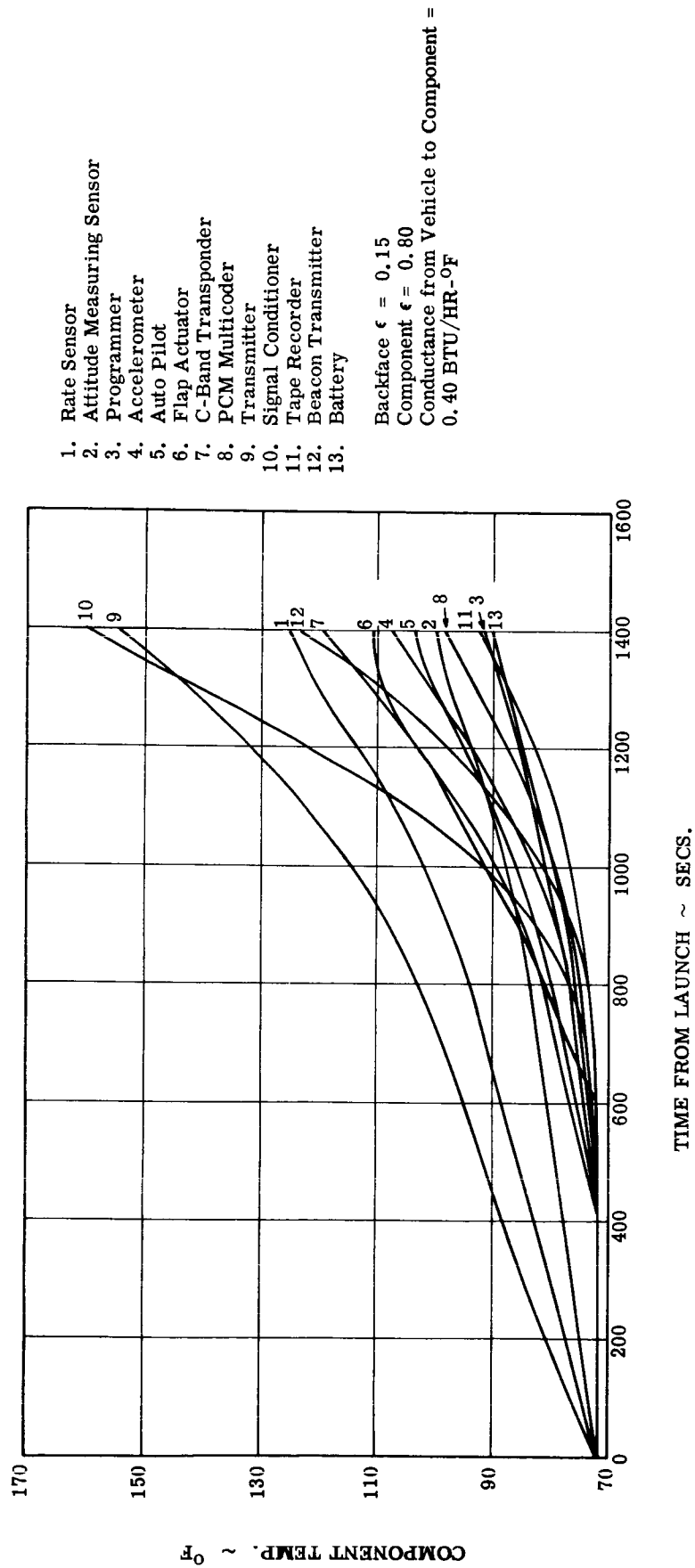


Figure 3.4-61. - Component Temperature Histories for Cold Structure, Air Conditioned With Insulating Washers

REFERENCES

- 3.4-1a Dewees, L. , "Re-entry Vehicle Design (Ablating) Computer Program, TIS R59SD391
- 3.4-1b DiChristina, V. , "Addendum to Ablation Design (Ablating) Computer Program", TM 152, 2/60
- 3.4-2 Lees, L. , "Laminar Heat Transfer Over Blunt Nosed Bodies at Hypersonic Speeds", Jet Propulsion, 4/56
- 3.4-3 Eckert, E.R.G., "Engineering Relationships for Heat Transfer and Friction in High Velocity Laminar and Turbulent Boundary Layer Flow over Surfaces with Constant Pressure and Temperature", ASME Paper No. 55-a-31, 1955
- 3.4-4 Reshotko, E. , "Heat Transfer to a General Three-Dimensional Stagnation Point", Jet Propulsion, pp 58-60, 2/58
- 3.4-5 Walker, G. K. , "Some Comments on Laminar and Turbulent Heat Transfer Equations", GE-RSD AETM 147, 12/59
- 3.4-6 Walker, G. K. , "Turbulent Boundary Correction at High Reynolds Numbers", GE-RSD TFM 8151-006, 11/2/62
- 3.4-7 Walker, G. K. , "Some Aerothermodynamic Information in Convenient Curve Form", Aerophysics Eng. Tech. Memo. 183
- 3.4-8 Berkowitz, A.M. , "Review and Applicability of Available Boundary Layer Transition Data on Elliptic Cones", PIR HTT-8151-688, 1/3/67
- 3.4-9 Nestler, D. E. , "Prediction of Laminar Heat Flux for Elliptic Cones", PIR 8159-1599, 12/30/66
- 3.4-10 Heins, A.E., and Estes, T.J. , "Effect of Angle-of-Attack on Laminar Convective Heat Transfer on Sharp and Blunt Cones", TIS 61SD70, 4/61
- 3.4-11 Barte, G.R. , Jr. , "Estimated Loads, Hinge Moments, and Pressure Distributions for the Single-Flap of the Basic SLAMAST Configuration", Data Memo. 67-01, 1/20/67
- 3.4-12 Nestler, D. E. , "Correlation of Turbulent Heat Flux to Flaps", PIR 8159-1074, 10/26/65
- 3.4-13a Segletes, J. , "Thermal Degradation of a Thermosetting Plastic, GE-RSD TIS 62SD202, 11/62
- 3.4-13b Gordon, P. , "Analysis of a One Dimensional Heat Conduction Digital Computer Program "GE TIS 64SD201, 1/64
- 3.4-14 Wesendorf, L.E., "Property Data for ATJ Graphite", PIR-8157-081, 1/27/64

REFERENCES (Continued)

- 3.4-15 Scala, S.M., and Nolan, E.J., "Aerothermodynamic Feasibility of Graphite for Hypersonic Glide Vehicles", GE TIS R60SD425, 8/2/60
- 3.4-16 Underhill, W.S., Thermodynamic Ablation Data Analysis - Phenolic Refrasil Tech. Fund. Memo 050, Mar 1960
- 3.4-17a Florence, D.E., ESM PERFORMANCE - GROUND and FLIGHT TEST 4/8/67 PIR8151-ARSTA-142, to be published
- 3.4-17b "Shield Material: Elastomeric ESM 1004 AP Series (Unsupported)", GE Specification S0060-00-0006A
- 3.4-18 Kohr, J.W.C., "REKAP Model for NASA 602 Ablator (Purple Blend) Mod 5", PIR 8151-126, 2/15/67
- 3.4-19 Kottok, S., "The Development of a Phenolic Nylon Model for a Reaction Kinetics Ablation Program", TIS 65SD320, 9/65
- 3.4-20 Chmielewicz, L., "SLAMAST Flight Trajectory and Sequence of Events", GE PIR 8142-1079
- 3.4-21 Weaver, J.D., "Revised SLAMAST Battery Considerations", GE PIR 8252-5583
- 3.4-22 Celebrese, F., and Thurston, R., "Preliminary Sizing of the SLAMAST Control System", GE PIR 8241-R3-993
- 3.4-23 Klammer, R.J., "I and C Subsystem Definition for SLAMAST Feasibility Study", GE PIR 8233-2212
- 3.4-24 Dolan, C.M., et al, "Elastomeric Thermal Shield Systems for Lifting Re-entry Vehicles", J. of Spacecraft and Rockets, Vol. 3, No. 6, pp. 867-872, 6/66
- 3.4-25 Brunner, M.J., et al, "Study of Thermal Protection Requirements for a Lifting Body Entry Vehicle Suitable for Near-Earth Missions", Final Report - NASA Contract No. NAS-2-2974, GE Document No. 66SD253, 5/66
- 3.4-26 Clark, R.K., "Effect of Environmental Parameters on the Performance of Low Density Silicone Resin and Phenolic Nylon Ablation Materials", NASA TN D-2543, 1/65
- 3.4-27 Welsh, W.E., Starnes, K.E., Leeds, D.H., and Slaughter, J.L., "Low Density Ablation Materials Survey", SSD-TR-66-35, 1/66
- 3.4-28 Schmidt, D.L., "Ablation Polymers for Hypersonic Atmospheric Flight", AFML-TR-66-78, 5/66

REFERENCES (Continued)

- 3.4-29 Schmidt, D.L., "Interdisciplinary Research on Ablative Materials",
Technical Report AFML-TR-65-62, 8/65
- 3.4-30 Dolan, C.M., "Study for Development of Elastomeric Thermal Shield
Materials", NASA CR-186, 3/65
- 3.4-31 Bauer, P.E., and Kummer, D.L., "Development and Performance of
the Gemini Ablative Heat Shield", J. of Spacecraft and Rockets, Vol. 3,
No. 10, pp. 1495-1500, 10/66
- 3.4-32 GE Specification S0060-00-0006A
GE Specification ERS 9330-21-0012
GE MSI with QAP MSI 242366

3.5 INSTRUMENTATION AND COMMUNICATION STUDIES

3.5.1 PLASMA ATTENUATION

3.5.1.1 Summary and conclusions. - A plasma attenuation study to establish recorder and playback requirements has been performed for the SLAMAST 1⁰ design trajectory for both telemetry and tracking frequencies. Results are presented in Figures 3.5-1 and 3.5-2. These results (upper bound curves) are felt to be conservative for the following reasons:

(1) The design trajectory used in this analysis constitutes a worst case, whereas the actual flight trajectory will be less severe.

(2) The two dimensional flow analyses used gives results which are conservative for an asymmetric vehicle.

(3) The results ignore the strong exponential dependence of reaction rates and contaminant ionization on flow field temperature, and thus on velocity (as explained below).

This analysis has led to the following conclusions:

(1) S-band blackout will begin (based upon a 20 db margin) at approximately 235K feet and end sometime during the horizontal portion of the flight.

(2) The duration of S-band blackout will be no more than 405 seconds.

(3) C-band blackout (based upon 20 db margin) will begin at approximately 225K feet and end before the end of S-band blackout (during horizontal flight).

(4) The duration of C-band blackout will be no more than 325 seconds.

3.5.1.2 Discussion. - A major assumption made in this analysis was that of two dimensional flow. This simplification was necessary because three dimensional flow field techniques are not available to handle the asymmetric configuration of the re-entry vehicle. Results of this analysis of a two dimensional blunted wedge (flat plate at angle of attack) should provide conservative attenuation predictions with respect to the actual case.

The primary tool used in this analysis is the Equilibrium Chemistry Contaminated Boundary Layer and Inviscid Flow Computer Program which is coupled with the Plane - Wave Electromagnetic Transmission analysis to give plasma attenuation. (refs. 3.5-1, 3.5-2, 3.5-3, and 3.5-4). Necessary input parameters for this program include nose radius, cone angle, antenna location, signal frequency, altitude, velocity, angle-of-attack, surface temperature, mass loss rates, and contaminant levels. The program has options for both two dimensional and axially symmetric flow and uses the method of characteristics to calculate the flow properties and then performs an exact integration of Maxwell's equations with the assumption of plane wave geometry and normal incidence to give attenuation. The program has the ability to handle three

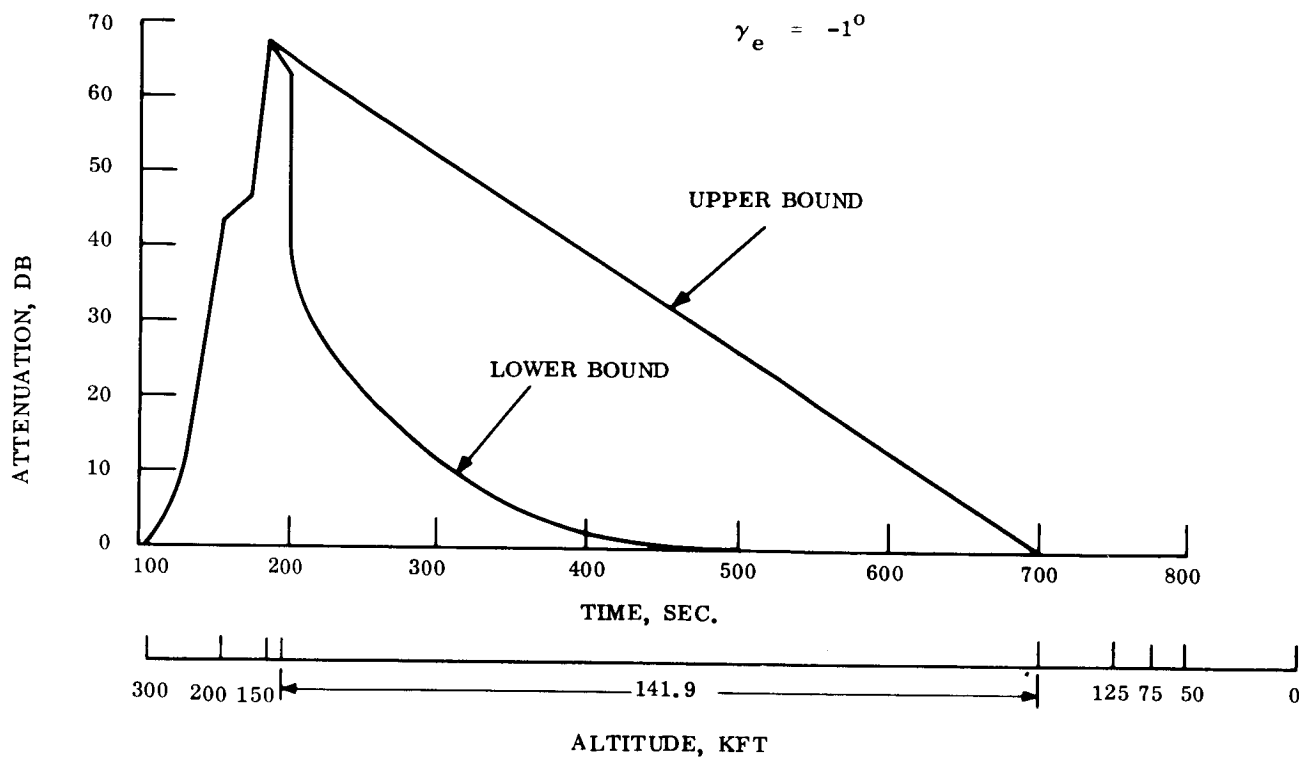


Figure 3.5-1. - Plasma Attenuation, S-band

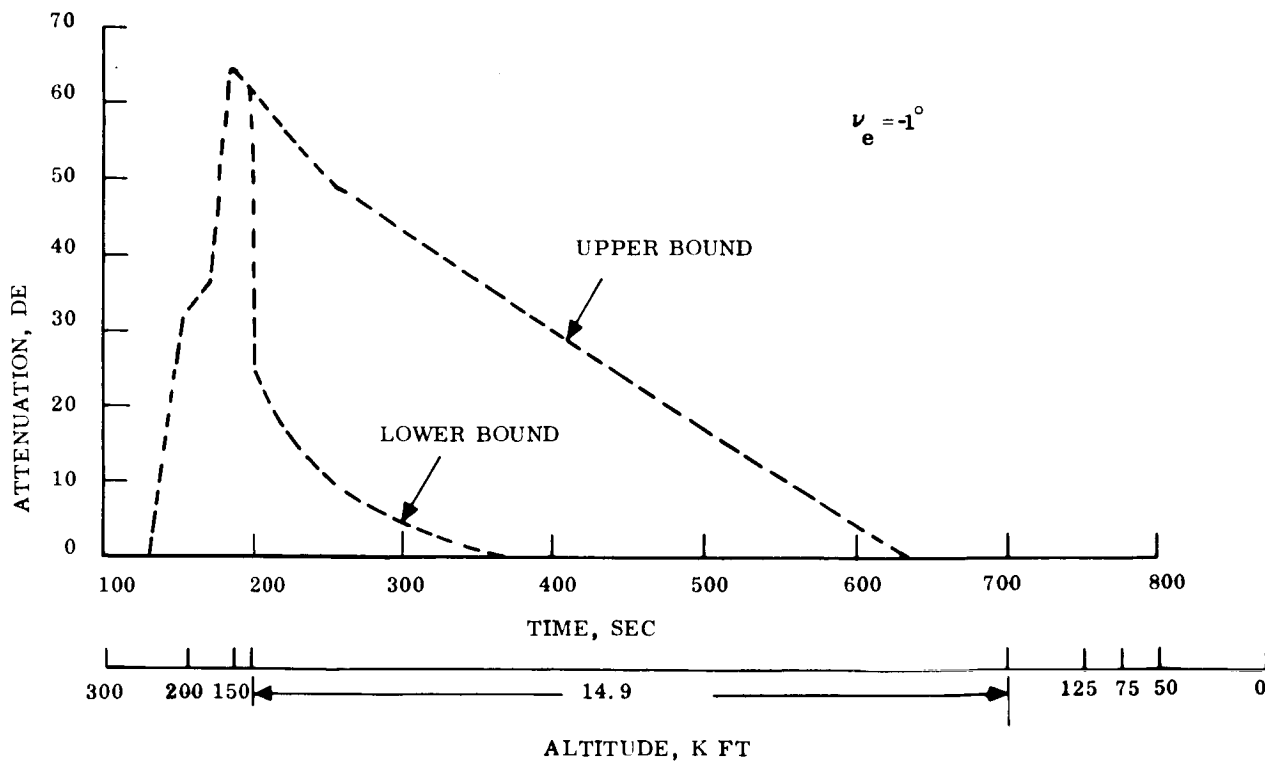


Figure 3.5-2. - Plasma Attenuation, C-band

classes of cases; inviscid flow only, a combination of inviscid flow plus a pure air boundary layer, or a boundary layer only, with or without contaminants.

This equilibrium program was run using a velocity-altitude profile for the design trajectory corresponding to an entry angle of 1° . This trajectory was chosen for the detailed analysis since it is expected to constitute a worse case. The angle of attack at each point of interest was added to the side view angle to give an effective wedge angle at each point. The nose radius used was 0.655 inch and the axial station studied was 48 inches from the nose on the bottom centerline. The inviscid alone and the pure air plus inviscid subroutines both show the effect of nose bluntness on electron production and subsequent plasma attenuation. This production should dominate at high altitudes where heat shield ablation and resulting boundary layer contamination is at a minimum. At lower altitudes, the dominant electron producing mechanism is contaminant ionization and, therefore, the attenuation predicted by the contaminated boundary layer sub-routine should be used. However, results of this option were not used for reasons discussed below.

The equilibrium chemistry assumption leads to results which do not always compare well with actual flight data due to the fact that non-equilibrium chemistry effects are important in the altitude range of interest. A non-equilibrium stream-tube analysis for bluntness ionization has thus been performed for the purpose of checking the accuracy of the results provided by the equilibrium program. This analysis involves a system of three computer programs. The first two of these programs calculate transonic properties near the nose and supersonic flow field properties along streamlines using the method of characteristics. The third program calculates species concentration along streamlines. A normal to the body at any chosen station can be constructed and using results of the stream-tube program $\int N_e dy$ and plasma attenuation can be found.

Results of the non-equilibrium stream-tube analysis compared favorably with those of the equilibrium inviscid results. Figure 3.5-3 shows electron density profiles for both equilibrium and non-equilibrium flow at a velocity of 19,026 ft/sec and an altitude of 141,900 feet at an antenna location of 48 inches from the nose tip. The area under each curve, which is equal to $\int N_e dy$, is approximately the same and, thus, equilibrium flow attenuation levels were used for subsequent high altitude predictions.

At lower altitudes, the non-equilibrium nature of the system does not allow the metallic contaminants to ionize at the rapid rate assumed by the equilibrium program. Therefore, the program over-predicts the electron concentration in the flow and, thus, should not be used at these lower altitudes. The non-equilibrium analysis mentioned above is not able to handle contaminant ionization. Therefore, the following approach was used. A classified test program presently under way for the Air Force has resulted in a set of excellent data on plasma attenuation. Flow field data from this program were used to obtain temperature in the boundary layer at the altitude-velocity point corresponding to the end of the horizontal portion of the SLAMAST flight trajectory. The temperature at that point from the SLAMAST equilibrium calculations was then scaled to a non-equilibrium value using a scaling law derived from the non-equilibrium stream-tube analysis. These two temperatures; the flight data results and the calculated

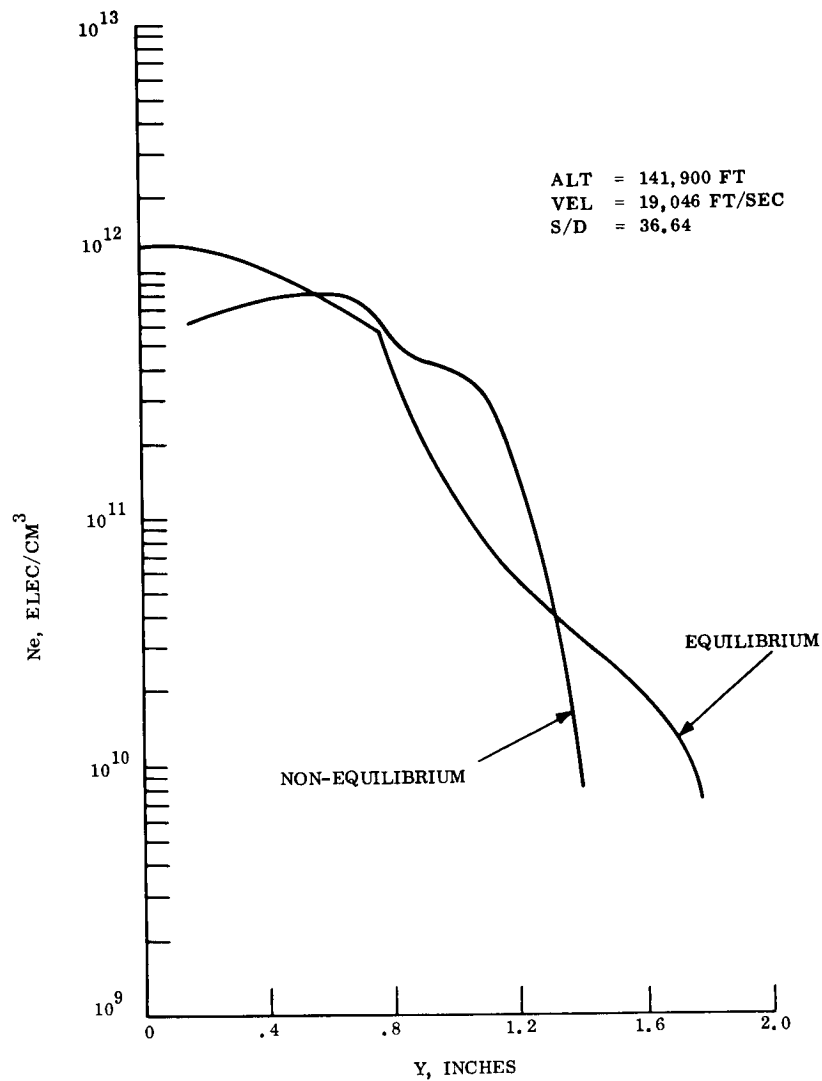


Figure 3.5-3. - 2D Inviscid Electron Density Profile Comparison

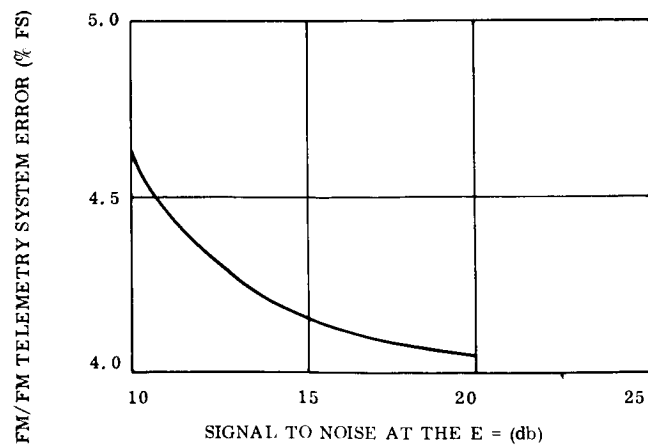


Figure 3.5-4. - FM/FM Telemetry System Error Versus Signal to Noise Ratio at I. F.

SLAMAST equilibrium value scaled for non-equilibrium effects, were used to obtain reaction rates based on kinetic coefficients recommended by Bortner (ref. 3.5-5). The reaction rates thus obtained were then compared and it was found that the SLAMAST calculated reaction rates were several orders of magnitude lower than those obtained from the flight data. Since the flight data were contaminant dominated (nose bluntness effects are negligible in the region of interest), and the attenuation was on the order of 16 to 20 db the conclusion was reached that the attenuation for the SLAMAST case at that trajectory point would be negligible.

The same analysis was applied to a point somewhat earlier on the horizontal portion of the SLAMAST trajectory. Results showed that the reaction rates were no longer orders of magnitude apart. It was thus concluded that the attenuation would not be negligible at this point. Fixing the value of the attenuation at this point, however, proved to be extremely difficult due to the inaccuracies involved. Thus an upper bound prediction was obtained by interpolating linearly between the point of negligible attenuation at the end of the horizontal flight path, and the peak value obtained by the inviscid analysis at an altitude just prior to the initiation of horizontal flight. This prediction constitutes an upper bound due to the fact that the reaction rates are a strong exponential function of temperature and thus of the trajectory. The actual case (for both S and C-bands) would thus show attenuation dropping rapidly from the peak value which occurs at about 185 seconds from entry at 400K feet (Figures 3.5-1 and 3.5-2) and leveling off to the zero value at about 700 seconds in the case of S-band frequency (Figure 3.5-1) and about 630 seconds in the case of the C-band frequency (Figure 3.5-2). The lower bound on the two figures is just the inviscid flow prediction, which excludes contaminant effects, and thus does not represent a realistic case.

3.5.2 T/M AND INSTRUMENTATION SYSTEM SELECTION

In order to select an information retrieval system which will effectively fulfill the SLAMAST objectives, the following criteria have been identified.

- (1) The system shall provide adequate accuracy and time response resolution to permit reliable quantitative delineation of the Thermal Structural phenomena of interest.
- (2) The system shall provide sufficient diagnostic information to adequately interpret the control system functions during the vehicle development phase of operational testing.
- (3) The system shall require a minimum surface support force.
- (4) The system shall, if possible, be compatible with both the Eastern test range and the Apollo Ship data acquisition equipments.
- (5) The system shall be configured to provide in-flight data acquisition to minimize the probability of data loss.

In meeting these criteria, the following specific factors must be considered:

- (1) Shipboard system acquisition capabilities
- (2) Communication signal strength margins
- (3) Shipboard system tracking rate limitations
- (4) Flight path dispersion as it affects shipboard system coverage
- (5) Structural temperature flight profile
- (6) Accuracy capability of digital and analog encoding and modulation techniques (PCM/FM versus PDM/FM and PAM/FM)
- (7) Data degradation in storage
- (8) Reliability and packaging efficiency

Consistent with these criteria and design considerations, the following information retrieval configuration has been selected for the SLAMAST feasibility study. (Criteria is discussed further under the trade-offs section.)

- (1) PCM/FM Telemetry with digital on-board data handling (eight bit sample encoding)
- (2) Capability for ground command initiated recorder playback
- (3) Non-destructive data playback (data remains on tape) from the on-board recorder with no provision for simultaneous record and playback
- (4) Programmed playback of the on-board recorder during the retardation sequence as backup
- (5) Continuous real-time telemetry at a power level of two watts except during recorder playback. During playback, the recorder and real-time information shall be mixed and transmitted at a two watt level.
- (6) Utilization of the predetection recording capability of the shipboard systems.
- (7) Incorporation of a C-band transponder and command receiver.

This system configuration provides the following advantages:

- (1) Experiment data can be recovered in four fashions:
 - (a) Data playback during the terminal portion of the experiment period. (If tracking acquisition is not obtained by the shipboard system, the record mode continues.)

(b) Real time acquisition, ship availability and plasma attenuation permitting.

(c) Playback acquisition during the retardation sequence.

(d) Recovery of the on-board tape.

(2) Utilization of minimum surface support forces as desired (convenient transition to minimum support forces as vehicle performance confidence is obtained)

(3) Diagnostic information recoverable from the entire flight

(4) Digital encoding and data handling provides an excellent data accuracy capability.

(5) Digital recording preserves data accuracy during the on-board record cycle (see trade-off discussion, paragraph 3.5.3).

3.5.3 TRADE-OFFS

3.5.3.1 Digital versus analog data handling. - The primary reason for selection of a digital on-board system is to obtain high quality accurate information retrieval. A typical measurement list is illustrated in Table 3.5-1. This list specifies the desired accuracy to be obtained end to end (exclusive of the sensor), for each measurement. The highest accuracy requirements listed are for the control system diagnostic measurements. However, flight dynamics measurements to 1 percent are indicated and thermo structural measurements to 3 percent are desired. In addition, it is felt that for a research program, the greatest achievable accuracy is desirable.

End to end accuracies obtainable with analog systems (PAM/FM & PDM/FM) deteriorate to 5 percent 3σ or greater at received signal to noise ratios of 9 db. Figure 3.5-4 illustrates the accuracy-signal/noise ratio relationship for a typical PAM/FM system. The incorporation of an on-board recorder further deteriorates attainable accuracy by about 2 percent 3σ for typical recorders used in analog fashion.

A factor of significance when comparing analog and digital data handling is data confidence. This factor is of concern for the SLAMAST application. Accuracies quoted in the customary manner for analog systems are attainable accuracies for 3σ confidence. However, during post flight data analysis, the accuracy achieved is not known quantitatively. Only a statistical bound is known and this bound is a function of signal to noise ratio (as was illustrated in Figure 3.5-4). This disadvantage is particularly acute when attempting to establish the magnitude of short term parameter fluctuations, for in this case, data smoothing is not appropriate.

The use of running scale references while effectively correcting for drift due to system gain changes does not reduce the error due to signal/noise content. In fact, since the reference samples are no less noisy than the data samples, the scaling operation during data reduction adds to the statistical variance of the measurement.

TABLE 3.5-1. - SLAMAST MEASUREMENTS

Designation	Description	Diagnostic	Experiment	Range	Reqd. F.S. Accuracy	SPS (MIN)
101-110	Body Pressure (10)		X	0-20 psia	±2%	20
111-115	Body Pressure (5)		X	0-5 psia	±2%	20
116-119	Flap SFC Press (4)		X	0-20 psia	±2%	40
120	Flap Cavity		X	0-5 psia	±2%	10
121	Body Base	X	X	0-1 psia	±2%	10
122	Body Base	X	X	0-0.5 psia	±2%	10
123-135	S/C Backface Temps. (13)	X	X	0-1000°F	±1%	2
136-150	S/C Calorimetric (15)	X	X	0-3000°F	±2%	10
151-198	S/C Temp. in Depth (48)	X	X	0-3000°F	±1%	5
199-200	S Spare Veh. (2)		X	-		10
201-224	#1 Panel Substrate Strain (24)		X	0-5000 μ in/in	5%	5
225	#1 Panel Displacement		X	0-.2 in	±5%	10
226-230	#1 Panel Vibration Envelope (5)		X		±5%	5
231-232	Flap Panel Strain (Moment) (2)		X	0-5000 μ in/in	5%	20
233-236	Flap Panel Temps. (4)		X	0-3000°F	±1%	20
237-246	Panel #2 Temps. (10)		X	0-1000°F	±1%	2
247-250	Panel #2 Temps. (4)		X	0-3000°F	±1%	5
250-254	Panel #2 Subs-Temp. (4)		X	0-500°F	±1%	2
255-256	Panel #2 Strain (2)		X	0-5000 in/in	5%	2
257-266	Panel #1 Temps. (10)		X	0-1600	±1%	2

TABLE 3.5-1 Continued

Designation	Description	Diagnostic	Experiment	Range	Reqd. F.S. Accuracy	SPS (MIN)
267-271	Panel #1 Temps. (5)		X	0-3000	±1%	5
272	Body Base	X	X	0-10 PSI	±2%	10
301	Flap Control Signal - Autopilot	X		-10 10 volts	±1%	40
302	Flap Error Signal - Autopilot	X		-10 10 volts	±1%	40
303	Autopilot Supply #1	X		0 - 28 volts	±1%	2
304	Autopilot Supply #2	X		0 - 28 volts	±1%	2
305	Autopilot Supply #3	X		0 - 28 volts	±1%	2
306	Autopilot Supply #4	X		0 - 28 volts	±1%	2
307	Autopilot Supply #5	X		0 - 28 volts	±1%	2
308	Roll Rate Gyro	X	X	0 - 28 volts	±1%	2
309	Pitch Rate Gyro	X	X	±20°/sec	3%	20
310	Yaw Rate Gyro	X	X	±20°/sec	3%	40
311	Platform Temp.	X		±20°/sec	3%	40
312	Platform ϕ	X		0 - 200°F	3%	2
313	Platform θ	X		±180 deg	5%	10
314	Platform ψ	X		± 90 deg	5%	10
315	Drag Brake Position	X		0-40 deg	±.5°	20
316	Platform Supply Monitor #1	X		0 - 50° volts	±.5°	2
317	Platform Supply Monitor #2	X		0 - 5 volts	±1%	2
318	Platform Supply Monitor #3	X		0 - 5 volts	±1%	2

TABLE 3.5-1 Continued

Designation	Description	Diagnostic	Experiment	Range	Reqd. F.S. Accuracy	SPS (MIN)
319	Platform Supply Monitor #4			0 - 5 volts	±1%	2
320	Platform Supply Monitor #5			0 - 5 volts	±1%	2
321	Flap Actuator Position			0 - 50°	±.5°	40
322	Clock Coarse	X	X	2 ⁸ 0-2048 sec.	±1/2 sec	Frame Rate
323	Clock Fine	X	X	2 ⁸ 0-2048 ms	±1/2 ms	
324	CG Axial Ax fine (Ax) body mtd.	X	X	0-2.5g	±.01g	
325	CG Yaw Ay fine (As) body mtd.	X	X	-1 +1g	±.01g	20
326	CG Pitch Az fine (An) body mtd.	X	X	-1+5g	±2%	20
327	Foreward Ax body mtd.	X		-10+10g	±2%	10
328	Foreward Ay body mtd.	X		-10+10g	±2%	10
329	Foreward Az body mtd.	X		-10+10g	±2%	20
330	Dynamic Ax forward (derived from 27)	X	X	±1g (H.P. FL 1/2 cps)	±5%	20
331	Dynamic Ay forward (derived from 28)	X	X	±1g (H.P. FL 1/2 cps)	±5%	20
332	Dynamic Az forward (derived from 29)	X	X	±1g (H.P. FL 1/2 cps)	±5%	40
333	Flap Actuator load	X		0 - 400 in lbs	±5%	10
334	Gas Storage Temp	X		0-300°F	±3%	2
335	Gas Storage press.	X		0-4000 psia	±5%	2

TABLE 3.5-1 Continued

Designation	Description	Diagnostic	Experiment	Range	Reqd. F.S. Accuracy	SPS (MIN)
336	Regulator press	X		0-100 psia	±3%	2
337	(G Lqt Accel. Coarse (As)	X	X	-20 +20g	±1%	10
338	(G Pitch Accel. Coarse (An)	X	X	+ 2 -25g	±1%	20
339	(G Axial Accel. Coarse (Ax)	X	X	+ 2 -20g	±1%	10
340	Pitch Attitude Error (Ap)	X		-30° +30°	±5%	10
341	Yaw Attitude Error (Ay)	X		-30° +30°	±.5°	20
342	Roll Attitude Error (Ar)	X		-30° +30°	±.5°	20
343	Pitch Calc. Error (Ep)	X		-30° +30°	±.5°	10
344	Yaw Calc. Error (Ey)	X		-30° +30°	±.5°	20
345	Roll Calc. Error (Er)	X		-30° +30°	±.5°	20
346	Meas. Velocity Derive (Vx)	X		10-25 K ft/sec	±1%	20
347	Desired Velocity Sched. (vxd)	X		10-25 K ft/sec	±1%	20
348	Pitch Command (θ pc)	X		0-40°	±.5°	10
349	Desired Axial Accel. (Ax)d	X		0-10g	1%	20
350	Autopilot Signal Bc	X		±50°	1%	20
351	Autopilot Spare	X		-	-	10
352	Event Word	X		Digital		20
352a	Platform Event #1	X				
352b	Separation	X				

TABLE 3.5-1 Continued

Designation	Description	Diagnostic	Experiment	Range	Reqd. F.S. Accuracy	SPS (MIN)
352e	Initiate 3 Axis AA Control	X				
352f	Start Programmed Flt.	X				
352g	Start Recovery Seq.	X				
352h		X				
353	Spare	-				10
354	Event Word	X				20
354a	Exo-Solenoid Discrete #1	X				
354b	Exo-Solenoid Discrete #2	X				
354c	Exo-Solenoid Discrete #3	X				
354d	Exo-Solenoid Discrete #4	X				
354e	Exo-Solenoid Discrete #5					
354f	Exo-Solenoid Discrete #6					
354g	Platform Alignment Discrete					
354h	Event Spare					
355	Event Word			Digital		10
355a	Exo-High Thrust #1					
355b	Exo-High Thrust #2					
355c	Exo-High Thrust #3					
355d	Exo-High Thrust #4					
355e	Event Spare					

TABLE 3.5-1 Continued

Designation	Description	Diagnostic	Experiment	Range	Req'd Accuracy	SPS (MIN)
355f	Event Spare			Digital		10
355g	Event Spare					
355h	Event Spare					
356	Event Word					
356a	Retardation Event #1					
356b	Retardation Event #2					
356c	Retardation Event #3					
356d	Retardation Event #4					
356e	Retardation Event #5					
356f	Retardation Event #6					
356g	Retardation Event #7					
356h	Retardation Event #8					
357	Event Word					
357a	Retardation Event #9					
357b	Retardation Event #10					
357c	Retardation Event #11					
357d	Retardation Event #12					
357e	Retardation Event #13					
357f	Retardation Event #14					
357g	Retardation Event #15					

TABLE 3.5-1 Concluded

Desig- nation	Description	Diagnostic	Experiment	Range	Req'd Accuracy	SPS (MIN)
357h	Retardation #16			0-10 volts	1/2%	10
357-361	Instr. References (6)					
362	Recorder Monitor			0-35 volts	±1%	2
363	Battery Voltage			0-25 amps	±1%	2
364	Battery Current					2
	Transponder Voltage					2
	Transponder Perfection					
	Component Voltage (8)			0-35v	±1%	2
	Component Temp.			0-200°F	±5%	2

In summary, the accuracy and data confidence desired are not obtainable with an analog system for the signal levels expected in the SLAMAST application.

In contrast, the utilization of a Pulse Code Modulation system with digital on-board data handling can provide very accurate (1 part in 256 plus sensor error) information. In addition for signal levels sufficiently above threshold (which is determinable from the observed bit error rate) the accuracy is adequately bounded and data confidence is obtained.

For these reasons, a PCM telemetry system used in conjunction with digital on-board recording is considered superior for the SLAMAST application. It should be noted that the cost trade-off is no longer unfavorable for digital systems and when processing costs are included the trade-off is favorable.

3.5.3.2 Tracking system requirements. - A knowledge of the altitude-velocity profile is essential to interpreting the S/C function since the experiment environment is in part, a function of the trajectory. The on-board controller is designed to provide a desired altitude profile. The controller parameters and the S/C dynamics will be monitored by telemetry, enabling a reconstruction of the trajectory from the on-board measurements. However, in order, to correlate and establish tolerances for the derived trajectory, it is required to provide a surface tracking capability. Radar track information is also necessary for recovery. It is also desirable to obtain diagnostic information in the event of an unsuccessful flight. This is especially pertinent during the pullup maneuver.

Thus, the S/C tracking requirement is identified as coverage during pullup maneuver, during the terminal portion of the experiment period, and during retardation. Continuous coverage is not considered necessary as the on-board information will provide adequate extrapolation between surface coverage periods.

Exospheric coverage can be obtained from the radar installation on Bermuda. However, the pullup maneuver will be completed beyond the Bermuda useful horizon and look angle. Therefore, a nominal surface ship configuration should consist of one tracking ship positioned to cover pullup and the early experiment period and a second ship positioned to cover the terminal experiment period and the early retardation sequence. (Ship placement is discussed under separate heading.)

3.5.3.3 Trajectory reconstruction. -

3.5.3.3.1 Introduction: The Data Acquisition and Coverage presently planned for the SLAMAST Flight Test Program will consist of two ships with metric radar data measurement, one ship located to track the spacecraft during the re-entry maneuver southwest of Bermuda, and the second ship strategically placed at the retardation location to record metric radar and playback/real time telemetry data.

The reconstruction of the experiment phase of the trajectory from two radar locations in conjunction with spacecraft telemetry data presents a problem of which GE-RSD has available techniques for Ballistic Re-entry Trajectories.

The identification and proposed methods of extending these techniques to lifting re-entry vehicles is discussed in the following sections.

3.5.3.3.2 Present techniques for optimizing ballistic radar trajectories: At the present time, within GE-RSD a technique is available for determining the optimum initial conditions to use for "fitting" a point mass trajectory from selected metric radar data. The resulting trajectory provides a least squares fit to selected radar measurements of spacecraft position prior to and during re-entry. This technique has been utilized for the on board data analysis of 6 RMV program flight tests, with very satisfactory results and provides metric data in periods where there was no radar coverage.

The trajectory processing is conducted in five basic steps which are described below.

3.5.3.3.3 Smoothing, refraction correction and coordinate conversion: The measured range, azimuth, and elevation may be smoothed, if desired, by a digital filter which spans one second of data (at 100 samples/second) and has a cutoff frequency of 2.6 cycles/second.

The corrections for atmospheric refractions are applied to range and elevation and are calculated by a ray tracing technique which assumes constant refractivity through layers of the atmosphere. Values of refractivity are derived from measured atmospheric data if available. Otherwise, an exponential model atmosphere is used to compute refractivity.

Smoothed and refraction corrected range, azimuth, and elevation are converted to inertial geocentric coordinates (XYZ) for use in fitting the optimum trajectory.

3.5.3.3.4 Fitting: For a given vehicle drag model or measured deceleration history, a point mass trajectory through re-entry is completely specified by knowledge of vehicle position and velocity at some initial time. To determine the optimum initial conditions, approximate re-entry, vehicle position and velocity, determined from high altitude radar data, are used as initial conditions for calculation of a preliminary point mass trajectory. The differences between this first estimate of trajectory and the radar measured values are combined with partial derivatives obtained from perturbations of the first estimate of trajectory to yield revised initial position and velocity. Iterations of this process continue until initial conditions are determined which yield the trajectory which best fits the radar data.

The criterion for best fit is the minimization of the weighted sum of the squares of the distance between the computed positions and the radar measured positions.

Measured atmospheric quantities plus theoretical models of the earth and of vehicle mass, area and drag are used for the re-entry portion of the trajectory calculation.

3.5.3.3.5 Trajectory comparison: The fitted trajectory is evaluated by comparison of vehicle position as measured by the radar and the position determined from the fitted trajectory. Radar measured position is converted to geodetic coordinates and calculated position is converted to radar coordinates. Differences are expressed in terms of altitude, geodetic latitude, longitude, radar range, azimuth, and elevation. Means and standard deviations of the differences are calculated and the differences are plotted.

For several of these flights, comparison of the fitted trajectory and the radar data indicated an excellent high altitude fit, with divergence at lower altitudes which were evidently caused by inaccuracies in the drag model.

After processing of spacecraft motion data (accelerations and angular rates), a drag deceleration history was obtained from the telemetry data. Values selected from this unsmoothed drag history were substituted for the model and a new trajectory was fitted to the radar data. In general, this trajectory resulted in a significant decrease in the divergence which was previously observed.

3.5.3.3.6 Proposed trajectory reconstruction method for SLAMAST vehicle: The trajectory fitting technique described in the previous section will be the method used for trajectory reconstruction with the modifications discussed below. The current technique includes the equations of motion for determining the re-entry trajectory based on a ballistic re-entry, considering only the drag component of force. The equations of motion in this program can be modified to include the lift and yaw components of force. The lift and drag accelerations are functions of the pitch angle of attack during the experiment phase of the trajectory.

To apply this technique, the trajectory is considered to have three phases: Re-entry, experiment, and recovery. It is required that metric radar data be available for re-entry and recovery with telemetry data (accelerations and attitude) being available for the entire flight. Using the smoothed radar metric data for the initial conditions, an initial trajectory from high altitude re-entry through low altitude impact will be determined by fitting directly to radar metric data, and using yaw, normal and axial accelerations time histories and inertial attitude data.

The residuals remaining from this initial fit will be examined. If required, a second iteration on the trajectory will be determined based on perturbations induced into the lift and drag acceleration time histories. This iteration will continue until a specified degree of fit is obtained with measured recovery data. An error analysis based on sources of error and magnitude (Radar, telemetry measurements) will be conducted prior to actual use of the data for trajectory reconstruction.

3.5.3.4 Apollo ship capability*. - The Apollo project ships are configured to provide both S-band and C-band metric data. The plasma attenuation consideration is discussed under separate heading and indicates the desirability of utilizing the C-band

*Mission Support Capabilities - Apollo Instrumentation Ships
1 June 1966 - Apollo Instrumentation Ships Program Office

capability. The use of C-band is compatible with the ARIS ship configuration* and enables interchangeability. In addition, the C-band link provides a convenient means of accomplishing surface initiated commands. The use of unified S-band commands would necessitate a complex on-board configuration and would not be compatible with the ARIS ship configuration.

The Apollo ship is configured to receive real time trajectory update information via a HF communication link. This information is then utilized by the central information processor (UNIVAC 1230 computer) which generates scan commands for the antenna controllers. This capability should be of considerable advantage to SLAMAST in mitigating the acquisition problem downrange.

3.5.3.5 On-Board transponder requirement. - A C-band transponder has been selected for the SLAMAST S/C configuration. This transponder is desirable to extend the accurate tracking capability of the FPS/16 radar to 200 nautical miles and provide a reliable acquisition sequence.

The published FPS/16 range capability (see reference 3.5-6) for a $.1M^2$ target in skin track mode is 43 nautical miles. This is the maximum distance for which a 12 db S/N ratio can be maintained, which is the ratio required for accurate track and secure lock. At 200 n. mi., the S/N for a $.1 M^2$ target is down to -14 db which is inadequate for maintaining track. The use of an on-board transponder with a pulse power of 500 watts and a receiver sensitivity of -70 db extends the range considerably and yields a S/N ratio of +45 db at 200 n. mi., neglecting plasma attenuation. This 45 db C-band gain margin provides desirable immunity to plasma attenuation and should provide a reliable acquisition sequence.

* ARIS orientation manual - RCA Service Co.
Missile Test Project
Patrick Air Force Base, Florida

3.5.3.6 Measurement requirements. - Table 3.5-1 presents a compilation of typical measurements for a SLAMAST Spacecraft. Measurement designation 100-300 are primarily thermo structural experiment or related information, whereas diagnostic control system and other necessary measurements are designated 300 and above.

3.5.3.7 Experimental. - Panel measurements indicated are temperature, strain, displacement, calorimetric, and vibration. Strain measurements would typically be obtained by 0-5000 μ in/in rosette gages mounted at opposite panel wall locations, near the panel center and near the edges. The gages mounted on the ablator side of the panel would be invalid after approximately 600°F is reached but the strain history prior to loss is of interest. The strain information desired is the static component. Thus, the sensor output can be low pass filtered, eliminating the vibration components and permitting adequate sampling at a rate of 5 samples per second.

Displacement characteristics of the panel can be obtained by the installation of a single displacement monitor located at the center of the panel. A differential transformer technique is preferred to eliminate mechanical coupling errors.

Vibration information is desirable to complete the knowledge of the panel environment. Spectral range envelope information is adequate. The filtering requirements are rudimentary and implementation will not present a packaging problem. The envelope waveform can be adequately monitored at a sampling rate of 5 samples per second yielding dynamic resolution beyond 1 cycle per second.

3.5.3.8 Diagnostic measurements. - The diagnostic measurements provide functional information relative to on board system performance and the spacecraft dynamics. Standard measurement techniques are appropriate for the majority of the information. A typical measurement configuration is indicated in the measurement list. S/C body pressures and shield temperatures in depth are provided in order to establish physical design tolerances and to provide substrate panel environment information. A set of accelerometers (meas # 27-29) are incorporated at a location well forward of the S/C center of gravity. These units should be of the high quality force balance type construction for accuracy and rejection of cross coupling components. The ± 10 g ranges indicated prevent saturation over the range of the slowly varying linear acceleration components expected. The dynamic components generated by S/C rotational moments are obtained by high pass filtering of the sensor outputs. These waveforms (meas # 30-32) are then conditioned to provide ± 1 g full scale. The information obtained should be valuable in defining the vehicle stability characteristics and dynamic response. In addition the correlation with the rate gyro information and dynamic pressure fluctuation provides supporting panel environment data.

3.5.3.9 Ship placement considerations - data acquisition and tracking. - In order to establish the surface ship support required for SLAMAST, the effects of trajectory dispersion on the following factors must be considered:

- (1) Shipboard system coverage capability including
 - (a) tracking rate constraints
 - (b) horizon limitations

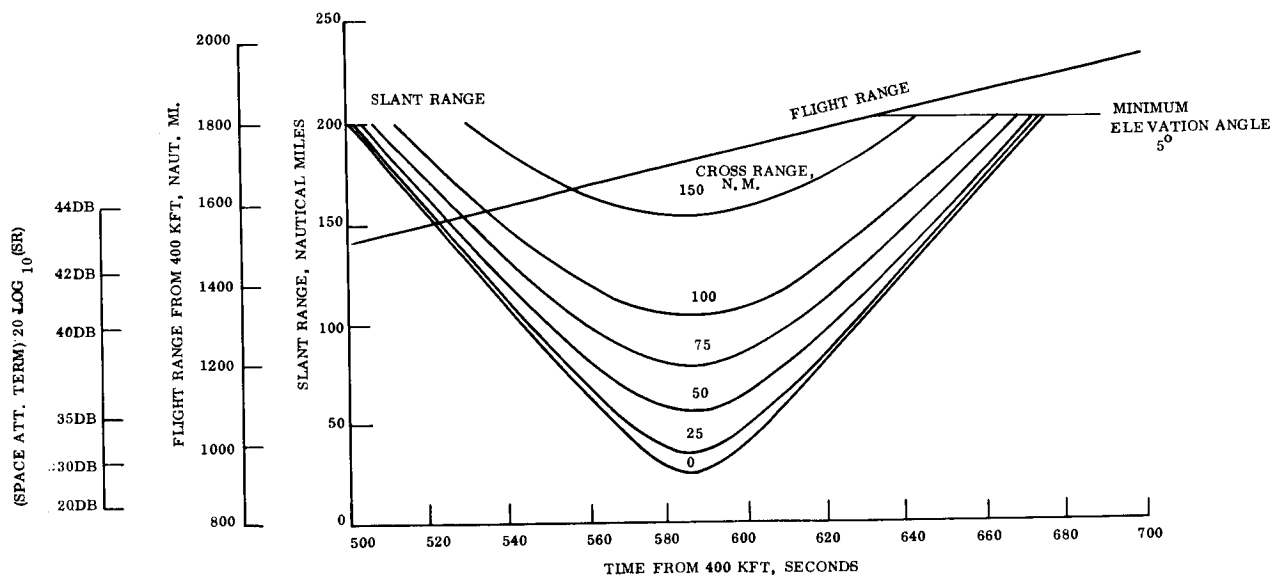


Figure 3.5-5. - Slant Range and Flight Range Histories for Ship Location at 1700 Nautical Miles Downrange, - 1° Re-entry Angle Trajectory

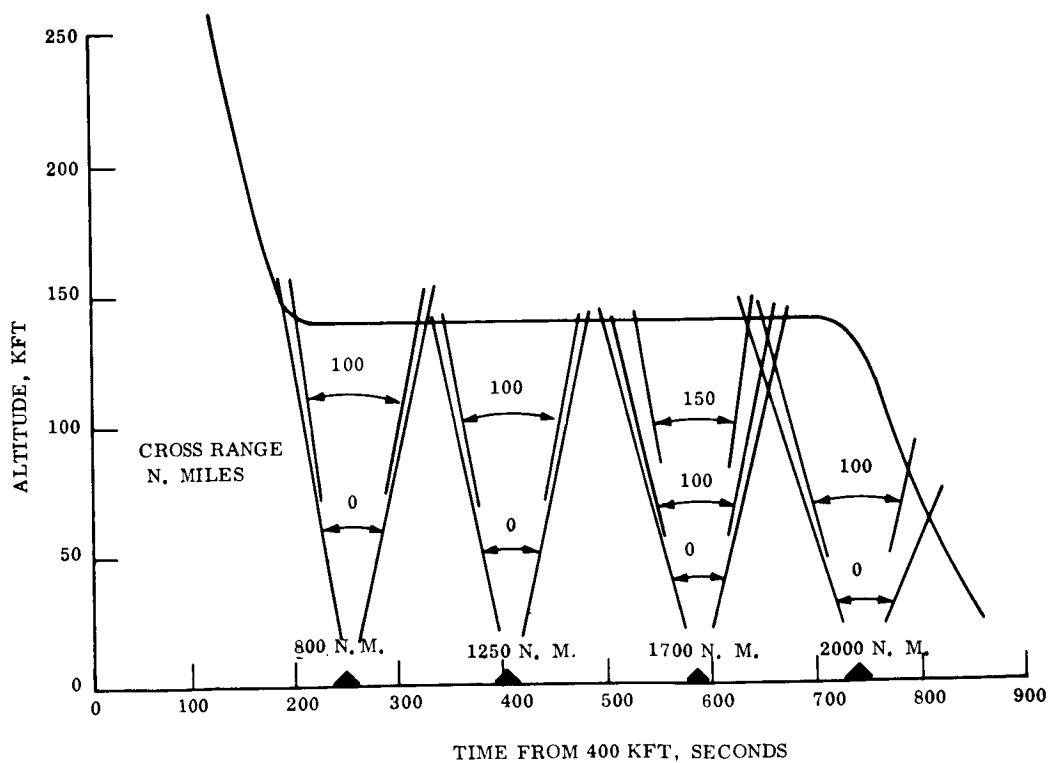


Figure 3.5-6. - Down Range Ship Reception, Window Based on 5° Minimum Elevation Angle, - 1° Re-entry Angle

(2) Slant range (gain margin)

(3) S/C antenna pattern

Due to the uncertainty in the location of the trajectory plane, the subsequent presentation evaluates the above parameters for various cross ranges, at several points along the trajectory. Tracking rates are limited to 10 degrees/second maximum and elevation angles between 5 degrees and 80 degrees are considered. The trajectory considered is the -1° re-entry angle design trajectory.

For the downrange S/C recorder playback location, the crossrange capability of the shipboard system is established as 14 to 160 nautical miles (see following development and Figure 3.5-5). Thus, a nominal crossrange position of 85 nautical miles will provide 100 seconds coverage for a crossrange flight path dispersion of ± 70 nautical miles.

Plots of S/C pitch and yaw aspect angle components are provided as a function of ship location. These plots illustrate the S/C antenna pattern requirement as a function of ship location.

3.5.3.10 Analysis. - In the analysis of the ship placement problem, several nominal downrange positions were chosen and the effect of cross range on elevation angle, elevation and azimuthal angle rates, and horizon limitations was investigated. The positions selected for investigation were the 800, 1250, 1700, and 2000 nautical mile points downrange from 400K feet re-entry. These positions are shown in Figure 3.5-6 together with an indication of the available span of coverage. An elevation angle of 5 degrees was set as a lower limit and 80 degrees as the upper limit. The latter limitation produced a "blind" spot for 0 crossrange of 3 to 8 seconds depending on the velocity and altitude and is not shown on the figure.

Due to the constant altitude and similar velocities, it was found that the results of the 800, 1250, and 1700 n.mi. stations were approximately of the same magnitude. To avoid unnecessary duplication, only the 1700 n.mi. case is presented which is representative of the other two positions. However, at the 2000 n.mi. location, the major portion of the coverage is affected by decreasing altitude and velocity and is therefore treated separately.

To obtain the variation of horizon limitations for various cross ranges, plots of slant range versus time were made. For any given cross range, the curve of slant range is limited by the minimum elevation angle, 5° . The observation time is the time interval between the end points which can be evaluated against the 100 second link requirement. Figure 3.5-5 illustrates that to maintain the 100 second time interval at the 1700 n.mi. location, a maximum crossrange of about 160 n.mi. can be tolerated before data loss becomes unavoidable.

A similar plot for the 2000 n.mi. position is shown in Figure 3.5-7. Here, the tendency to lose the S/C over the horizon because of decreasing altitude is compensated by the deceleration so that the communication times are comparable to the 1700 n.mi. case.

In order to determine the lower limit of cross range, tracking rates and maximum elevation are considered.

A maximum elevation of 80° imposes a 5 n. mi. minimum for the 1700 n. mi. position, as illustrated in Figure 3.5-8. A plot of elevation rates, Figure 3.5-9, indicates a low elevation rate (6° per second) so that the maximum of $10^\circ/\text{sec}$ is not exceeded at this position. Azimuth rates, however, can become quite high since the rate is infinite at 0 crossrange when the vehicle is directly overhead. This is shown in Figure 3.5-10 for the 1700 n. mi. position and the corresponding maximum rates versus crossrange in Figure 3.5-11. From the latter figure, it is seen that the maximum rate of $10^\circ/\text{sec}$ imposes a minimum crossrange of 14 n. mi. and therefore overrides the minimum of 5 n. mi. imposed by the elevation angle. Shown in Figure 3.5-12 are the azimuth rates for the 2000 n. mi. position where it is seen the minimum crossrange is determined at 10 n. mi. It should be mentioned that if the shipboard system is the 3-gimbal type allowing a full 180° overhead rotation, azimuth rates do not impose any restrictions.

In the event that various flight maneuvers such as pitch, roll, and yaw are considered necessary for the satisfactory completion of mission requirements, it is realized that severe penalties may be incurred due to these effects on the orientation of the S/C antenna pattern. It is desired that the line of sight vector from the S/C to the receiver pass through that portion of the antenna pattern which does not produce significant transmission losses (null spots). Figures 3.5-13 and 3.5-14 give the time variation of the pitch pointing angle (positive down from velocity vector) and yaw pointing angle for various crossrange distances of the ship location. Values of antenna gain (negative) were obtained from the antenna pattern shown in Figure 3.5-15. The severity of these losses cannot be evaluated by themselves but are dependent on the additional factors such as plasma attenuation, space attenuation, etc. The levels indicated show, however, the effect of crossrange on available transmission gain for the centerline location of the slot antenna. Note that these curves can be used to determine the radiation pattern requirements.

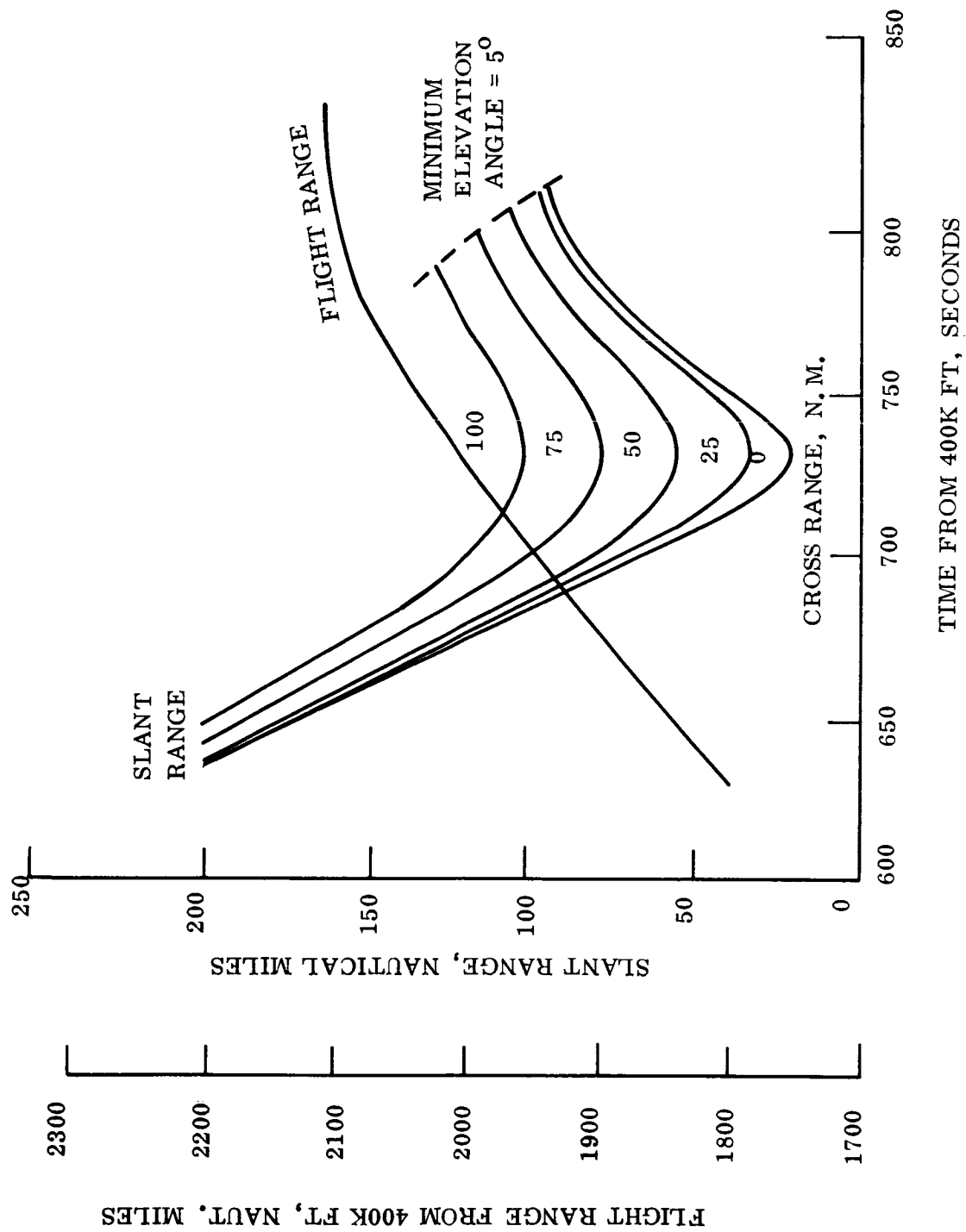


Figure 3.5-7. - Slant Range and Flight Range at 2000 N. Mi. Down Range, - 1° Re-entry Angle

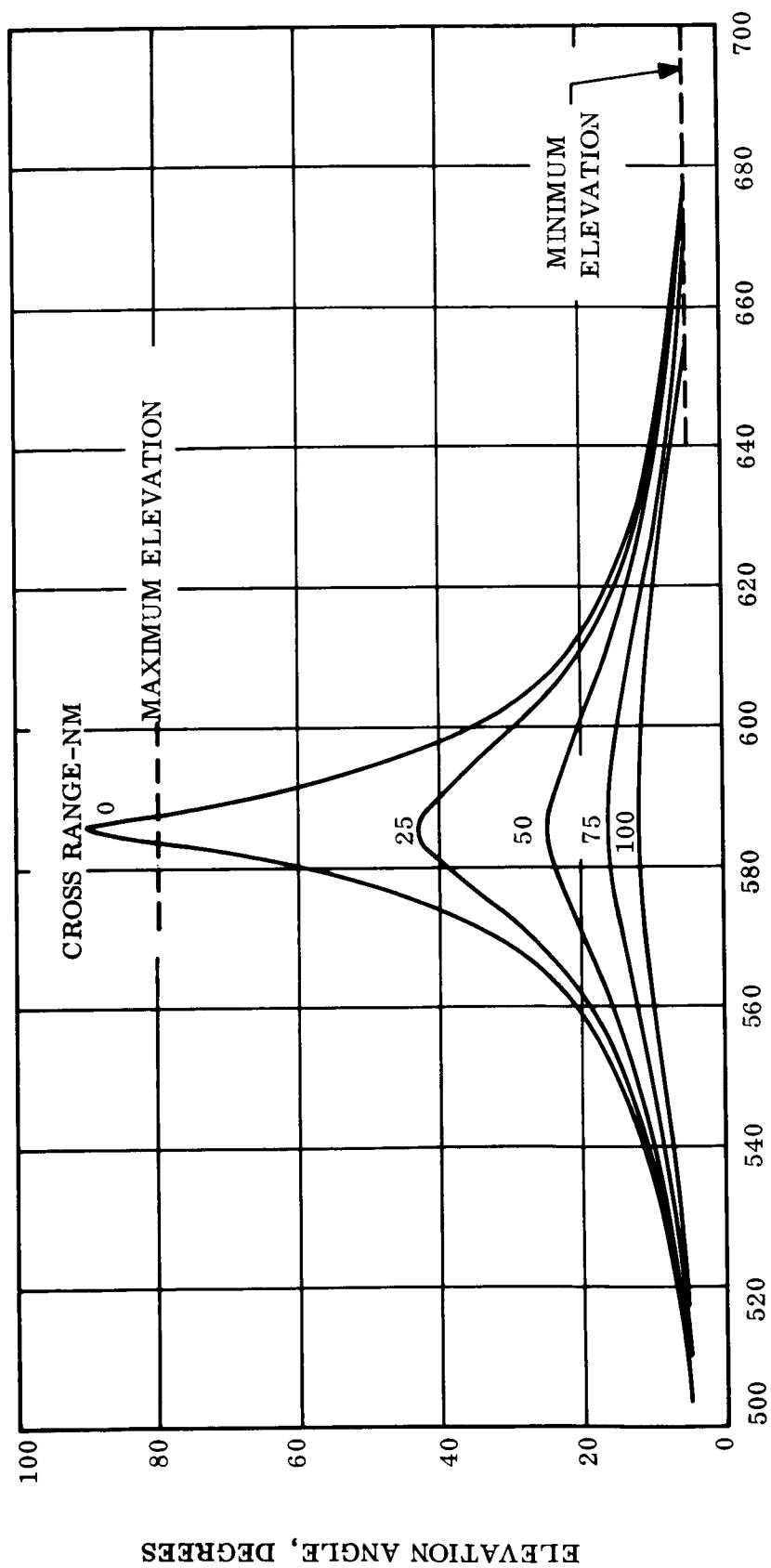


Figure 3.5-8. - Elevation Angle at 1700 N. Mi. Down Range Location, - 1° Re-entry Angle

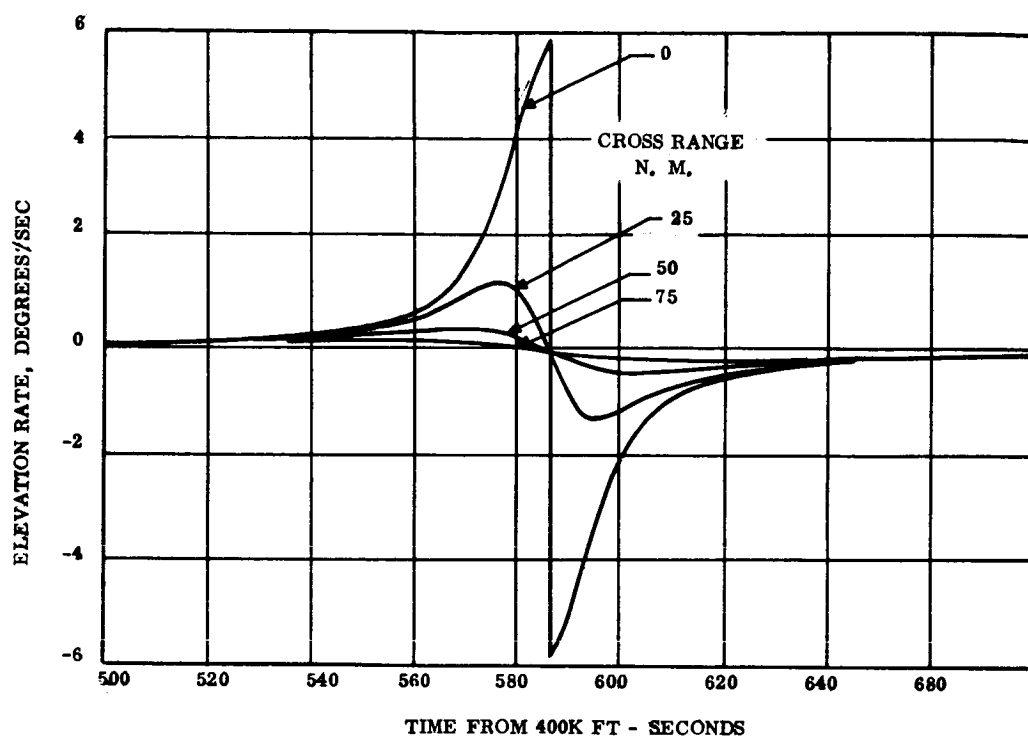


Figure 3.5-9. - Elevation Rates at 1700 N. Mi. Down Range Location, - 1° Re-entry Angle

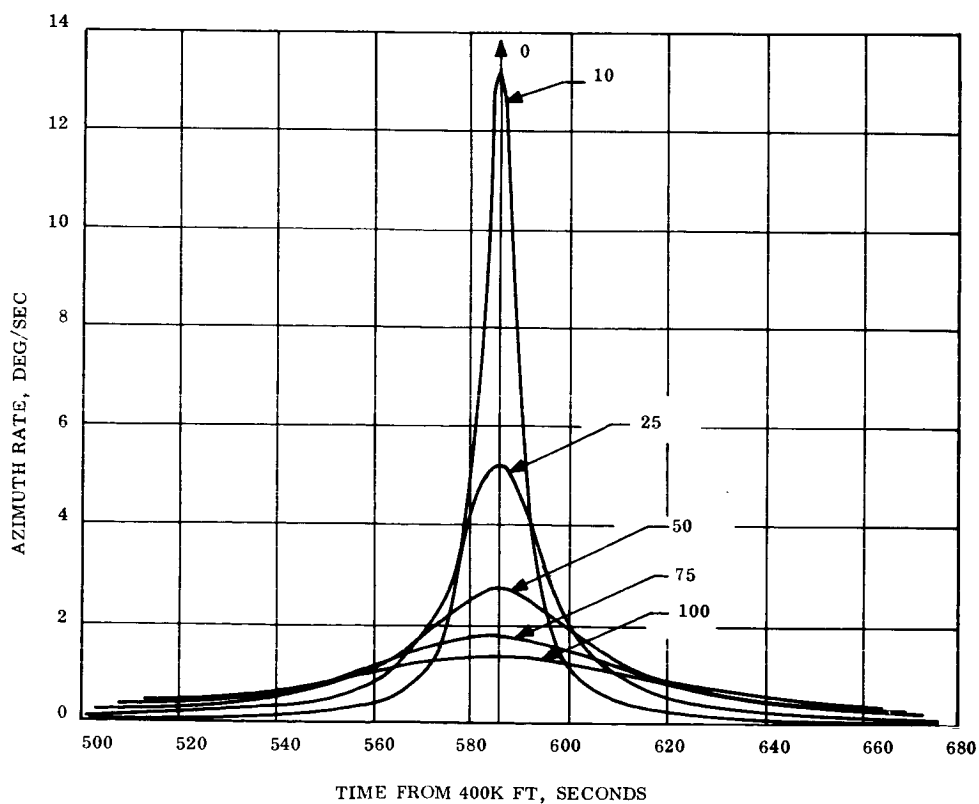


Figure 3.5-10. - Azimuth Rates at 1700 N. Mi. Down Range Location, - 1° Re-entry Angle

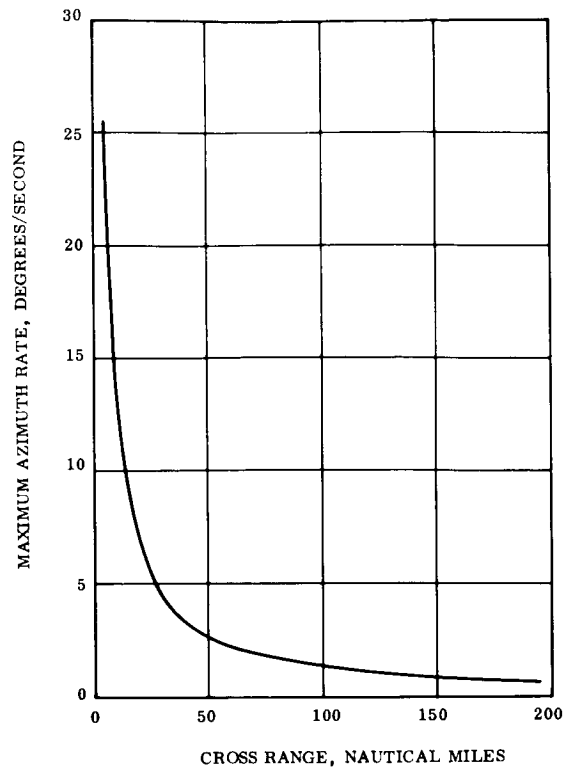


Figure 3.5-11. - Maximum Azimuth Rates at 1700 N. Mi. Down Range, -1° Re-entry Angle

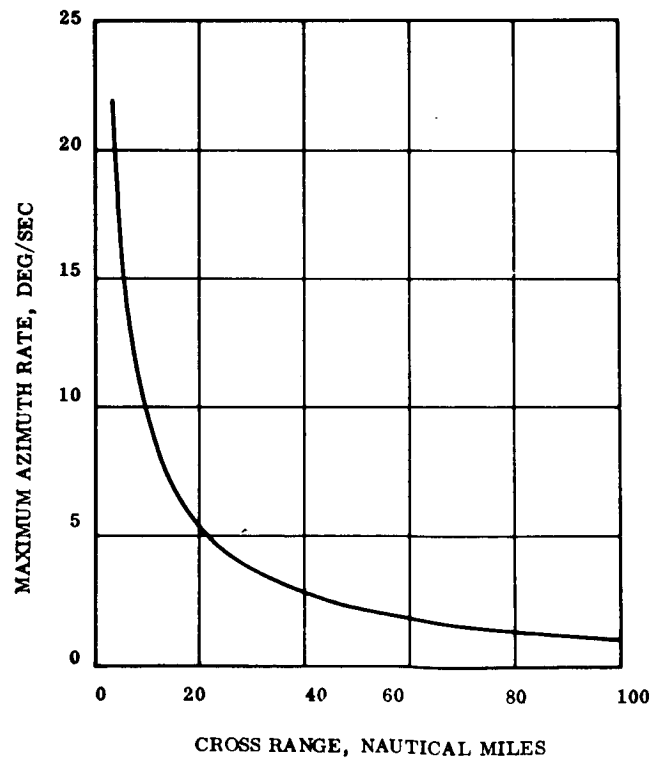


Figure 3.5-12. - Maximum Azimuth Rates at 2000 N. Mi. Down Range Location, -1° Re-entry Angle

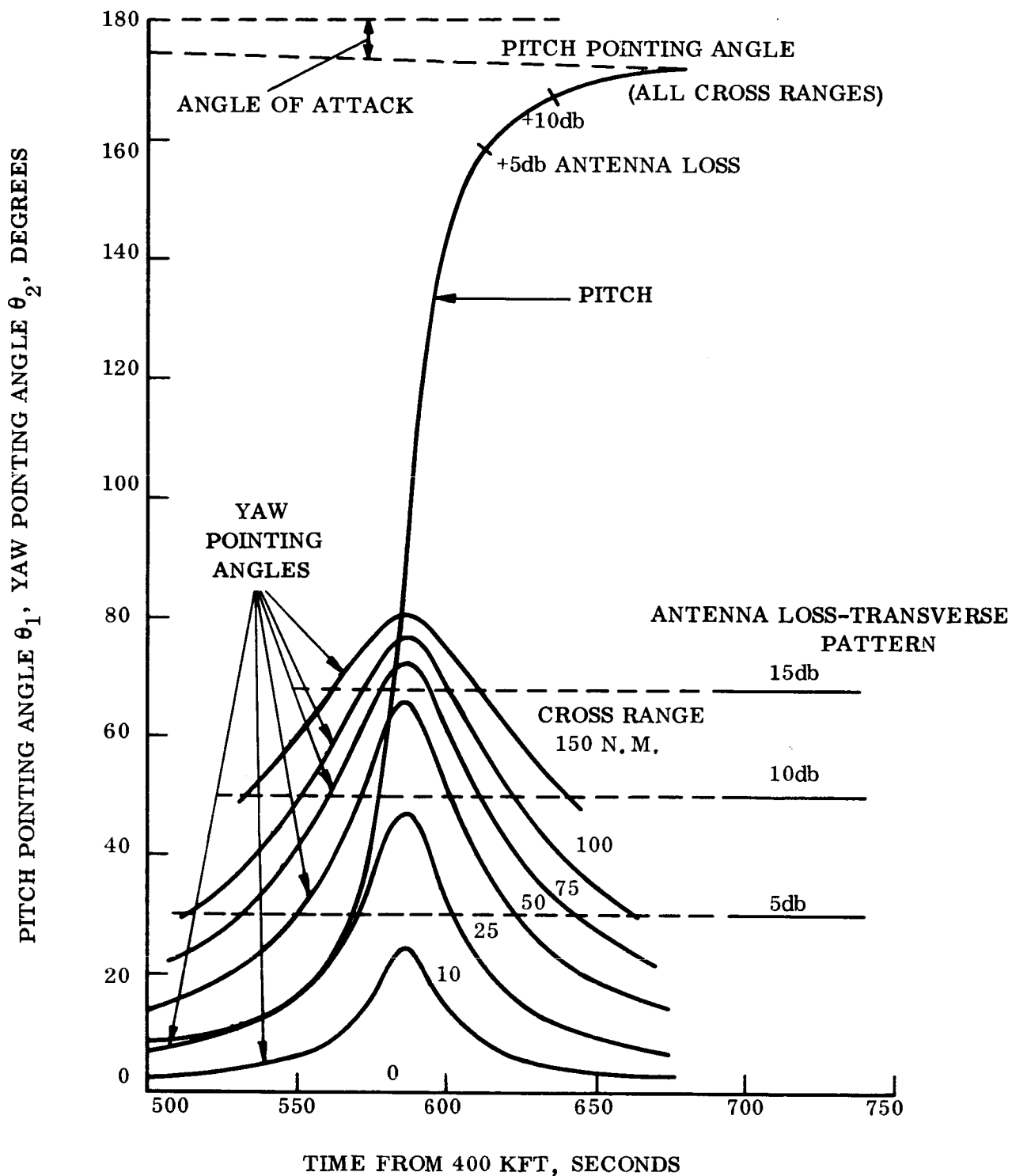


Figure 3.5-13. - Pitch and Yaw Components of Aspect Angle for 1700 N. Mi. Down Range Location, -1° Re-entry Angle

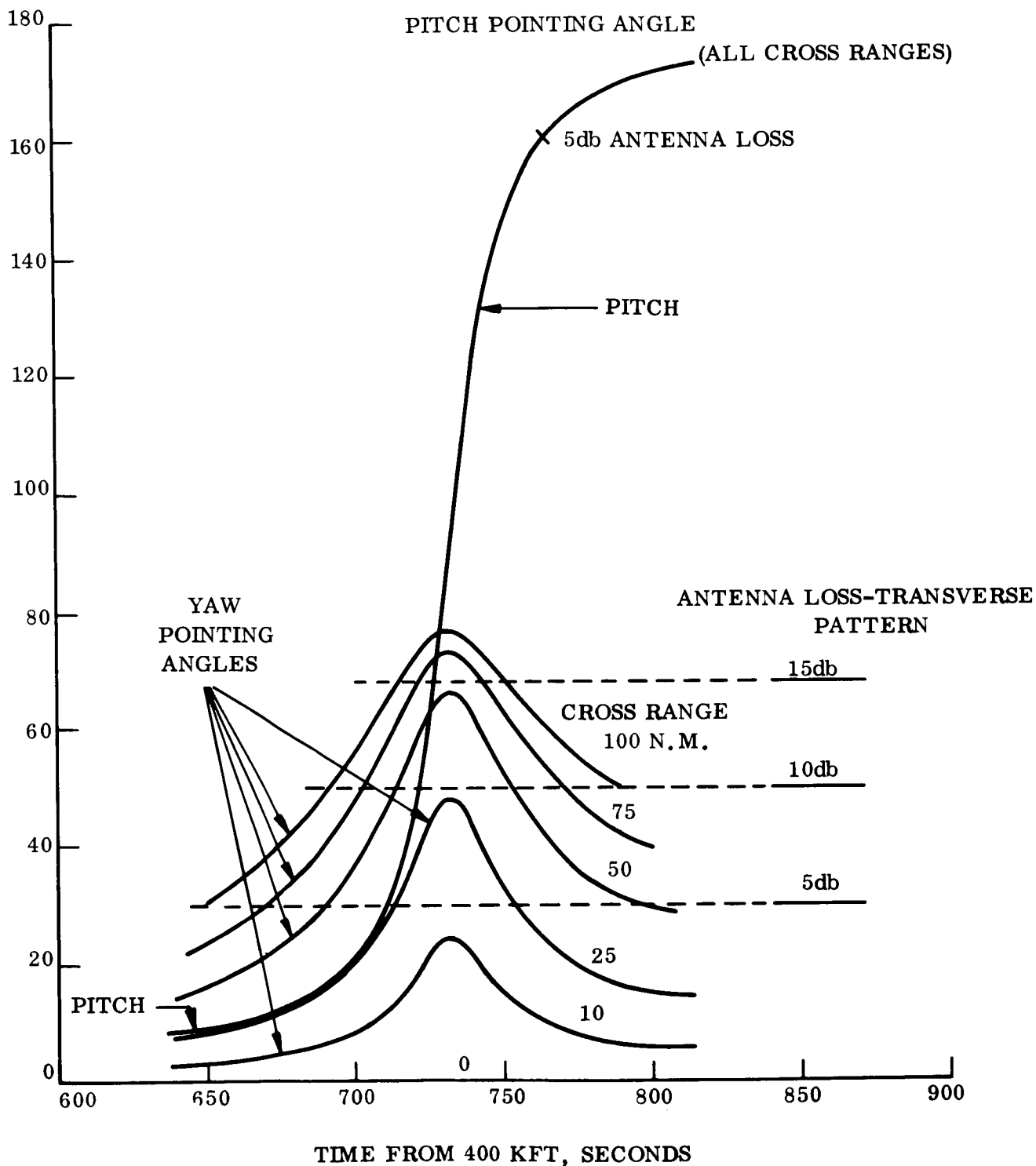


Figure 3.5-14. - Pitch and Yaw Components of Aspect Angle at 2000 N. Mi.
Down Range Location, - 1° Re-entry Angle

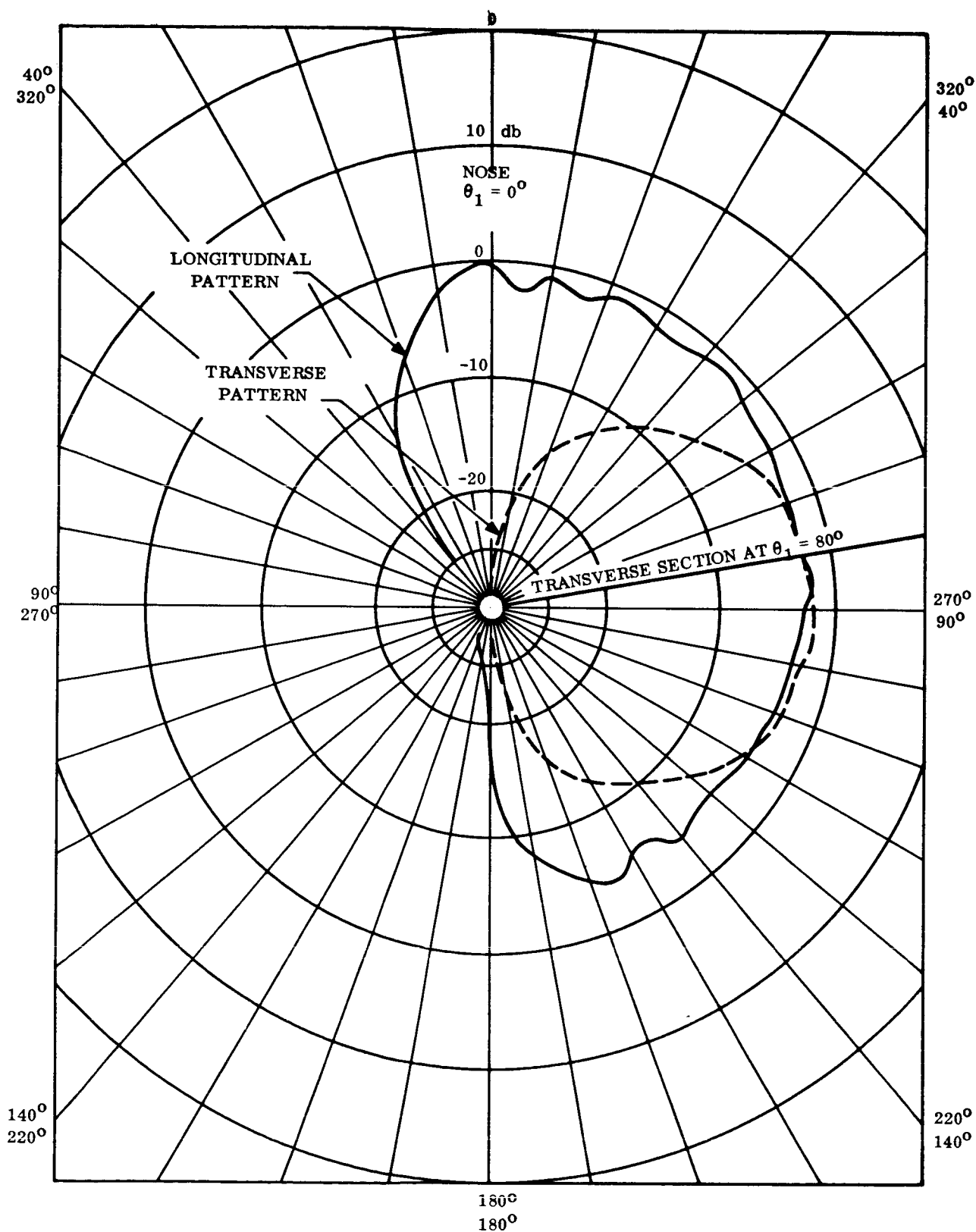


Figure 3.5-15. - Antenna Pattern

REFERENCES

- 3.5-1. Bisbing, P., Kohrs, R. and Lusen, R.: "Electromagnetic Signal Attenuation Through Hypersonic Viscous Flow Over Slightly Blunted Bodies". GE-RSD, Radiation and Space Physics TM Number 5, February, 1963.
- 3.5-2. Bisbing, P. and McElvenny, M.: "Computer Solution for Plane Wave Propagation in One-Dimensional Plasmas". GE-RSD Electromagnetic and Plasma Physics TM Number 12, October, 1963.
- 3.5-3. Bisbing, P. and Edsall, R.: "Equilibrium Boundary Layers with Contamination and Seeding". GE-RSD, Fluid Mechanics FM Number 107, June, 1964.
- 3.5-4. Walbusser, E. and Edsall, R.: "Two Dimensional Flow Field Equations for Attenuation Calculations". PIR Number 8124-712 August, 1965.
- 3.5-5. Bortner, M.H.: "Suggested Standard Kinetics for Flow Field Calculations - A Concensus Opinion". AMRAC Proceedings, Volume 14, 1966.
- 3.5-6. Instrumentation Radar AN/FPS-16 (XN-2) Department of the Navy, Bureau of Aeronautics RCA Missile and Surface Radar Div., Moorestown, New Jersey

3.6 RECOVERY FORCE STUDIES

3.6.1 INTRODUCTION

This section of the SLAMAST study report provides a discussion of some of the general problems associated with recovery of an impacted vehicle, and contains an analysis of a recovery force configured for the SLAMAST operation. Included is a discussion of development of possible areas for normal recovery, generation of the nominal impact recovery box, capabilities of some of the probable components to be incorporated into the recovery force, suggested recovery force composition, and trade-offs developed for various possible staging points of the recovery operation.

3.6.2 BASIC FLIGHT CONDITIONS

Recovery planning during this study was developed simultaneously with development in other disciplines. As revised design trajectories were generated, the results were factored into the recovery planning effort. The SLAMAST trajectories as incorporated into this final planning effort were based on the following parameters: (ref. 3.6-1)

$$\begin{aligned}V_o &= 20000 \text{ fps} \\ W/C_L S &= 200 \text{ psf} \\ \alpha_o &= 16.0^\circ \\ \gamma_o &= -1^\circ, -10^\circ\end{aligned}$$

The subscript "o" refers to conditions at 400,000 feet during re-entry. In addition, from launch at Wallops Station to the 400,000-foot altitude on the descending trajectory, the SLAMAST vehicle has travelled 620 nautical miles downrange during 420 seconds of flight (ref. 3.6-2). These design trajectories provide the boundary conditions in sizing the recovery support requirements. Combining trajectory data for both the pre-experiment and experiment-to-impact phases yields the following:

γ_o	TOTAL RANGE - NAUTICAL MILES	TOTAL TIME - SECONDS
-1°	2730	1287
-10°	2100	1259

During this study all planning was based on a launch from Wallops Station, with the conditions at 400,000 feet being reached when the SLAMAST vehicle was off the coast of Bermuda.

3.6.3 DEVELOPMENT OF NOMINAL RECOVERY BOX

Sizing of a nominal recovery box was accomplished during the planning study. As developed the dimensions of the nominal recovery area (3σ) are ± 110 n.mi. crossrange by ± 170 n.mi. up/downrange. The crossrange figure developed from considering

a 0.020 inch CG offset, which contributes ± 20 n. mi. to the crossrange error, plus a 4.5° (3σ) roll bias, which contributes ± 90 n. mi. to the total crossrange error. Range error was determined by considering variations in C_L , C_D , atmospheric density, and re-entry path angle. (ref. 3.6-4)

Range errors are compensated to some extent by the A_X , \dot{A}_X control system which accounts for variations in some of the above parameters reducing the 3σ range error from ± 450 n. mi. to ± 170 n. mi.

3.6.4 CAPABILITIES OF RECOVERY FORCE COMPONENTS

Planning for a recovery force which has the mission to detect, identify, locate, and retrieve a vehicle which has traversed through space required an analysis of the capabilities of the individual components comprising the recovery force. Components normally included in a typical recovery force include fixed-wing aircraft, surface ships, and helicopters. During this study an investigation was conducted to determine the types of equipment which could be expected to be operational and available during the period of SLAMAST flight testing. One visit was made (ref. 3.6-5) to the Office of Instrumentation Ships, NASA-GSFC, to investigate the status of the Apollo Instrumentation Ships (AIS) Program. From this visit it was learned that the primary use of the AIS assigned to the Atlantic Ocean area will be for tracking purposes. Little retrieval and recovery effort is currently envisioned for this ship. As a result, planning proceeded on the assumption that any ship assigned to the recovery force would be similar to the ARIS type, with a speed capability of 15 knots. Aircraft planning was based on the assumption that the JC-130B type would be utilized in the make-up of the recovery force. As such, all planning was based on impact occurring within an area such that this type of aircraft would have a minimum time available for search of one hour, including the effect of a one-hour launch window. The JC-130B aircraft has a cruising speed of 270 knots and an operational endurance of 10 hours. This aircraft, when assigned to recovery operations, carries standard direction finding (DF) equipment on board. An updated version of the JC-130B type aircraft, the JC-130H, is under procurement, but it is not known at this date when this aircraft is scheduled to become available in the Atlantic recovery area. The search range of the JC-130H is approximately 40 percent greater than that of the JC-130B aircraft.

The use of land based helicopters in the recovery force for the SLAMAST operation is not considered feasible due to the limited range of these vehicles. The present capability of the CH-3B helicopter is 250 n. mi., when operating from either a ship or from land. It is anticipated that range from land for this vehicle will be increased to 350 n. mi. by modifications to the aircraft. Even when so modified, however, the proposed impact areas are not within the range of capability.

3.6.5 RECOVERY FORCE COMPOSITION

Based on the size of the nominal recovery box and the capabilities of the components expected to be included, the typical recovery force for a SLAMAST operation may be configured. It is recommended that one recovery ship be assigned to this force. The purpose for this ship would be to make the actual retrieval of the SLAMAST vehicle

after the search aircraft have located it on the surface of the ocean. For purposes of search it is recommended that a minimum of three JC-130 type aircraft be assigned to the operation. It is recommended that pararescue teams are provided as an integral part of the aircraft complement. When flying at 30,000 feet altitude these aircraft have a line-of-sight capability of approximately 200 n.mi.; therefore, three aircraft would provide complete coverage of the nominal recovery box.

3.6.6 PROPOSED RECOVERY AREA

Figure 3.6-1 depicts a proposed recovery area for each of two typical trajectories under consideration for SLAMAST flight testing. Both trajectories are based on a launch from Wallops Station, with the 400,000-foot re-entry point being reached when the trajectory ground trace is approximately southeast of the island of Bermuda. The Range Safety Limit Line constraint was arbitrarily placed at 100 n. mi. from any inhabited areas. The capability of the JC-130 aircraft to maintain a one-hour (minimum) "On-Station" search capability is also depicted. It is shown that for the case of the 1⁰ DFH trajectory it would be necessary to stage from San Fernando Island, while for the 10⁰ DFH case staging should be made from Trinidad. It should be noted that Trinidad is an active installation of the Air Force Eastern Test Range (AFETR) and all requirements for staging may be easily met; staging from San Fernando, however, would require more extensive preparations in as much as this location, although a station of AFETR, is on an inactive status, and would have to be reactivated.

REFERENCES

- 3.6-1. R. Grasier, Private Conversations.
- 3.6-2. L. Chimielewicz, PIR 8142-1095 3/9/67.
- 3.6-3. F. Bailey, PIR 8193-343.
- 3.6-4. R. Grasier, Private Conversation.
- 3.6-5. E. Simpson, TR #29, 2/23/67.

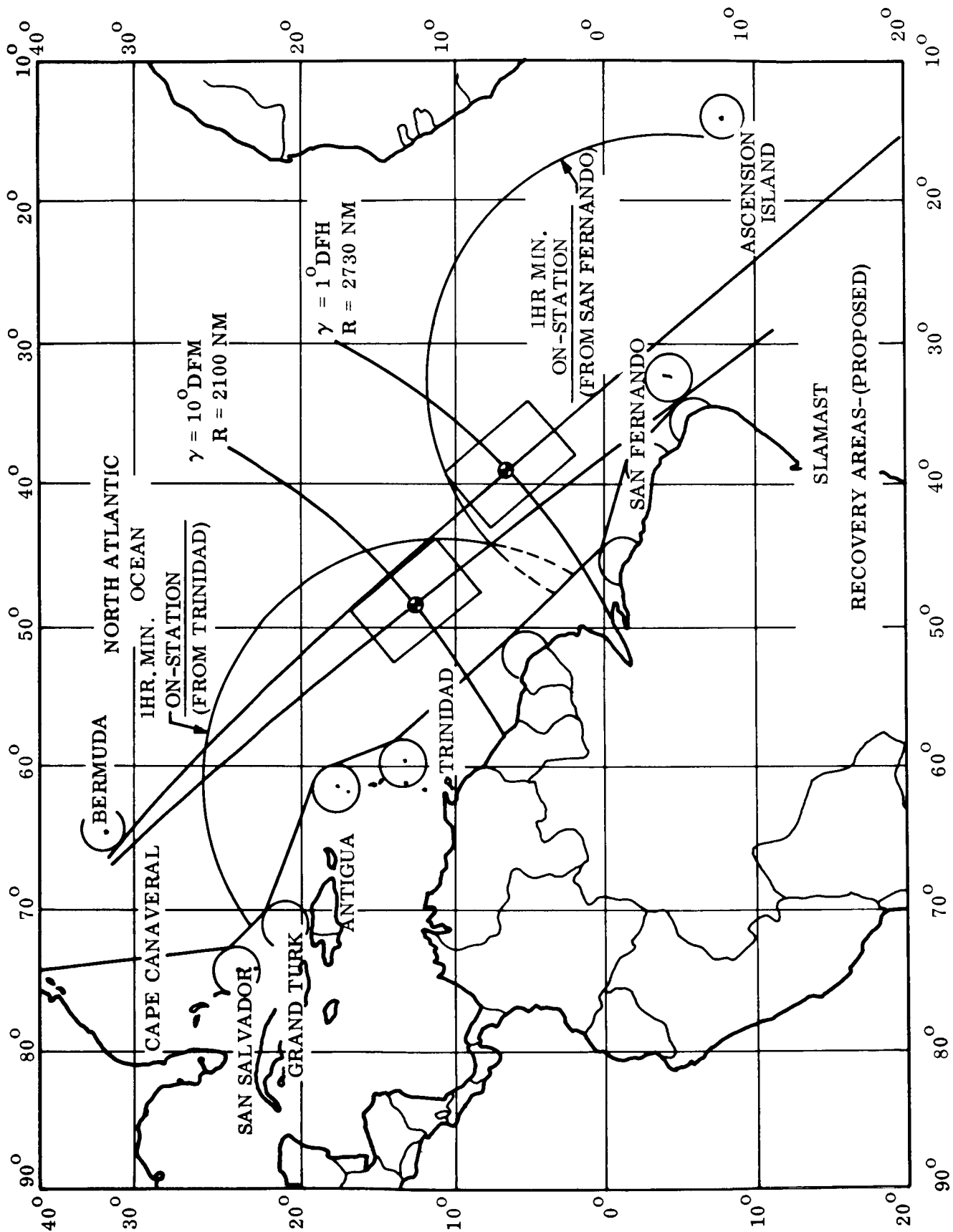


Figure 3.6-1. - Proposed Recovery Area

3.7 RANGE SAFETY STUDIES

3.7.1 INTRODUCTION

A preliminary study of the Range Safety Constraints for conducting SLAMAST flight tests from Wallops Island to an impact area suitable for recovery has been investigated. For the two design trajectories ($V_e = 20,000$ fps @ $-1^\circ \leq \gamma_e \leq -10^\circ$) a worst case malfunction footprint has been computed. This footprint assumes failures at Re-entry (400,000 feet) and at 350 seconds after re-entry.

The simultaneous failures assumed for generating the footprint for both cases produces the maximum range and cross dispersion possible based on the known performance characteristics of the SLAMAST spacecraft.

3.7.2 DISCUSSION

3.7.2.1 Range safety definition. - The criteria to be used in determining the extent of any range safety problem is shown in Figure 3.7-1. This figure presents typical flight trajectories for the -1° and -10° design trajectories constructed to allow the maximum distance from inhabited land masses, while still providing a reasonable capability of supporting a recovery operation.

A 100 nautical mile radius was constructed around each land mass as a range safety provision and then each point was connected to derive the range safety limit line.

At critical points along each design trajectory, the range and cross range limitations were determined and is plotted as a range safety limit line in Figures 3.7-2, 3.7-3, 3.7-4 and 3.7-5.

3.7.2.2 Range safety footprint. - In order to determine the worst case failures; i.e. maximize spacecraft range and cross range, the following two sets of conditions were assumed:

(1) Failure at re-entry

(a) $\text{Max } \frac{L}{D}$

(b) Pitch flap fixed at 13 degree for entire flight (αF)

(c) Trim angle of attack is 9 degree for entire flight (αT).

(d) Bank angle (ϕ) fixed at positions from 0 to 180 degrees.
for entire flight.

(2) Same as preceding, except failure is assumed at 350 seconds from re-entry.

The footprints resulting from each set of assumed conditions is shown in Figures 3.7-2 through 3.7-5. With the exception of the failure at 350 seconds, ($V_e = 20,000$ FB, $\gamma_e = -10^\circ$) the cross range safety limits were exceeded. In addition, for the bank angles of less than -15 degrees, the extension in range will produce a downrange safety condition in the vicinity of San Fernando Island. Therefore, the cross range and downrange control problem is significant for failures at re-entry, and somewhat relieved at failures occurring at 350 seconds, but in either case a flight termination method/system must be used in order to satisfy the range safety constraints.

3.7.3 FLIGHT TERMINATION CONSIDERATIONS

The design of a flight termination system for this study contract phase was considered to be an unrealistic goal, based on the probable failure modes to be investigated to incorporate all contingent malfunctions, and therefore a discussion of possible flight termination methods is presented with the actual requirements remaining for a future study.

Figures 3.7-6 through 3.7-9 present the time dependent range and cross-range dispersion based on failures at re-entry for both design trajectories. We shall limit the discussion to Figures 3.7-6 and 3.7-7 as a representative case.

In Figure 3.7-6 at the normal retardation time of 700 seconds, the deviation from the nominal range of 1360 n. mi. can be +480 miles - or - -780 n. mi. for $\text{MAX } \frac{L}{D}$ and bank angles of $\phi = 0$ and $\phi = \pm 60$ degrees respectively. In addition

to the range safety problem this creates, there will be no possibility of recovering the spacecraft. Therefore, a time/range requirement must be imposed on the spacecraft control system to constrain the dispersion to at least the nominal recovery footprint which is ± 170 n. mi. in range and ± 110 n. mi. in cross range, at the nominal time for retardation or 700 seconds, with the flight terminating at any time beyond this time.

This means that an on-board system/systems will be required to determine downrange and crossrange from nominal in order to anticipate flight termination conditions. The on-board system is recommended because the present planning for ship placement only utilizes one tracking ship at each extreme end of the constant altitude trajectory with the decision time for flight termination at a minimum. In addition command destruct requires omnidirectional antenna capability.

The use of spinup as a flight termination method requires that the spacecraft maintain roll reference, and have the required gas system capability to provide the spinup conditions. The mechanics and details in determining the optimum spinup conditions, the gas system adequacy, and provisions for a possible redundant roll reference system is beyond the scope of this report, and should be studied in detail at a later date.

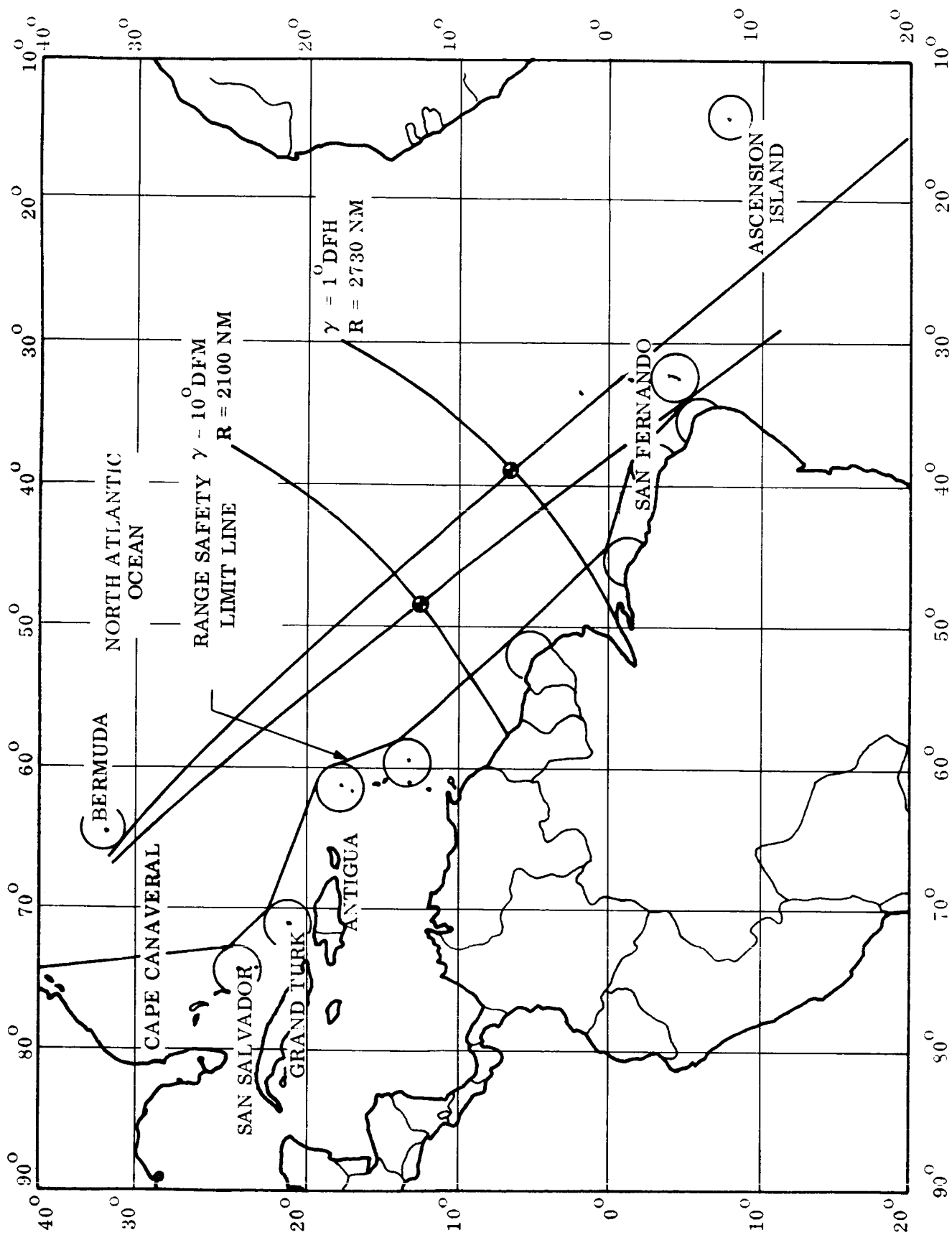


Figure 3.7-1. - Range Safety Definitions

$V_e = 20,000 \text{ FPS.}$ $\alpha_T = 9^\circ$
 $\gamma_e = -1^\circ$ $\delta_F = 13^\circ$
 MAX L/D

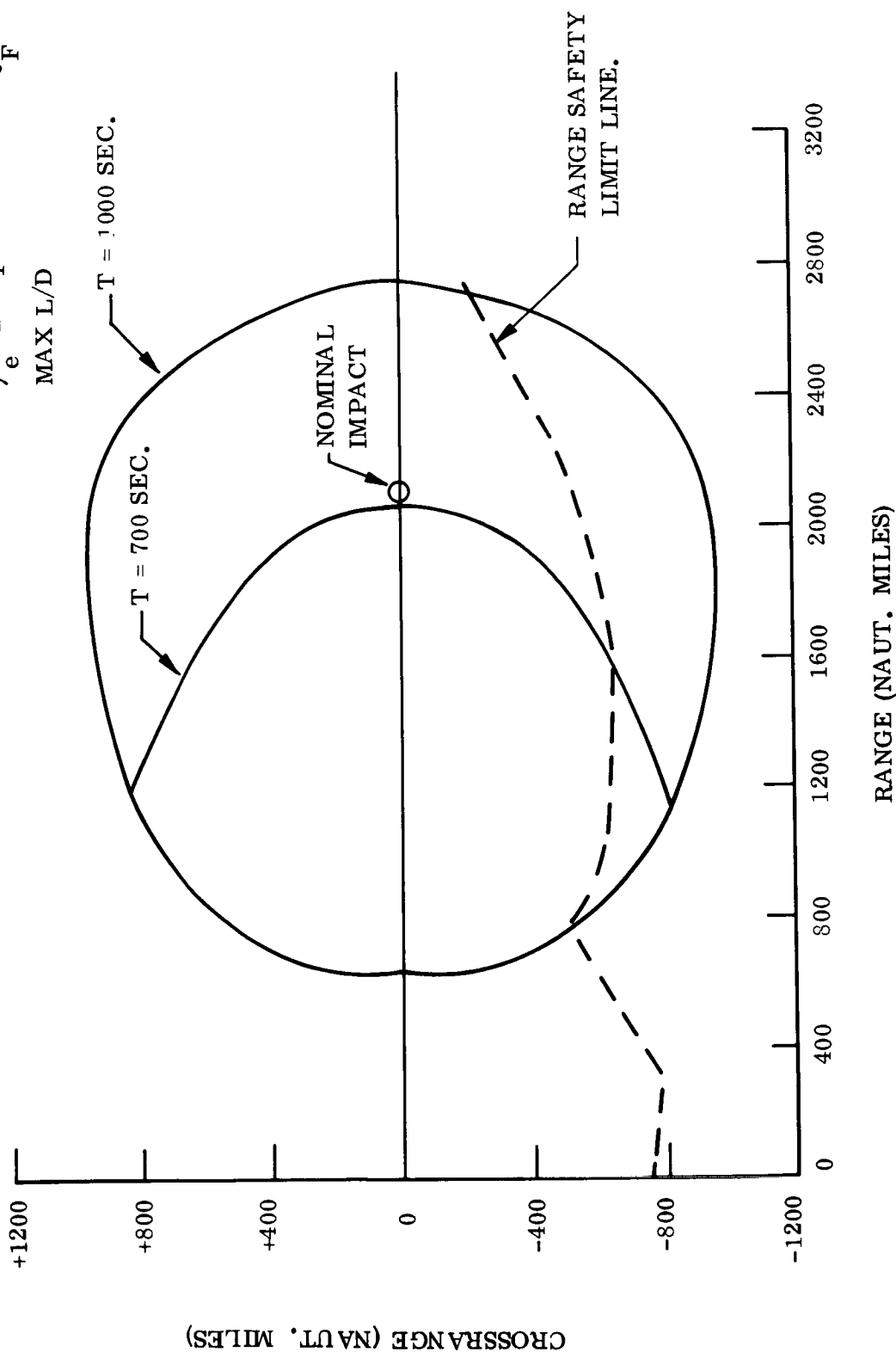


Figure 3.7-2. - SLAMAST Range Safety Footprint, Failure at Re-entry at -1°

$V_e = 20,000 \text{ FPS}$
 $\gamma_e = -10^\circ$
 $\text{MAX } L/D$
 $\alpha_T = 9^\circ$
 $\delta_F = 13^\circ$

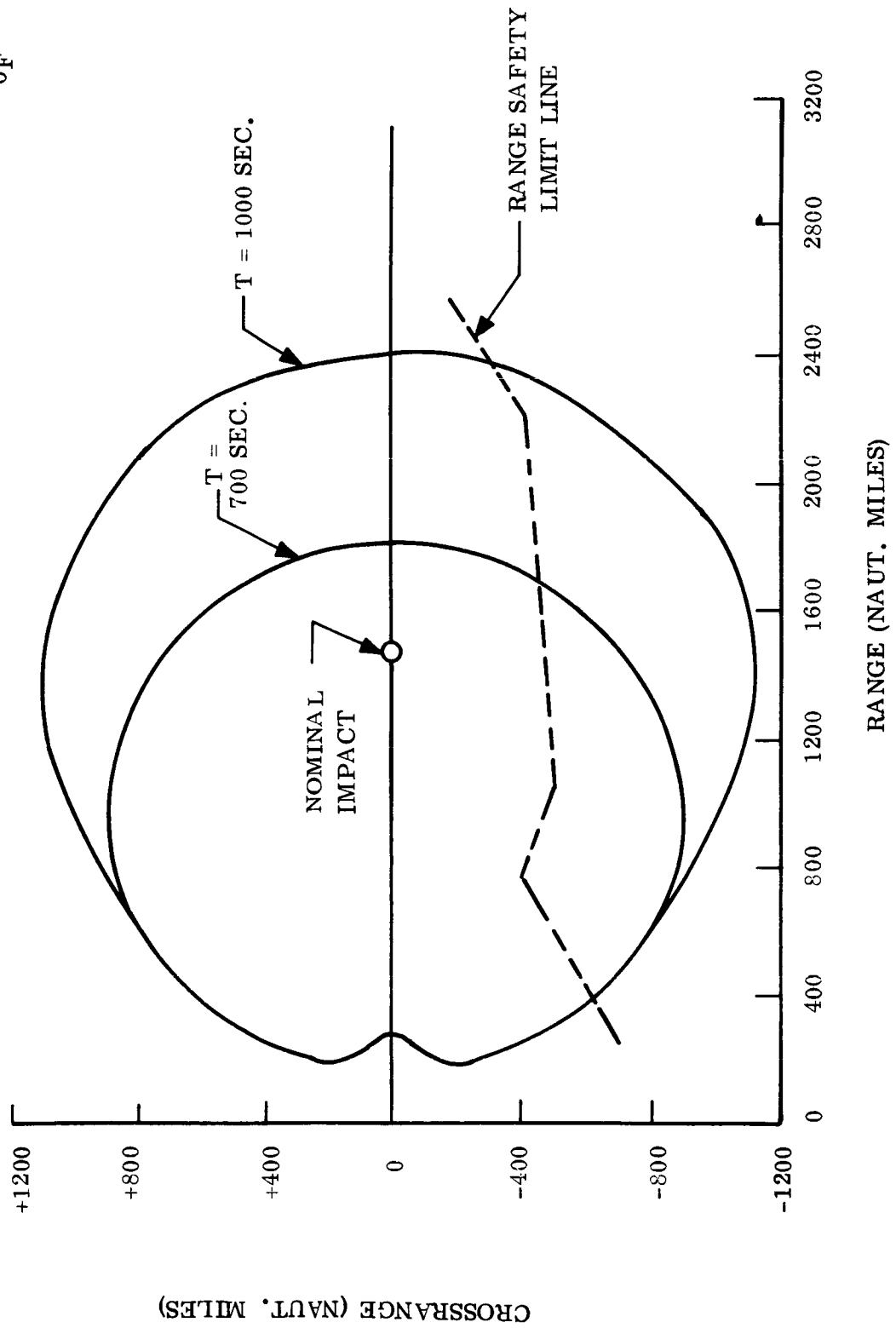


Figure 3.7-3. - SLAMAST Range Safety Footprint, Failure at Re-entry at -10°

$V_e = 20,000 \text{ FPS}$
 $\gamma_e = -1^\circ$
 $\text{MAX } L/D$
 $\alpha_T = 9^\circ$
 $\delta_F = 13^\circ$

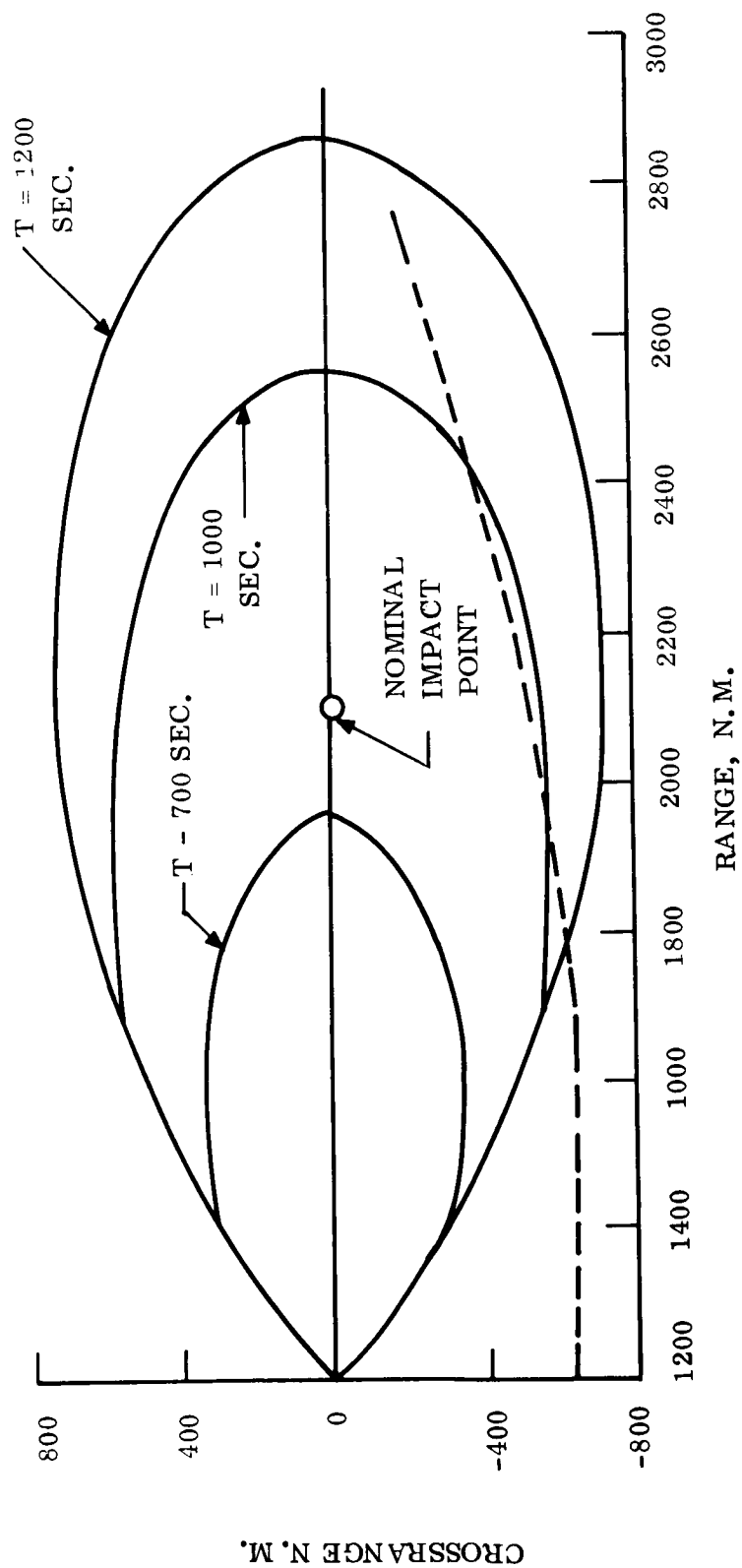


Figure 3.7-4. - SLAMAST Range Safety Footprint, Failure at 350 Secs. from Re-entry at -1°

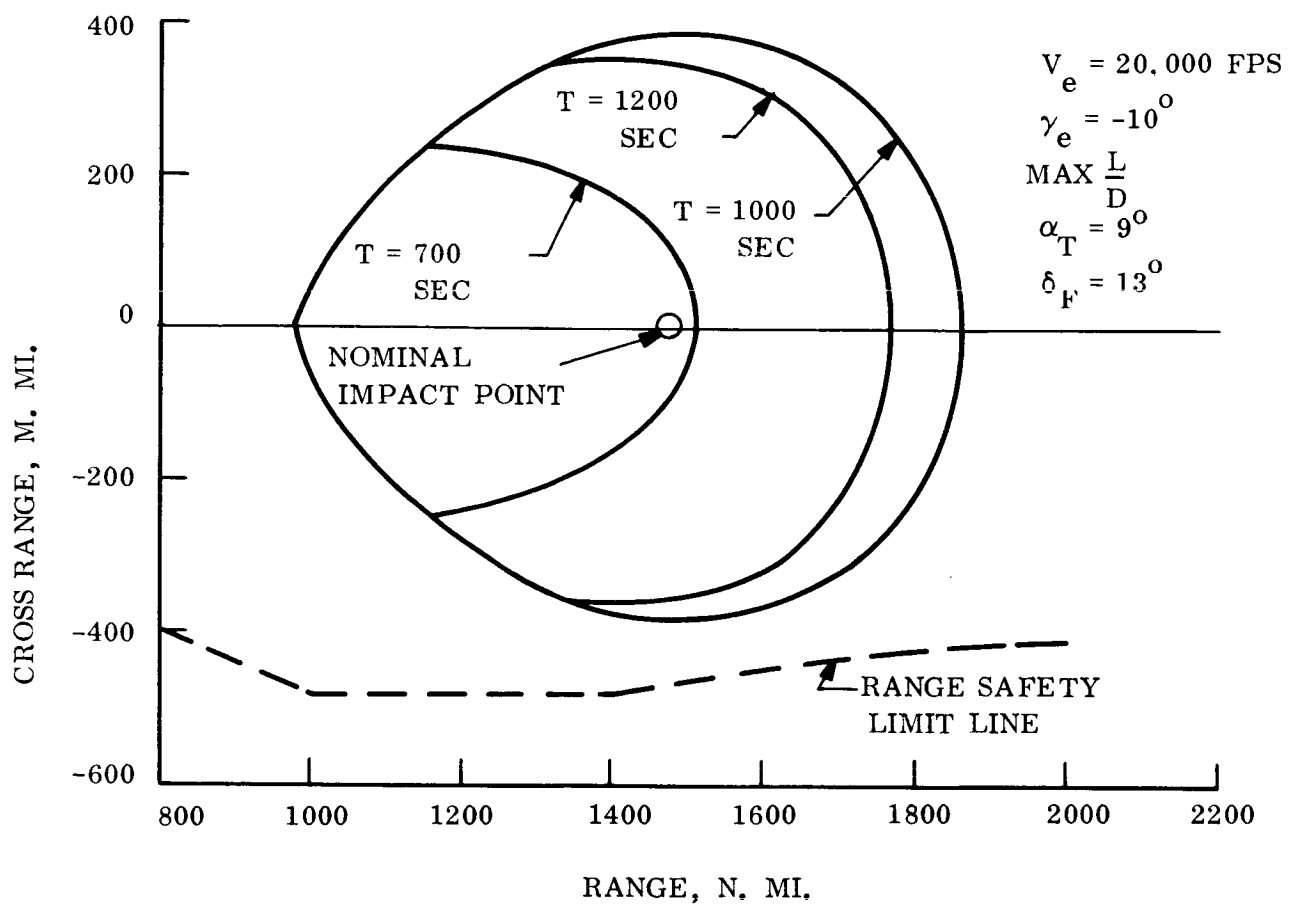


Figure 3.7-5. - SLAMAST Range Safety Footprint, Failure at 350 Secs. from Re-entry at -10°

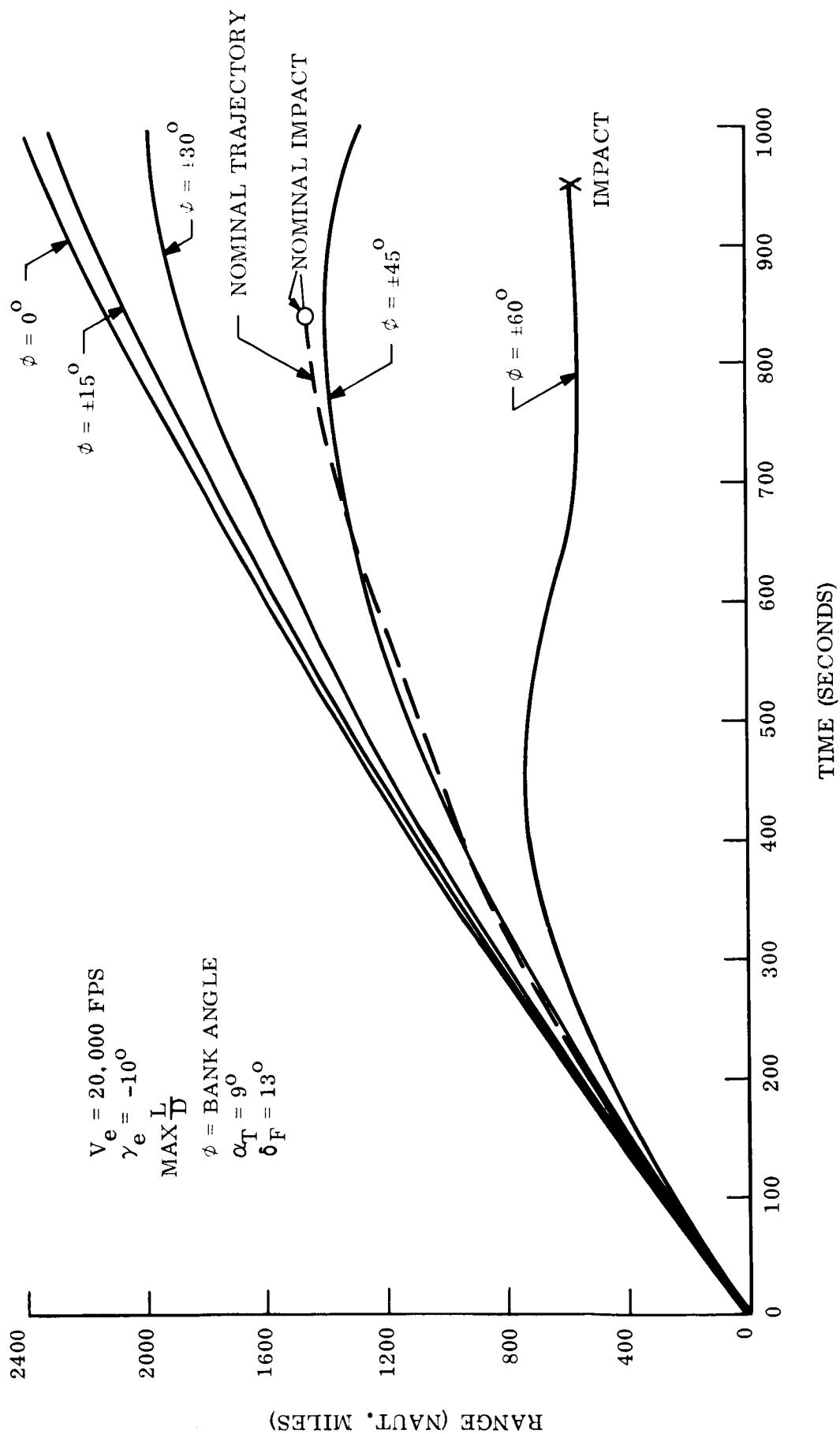


Figure 3.7-6. - Downrange Dispersion Failure at Re-entry, $\gamma_E = -10^\circ$

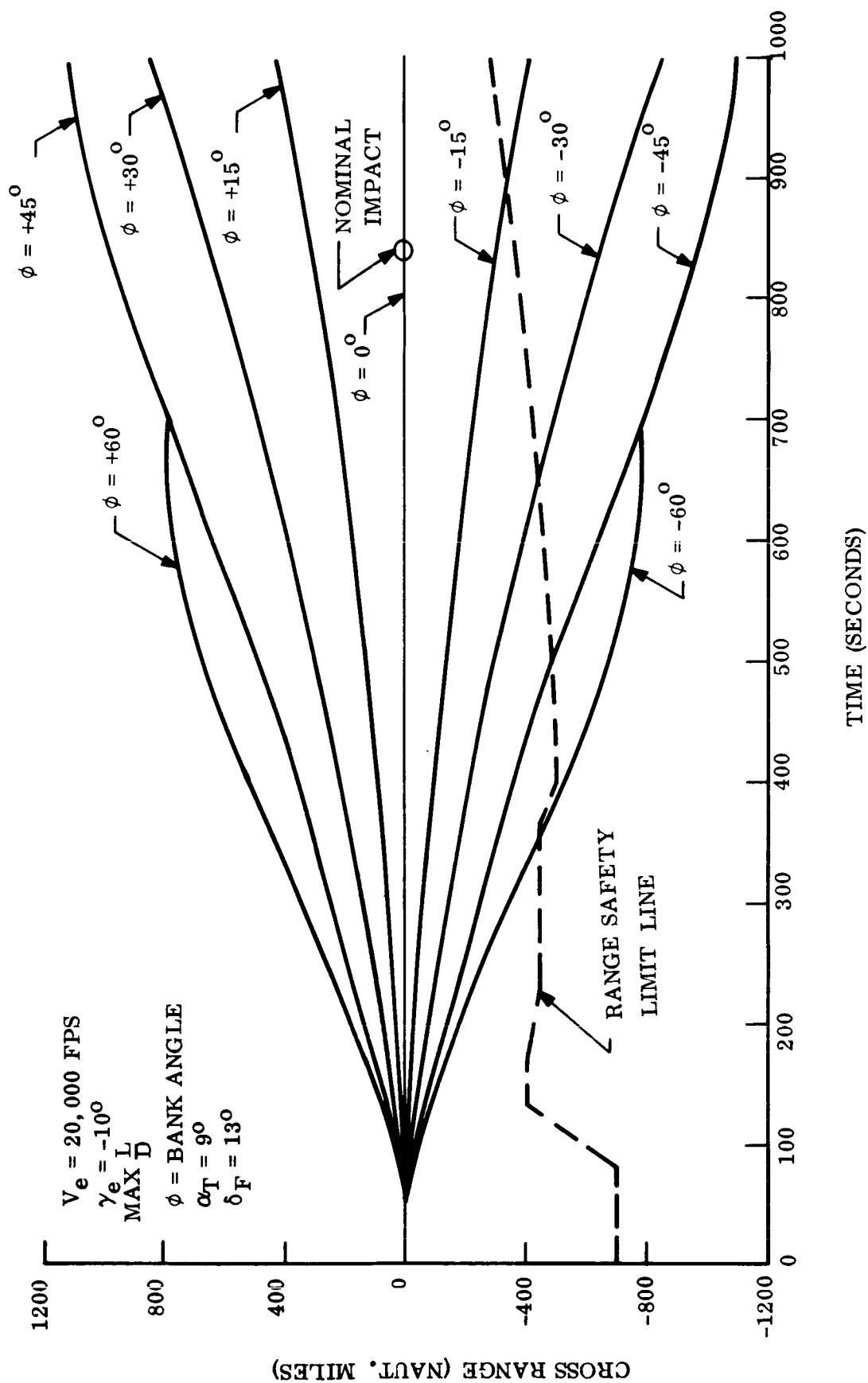


Figure 3.7-7. - Crossrange Dispersion Failure at Re-entry, $\gamma_E = -10^\circ$

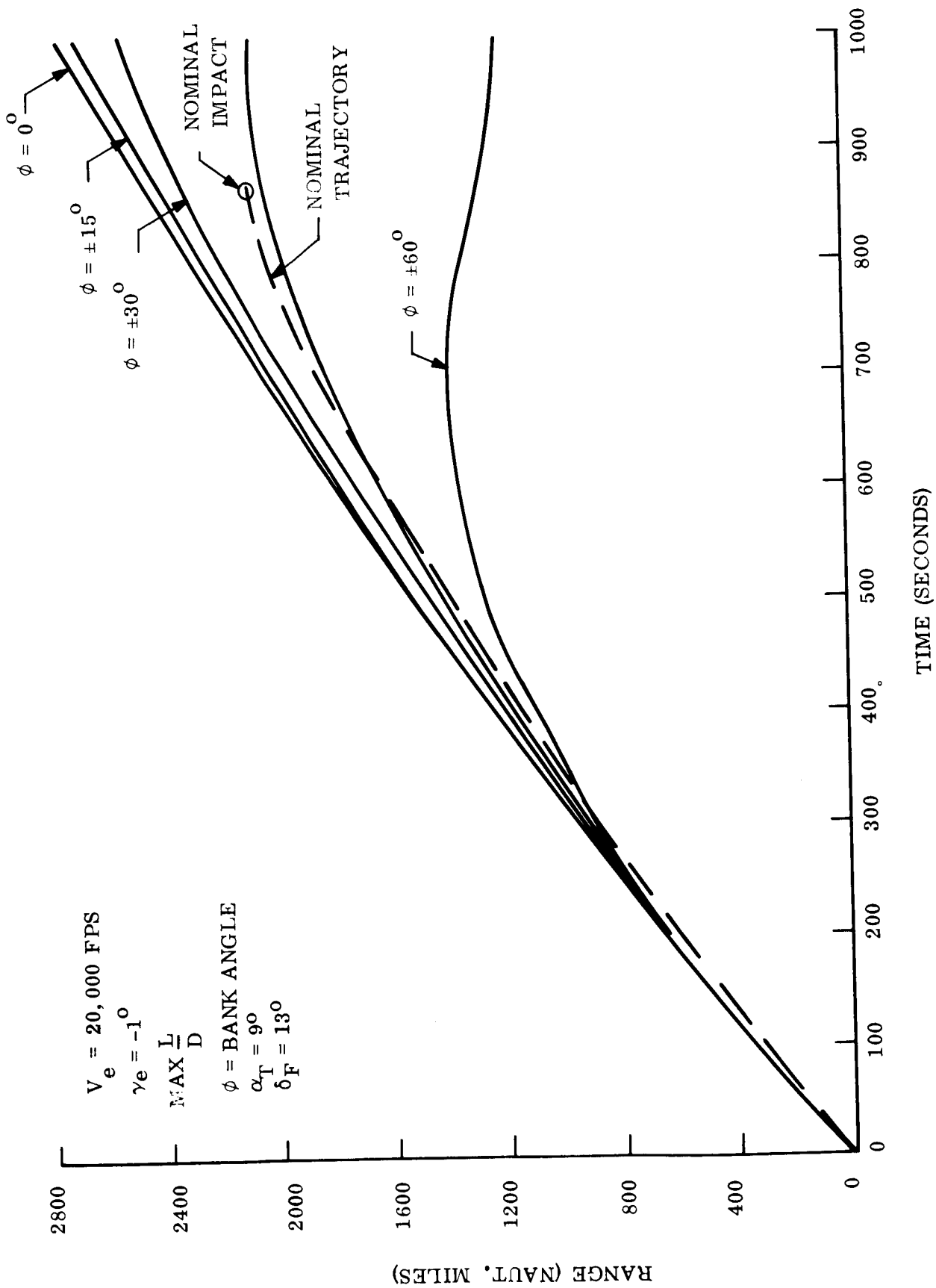


Figure 3.7-8. - Downrange Dispersion Failure at Re-entry, $\gamma_E = -1^\circ$

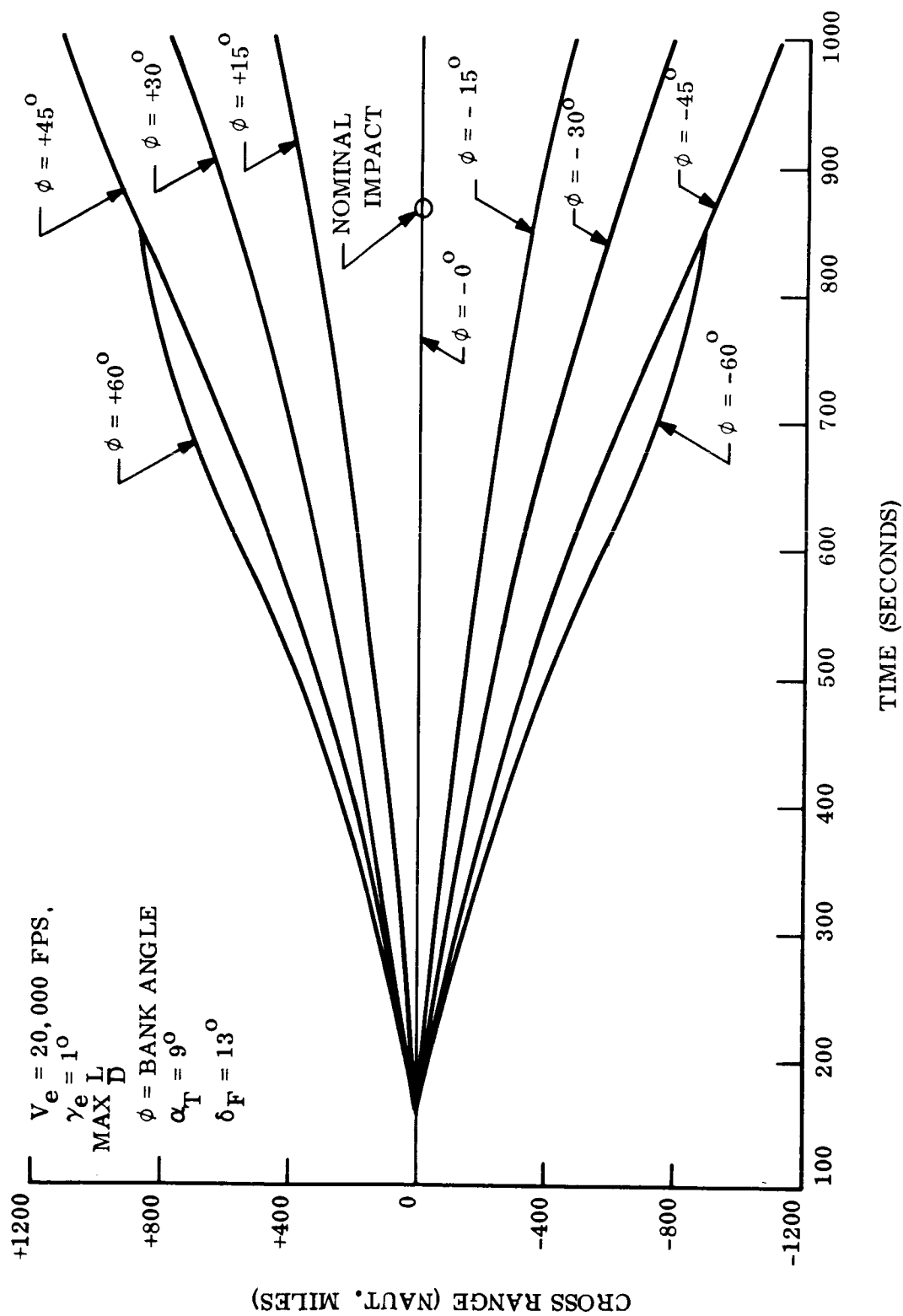


Figure 3.7-9. - Crossrange Dispersion Failure at Re-entry, $\gamma_E = -1^\circ$